DOE/ER-0045/10

Alloy Development for Irradiation Performance

Semiannual Progress Report
For Period Ending March 31, 1983

U.S. Department of Energy
Office of Fusion Energy

Printed in the United States of America Available from
National Technical Information Service
U S Department of Commerce
5285 Port Royal Road, Springfield, Virginia 22161
NTIS price codes—Printed Copy All Microfiche A01

DOE/ER-0045/10
Distribution
Category
UC-20, 20c

ALLOY DEVELOPMENT FOR IRRADIATION PERFORMANCE SEMIANNUAL PROGRESS REPORT FOR PERIOD ENDING MARCH 31. 1983

ARGONNE NATIONAL LABORATORY

GA TECHNOLOGIES, INC.

McDONNELL DOUGLAS ASTRONAUTICS COMPANY

MASSACHUSETTS INSTITUTE OF TECHNOLOGY

NAVAL RESEARCH LABORATORY

OAK RIDGE NATIONAL LABORATORY

SANDIA NATIONAL LABORATORIES

WESTINGHOUSE ADVANCED ENERGY SYSTEMS DIVISION

WESTINGHOUSE HANFORD COMPANY

Date Published: October 1983

Prepared by
OAK RIDGE NATIONAL LABORATORY
Oak Ridge, Tennessee 37830
operated **by**
UNION CARBIDE CORPORATION
for the
U. S. DEPARTMENT OF ENERGY
Under Contract No. W-7405-eng-26

previously issued in this series are as follows:

DOE/ET-0058/1	Period Ending March 31, 1978
DOE/ET-0058/2	Period Ending June 30, 1978
DOE/ET-0058/3	Period Ending Seotember 30, 1978
DOE/ET-0058/4	Period Ending December 31, 1978
DOE/ET-0058/5	Period Ending March 31, 1979
DOE/ET-0058/6	Period Ending June 30, 1979
DOE/ET-0058/7	Period Ending September 30, 1979
DOE/ER-0045/1	Period Ending December 31, 1979
DOE/ER-0045/2	Period Ending March 31, 1980
DOE/ER-0045/3	Period Ending June 30, 1980
DOE/ER-0045/4	Period Ending September 30, 1980
DOE/ER-0045/5	Period Ending December 31, 1980
DOE/ER-0045/6	Period Ending March 31, 1981
DOE/ER-0045/7	Period Ending September 30, 1981
DOE/ER-0045/8	Period Ending March 31, 1982
DOE/ER-0045/9	Period Ending September 30, 1982

This report is the seventeenth in a series of Technical Progress Reports on ***"Alloy Development far Irradiation Performance"*** (ADIP), which is one element of the Fusion Reactor Materials Program, conducted in support of the Magnetic Fusion Energy Program of the U.S. Department of Energy. Other elements of the Materials Program are

- *Damage Analysis* ***and Fundamental Studies*** *(DAFS)*
- ***Plasma-Yaterials*** *Interaction (PMI)*
- *Special-Purpose* ***Materials*** *(SPM)*

The first seven reports in this series are numbered DOE/ET-0058/1 through 7. This report is the tenth in a new numbering sequence that begins with DOE/ER-0045/1.

The ADIP program element is a national effort composed of contributions from a number of National Laboratories and other government laboratories, universities, and industrial laboratories. **It** was organized by the Materials and Radiation Effects Branch, Office of Fusion Energy, DOE, and a Task Group on *Alloy* ***Development*** *for Irradiation* ***Performance,*** which now operates under the auspices of the Reactor Technologies Rranch. The purpose of this series of reports is to provide a working technical record of that effort for the use of the program participants, for the fusion energy program in general, and for the Department of Energy.

This report is organized along topical lines in parallel to a Program Plan of the same title so that activities and accomplishments may be followed readily relative to that Program Plan. Thus, the work of a given laboratory may appear throughout the report. Chapters 1, 2, 8, and 9 review activities on analysis and evaluation, test methods development, status of irradiation experiments, and corrosion testing and hydrogen permeation studies, respectively. These activities relate to each of the alloy development paths. Chapters 3, 4, 5, 6, and 7 present the ongoing work on each alloy development path. The Table of Contents is annotated for the convenience of the reader.

This report has been compiled and edited under the guidance of the Chairman of the Task Group on *Alloy* ***Development*** *for* ***Irradiation*** *Performance.* E. E. Bloom, Oak Ridge National Laboratory, and his efforts and those of the supporting staff of ORNL and the many persons who made technical contributions are gratefully acknowledged. T. C. Reuther, Reactor Technologies Branch, is the Department of Energy Counterpart to the Task Group Chairman and has responsibility for the AOIP Program within DOE.

G. M. Haas, Chief
Reactor Technologies Branch
Office of Fusion Energy

CONTENTS

1. ANALYSIS AND EVALUATION STUDIES

1.1 MATERIALS HANDBOOK TOR FUSION ENERGY SYSTEMS - J. W. Davis (McDonnell Douglas Astronautics Company - St. Louis Division) and T. K. Bierlein (Westinghouse Hanford Company)

1.1.1 ADIP 'Task

Task Number 1.A.1 - Define material property requirements and make structural life predictions

1.1.2 Objective

To provide a consistent and authoritative source of material property data for use by the fusion community in concept evaluation, design, safety analysis, and performance/verification studies of various fusion energy systems. A secondary objective is the early identification of areas in the materials data base where insufficient information or voids exist.

1.1.3 *Summary*

During the past year the handbook effort has been directed towards developing data sheets. For this year the effort has been to incorporate those data sheets into the handbook. Substantial progress has been made towards the achievement of this goal with the publication of more than *30* new data pages covering the properties of bulk graphites, liquid lithium, and ceramic lithium compounds.

1.1.4 Progress and Status

While the Materials handbook fur fusion energy systems (MHFES) still has a long way to go it is beginning to look like a materials handbook. With the addition of the last three publication packages (5, 6, and 7) the MHFES now contains information on materials for four of its eight major chapters. The latest additions to the handbook consist of data pages on the propertics of hulk or structural graphite, prepared by D. J. Suiter of MDAC; properties of liquid lithium, prepared by W. Brehm of HEDL; and properties of ceramic lithium compounds prepared by G. W. Hollenberg of HEDL. These data sheets cover materials used in two important areas in reactor design: 1st wall protection and tritium production.

The impact of particles emitted from the plasma on the first wall can lead to rapid erosion of the structure or in the case of plasma disruptions vaporization of the surface layer. A number of approaches have been proposed to protect this structure ranging from coatings Lo tiles. Carbon or more specifically graphite is one of the materials proposed for use as tiles. In the application of carbon to fusion reactor components, it is often treated as a material with a single set of propertics rather than as a family of materials whose properties are tailored to fit a specific application. Depending upon the degree of crystallinity and crystal orientation, it can be described as bulk graphite, fibrous graphite, pyrolytic, or vitreous carbon each having different properties. The data sheets in the MHFES presents the properties of five different types of bulk graphite. These data pages allow the designer to compare the various bulk graphites available and then to select the one most suited to his needs using a consistent data set.

Fusion reactors that are based on the D-T fuel cycle will be required to breed their own tritium fuel. The production of tritium can be accomplished through the use of liquid lithium, lithium bearing salts, or lithium ceramic compounds. The handhook concentrated on two areas: liquid lithium and lithium oxide ceramic compounds (binary and ternary). The liquid lithium data sheets were prepared in support of work performed for FMIT and consist of information needed to use liquid lithium as a coolant, e.g. thermal conductivity, viscosity, and surface tension. The lithium ceramic data sheets were prepared in support of the solid breeder studies. These data sheets cover four separate lithium ceramic compounds (Li_2O, Li_4SiO_4, Li_2ZrO_3 and $LiAlO_2$) and represent new data specifically developed for the fusion program. These data sheets consist of specific heat and thermal expansion both as a function of temperature and the theoretical density as a function of isotopic enrichment. Additional lithium ceramic: data sheets are in development and will he released at a later date.

In addition to the data sheets that have been incorporated into the handbook during this reporting period there are a number of data sheets in the review cycle and, pending approval, will be released in the next period. These data sheets will cover two different areas of reactor design: 1st Wall/Blanket structural material and magnet materials. The 1st Wall/Blanket structural material is a Ferritic Steel designated HT-9, while the magnet structural material is 31h *LS*. The inclusion of HT-9 in the handbook represents the first step in expanding the information in each handbook chapter Lo include more than one material.

1.1.5 Conclusions

While substantial progress has been made with regard to putting information in the handbook during this period, more work is needed on the part of everyone, reviewers and page preparers included. There are still a number of data pages in the review cycle awaiting approval, however, once these data pages are included in the handbook additional new data pages will be needed if the current momentum is to be sustained. Researchers in ADIP and other task groups can help by turning their experimental results into data sheets.

1.2 LOW ACTIVATION APPROACHES TO MATERIALS DEVELOPMENT - D. S. Gelles, H. R. Brager and F. A. Garner (Uestinghouse Hanford Company)

1.2.1 ADIP Task

The Department of Energy Office of Fusion Energy has cited the need for development of low activation alloys. While such development could be undertaken as part of Path D (Innovative Materials), it is proposed that portions of this effort proceed in the established Path A (Austenitic) and Path E (Ferritic) programs. The scope of such an effort is similar to that described in Task 1.A.2, "to define material property test matrices and test procedures that will provide efficient develooment of long life and reliable alloys considering time, cost and test facility constraints."

1.2.2 Objective

The objective of this work is to identify three orornising compositional regimes with potential for low activation structural alloys.

1.2.3 Summary

An effort has been initiated to develop low-activation alloys for fusion reactor service. Several major compositional regimes have been identified for development. The aporoach employed has been to develoo low activation alloys via routes which may mitigate oreviously identified material problems.

1.2.4 Proqress and Status

1.2.4.1 Introduction

The Nuclear Regulatory Commission in January 1983 established a regulation designated 10-CFR-61, which governs the land disposal of nuclear waste. This regulation is based on fission reactor experience and currently covers a limited number of radionuclides. The limits established fnr each isotope involve not only activity and decay rate considerations but also heat generation and rate of transport in the biosphere. It is anticipated that the list of covered radionuclides will expand as fusion-relevant spectra and materials are consiaerea.

Calculations of the induced radioactivity in the STARFIRE first wall position have recently been performed and compared to the restrictions Dosed by 10-CFR-61.[1-3] Serious limits are found to be olaced on N (3300 ppm) Ni (9100 ppm), Nb (2.9 ppm) and Mo (470 ppm).[3] The restriction on nickrl in particular seriously complicates alloy development via paths A, B and D and the restriction on molybdenum siqnificantly restricts the Paths C and E options. Therefore, new alloy compositional reqimes must be developed if low activation materials are required for first wall applications.

Several promising compositional reqimes have been identified wherein the potential for low-activation structural alloys is perceived. One of these lies in the austenitic system and two others lie in the ferritic system. There is an interest in these materials both in the ADIP proqram and the Damaoe Analysis arid Fundamental Studies (DAFS) Program of the U. S. Fusion Materials effort .

1.2.4.2 Austenitic Alloys

The nickel and chromium Content of Fe-Cr-Ni alloys has been shown to have a large effect on the swelling behavior of irradiated ternary alloys.[4-6] In general the qreatest resistance to the onset of accelerated swelling in this system corresponds to the comoositional regime which possesses anomalous hehavior of properties such as low-temperature expansivity, lattice parameter, Curie temperature, temperature dependence of the magnetization, resistivity, increases in magnetization upon application of magnetic fields, and forced volume magnetostriction. One of the most marked consequences of this anomalous behavior is the Invar anomaly, the very small coefficient of thermal expansion.

The possible relation between swelling resistance and Invar-like hehavior is supported hy the fact that the dependence of swelling with chromium content is similar to that exhihited by the low-chromium Invar-like alloys'designated aS Elinvar.[4] If the Invar-swelling relationship is valid then there is optimism that other anarnalous alloys may also exhibit minimums in swelling. Invar anomalies have been observed in the Fe-Mn[7-10] and Fe-Mn-Cr[7] systems. Although Fe-Mn allovs have anomalous thermal exoansion similar to that of Invar alloys, they are nonferromagnetic in nature, in contrast to Fe-Ni, Fe-Pt and Fe-Pd hase Invar alloys.[12] Therefore, substitution of manganese for nickel appears to be a possible approach within Path A to develop low activation alloys.

The motivations for substituting manganese for nickel include in addition its abundance within the U. S., its lower residual activity and the possibility that manqanese-based alloys might exhibit different swelling properties than nickel-based alloys. Research on such alloys has been pursued for non-radiation environments (e.g. ref 13, 14) and some swelling studies have been conducted using high energy electrons.[15]

The Fe-Cr-Mn system is now being studied in the DAFS program and an experimental alloy matrix is heinq prepared for possible inclusion in upcoming fast reactor irradiations. Manqanese-stahilized alloys are not anticipated for inclusion in mixed spectrum reactors such as HFIR because of the rapid depletion of manganese arising from its transmutation to iron.[7]

1.2.4.3 Ferritic Alloys

Molybdenum is added to ferritic alloys to provide solid solution hardening for improved high temperature strength. Removal of molybdenum for low activation will therefore degrade high temperature Properties. Possible alloying substitutes are vanadium[18], tantalum and tungsten. However, it is likely that low activation alloys will not have the high temperature strength now available in Path E alloys.

Nickel is often found in ferritic alloys above 0.91 percent (the 10-CFR-61 limit for Starfire) and niobium has been used as an effective carbide former. Low activation alloy design will therefore restrict aooitions of these elements as well. Because nickel is an austenite former used to control the presence of delta ferrite, limitations on nickel levels must be offset by increases in other austenite formers or reductions in ferrite formers. However, such trade-offs can be expected to he beneficial. Removal of nickel should reduce the tendency for G-phase formation and reduce irradiation-induced changes in mechanical properties.[17] It should be possible to straightforwardly substitute other elements for niobium.

Two ferritic alloy classes appear to be feasible. An alloy similar to 2 1/4 Cr-1 Mo with vanadium substituted for molybdenum has been produced[18] and initial mechanical tests can be expected in the near future. The same approach is now being employed in the martensitic stainless steel regime.[19] However, careful alloy design will be required to ensure optimum properties.

1.2.5 Conclusions

Three regimes have been identified for low activation alloy development:

(1) Fe-Cr-Mn invar alloys designed for low swelling,
(2) Fe-Cr-V bainitic steels similar in properties to 2 1/4Cr-1 Mo,
(3) Fe-Cr-V martensitic steels similar in properties to HT-Q.

Due to the similarity of these alloys to present candidate alloys, they can be developed under Path A and Path E.

1.2.6 References

1. F. M. Mann, "Activation of Components of a Fusion Alloy," in *Damage Analysis and Fundamental Studies Quarterly Progress Report,* DOE/ER-0046/12, Oct-Dec 1982.
2. F. M. Mann, *Transmutation of Alloys in MFE Facilities as Calculated by REAC (A Computer Codes System for Activation and Transmutation),* HEDL-TME 81-37, Westinghouse Hanford Company, 1982.
3. F. M. Mann, "Activation of Components of a Fusion Alloy" in *Damage Analysis and Fundamental Studies Quarterly Progress Report,* DOE/ER-0046/13, Jan-Mar 1983.
4. J. F. Bates and W. G. Johnston, *Radiation Effects in Breeder Reactor Structural Materials,* AIME, New York, NY, p. 625, 1977.
5. H. R. Brager and F. A. Garner, "Dependence of Swelling of Fe-Ni-Cr Alloys on Chromium and Nickel Content," *Damage analysis and Fundamental studies Quarterly Progress Report,* DOE/ER-0046/11, PD. 221-231, Mar 1982.
6. F. A. Garner, "Impact of the Injected Interstitial on the Correlation of Charged Particle and heutron-Induced Radiation Damage," *J. Nucl. Mater.* 117, in Dress.
7. B. Window, *J. Appl. Phys.* 44 (6), p. 2853, 1973.
8. V. L. Sedov, Soviet *Physics JETP* 15 (1), p. 88, 1962.
9. O. G. Sokolov and A. I. Mel'ker, *Soviet Physics-Doklady,* 1 (11), n. 1019, 1965.
10. Y. Endoh, Y. Noda and M. Itrumi, *J. Phys. Soc.,* 50 (2), Japan, p. 469, 1981.
11. C. Kimball and W. D. Gerber, *J. Applied Physics,* 34, (4), (Part 2), p. 1046, 1963.
12. O. A. Khomenko and I. F. Khil'kevich, *Metal. Term. Obra. Met.,* (6), p. 42, 1982.
13. G. T. Haddick, L. D. Thompson, E. A. Parker and V. F. Zackay, *Metal Progress,* p. 37, Nov 1978.
14. S. Floreen, Met. *Trans.* A, 13A, p. 7003, Nov. 1982.
15. M. Snykers and E. Ruedl, *Proc. 11th Symposium on Fusion Technology,* Oxford. Pergamon Press. p. 1269, 1980.
16. J. F. Bates, F. A. Garner and F. M. Mann, *J. Nucl. Mater,* 103 and 104, p. 999, 1981.
17. O. S. Gelles and L. E. Thomas. Allov Development for Irradiation Performance Semiannual Progress Keport DOE/ER-0045/9, Sept. 1987, p. 162.
18. N. M. Ghoniem, A. Shabaik and M. Y. Youssef, *Development of a Low Activation Vanadium Steel for Fusion Applications,* to be Presentea at the Topical Conference on Ferritic Allovs for Use in Nuclear Eneray Technologies, June 19-23, 1983 in Snowbird, Utah.
19. Discussions on January 21, 1483 between N. M. Ghoniem of UCLA, and R. W. Powell and D. S. Gelles, of Westinghouse Hanford Company:

1.3 AN ASSESSMENT OF MARTENSITIC STAINLESS STEELS FOR LOW ACTIVATION STATUS - T. LECHTENEERG (GA TECHNOLOGIES)

1.3.1 ADIP Task

The Alloy Development for Irradiation Performance task is currently evaluating the 9-12 Cr class of steels for applications in first wall/ breeding blankets. Recently the Low Actlvatlon Panel constituted by DOE has assessed the requirements for low activation materials in fusion machines and has recommended that, "Actlvatlon of structural material should remain one of the primary considerations in the development of fusion reactor materials"[1]. Furthermore, the goals of the AOIP program state[2]: "Since at this tlme no single alloy can be shown to satisfy the probable fusion environment ... the long-term goals are focused on developlng alloys wlth mechanical and physical properties tailored for fuslon power reactor applicatlons."

1.3.2 Objectlve

The objectlve of this work was to assess the Path E alloy, HT-9, relative to its qualifying for low actlvatlon status as defined in the Low Activatlon Panel report. This qualiflcatlon would requlre it meet two of the three goals of safety, surface waste disposal, and contact maintenance. Furthermore the feasibllity of producing low activation alloys of this type was assessed by Interactlon wlth two producers of those alloys.

1.3.3 Summary

This work was privately funded by the Fusion and Advanced Technology Division of GA Technologies Incorporated (GA) fran its office of Research and Development as a part of GA's continuing interest In actlvatlon Issues as they Impact fusion technology development. The Interactlon of neutrons fran a fusion machlne wlth the structural material will cause all conventional alloys and materlals to activate[3]. There are three results of this: (1) special safeguards wlll be required for the removal and storage of the activated materlal wastes after service, (2) the potential safety risk resulting fran release of activated specie during an accident will require mitigation, and (3) Increased costs of developing and Incorporatlng remote maintenance equipment. These results address the waste management concerns and the safety Issues.

Currently, the light water reactor (LWR) waste guideline, 10CFR61, has four classes of waste. Classes A, E and C, which are all surface disposal, and Class D which Is geologic disposal. All conventional materials will actlvate such that they would not qualify for surface waste disposal, and would require deep, geologic disposal for many generations because of major constituent elements or levels of Impurltles too hlgh for surface disposal. While all elements will actlvate. it Is a relatively few that have daughter radionuclides that decay quickly enough or are weak enough such that they could be disposed of as surface waste. The relatlve cost advantages of surface disposal vs. geologic disposal cannot be estimated easily, but for packaging and burying without monitoring, they have been estimated at $200-600 per cubic foot for any of the three classes of surface waste. whlle costs for the only other alternative, geologic disposal, will likely be closer to $200.000 per cublc foot.

The issue of the safety Implications of materials activation is less well defined. Currently, the most Important mechanism for release of activated material off-site Is considered to be through volatilization following lithium or other breeder material fires, or by loss of coolant to a structure of highly activated material which has its own self-heating due to radloactlve decay[4]. Both scenarios raise the temperature of the Structural materlal. The hlgher the melting point of a material, the less llkely the materlal will volatilize unless the material forms a surface oxide that Is volatile at temperatures well below the melting polnt of the unoxldlzed structural material. Manganese as an alloying element is a major concern due to Its hlgh vapor pressure and formatlon of a volatile oxlde[5].

1.3.4 Status

12% Cr-martensitic steels that meet the requirement for surface waste disposal probably can be melted and fabricated. The guidelines for maximum allowable residual impurity levels must be adhered to and will Impact the design philosophy for any alloy camposition. A design equation was written for allowable amounts ot impurities such that the producer and alloy design team could trade-off certain strengthening additions for others when those pure-element alloy addltlons Introduce unacceptable levels of impurities. Currently, the levels of Impurities for several different lots of starting material are being reviewed, and implications to alloy canpositions assessed.

1.3.5 Results

In order to achieve minimum activatlon alloys based on modifcations of conventional materials (such as HT-9), certain alloying elements such as nlckel and molybdenum must be reduced to low levels and all impuritles In the matrix that transmute to unacceptable radionuclides must be reduced to stringent limita-

tions proposed in waste regulation 10CFR61 in order to qualify for class a waste. for example, transmutation products from nickel are Co^{60}, Fe^{55}, and Ni^{63}. Calculations have shown that the maximum allowable amount of nickel in a first wall material like HT-9 would have to be less than 380 appm, or 0.040 wt-% (based on 8 x 10^{22} atoms/mole and an alloy atomic weight estimated to be 55.2 gms). A list of radionuclides In a 12Cr-1Mo material is given in Table I. The total amounts of impurities Introduced by alloying should not exceed the amount dictated by regulation 10CFR61, such that the following "impurity" equation requirement must be met:

$$\sum_i \chi_i \, \eta_i / K_i < 1$$

where χ_i Is the atom part per million of residual element I, η_i is the Specific activity, and K_i Is the allowable radioactivity according to 10CFR61. This equation says the fractlon of allovable radioactlvity due to any Impurity element times the atomic fractlon of that element (in appm) is to be summed over all expected impurity elements, and that summation must be less than unity.

Thus, as a good approximation, an empirical equation can be written accounting for only those specie that would dominate the radioactivity levels. For example, Co^{60} is produced by transmutations from Ni, Cu, and Co. But the η/K factor Is very low (one or two orders of magnitude lover) for Cu and Co as compared to Ni transmutations. So, only those radionuclides that appear to be major contributors to activity are Included in the equation. In this example, Ni would be included. So, an approximotion for Class A waste is -

$$5.14 \times 10^{-3} \chi_{Ni} + 1.43 \times 10^{-2} \chi_{Mo} + 2.45 \times 10^{-2} \chi_{Cu} + 1.8 \times 10^{-3} \chi_{N}$$

$$+ \; 1.2 \times 10^{-5} \chi_{Co} + 10 \chi_{Nb} + 8.44 \times 10^{-3} \chi_{Al} + 1.6 \times 10^{-5} \chi_{Mn} < 1$$

while for Class B, the equation would be -

$$2.57 \times 10^{-4} \chi_{Ni} + 3.25 \times 10^{-4} \chi_{Mo} + 1.22 \times 10^{-3} \chi_{Cu} + 1.8 \times 10^{-3} \chi_{N}$$

$$+ 1.27 \times 10^{-6} \chi_{Co} + 10 \chi_{Nb} + 1.6 \times 10^{-7} \chi_{Mn} + 1.91 \times 10^{-4} \chi_{Al} < 1$$

1.3.6 Feasibility of Producing Minimum Activation Steels and Other Proposed Solutions

Two producers and fabricators of steels similar to those being considered in the minimum actlvatlon ferritic steels program were vlslted. They were Special Metals in Utica, N.Y. and Carpenter Technology In Reading, PA. They purpose of the trip was to discuss the methods and state-of-the-art of steel production to determine what purity could be achieved for special application steels.

The production staff at Special Metals and Carpenter Technology were consulted on the problem concerning activation products and the careful quality control that Is necessary if these materials are to be produced. They thought that the residual amounts discussed could probably be met. but that specific compositions with specifications should be submitted to them for analysis. They would then review the available virgin materials and their residuals content. This Is Important because, for example, to reduce the molybdenum content to as low as possible, other strengtheners such as tungsten must be addea to compensate. The ore from which tungsten Is made may have other residuals in it such as niobium which may Increase the Nb content to above the specifications. So, a trade-off may be necessary between adding tungsten and, for example, more chromium in order to minimize impurity contamination fran further additions yet also maintaln desirable mechanical properties.

Other proposed solutions are (1) isotopic tailoring of the elements that are used In the material[6], or (2) the use of conventional materials without certain alloying elements that activate to controlled radionuclides[1]. Isotopic tailoring means to remove certain naturally occurring Isotopes of elements. For example, molybdenum has nlne stable occurring isotopes, two of which ^{94}Mo and ^{95}Mo activate by interacting with neutrons to unacceptable radionuclides ^{93m}Nb and ^{93}Mo respectively. Isotopic tailoring would cause ^{94}Mo and ^{95}Mo to be removed durlng isotopic processing such that the dominant radionuclides ^{93m}Nb and ^{93}Mo could, therefore, not be produced. The disadvantages of this is that an entire industry would have to be created to separate the offending isotopes in every alloying element addition, and quality control of produced heats would be very risky because of the difficulty of determining the differences between an isotopically tailored steel versus a conventional alloy of the same composition. Also, work done at GA has shown that the residual impurity levels must be very small[7], and it is not clear that isotopic tailoring on a large scale could produce elements with the required controlled levels of offending isotopes.

Two major influences In eliminating the molybdenum and, to a lesser extent, the nickel are (1) a decrease in strength due to eliminating molybdenum which if present would stabilize carbides with respect to temperature, and (2) a shift in the phase contents of the steel to a dual phase alloy which is not fully martensitic but containing some ferrite. While this has no adverse effect on activation properties,

it may effect the strength, corrosion, radiation damage and swelling. Both phases, martensite and ferrite, are body-centered cubic and, therefore, inherently resistant to swelling[8], but the large number of dislocations in martensite act to getter vacancies, thus greatly increasing the incubation time for swelling. So, a fully martensitic structure is more attractive. In order to counter this phase shift, and to increase the strength without adversely affecting activation characteristics. tungsten can be added in the same atomic amounts as molybdenum had been in HT-9. Tungsten will shift the composition into a fully martensitic phase field and also has the property of precipitating and stabilizing the same strengthening $M_{23}C_6$ carbide as molybdenum in HT-9. The exact amount of the shift is about the same as for molybdenum in atomic percent. Proposed alloys should have a small amount of titanium which further promotes martensite and stabilizes the carbides further. Silicon should be reduced to impurity levels because of recent data suggesting that a nickel silicide may be a factor in causing irradiation embrittlement[9].

1.3.7 References

1. "Panel Report on Low Activation Materials For Fusion Applications", presented at DOE, 18 December 1982, (R. Conn, ed.) in press.

2. "Fusion Technology Development Plan - Draft", Department of Energy, Office of Fusion Energy, May 1983.

3. Vogelsang, W., G. Kulcinski, R. Lott, and T. Sung, "Transmutations, Radioactivity, and After-heat in a Deuterium-Tritium Tokamak Fusion Reactor", Nuclear Techno——, 22 (1974) 379.

4. Hoidren, J., "Fusion Energy in Context: Its Fitness for the Long Term", Science, 200 (1978) 168.

5. Hoidren, J., "Aspects of Safety for Fusion Machines", presented at ANS meeting, 16 November 1983, Washington, D.C.

6. Conn, R., Okula, K., and Johnson, A. "Minimizing Radioactivity and Other Features of Elemental Tailoring of Materials For Fusion Reactors", Nuclear Technology, 41 (1978) 389.

7. Memorandum, Battaglia, J., to Lechtenberg, T., "Radioactivity Calculations for Low Activation Alloy Design", GA memo JMB:MAMS:8202, September 28, 1982.

8. Little, E., "Void Swelling in Irons and Ferritic Steels", J. Nuclear Materials, 87 (1979) P. 11.

9. Geiies, D., "Microstructural Examination of HT-9 Irradiated in the HFIR-CTR-32 Experiment", Alloy Development for Irradiation Performance Semiannual Progress Report, DOE/ER-0045/9, p. 161.

Table 1.3.1

Maximum elemental concentrations of Impurities In HT-9 to qualify for Class A waste

Element	Dominant Nuclide	Maximum Concentration* Appm. 10 YR.
Ni	Co 60	1,220
	Fe 55	2,550
	Ni 63	200
Mo	Mo 93	70
	Nb 93m	190
V	V 49	---
Ti	Ca 45	---
W	W 181	---
cu	Co 60	5.250
	Ni 63	41
N	C 14	550
Mn	Mn 54	60.000
Al	Al 26	270,000
Co	Co 60	83,000
Nb	Zr 93	13.000
	Nb 92	260.000
	Nb 94	0.1
B	Be 10	49,000

* Maximum concentrations calculated as *if* each were the only impurity in the material

Table 1.3.2

Element	Dominant Radionuclides	Specific Activity, (Ci/cm³/appm)	Regulation Requirements, K Class A	(η/K) Class A
Ni	Co60	5.72	7000	8.17×10^{-4}
	Fe55	2.74		
	Ni63	0.28	35	5.14×10^{-3}
Mo	Mo92	0.143	10	1.43×20^{-2}
	Nb93m	0.052	10	5.2×10^{-3}
cu	Co60	1.33	7000	1.9×10^{-4}
	Ni63	0.66	35	2.457×10^{-2}
N	C14	0.0145	8	1.8×10^{-3}
Co	Co60	0.0844	7000	1.2×10^{-5}
Nb	Zr93	3×20^{-5}	10	3×10^{-6}
	Nb92	3×20^{-5}	(20)	(3×20^{-6})
	Nb94	**0.20**	**0.02**	10
Mn	Mn54	0.117	7000	1.6×10^{-5}
Al	Al26	0.0844	10	8.44×10^{-3}
B	Be10	8.10^{-6}	( )*	( )*

* Calculations in **Progress**

2.1 NEUTRON SOURCE CHARACTERIZATION FOR MATERIALS EXPERIMENTS - L. R. Greenwood (Argonne National Laboratory)

2.1.1 ADIP/DAFS Tasks

ADIP - Task I.A.2 - Define Test Matrices and Procedures
DAFS - Task II.A.1 - Fission Reactor Dosimetry

2.1.2 Objective

To characterize neutron irradiation facilities in terms of neutron flux, spectra, and damage parameters (DPA, He, transmutation) and to measure these exposure parameters during fusion materials irradiations.

2.1.3 Summary

Results are summarized for four separate irradiations in HFIR, designated CTR-31, 32, 34, and 35. The neutron fluxes and energy spectra agree quite well between the runs. Small corrections have been made to the CTR32 reaction rates due to improved burnup calculations. Helium production in nickel and stainless steel is being revised slightly according to new neutron cross section evaluations for ^{59}Ni. The status of all other experiments is sumnarized in Table 2.1.1.

Table 2.1.1. Status of Dosimetry Experiments

	Facility/Experiment	Status/Comments
ORR	- MFE 1	Completed 12/79
	- MFE 2	Completed 06/81
	- MFE 4A1	Completed 12/81
	- MFE 4A2	Completed 11/82
	- MFE 4B	Samples Expected 04/83
	- MFE 4C	Irradiation in Progress
	- TBC 07	Completed 07/80
	- TRIO-Test	Completed 07/82
	- TRIO-1	Irradiation in Progress
HFIR	- CTR 32	Completed 04/82
	- CTR 31, 34, 35	Completed 04/83
	- CTR 30	Irradiation in Progress
	- T1, RB1, CTR39	Samples Received 03/83
	- T2; T3	Irradiations in Progress
	- RB2, RB3	Irradiations in Progress
	- CTR 40-45	Samples Sent 10/82
Omega West	- Spectral Analysis	Completed 10/80
	- HEDL1	Completed 05/81
EBR II	- X287	Completed 09/81
IPNS	- Spectral Analysis	Completed 01/82
	- LANL1 (Hurley)	Completed 06/82
	- Hurley	Completed 02/83
	- Coltman	Irradiation in Proqress

The first version of our standardized dosimetry and damage data computer file (DOSFILE) has been completed. At present, data is available for 17 recent irradiations at ORR, HFIR, EBRII, Omega West, CP5, HFBR, and IPNS. Copies of the data file and retrieval programs will be made available to interested parties for testing.

2.1.4 Progress and Status

2.1.4.1 Dosimetry for the HFIR-CTR31, 32, 34, and 35 Irradiations

Measurements and calculations have been completed for four separate irradiations in the High Flux Isotopes Reactor (HFIR) at Oak Ridge National Laboratory. The irradiation histories are, as follows:

Experiment	Dates	Power (MWD)
CTR31	10-03-80 to 05-25-81	21,853
CTR32	08-17-80 to 12-12-80	10,863
CTR34, 35	12-24-81 to 04-17-82	10,614

Results from CTR32 were reported previously (L. R. Greenwood, Damage Analysis and Fundamental Studies, Quarterly Progress Report, DOE/ER-0046/9, pp. 32-40, 1982). However, slight revisions have been made in activation and helium production rates according to new nuclear data.

Radiometric and helium accumulation dosimeters were located at eight different vertical heights in each experimental assembly, either at the top or bottom of each level. All samples were gamma counted at ANL and then sent to Rockwell International for helium analysis.

The radiometric dosimetry results are listed in Tables 2.1.2 and 2.1.3. Burnup corrections are required for all of the reactions and these are typically 5-10% for the fast reactions but as high as 20-50% for thermal reactions. These corrections can be checked in several ways. In the case of thermal reactions, a simple iterative technique provides a unique reaction rate since the reaction in question is responsible for the burnup of the target nuclei. Once the thermal flux is known, it can then be used to estimate the much smaller corrections for the threshold reactions. Since the flux spectrum is apparently quite constant in HFIR, we can check the final results by demanding internal consistency within each run and between different runs. In the case of $^{58}Fe(n,\gamma)^{59}Fe$, corrections must be made for the burnin of ^{58}Fe from both ^{56}Fe and ^{57}Fe. Corrections for $^{54}Fe(n,p)$ and $^{55}Mn(n,2n)$ are hampered by the lack of any cross section measurements on ^{54}Mn (<10 b). Excellent consistency is obtained for both reactions if we assume a ^{54}Mn thermal cross sections of about 5 b. The $^{58}Fe(n,\gamma)$ and $^{63}Cu(n,\alpha)$ reaction rates have been adjusted slightly from the rates published previously (CTR32) according to these new burnup calculations. The $^{58}Fe(n,\gamma)$ values are about 4% lower and the $^{63}Cu(n,\alpha)$ values about 7% higher than reported previously for CTR32. Some of the values reported for $^{63}Cu(n,\alpha)^{60}Co$ appear to be inconsistent, although the reasons for these differences are not understood. Random cobalt impurities could explain the problem; however, overall the cobalt impurity level should be less than 0.1 ppm.

Table 2.1.2. Thermal Activation Measurements in HFIR
Values corrected for burnup and normalized to 100 MW; uncertainty ±2%

Height, cm	σφ (atom/atom-s)						
	$^{59}Co(n,\gamma)(10^{-8})$				$^{58}Fe(n,\gamma)(10^{-9})$		
	31	32	34	35	32	34	35
20.8	3.64	4.18	--	--	1.26	--	--
18.8	--	--	4.35	4.50	--	1.28	1.30
16.7	--	--	--	--	1.35	--	--
12.5	5.56	5.55	5.56	5.64	1.67	--	1.59
6.3	--	--	6.68	6.63	--	1.95	1.92
4.2	7.10	7.21	--	--	2.08	--	--
-3.1	--	--	6.72	6.35	--	1.93	--
-4.2	6.67	7.28	--	--	2.10	--	--
-8.3	--	--	--	--	1.82	--	--
-9.4	--	--	5.92	5.94	--	1.68	1.74
-12.5	5.63	5.76	--	--	1.70	--	--
-15.6	--	--	5.11	5.07	--	1.48	1.46
-20.8	4.28	4.22	--	--	1.20	--	--
-21.9	--	--	3.67	3.69	--	1.09	1.09

	$^{93}Nb(n,\gamma)(10^{-9})$	
	31	32
20.8	1.63	1.73
12.5	2.46	2.43
8.3	--	2.78
4.2	3.04	3.05
0.0	3.26	--
-4.2	3.02	3.08
-12.5	2.46	2.49
-20.8	1.73	1.67
-25.0	--	1.43

Table 2.1.3. Threshold Activation Measurements in HFIR
Values corrected for burnup and normalized to 100 MW; uncertainty ±2%

Height, cm	σφ (atom/atom-s) $^{54}Fe(n,p)(10^{-11})$				$^{46}Ti(n,p)(10^{-12})$		
	31	32	34	35	31	32	34
20.8	3.94	4.13	--	--	5.86	--	--
18.8	--	--	4.79	4.58	--	--	6.82
16.7	--	5.22	--	--	--	--	--
12.5	5.81	6.44	--	6.08	9.02	9.43	--
6.3	--	--	6.82	6.85	--	--	9.81
4.2	6.43	6.99	--	--	10.16	10.46	--
0.0	--	--	--	--	--	10.34	--
-3.1	--	--	7.13	--	--	--	10.54
-4.2	6.95	6.86	--	--	10.98	10.23	--
-8.3	--	6.77	--	--	--	--	--
-9.4	--	--	6.62	6.58	--	--	9.69
-12.5	5.85	6.08	--	--	9.16	8.89	--
-15.6	--	--	5.19	5.41	--	--	7.60
-16.7	--	--	--	--	--	7.28	--
-20.8	3.94	3.86	--	--	5.98	5.66	--
-21.9	--	--	3.69	3.82	--	--	5.28

Height, cm	$^{55}Mn(n,2n)(10^{-13})$				$^{63}Cu(n,\alpha)(10^{-13})$	
	31	32	34	35	31	32
20.8	1.18	1.23	--	--	2.73	3.22
18.8	--	--	1.50	1.35	--	--
12.5	1.74	1.94	1.75	1.78	4.44	4.65
6.3	--	--	2.02	2.06	--	--
4.2	1.94	2.13	--	--	6.50	5.18
0.0	--	--	2.07	--	6.01	--
-3.1	--	--	2.08	--	--	--
-4.2	2.02	2.10	--	--	5.94	5.18
-9.4	--	--	1.93	2.14	--	--
-12.5	1.87	1.83	--	--	5.00	5.42
-15.6	--	--	1.59	1.61	--	--
-20.8	1.26	1.23	--	--	3.20	2.98
-21.9	--	--	1.10	1.15	--	--

Activation rates for threshold reactions from all four runs are compared in Fig. 2.1.1. As can be seen, the consistency is excellent demonstrating the repeatability of the neutron flux and spectrum in HFIR. The maximum activation rates are listed below, as determined by a least-squares fit to the data in Table 2.1.2.

Reaction	Midplane Activation Rate(atom/atom-s)			
	CTR31	CTR32	CTR34	CTR35
$^{58}Fe(n,\gamma)^{59}Fe(10^{-9})$	--	2.04	1.94	1.92
$^{59}Co(n,\gamma)^{60}Co(10^{-8})$	6.87	7.12	6.72	6.57
$^{54}Fe(n,p)^{54}Mn(10^{-11})$	6.83	7.22	7.16	7.17
$^{46}Ti(n,p)^{46}Sc(10^{-11})$	1.08	1.05	1.05	--
$^{63}Cu(n,\alpha)^{60}Co(10^{-13})$	6.13	5.51	--	--
$^{55}Mn(n,2n)^{54}Mn(10^{-13})$	2.05	2.18	2.08	2.22
$^{93}Nb(n,\gamma)^{94}Nb(10^{-9})$	3.05	3.06	--	--

These data were used with the computer code STAYSL to adjust the neutron flux spectrum calculated by Kam and Swanks.[1] The adjusted flux and fluence values are listed in Table 2.1.4. The last column of fluxes is the average for all four runs. The run-to-run scatter from the average is only ±5%; however, there does appear to be real differences in the thermal flux level. Differences in the fuel cycle and variations in shielding by the experimental assemblies can of course perturb the thermal flux. The flux spectra adjusted by STAYSL are all quite similar and are represented by Fig. 2.1.2.

Table 2.1.4. Midplane Neutron Fluxes and Fluences Measured in HFIR
Values normalized to 100 MW; uncertainty +5-10%

Energy, MeV	Flux, x 10^{15} n/cm^2-s				
	CTR31	CTR32	CTR34	CTR35	Average
Total	4.95	5.10	4.87	4.71	4.92
Thermal (<.5 eV)	2.04	2.11	1.99	1.94	2.02
>0.11	1.29	1.34	1.30	1.28	1.30
0.5 eV - 0.11	1.62	1.65	1.59	1.55	1.60
0.11 - 1	0.643	0.655	0.629	0.617	0.636
1 - 5	0.598	0.630	0.616	0.610	0.614
5 - 10	0.051	0.051	0.050	0.049	0.050
10 - 20	0.0016	0.0016	0.0016	0.0016	0.0016

	Fluence, x 10^{22} n/cm^2			
	CTR31	CTR32	CTR34	CTR35
Total	9.34	4.78	4.47	4.38
Thermal (<.5 eV)	3.84	1.98	1.82	1.78
>0.11	2.45	1.26	1.19	1.17
0.5 eV - 0.11	3.06	1.55	1.45	1.42
0.11 - 1	1.21	0.614	0.577	0.565
1 - 5	1.13	0.590	0.564	0.560
5 - 10	0.097	0.048	0.045	0.045
10 - 20	0.0031	0.0015	0.0014	0.0014

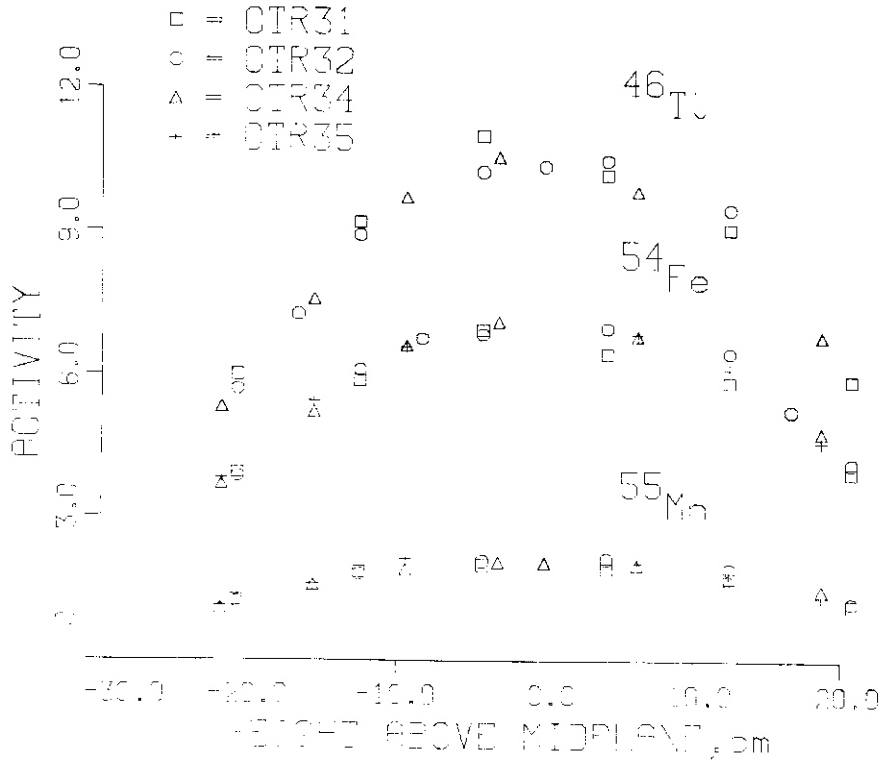

Fig. 2.1.1. Relative activation rates are shown as a function of height above midplane for the ^{46}Ti(n,p)^{46}Sc, ^{54}Fe(n,p)^{54}Mn, and ^{55}Mn reactions. Four irradiations are compared in HFIR-CTR31, 32, 34, and 35.

Fig. 2.1.2. The adjusted neutron spectrum is shown for the HFIR-CTR31 irradiation. This spectrum is nearly identical for the CTR32, 34, and 35 irradiations. Flux per unit lethargy is energy times flux. The dotted and dashed lines represent one standard deviation; however. uncertainties are highly correlated.

Flux gradients were deduced from the activities in Tables 2.1.2 and 2.1.3, as shown in Fig. 2.1.1. All of the data for each reaction and run were fitted to a quadratic function by the least-squares method. The average fits for each reaction are listed in Table 2.1.5. The linear term b is quite insignificant, confirming that the maximum flux is centered within ±1 cm of midplane for all reactions. The quadratic term c is very nearly the same for all reactions; however, the thermal gradient is slightly flatter than the fast gradient, as might be expected. This spectral difference is less than 7% over ±20 cm of interest. The flux gradients in Table 2.1.5 were determined by averaging the thermal and fast gradient coefficients. Displacement damage and gas production would also be expected to follow the same gradients except for helium production *in* nickel which is a two-step thermal reaction. Work on these gradients *is* now in progress.

Table 2.1.5. Flux and Activity Gradients for HFIR
Least-squares fit to data in Tables 2.1.2-2.1.3
$f(z) = a[1 + bz + cz^2]$, z = height (cm)

Reaction	a	$b(10^{-3})$	$c(10^{-3})$
$^{59}Co(n,\gamma)^{60}Co$	6.82×10^{-8}	-0.365	-0.968
$^{58}Fe(n,\gamma)^{59}Fe$	1.97×10^{-9}	+0.066	-0.944
$^{54}Fe(n,p)^{54}Mn$	7.10×10^{-11}	+0.284	-0.994
$^{46}Ti(n,p)^{46}Sc$	1.06×10^{-11}	t0.841	-0.995
$^{55}Mn(n,2n)^{54}Mn$	2.13×10^{-13}	t0.147	-0.974
Flux (n/cm^2-s)	**a**	**$b(10^{-3})$**	**$c(10^{-3})$**
Thermal (<.5 eV)	2.02×10^{15}	-0.150	-0.956
Fast (>0.1 MeV)	1.30×10^{15}	+0.563	-0.995
Total	4.92×10^{15}	+0.195	-0.975

2.1.4.2 Standardized Dosimetry and Damage Data File

Version I of our standardized dosimetry and damage data file, DOSFILE, is now available. Data has been recorded for 17 recent irradiations, as listed in Table 2.1.6. Older data is now being reviewed for entry into the file. The data is written in a simple card-image format similar to ENDF. However, alpha numeric titles and header records have been used extensively to make the files more readable, without the need to reference external manuals.

Table 2.1.6. Irradiations Included in DOSFILE

Irradiation*	Key Word
HFIR-CTR32	HFR32
HFIR-CTR34	HFR34
HFIR-CTR35	HFR35
ORR-MFE1	ORMF1
ORR-MFE2	ORMF2
ORR-MFE4A-1	OR4A1
ORR-MFE4A-2	OR4A2
ORR-Spectral Run	ORRLP
ORR-TBC07	ORRT7
ORR-TRIO-1	TRIO1
Omega West-Spectral Run	OMWSP
Omega West-HEDL-1	OMWH1
IPNS-9-VT2-REF	IPN9C
EBRII-X287	EB287
CP5-Fission Converter	CP5FC
HFBR-VT15-2	HFBR2
HFBR-VT15-3	HFBR3

*HFIR: High Flux Isotope Reactor (ORNL)
ORR: Oak Ridge Research Reactor (ORNL)
Omega West Reactor (LANL)
IPNS: Intense Pulsed Neutron Source (ANL-E)
EBRII: Experimental Breeder Reactor II (ANL-W)
CP5: Chicago Pile 5 (ANL)
HFBR: High Flux Beam Reactor (BNL)

The types of data stored in the file are listed in Table 2.1.7. A short fortran retrieval program is provided to aid users. By typing in the key words for the irradiation and type of data wanted, a user can rapidly obtain a listing. For example, the key words HFR-32 and FSM would instruct the program to list a flux and fluence summary table for the HFIR-CTR32 irradiation. The identification (IDN) file contains a plain-English description of the irradiation history, gradients, and references to more complete publications as well as reference cross section, self-shielding, and uncertainty data files. These latter files are also contained in the DOSFILE package to facilitate cross-referencing.

Table 2.1.7. Data Key Words for DOSFILE

Key Word	Description
IDN	Identification, irradiation history, gradients, references
ACT	Activities with uncertainties, covers, and self-shielding
FLI	Input flux data
FUN	Input flux uncertainties
FLO	Output flux data
FCV	Output flux covariance matrix
FSM	Flux, fluence summary
DAM	Damage Parameters

In establishing the file we have attempted to not only document data and procedures, but also provide all input data required for spectral adjustment. Specifically, the input data is provided for the **STAYSL** computer code which is used for spectral adjustment. Uncertainties and covariances are thus listed for the activities, cross sections, input, and output flux spectra. Covariances on the input spectrum and cross sections are assumed to be described by a Gaussian function. However, the output covariances have no such simple functional dependence and hence must be reported as a complete 100 x 100 element matrix, although only half the terms need be listed since the matrix is symmetric. This output matrix must be used to determine errors on derived quantities such as DPA or gas production.

At present copies of DOSFILE will be sent to interested parties for testing. Feedback from the user comnunity would be particularly useful at this stage in determining suitability of data and formats as well as future changes and additions to the file. In the near future the file will be placed on the NMFE Computer System at Lawrence Livermore Laboratory for general access by the fusion comnunity. A manual is now beino written and this will be published as an Argonne report.

2.1.5 Conclusion

Helium and displacement calculations are now in progress for all four irradiations. Helium values are being reevaluated in terms of new cross section evaluations for ^{59}Ni. Dosimeters are now being analyzed for the T1, T2, RB1, and CTR-39 irradiations in HFIR.

Older dosimetry data will be included in OOSFILE. This data will require some review to update nuclear data and procedures to ensure complete compatibility of all data in the file.

2.1.6 References

1. F. B. K. Kam and J. H. Swanks, Neutron Flux Spectrum in the HFIR Target Region, ORNL-TM-3322 11971).

7.7 NEUTRONICS CALCULATIONS IN SUPPORT OF THE ORR-MFE-4 SPECTRAL TAILORING EXPERIMENTS — R. A. Lillie and T. A Gabriel (Oak Ridge National Laboratory)

2.2.1 ADIP Task

ADIP Task I.A.7, Define Test Matrices and Test Procedures.

2.7.7 Objective

The objective of this work is to provide the neutronic design for materials irradiation experiments in the Oak Ridge Research Reactor (ORR). Spectral tailoring to control the fast and thermal fluxes is required to provide the desired displacement and helium production rates in alloys containing nickel.

2.7.3 Summary

New scaling factors have been obtained to force agreement between the experilnentally measured and calculated fluences. As of March *31*, 1983, these factors yield 89.6 at. ppm He (not including 2.0 at. ppm He from ^{10}B) and 6.18 dpa for type 316 stainless steel in ORR-MFE-4A and 57.7 at. ppm He and 4.48 dpa in ORR-MFE-4B.

2.2.4 Progress and Status

Experimentally measured fluences from a second set of dosimeters in the ORR-MFE-4A capsule became available on November 7, 1987. These data lead to a drastic change in the ratio of calculated to experimentally measured thermal fluence, C/E. Previously, a C/E ratio of 0.76 had been applied to the calculated thermal fluences. This ratio resulted frorn comparing the calculated total thermal fluence at 95°C (i.e., the effective ORR moderator temperature) with an experimentally measured thermal fluence at 20°C. In addition, it was determined that the fluence to be used in the helium production equations should be the effective 2200-m/s fluence, which is the experimentally measured total thermal fluence at 95°C divided by 1.28. The end result is that a new C/E ratio of 0.99 is now being used to scale the calculated thermal fluences, whereas 0.76 is still being used to scale the calculated total fluences.

The operating and current calculated data based on the new fluence scaling factors are summarized in Table 2.2.1 for the ORR-MFE-4A and -45 experiments. The change in thermal fluence scaling has produced a large increase in the He production frorn that reported previously.[1] In addition, the dpa rates in both the ORR-MFE-4A and -4B experiments have dropped slightly because of a slight decrease in the time averaged total flux.

The real-time projections of the helium-to-displacement ratios based on current calculated data as of March 31, 1983, are presented in Figs. 2.2.1 and 2.7.7 for the ORR-MFE-4A and -4B experiinents, respectively. The projected dates were obtained assuming an ORR duty factor of 0.86. Because the ORR-MFE-45 experiment was removed from the reactor on October 21, 1982, its real-time projected dates are given in calendar months after insertion. The solid aluminum corepiece was placed in the ORR-MFE-4A experiment on December 7, 1982. This change was precipitated by the large increase in the calculated helium production, which is now consistent with the measured helium production in the second set of dosimetrv wires.

Table 7.2.1. Operating and calculated data for experiinents ORR-MFE-4A and -4B as of March 31, 1983

	ORR-MFC-4A	ORR-MFE-4B
ORR cycles	44	37
Power (MWh)	381.096	305.280
Equivalent full-power days[a]	529.3	424.0
Thermal fluence (neutrons/m^2)	9.16×10^{25}	7.15×10^{25}
Total fluence (neutrons/m^2)	7.40×10^{26}	1.75×10^{26}
Helium (at. ppm)[b]	89.6	57.7
dpa[b]	6.18	4.48

[a] Full power for ORR is 30 MW.

[b] Helium and dpa values are for type 316 stainless steel.

Although the He-to-dpa ratio for the ORR-MFE-4A experiment is currently above the first-wall ratio and will continue to be above the first-wall ratio, the solid aluminum corepiece may be used until the 10-dpa level is reached, provided it is then replaced with an aluminum corepiece containing a 1.0-mm-thick hafnium insert rather than the 0.65-mm-thick hafnium insert previously required.[2] The required hafnium thickness for the ORR-MFE-45 experiment at the 10-dpa level will be between 0.65 and 1.0 mm, provided the solid aluminum corepiece is used when the experiment is reinserted in ORR.

7.7.5 Future Work

The neutronics calculations that monitor the radiation environment will continue with each ORR cycle. The fluences from these calculations will continue to he scaled for agreement with experimentally determined fluences. 4s experimental data become available from the ORR-MFL-45 experiment dosimeters, it will be used to determine the hafnium thickness needed in the ORR-MFE-4B corepiece at the 10-dpa level.

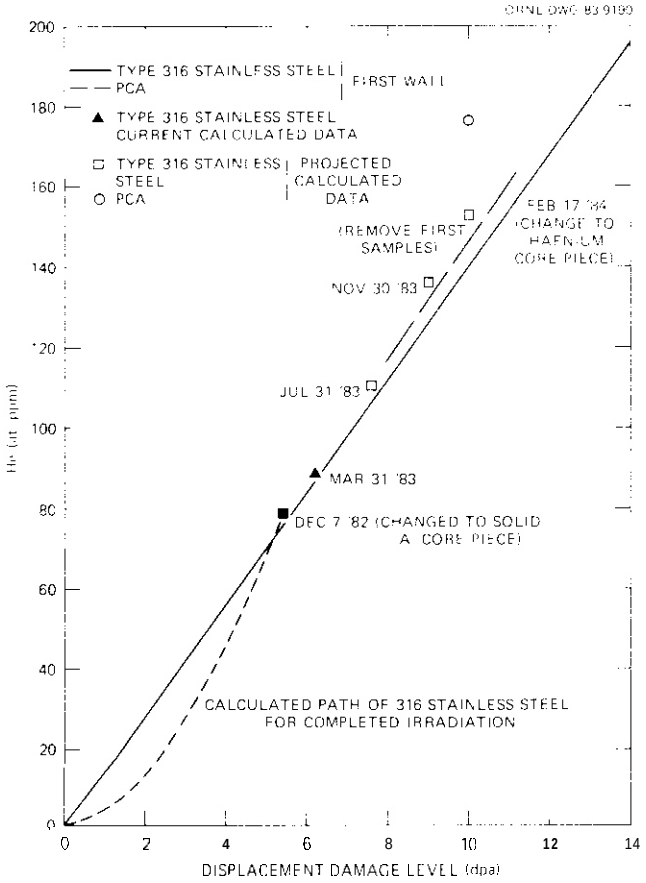

Fig. 2.2.1. Current and projected helium and displacement damage levels in the ORR-MFE-4A experiment.

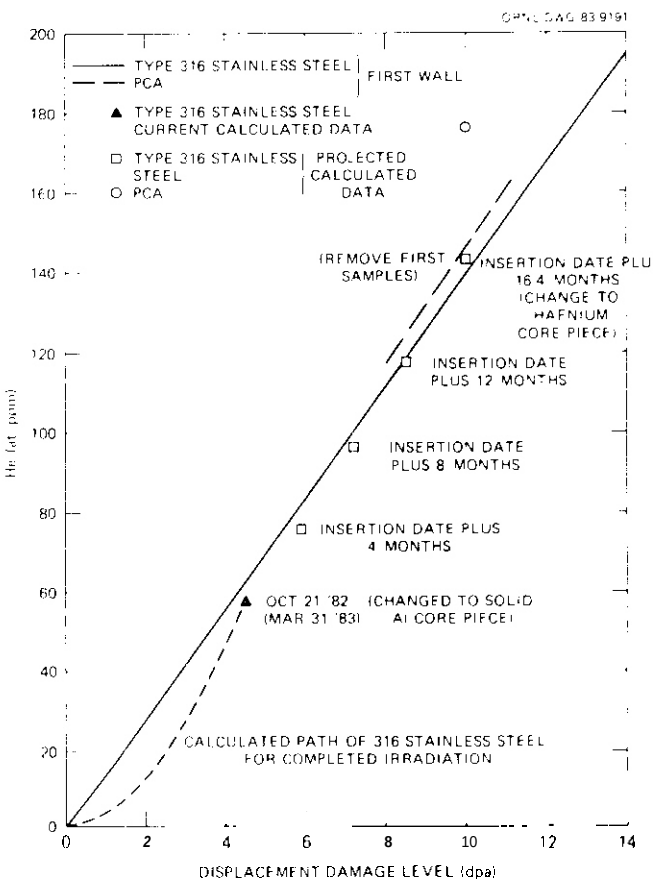

Fig. 2.2.2. Current and projected helium and displacement. damage levels in the ORR-MFE-4B experiment.

2.2.h References

1. R. A. Lillie, T. A. Gabriel. and R. L. Childs. "Neutronics Calculations in Support of the ORR-MFE-4 Spectral Tailoring Experiments," pp. 32–35 in *ADIP Semiannu. Prog. Rep. Sept. 30, 1982*, DOE/ER-0045/9, U.S. DOC, Office of Fusion Energy.

2. 4. A. Lillie, R. L. Childs, and T. A. Gabriel, "Neutronics Calculations in Support of the ORR-MFE-4 Spectral Tailoring Experiments," pp. 20–23 in *ADIP Semiannu. Prog. Rep. Sept. 30, 1981*, DOE/ER-0045/7, U.S. DOE, Office of Fusion Energy.

2.3 OPERATION OF THE ORR SPECTRAL TAILORING EXPERIMENTS ORR-MFE-4A AND ORR-MFE-4B — J. A. Conlin, I. T. Dudley, and E. M. Lees (Oak Ridge National Laboratory)

2.3.1 ADIP Task

ADIP Task I.A.2, Define Test Matrices and Test Procedures.

2.3.2 Objectives

Experiments ORR-MFE-4A and -4B, which irradiate austenitic stainless steels, use neutron spectral tailoring to achieve the same helium-to-displacement-per-atom (He/dpa) ratio as predicted for fusion reactor first-wall service. Experiment ORR-MFE-4A contains mainly type 316 stainless steel and Path A Prime Candidate Alloy (PCA) at irradiation temperatures of 330 and 400°C. Experiment ORR-MFE-43 contains similar materials at irradiation temperatures of 500 and 600°C.

2.3.3 *Summary*

The specimens contained in the ORR-MFE-4A experiment have been in reactor for an equivalent of 529.3 d at 30 MW reactor power, with temperatures of 400 and 330°C. The ORR-MFC-4R experiment, with specimen temperatures of 500 and 600°C, has operated for an equivalent of 424 d at 30 MW reactor power. It was removed from the reactor October 21, 1982, for specimen inspection and transfer to a new capsule.

2.3.4 Progress and Status

The details of the Oak Ridge Research Reactor (ORR) Spectral Tailoring Experiments have been described previously.[1-5]

The ORR-MFE-4A capsule experiment continues to operate. This capsule was disassembled, the test specimens transferred to a new capsule assembly, and the new capsule assembly then reinstalled in the ORR in September 1982. The new capsule was modified to eliminate the faults of the first capsule and to incorporate other changes, which provide an improved and more reliable capsule. The modifications have been described previously.[5]

Unusual He/Ar ratios for the control gases were required to bring the upper and lower regions of the capsule to the normal operating temperatures. Temperature responses to a series of tests in which control gas flow rates and He/Ar ratios were varied were similar to those that would be expected if the upper region control gas line and the common control gas line were reversed. During the following reactor shutdown on October 11, 1982, the two gas lines in question were reversed at the in-pool junction box. After the reactor started, a slight improvement in the capsule temperature distribution was observed; however, the unusual control gas He/Ar ratios remained essentially unchanged. This indicated that the control gas lines in question had not been reversed as first suspected. We have concluded that some of the lower region control gas is mixing with the upper region control gas within the capsule. This could occur by leakage either at the slip joint that separates the two regions or in the control gas passage to the lower region at some point where it passes through the upper region of the capsule. This condition does not prevent the capsule operation at specified temperatures.

As operation of the experiment progressed, the temperature indicated by thermocouple 4 began to show an increase relative to the other thermocouples in the lower reaion of the caosule. A vertical temoerature profile of the center temperature of the capsule was made by step adjustments of the central thermocouple. That temperature profile indicated a higher than normal center temperature in the immediate vicinity of thermocouple 4. This was interpreted to be an indication that a small gas bubble had formed and become trapped in the NaK at that point. The primary system was evacuated to approximately 12.6 Pa, then pressured to $\sim 1.38 \times 10^5$ Pa (20 psia) with helium during the reactor shutdown on December 8, 1982. The evacuation and pressurization procedure was repeated three times. The bubble was successfully removed by this operation, as evidenced by norinal temperature gradients following the next reactor startup.

The aluminum corepiece for the ORR-MFE-4A experiment was changed on December 7, 1982. The lightweight aluminum corepiece identified as MFE-4-1-E3 was removed and a solid aluminum corepiece identified as MFE-4-2E3 was installed. This corepiece change was made to ensure the proper He/dpa ratio in the stainless steel specimens.

The only thermocouple failure to date in ORR-MFE-4A is TC 3, which failed Deceinber 10, 1982. Through Mdrch 31, *1983*, this experiment has accumulated an eouivalent of 529.3 d at 30 MW reactor Dower. with specimen temperatures of 400°C and 330°C.

The ORR-MFE-43 experiment developed a leak between the control gas system and the lead tube. The fact that the leak had no effect on the cansule temoerature control indicated that the leak was in the control gas outlet line. It became necessary to vent the iead tube volume more frequently as the control gas leak rate increased. The experiment was removed from the redctor on October 21, 1982, after having attained approximately 5 dpa. Hot-cell examination of the capsule during disassembly indicated that the leak in the control gas outlet line was caused by corrosion above the capsule bulkhead. This corrosion is believed to be the result of NaK vapor leakage through a braze joint in the bulkhead. The NaK that leaked into the cavity above the bulkhead then reacted with the air in that region, producing a corrosive atmosphere. This is believed to be the same type of failure as occurred in the ORR-MFE-4A capsule.[5] The test specimens have been removed

from the capsule for inspection and will be loaded into a new capsule. The new capsule assembly design has been modified to eliminate the faults of the capsule and *to* incorporate other changes, which should provide an improved, more reliable capsule. These changes are similar to the design changes made to the ORR-MFE-4A capsule reported previously.[5]

Through March 31, 1983, the ORR-MFE-4B experiment has accumulated an equivalent of 424 d at 20 MW reactor power, with specimen temperatures of 500°C and 600°C.

2.3.5 References

1. K. R. Thoms and M. L. Grossbeck, "Operation of the ORR Spectral Tailoring Experiment ORR-MFE-4A," pp. 20–24 in *ADIP Semiannu. Quart. Rep. Sept. 30, 1980*, DOE/ER-0045/4, U.S. DOE, Office of Fusion Energy.

2. K. R. Thoms, "Operation of the ORR Spectral Tailoring Experiment ORR-MFE-4A," pp. 18–21 in *ADIP Quart. Prog. Rep. Mar. 31*, 1901, DOE/ER-0045/6, U.S. DOE, Office of Fusion Energy.

3. I. T. Dudley, "Operation of the ORR Spectral Tailoring Experiments ORR-MFE-4A and ORR-MFE-4B," pp. 24-29 in *ADIP Semiannu. Prog. Rep. Sept. 30, 1981*, DOE/ER-0045/7, U.S. DOE, Office of Fusion Energy.

4. I. T. Dudley and J. A. Conlin, "Operation of the ORR Spectral Tailoring Experiments ORR-MFE-4A and ORR-MFE-4B, pp. 10–12 in *ADIP Semiannu. Prog. Rep. Mar. 32, 1982*, DOE/ER-0045/8, U.S. DOE, Office of Fusion Energy.

5. J. A. Conlin, 1. T. Dudley, and E. M. Lees, "Operation of the ORA Spectral Tailoring Experiments ORR-MFL-4A and ORR-MFE-4B," pp. 17–20 in *ADIP Semiannu. Prog. Rep. Sept. 30, 1982*, DOE/ER-0045/9, U.S. DOE, Office of Fusion Energy.

2.4 IRRADIATION OF MINIATURE CHARPY SPECIMEN OF 12 Cr-1 MoVW: EXPERIMENT HFIR-CTR-46 — J. M. Vitek (Oak Ridge National Laboratory)

2.4.1 ADIP Task

ADIP Task I.A.2, Define Test Matrices and Test Procedures.

2.4.2 Objective

This experiment will evaluate the impact properties of the national fusion heat of 12 Cr-1 MoVW steel after elevated temperature irradiation in HFIK. A second objective is to correlate the results of this experiment with a low-fluence irradiation experiment in the University of Buffalo reactor. The correlation will assess the fluerce dependence of the impact properties of 12 Cr-1 MoVW. Finally, this experiment will provide information or the effect of heat-to-heat variations on the postirradiation impact properties of 12 Cr-1 MoVW since other heats of this alloy have been irradiated in HFIR under identical conditions.

2.4.3 *Summary*

The HFIR-CTR-46 experiment contains miniature Charpy V-notch specimens of the national fusion heat of 12 Cr-1 MoVW steel. Irradiation at 300°C and 400°C will achieve a midplane damage level of 10 dpa.

2.4.4 Progress and Status

2.4.4.1 Introduction

The impact properties of ferritic steels following irradiation are of primary concern when considering the applicability of ferritic steels as a first wall and structural inaterial. Irradiation experiments on these steels are being conducted in the HFIR, EBR-II, and University of Buffalo reactors as a part of the ADIP program. However, earlier experiments have involved differences in heats of steels, sample orientations, irradiation temperatures, and heat treatments. Conclusions regarding the fluence dependence of the impact properties of these steels are not possible. Therefore, a low-fluence irradiation in the University of Buffalo reactor[1] and a higher fluence irradiation in HFIR were planned for direct comparison. The HFIK experiment has been designated HFIR-CTR-46 and is described in this report.

The national fusion heat of 12 Cr-1 MoVW (ref. 2) was used for these irradiation experiinents. Use of this new heat of steel offers two immediate advantages. These experiments will provide the first data on the impact properties of this heat following irradiation. In addition, comparison with a previous HFIR experiment, HFIR-CTR-34 (ref. 3), will allow an assessment of the effect of heat-to-heat variations on the irradiation response of this alloy.

2.4.4.2 Experiment Design

The experimental design is identical with that used previously[1] for elevated temperature irradiation of miniature Charpy V-notch specimens in HFIK. The samples are contained in steel specimen holders, which are inserted in aluminum sleeves. The gamma heating of the specimen and the temperature gradient across the steel specimen holder set the sample irradiation temperature. These subassemblies are stacked in a water-cooled aluminum containment tube. Details of the design are given elsewhere.3

Two irradiation temperatures will be used. The 300°C irradiation will correspond to the low-fluence irradiation experiinent at the University of Buffalo. Irradiation at 400°C will also be carried out, and both irradiation temperatures duplicate previous elevated temperature HFIK experiinents.

Irradiation of nickel-hearing steels in HFIR produces helium as well as displacement damage. The production of helium occurs by the two-step transmutation reaction of ^{58}Ni to ^{4}He and ^{56}Fe. The nickel level of 0.51% in the 12 Cr-1 MoVW alloy will result in the production of approximately 20 at. ppm tie during the irradiation. The displacement damage level will be near 10 dpa at the experiment midplane.

2.4.4.3 Specimen Preparation

The specimens were prepared from 16-mm-thick plate stock of the national fusion heat of 12 Cr-1 MoVW, described elsewhere.2 The heat chemistry is given in Table 2.4.1. The same section of plate was used for preparation of specimens for both the HFIR and University of Buffalo reactor experiments. Heat treating and machining were performed under the direction of the Naval Research Laboratory (NRL). The heat treatment used was 1050°C/0.5 h/air cool + 780°C/2.5 h/air cool, to produce a tempered martensite structure.

The specimens to he irrddidted in HFIR were 5 mm × 5 mm in cross section, 25.4 mm long,

Table 2.4.1 Chemical composition of the national fusion heat of 12 Cr-1 MoVW steel (Heat 9607R2)

Element	Content (wt %)	Element	Content (wt %)
Cr	12.1	Si	0.17
Mo	1.04	N	0.027
Mn	0.57	P	0.016
Ni	0.51	Al	0.006
W	0.45	S	0.003
V	0.28	Ti	0.001
C	0.20		

and contained a notch 0.76 mm deep with a 0.08 mm root radius. The samples were not precracked. Full-size Charpy specimens to be used by NRL were machined from the same plate. The specimens were oriented in the plate-rolling direction with the notch running from the top to the bottom surface of the plate.

2.4.4.4 Test Matrix and Irradiation Conditions

The test matrix is similar to that used in HFIR-CTR-34, with only 11 Cr-1 MoVW samples used. Four specimens at each end of the capsule will be irradiated at 300°C, and eight specimens in the center zone will be irradiated at 400°C. The capsule is in the HFIR peripheral target position. Irradiation began in February 1983 and is scheduled for five cycles with completion in June 1983. Maximum displacement damage is estimated at 10 dpa at the experimental midplane, with the damage level decreasing to approximately 6 dpa at the capsule extremities. Approximately 20 at. ppm He will be produced at the midplane.

2.4.5 References

1. J. R. Hawthorne, "Preparation of ESR Alloy HT-9 and Modified 9 Cr-1 Mo Alloy for UBR Irradiation Experiments," pp. 252–54 in *ADIP Semiannu. Prog. Rep. Sept. 30, 1982*, DOE/ER-0045/9, U.S. DOE, Office of Fusion Energy.

2. T. A. Lechtenberg, "The Procurement and Characterization of the Electroslag Remelted National Fusion Program Heat of 12 Cr-1 Mo Steel," pp. 363–69 in *ADIP Semiannu. Prog. Rep. Mar. 31, 1982*, DOE/ER-0045/8, U.S. DOE, Office of Fusion Energy.

3. J. M. Vitek, "Elevated Temperature Irradiation of Ferritic Steel Charpy Specimens: Experiments HFIR-CTR-34 and -35," pp. 87–90 in *ADIP Semiannu. Prog. Rep. Mar. 31, 1982*, DOE/ER-0045/8, U.S. DOE, Office of Fusion Energy.

2.5 HIGH FLUENCE IRRADIATION OF FERRITIC STEEL CHARPY SPECIMENS: EXPERIMENTS HFIR-CTR-47 and -48 — J. M. Vitek (Oak Ridge National Laboratory)

2.5.1 ADIP Task

ADIP Task I.A.2, Define Test Matrices and Test Procedures.

2.5.2 Objective

This pair of experiments is a sequel to the earlier experiments HFIR-CTR-34 and -35, designed to determine the impact properties of irradiated 9 Cr-1 MoVNb and 12 Cr-1 MoVW steels. HFIR irradiation to approximately 40 dpa is planned. The transmutation of nickel to produce helium in alloys doped with varying amounts of nickel will allow an assessment of the effect of helium on the postirradiation impact properties.

2.5.3 *Summary*

The HFIR-CTR-47 and -48 experiments are companions of the earlier experiments HFIR-CTR-34 and -35 to achieve displacement damage levels up to 40 dpa in 9 Cr-1 MoVNb and 12 Cr-1 MoVW steels. Irradiation temperatures are 300 and 400°C. Nickel-doped alloys are included to assess the influence of helium on postirradiation impact behavior.

2.5.4 Progress and Status

2.5.4.1 Introduction

Two earlier experiments, HFIR-CTR-34 and -35, (ref. 1), were conducted to assess the effect of irradiation on the impact properties of 9 Cr-1 MoVNb and 12 Cr-1 MoVW steels. By taking advantage of the two-step transmutation reaction of nickel, which results in helium production, increasing levels of helium were generated during irradiation by increasing the initial nickel content of the alloys. The nickel-doped ferritic alloys described earlier,[2] with 0.1, 0.5, and 2% Ni, were used in these experiments.

Recent electron microscopy results (reported in Sect. 7.1) indicate significant cavity formation in 12 Cr-1 MoVW during irradiation in HFIR to a displacement damage level of 40 dpa. Therefore, a sequel experiment to HFIR-CTR-34 and -35 was initiated to evaluate the imoact properties of ferritic steels foilowing irradiation in HFIR to this same damage level of 40 dpa.' These experiments, designated HFIR-CTR-47 and -48, are described in this report.

2.5.4.2 Experiment Design

The experimental design is identical with that used previously for elevated temperature irradiation of miniature Charpy V-notch specimens in HFIR.[1] The specimens are contained in steel specimen holders, which are inserted into aluminum sleeves. Gamma heating and temperature gradients across these specimens and holders set the elevated irradiation temperatures. These subassemblies are stacked in a water-cooled aluminum containment tube.

The samples are miniature Charpy V-notch impact specimens. They are 5 × 5 mm in cross section, 25.4 mm in length, and contain a 0.76-mm-deep notch with a root radius of 0.05 to 0.10 mm. The samples were not precracked. Samples were machined from 5.3-mm-thick plate in the longitudinal orientation relative to the rolling direction and with the notch running frorn the top to bottom surface of the plate.

2.5.4.3 Test Matrix and Irradiation Conditions

Four different alloys are included in the experiment: two variations of 12 Cr-1 MoVW and two variations of 9 Cr-1 MoVNb. The alloys have been doped with 0 and 2% Ni in order to achieve different helium production rates during irradiation. Alloy chemistries have been reported elsewhere.2 The alloys are in the normalized and tempered condition. Table 2.5.1 lists the alloys and their heat treatments.

The HFIR-CTR-47 capsule contains the 12 Cr-1 MoVW series, whereas the 9 Cr-1 MoVNb alloys are in capsule HFIR-CTR-48. Each capsule contains 16 miniature Charpy V-notch specimens, 8 at 300°C and 8 at 400°C. The matrix for the two capsules is given in Table 2.5.2. This

Table 2.5.1. Alloys to be irradiated in HFIR-CTR-47 and -48

Alloy	Heat[a]	Normalizing		Temoering	
		(°C)	(h)	(°C)	(h)
12 Cr-1 MoVW	XAA-3587	1050	0.5	780	2.5
12 Cr-1 MoVW-2 Ni	XAA-3589	1050	0.5	700	5
9 Cr-1 MoVNb	XA-3590	1040	0.5	760	1
9 Cr-1 MoVNb-2 Ni	XA-3591	1040	0.5	700	5

[a]Vendor: Combustion Engineering.

matrix is nearly identical to the HFIR-CTR-34 and -35 matrix, with the exception of additional undoped alloy specimens substituted for nickel-doped specimens at the 400°C irradiation temperature.

The capsules are to be irradiated in the HFIR peripheral target positions. Irradiation for 20 cycles is planned, to yield a displacement damage level of approximately 40 dpa at the capsule midplane and approximately 25 dpa at the extremities. Calculated helium levels at the midplane are 25 and 85 at. ppm He in the 9 Cr-1 MoVNb and 12 Cr-1 MoVW base alloys, respectively, and about 300 at. ppm in the 2% Ni-doped alloys.

Irradiation is scheduled to begin in June 1983 and continue until September 1984.

2.5.5 References

1. J. M. Vitek, "Elevated Temperature Irradiation of Ferritic Steel Charpy Specimens: Experiments HFIR-CTR-34 and -35," pp. 87–90 in *ADIP Semiannu. Prog. Rep. Mar. 31, 1982*, DOE/ER-0045/9, U.S. DOE, Office of Fusion Energy.

2. R. L. Klueh and J. M. Vitek, "Characterization of Ferritic Steels for HFIR Irradiation," pp. 294–308 in *ADIP Semiannu. Prog. Rep. June 30, 1980*, DOE/ER-0045/3, U.S. DOE, Office of Fusion Energy.

Table 2.5.2. Irradiation matrix for miniature Charpy V-notch specimens in HFIR-CTP-47, -48

Position[a]	Temperature (°C)	HFIR-CTR-47 heat	HFIR-CTR-48 heat
1	300	XAA 3587	XA 3590
2	300	XAA 3587	XA 3590
3	300	XAA 3587	XA 3590
4	300	XAA 3587	XA 3590
5	400	XAA 3589	XA 3591
6	400	XAA 3589	YA 3591
7	400	XAA 3589	XA 3591
8	400	XAA 3587	XA 3590
9	400	XAA 3587	XA 3590
10	400	XAA 3587	XA 3590
11	400	XAA 3587	XA 3590
12	400	XAA 3587	XA 3590
13	300	XAA 7587	XA 3590
14	300	XAA 3589	XA 3591
15	300	XAA 3589	XA 3591
16	300	XAA 3589	XA 3591

[a]Axial position in each experiment.

3.1 SWELLING AND MICROSTRUCTURAL DEVELOPMENT OF PATH A PCA AND TYPC 316 STAINLESS STEEL IRRADIATED IN HFIR — P. J. Mariasr and D. N. Rraski (Oak Ridge National Laboratory)

3.1.1 ADIP Task

ADIP Tasks I.C.1, Microstructural Stability, and I.C.2, Microstructure and Swelling in Austenitic Alloys.

3.1.2 Objective

This work is intended to evaluate the effect of preirradiation microstructural variation on swelling of the Path A PCA irradiated in the HFIR. These results are compared with results on several heats of types 316 and 316 + Ti stainless steel similarly irradiated.

3.1.3 *Summary*

Evaluation of swelling of PCA variants and 20%-cold-worked (PI-lot) type 316 stainless steel (CW 315) irradiated at 300–600°C was extended to ~22 dpa. Voids continued to develop with increased fluence in PCA-Al. -B1, and CW 316. Void swelling saturated in PCA-B2 at ~10 dpa at 600°C and did not develop in PCA-A3 up to 22 dpa. A stable structure of fine titanium,-rich MC developed during irradiation of PCA-A3, while preexisting MC precipitate in PCA-82 redistributes during irradiation.

3.1.4 Progress and Status

This work continues the evaluation of swelling resistance in various preirradiation microstructural variants of the Path A Prime Candidate Alloy (PCA) begun previously.[1,2] The specimens were irradiated in experiments HFIR-CTR-30, -31, and -32. Irradiation parameters and the details of specimen preparation have been reported.[2-4] Tahle 3.1.1 lists the compositions of the steels, and Table 3.1.2 summarizes the various preirradiation microstructures and thermal-mechanical pretreatments of the PCA.

3.1.4.1 Temperature and Fluence Dependence of Swelling

Cavity volume fraction (cvf) swelling values for the several microstructural conditions of PCA and for CW 316 (ti-lot) irradiated in HFIR at 300–600°C to ~10 dpa and at 400–600°C to ~22 dpa are given in Table 3.1.3. Swelling as a function of temperature is plotted in Fig. 3.1.1 for PCA-Al, -A3, and CW 316 (?I-lot). Comparable results from previously determined[5,6] swelling of CW 316 (DO-heat) and CW 316 + Ti (R1-heat) frorn HFIR-CTR-9 through -13 are included in Fig. 3.1.1. Previous work' has narrowed the emphasis to PCA-A1, -A3, and -B2.

The PCA variants and CW 316 (N-lot) were previously shown to exhibit various levels of monotonically increasing swelling with increasing irradiation temperature for HFIR irradiation to 10 dpa at 300–600°C (ref. 2). Figure 3.1.1 shows these data for PCA-A1 and CW 316 (N-lot) at 10 dpa. The same trend was found for these steels at ~22 dpa. The temperature dependence also became steeper as fluence increased. Minimum swelling and the least temperature dependence were found for the PCA-A3 irradiated to 22 dpa at 400 and 600°C. In contrast with these data, the opposite temperature dependence of swelling was observed for CW 316 (DO-heat) and CW 316 + Ti (R1-heat) irradiated in HFIR to 8.4–17.8 dpa (Fig. 3.1.1). These steels showed the greatest swelling at 300 to 400°C, and then swelling decreased with increasing temperature.?.?

Swelling increased with increased fluence for almost all the steels for the temperatures examined (see Fig. 3.1.2). However, swelling rates, at least initially, depended strongly on temperature and/or pretreatment. PCA-B1 swelled the most at 600°C (1.4% at 22 dpa) and showed the most rapid rate increase with fluence. PCA-A1 at 600°C exhibited a lower rate of swelling than PCA-B1, but the curves could converge at higher fluence. Swelling was initially very low in PCA-A1 at 500°C, hut the rate between 10 and 20 dpa was similar to that observed at 600°C (~0.7%/dpa). Swelling and swelling rate are low but measurable for PCA-A1 irradiated at 400°C (0.2% and 0.017%/dpa, respectively). The PCA-A1 and -B1 are solution-annealed (SA) materials. A scatter hand for data on SA 316 (DO-heat) irradiated at 525–640°C (refs. 7,8) is included in Fig. 3.1.2 for comparison. Although swelling developed earlier in PCA-A1 and -B1, these steels were not yet exhibiting the high swelling rate (~0.33%/dpa) found in the SA 316 (DO-heat) at higher fluences.

Sweliing of PCA-B2, -A3, and CW 31h (N-lot) irradiated to 22 dpa at 400 to 600°C is less than 0.5% (Fig. *3.1.2).* The "incubation" period for CW 316 (PI-lot) was about 10 dpa at 500 and 400°C and considerably less at 600°C. Swelling rates were similar at 500 and 600°C and slightly less at 400°C. Swelling in the PCA-A3 irradiated to 22 dpa was slightly less than in CW 316 (N-lot) at 400°C; at 600°C the swelling of PCA-A3 was half that found in CW 316 (N-lot). The fluence dependence of swelling in PCA-B2 at 500°C is unusual: swelling of ~0.44 was observed in naterial irradiated to ~10 dpa, hut no additional swelling resulted on increased irradiation to ~22 dpa. A scatter hand for higher fluence HFIR data for CW 316 (30-heat) irradiated at 525–640°C (refs. 7–9) is included in Fig. 3.1.2. The data for PCA-A3 fell within this scatter hand, but PCA-B2 and CW 316 (N-lot) showed higher swelling.

Table 3.1.1. Compositions of several austenitic stainless steels

Alloy	Alloy composition (wt %)										
	Fe	Cr	Ni	Mo	Mn	Si	C	Ti	P	S	N
Path A PCA	Bal	14.0	16.2	2.3	1.8	0.4	0.05	0.24	0.01	0.003	0.01
316 + Ti (R1-heat)	Bal	17.0	12.0	2.5	0.5	0.4	0.06	0.23	0.01	0.013	0.006
316 (DO-heat)	Bal	18.0	13.0	2.6	1.9	0.8	0.05	0.05	0.01	0.016	0.05
31h (N-lot)	Bal	16.5	13.5	2.5	1.6	0.5	0.05		0.09	0.006	0.006

Table 3.1.2. Preirradiation microstructures of the Path A Prime Candidate Alloy (PCA)

Designation		Description of microstructure	Thermal-mechanical treatment
A		Simple microstructures resulting from:	
	A1	solution annealing,	25% cold worked plus 15 min at 1175°C
	A2	5 to 10% cold working, or	15 min at 1175°C (A1) plus 10% cold worked
	A3	20 to 25% cold working.	15 min at 1175°C (A1) plus 25% cold worked
B		Microstructures with both coarse grain boundary MC precipitation and intragranular MC precipitation consisting of:	
	B1	coarse particles or particle clusters, or	Solution annealed (A1) plus 8 h at 800°C plus 8 h at 900°C
	B2	fine matrix precipitation.	Solution annealed (A1) plus 8 h at 800°C plus 25% cold worked plus 2 h at 750°C
C		Microstructures with both fine grain boundary MC precipitation and fine intragranular MC matrix precipitation.	Solution annealed (A1) plus 25% cold worked plus 2 h at 750°C
D		Microstructures with both fine grain boundary MC precipitation and fine intragranular MC matrix precipitation plus increased dislocation density.	Solution annealed (A1) plus 10% cold worked plus 2 h at 750°C plus 10% cold worked

3.1.4.2 Microstructural Development

Previous work on stainless steels irradiated in HFIR to ~22 dpa at 500–600°C has generally shown that swelling greater than ~0.2–0.3% was due to void (or bias-driven cavity)[9] formation. Copious small bubbles (or stable cavities)[9] formed early in the irradiation to accommodate the helium generated. Some of these converted to voids which were then responsible for the swelling variation with temperature, fluence, or preirradiation microstructural condition. Figure 3.1.3, for example, shows many coarse precipitates and matrix voids in PCA-A1, less of these in PCA-B2 and CW 316 (N-lot), but only the small bubbles in PCA-A3 after irradiation to ~22 dpa in HFIR at 600°C. The low swelling at 400°C and ~22 dpa was primarily due to bubbles. Figure 3.1.4, however, shows that bimodal cavity distributions were developing in PCA-A1 and CW 316 (N-lot), but not in PCA-A3 at 400°C. Because the larger cavities are probably voids (or bias-driven cavities) beyond their critical radius,[9,10] swelling may be greater in PCA-A1 and CW 316 (N-lot) at higher fluence. Figure 3.1.5 compares the MC precipitate microstructures at 400°C; the refined MC distribution in PCA-A3 correlates with the lack of voids in that alloy [Fig. 3.1.4(c)] compared with PCA-A1 and may be a factor in the void suppression.[11]

Tahle 3.1.3. Swelling for 20:-cold-worked N-lot type 316 stainless steel and various pretreatments of prime candidate alloy irradiated in HFIR

Alloy and microstructural condition[a]	Irradiation temperature (°C)	Neutron fluence >0.1 MeV (neutrons/m²)	Displacement damage level[b] (dpa)	Helium content (at. ppm)	Cavit, vol. + fraction swelling (%)
N-lot 316	300	1.21 × 10²⁶[c]	9.6	375	n.d.[d]
	400	1.26	10.4	435	0.06
	400	2.52[e]	~21.8	1438	0.74
	500	1.26	10.4	435	0.05
	500	2.52[e]	~21.8	1438	0.26
	600	1.25	10.4	465	0.2
	600	2.50	−21.8	1474	0.4–0.5
PCA-A3	400	2.52	−22.3	1714	0.13
	600	2.50	−22.3	1757	0.20–0.25
PCA-A1	300	1.21	9.7	450	n.d.
	400	1.26	10.5	520	n.d.
	400	2.52	~22.3	1714	0.2
	500	1.26	10.5	520	0.05
	500	2.52	−22.3	1714	0.84
	600	1.25	10.6	555	0.66
	600	2.50	−22.3	1757	1.7
PCA-B1	300	1.21	10.5	510	n.d.
	400	1.26	10.5	510	0.14
	500	1.26	10.6	550	n.33
	600	1.25	10.6	550	1.2
	600	2.50	~22.3	1757	1.4
PCA-B2	300	1.21	10.5	510	n.d.
	400	1.26	10.5	510	n.d.
	500	1.26	10.6	550	0.16
	600	1.25	10.6	550	0.4
	600	2.50	−22.1	1751	0.3
PCA-A2	300	1.21	10.5	510	n.d.
	400	1.26	10.5	510	n.d.
	500	1.26	10.6	550	0.36
	600	1.25	10.6	550	1.1
PCA-C	300	1.21	10.5	510	n.d.
	400	1.26	10.5	510	0.25
	500	1.26	10.6	550	0.32
	600	1.75	10.6	550	0.7

[a] See Table 3.1.2.

[b] The contribution produced by recoils during helium production is included. See ref. 4.

[c] Dosimetry from Greenwood, ref. 4.

[d] Not detectable by transmission electron microscopy.

[e] Assuming double the fluence of HFIR-CTR-32; dosimetry is still in progress.

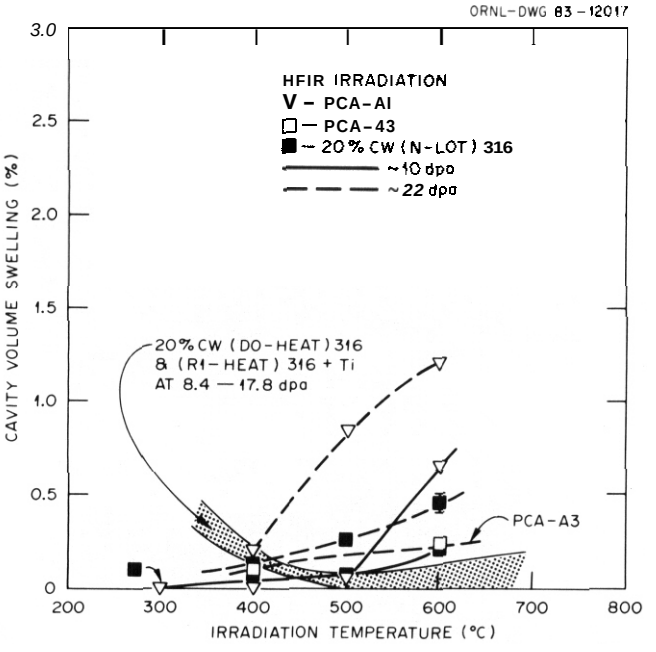

Fig. 3.1.1. Swelling as a function of irradiation temoerature in HFIR for fluences up to 22 dpa. Several microstructural variants of PCA, CW 316 (DO-heat). CW 316 (N-lot), and CW 316 + Ti (R1-heat) are included.

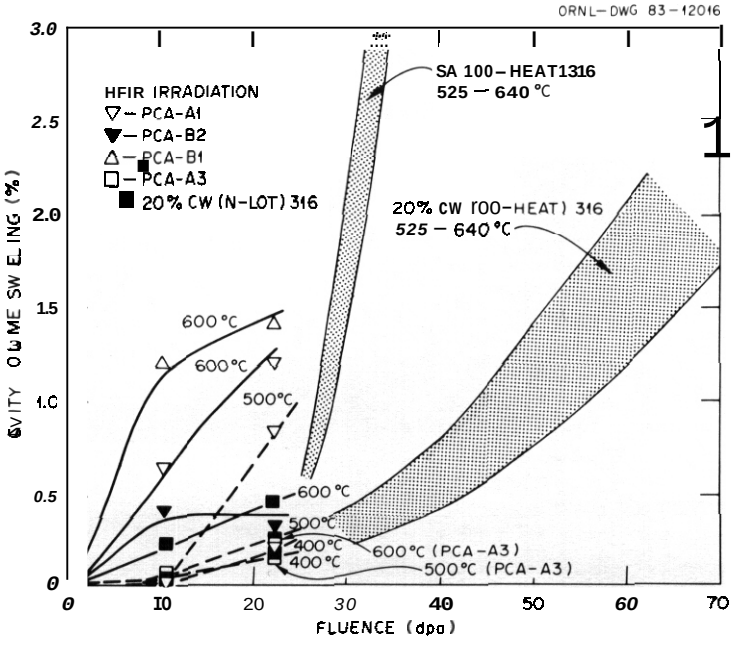

Fig. 3.1.2. Swelling as a function of fluence for PCA-A1 and CW 316 (N-lot) irradiated in HFIR at 400-600°C and PCA-B1 and -B2 at 600°C. PCA-A3 is included at 400 and 600°C and scatter bands for previous data on SA and CW 316 (DO-heat) irradiated at 525-640°C are included for comparison.

The development of stable, fine MC dispersions at higher irradiation temperatures correlated with void formation resistance in some PCA variants and was strongly influenced by preirradiation thermal mechanical treatment. Comparison of dislocation and MC precipitate microstructures for PCA-Al, -B2, and -A3 after irradiation at 600°C to ~22 dpa can be made in Fig. 3.1.6 and correlated with the cavity microstructures in Fig. 3.1.3. The dislocation comparison was not completely straightforward, but PCA-A3, which exhibits best void formation resistance, had the lowest network and/or Frank loop concentrations after the irradiation. The comparison of MC precipitation more clearly indicated that PCA-Al, which exhibited the greatest swelling and precipitation of coarse particles of eta and/or G phase, had the least amount of fine MC precipitate. The PCA-A3, which had the least swelling and no coarse precipitation, had the maximum amount of fine MC. The PCA-B2 fell between Al and A3 with regard to the amount of MC; however, the fluence dependence of the MC stability was unusual and appears to be related to the saturation of swelling at about 10 dpa at 600°C.

Figure 3.1.7 examines in detail the precipitate in PCA-B2. The fine MC particles distributed along the dislocation network before irradiation dissolve and redistribute into clusters nf particles, which then coarsen with increased fluence at 600°C. Faint images of loops can be seen in the regions denuded of MC

H-72312

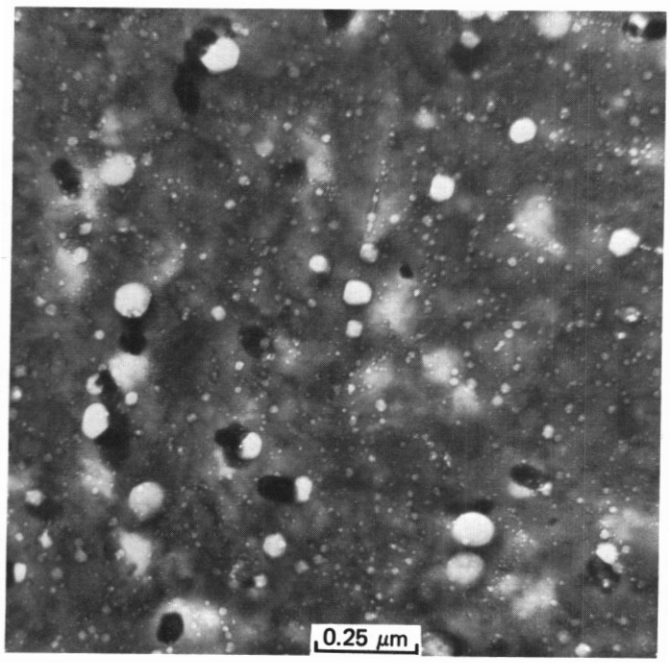

(a)

H-72147

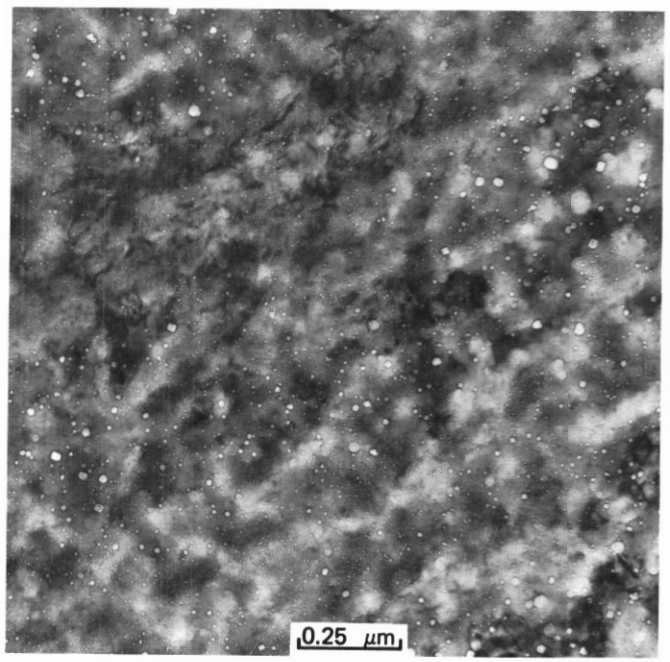

(b)

H-69230

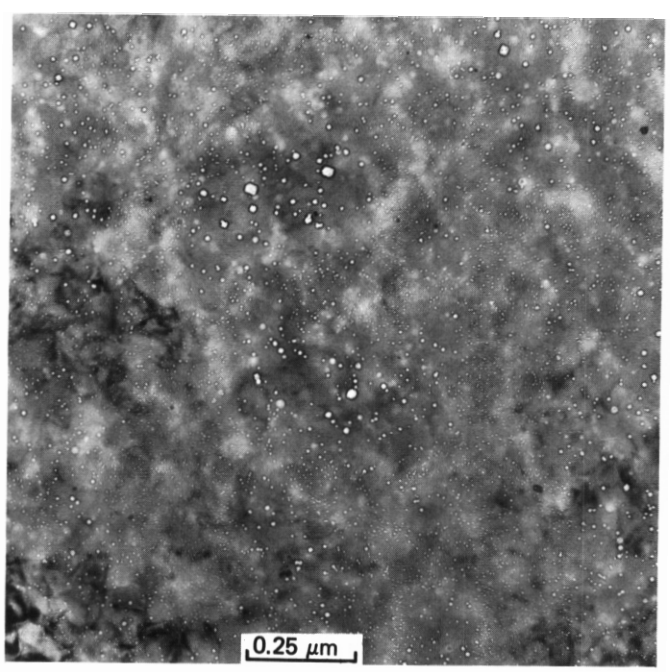

(c)

H-71442

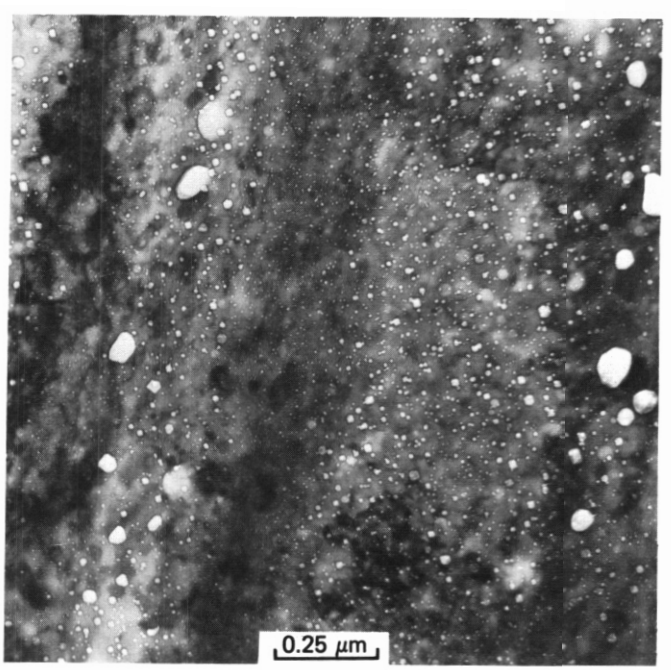

(d)

Fig. 3.1.3. Cavity microstructures of several austenitic stainless steels irradiated in HFIR to ~22 dpa at 600°C. Alloys are: *(a)* PCA-AI, *(h)* PCA-B2, *(a)* PCA-A3, and *(d)* 20%-cold-worked 316 (N-lot).

H-72849

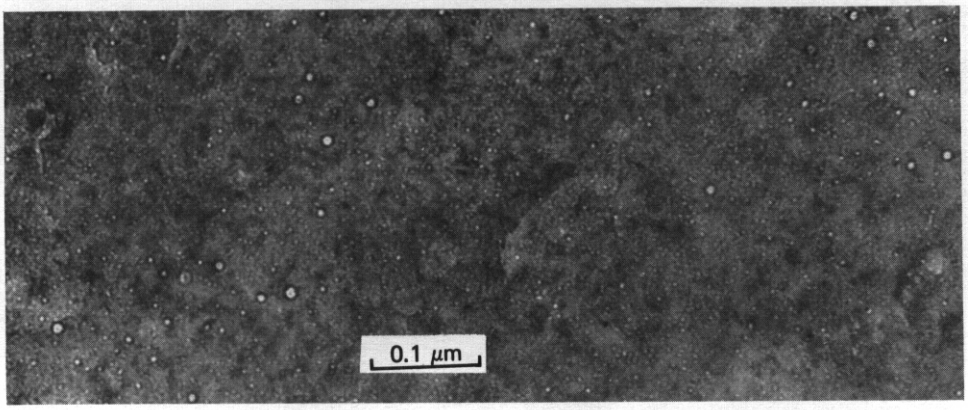

(*a*)

H-72954

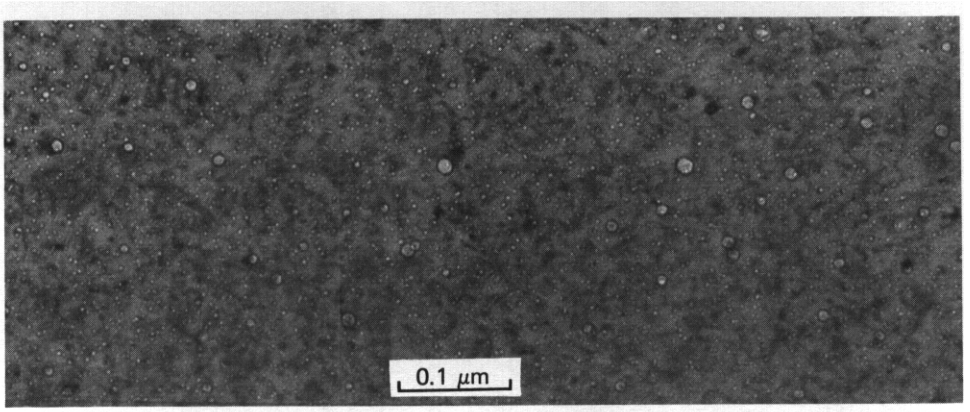

(*b*)

H-72872

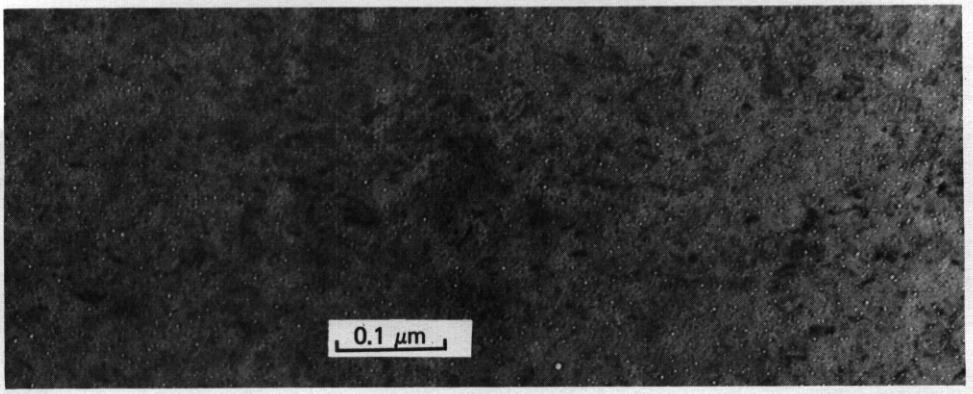

(*c*)

Fig. 3.1.4. Cavity microstructures of (*a*) CW 316 (N-lot), (*b*) PCA-A1, and (*c*) PCA-A3 after irradiation in HFIR to ~22 dpa at 400°C.

H-72944

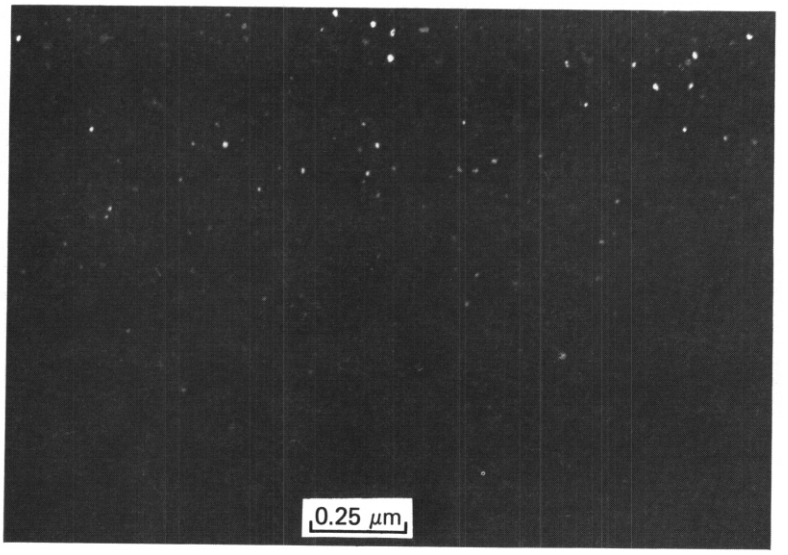

(*a*)

H-72844

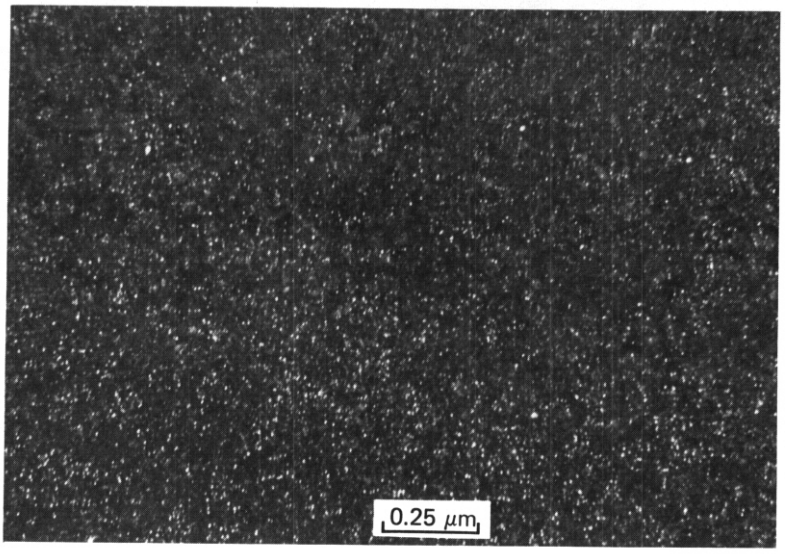

(*b*)

Fig. 3.1.5. Distribution of MC precipitate in (*a*) PCA-A1 and (*b*) PCA-A3 after HFIR irradiation at 400°C to ~22 dpa.

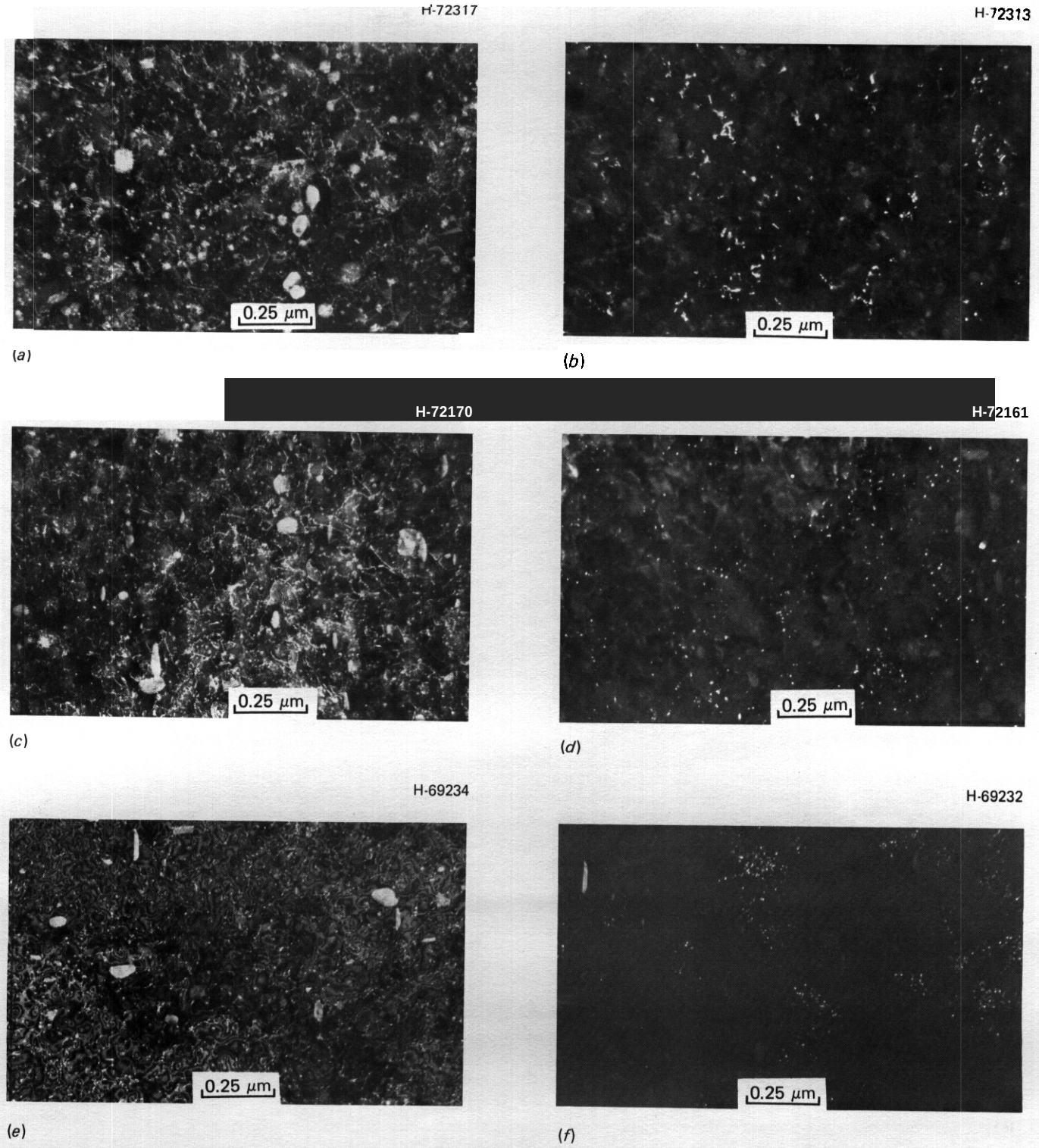

Fig. 3.1.6. The influence of pretreatment on the dislocation and MC precipitate microstructures developed in PCA by HFIR irradiation at 600°C to ~22 dpa. Dark field images were formed with a matrix reflection (left) to reveal dislocations and with a precipitate reflection (right) to show precipitate distributions. (*a*) PCA-A1 (*b*) PCA-B2 (*c*) PCA-A3.

E-23953

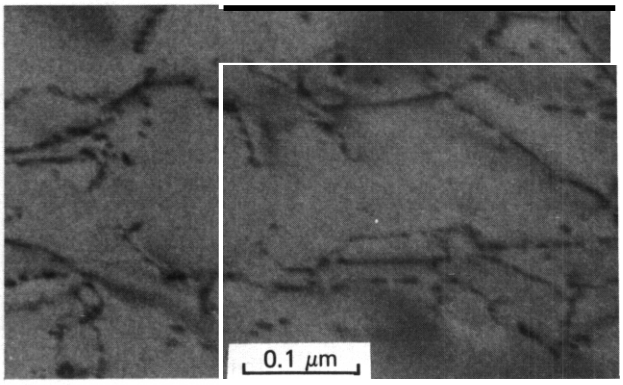

(a)

E-23954

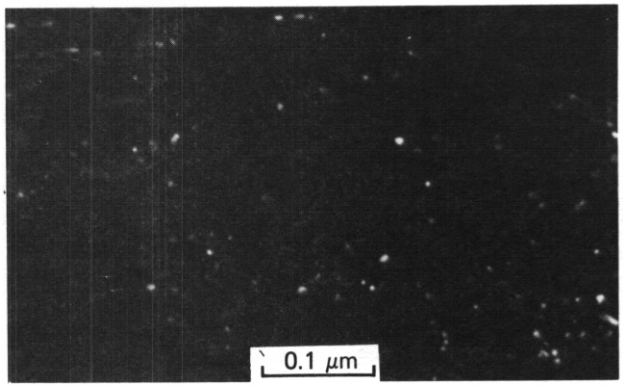

(b)

E-37929

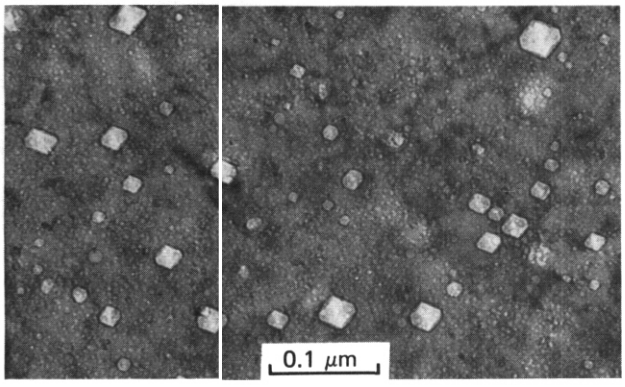

(c)

E-37920

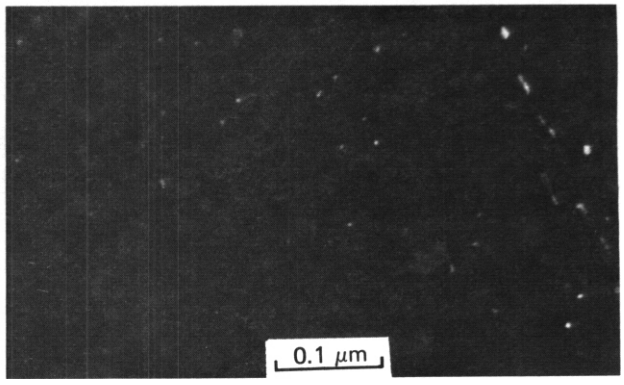

(d)

H-72166

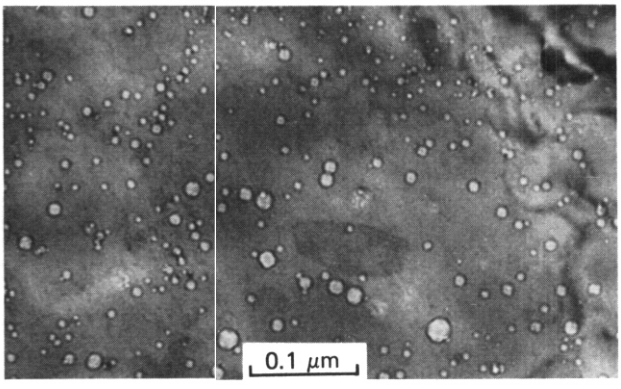

(e)

H-72167

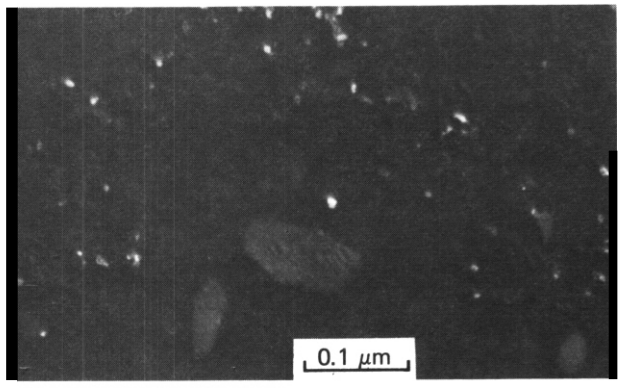

Fig. 3.1.7. **Stability as a function of fluence at 600°C for MC developed by pretreatment of PCA-B2.** Bright field and dark-field images are *(a, b)* as heat treated, *(c, d)* irradiated to 10.5 dpa, *(e, f)* irradiated to 22 dpa.

Fig. 3.1.7(f). Zones of radiation-induced solute segregation (RIS) forming around such sinks may be responsible for MC particles not nucleating near the loops.[12] Although the reprecipitation of dissolved MC is not usually observed, it does correlate with the saturation of swelling shown in Fig. 3.1.2.

3.1.4.3 Discussion

As reported previously,[1,2] this work continues to show different temperature dependences of swelling of several of the PCA variants and CW 316 (N-lot) compared with CW 316 (DO-heat) and CW 316 + Ti (R1-heat) for irradiation in HFIR at 400–650°C. The latter steels show low, nearly temperature-independent swelling because helium bubbles remain stable and do not develop into voids. The PCA variants A1 and B1 show strong increases in swelling as void formation increases with increasing irradiation temperature. Under the same conditions, the initially cold-worked PCA-A3 showed swelling with little temperature dependence. Like CW 316 (DO-heat) and CW 316 + Ti (R1-heat), bubbles remained stable in PCA-A3 and did not develop into voids. The underlying reasons for the bubble stability appear to have been early development of a high concentration of cavities that act as the dominant sinks, so neither RIS nor voids developed. Comparison of solution-annealed and CW 316 (DO-heat) irradiated in EBR-II and HFIR showed that increased helium generation could either increase or suppress void swelling.[11] Correlation of the precipitation development in these same samples illustrated that suppression of RIS effects coincided with suppression of void formation. These same correlations result from comparison of PCA-A1, -B2, and -A3 irradiated in HFIR at 600°C to ~22 dpa. Both minimum RIS and minimum swelling coincide with maximum stability of MC. Conversely, minimum MC stability coincides with maximum void swelling and development of coarse particles of G or eta phase.

The fluence dependent data extend the trends observed in the last report. When void development was minimal, swelling rates were low and showed little temperature dependence at 400–600°C. This was the general behavior of CW 316 (DO-heat), CW 316 + Ti (R1-heat), PCA-A3, and CW 316 (N-lot). Conversely, those PCA variants that developed voids easily also had the greatest temperature dependence of the swelling rates between 400 and 600°C. Although the SA 316 (DO-heat) shows little temperature dependence of the swelling rate at higher fluence, it does have high total swelling due to voids over the range 525–640°C. The unusual saturation of swelling with increasing fluence demonstrated in PCA-B2 at 600°C illustrates the important coupling of swelling and precipitation. Since RIS and MC development are generally not coincident phenomena, these data suggest that the development of RIS was interrupted as fluence increased. A similar, coupled reversal of void and RIS development (γ' formation, in that case) with increasing fluence had been reported previously[13] for CW 316 (DO heat) irradiated in HFIR at 425–450°C. (The uncorrected irradiation temperature had been reported earlier[13] as 375°C.) Blocking or disrupting the cooperative development of voids and strong RIS appears to be an effective way to resist continued void swelling.

3.1.5 Conclusions

1. Disks of PCA variants and CW 316 (N-lot) were irradiated in HFIR to ~22 dpa at 400–600°C. The void swelling was less than 0.2% for all samples irradiated at 400°C, and lowest in PCA-A3 (25% CW). Swelling was 1.2–1.4% at 600°C for PCA-A1 (SA) and PCA-B1 (SA + MC coarse precipitation), 0.3–0.5% for PCA-B2 (25% CW plus fine MC precipitation) and CW 316 (N-lot), and 0.13–0.15% for PCA-A3.
2. Swelling of the PCA variants and CW 316 (N-lot) generally increased with increased irradiation temperature and fluence. However, PCA-B2 differed, with no additional swelling with fluence above 10 dpa at 600°C.
3. Low swelling in some PCA conditions was associated with an irradiated microstructure containing a high concentration of fine MC particles, no coarse and/or RIS-induced phases, and a low density of irradiation-induced network dislocations and Frank loops.
4. Higher swelling in the PCA alloys correlated with a minimum or lack of fine MC, the presence of RIS-induced (or -increased) G (or eta phase), and more network dislocations and Frank loops.
5. Future work will extend evaluation of PCA variants to ~44 dpa.

3.1.6 References

1. P. J. Maziasz and D. N. Braski, "Swelling of Path A PCA Irradiated to 10 dpa in HFIR," pp. 98–116 in *ADIP Semiannu. Prog. Rep. Mar. 30, 1982*, DOE/ER-0045/8, U.S. DOE, Office of Fusion Energy.
2. P. J. Maziasz and D. N. Braski, "Swelling and Microstructural Development in Path A PCA and Type 316 Stainless Steel Irradiated in HFIR to about 22 dpa," pp. 44–61 in *ADIP Semiannu. Prog. Rep. Sept. 30, 1982*, DOE/ER-0045/9, U.S. DOE, Office of Fusion Energy.
3. M. L. Grossbeck, J. W. Woods, and G. A. Potter, "Experiments HFIR-CTR-30, -31, and -32 for Irradiation of Transmission Electron Disk Specimens," pp. 36–44 in *ADIP Quart. Prog. Rep. Sept. 30, 1980*, DOE/ER-0045/4, U.S. DOE, Office of Fusion Energy.
4. L. R. Greenwood, "Neutron Source Characterization for Materials Experiments," pp. 66–86 in *ADIP Semiannu. Prog. Rep. Mar. 31, 1982*, DOE/ER-0045/8, U.S. DOE, Office of Fusion Energy.

5. P. J. Maziasz and M L. Grossbeck, "Swelling and Microstructure of HFIR-Irradiated 20%-Cold-Worked Types 316 Stainless Steel and 316 + *0.23* wt % Ti," pp. 43-69 in *ADIP mart. Frog. Rep. Dec. 31, 1980,* DOE/ER-0045/5, U.S. DOE, Office of Fusion Energy.

6. P. J. Maziasz and M L. Grossbeck, "Microstructural Development in 20%-Cold-Worked Type 316 Stainless Steel and Titanium-Modified Type 316 Stainless Steel Irradiated in the HFIR. Fluence Dependence of the Cavity Component," pp. 28–56 in *ADIP mart. Prog. Rep. Mar. 31, 1981,* DOE/ER-0045/6, U.S. DCE, Office of Fusion Energy.

7. P. J. Maziasz, F. W Wiffen, and E. E. Bloom, "Swelling and Microstructural Changes in Type 316 Stainless Steel Irradiated under Simulated CTR Conditions," pp. 259–88 in *Radiation Effects and Tritium Technology for Fusion Reactors*, CONF-750989, Vol. 1 (March 1976).

8. P. J. Maziasz, unpublished data, 1983.

9. L. K. Mansur and W. A. Coghlan, "Mechanisms of Helium Interaction with Radiation Effects in Metals and Alloys," to be published in *Journal of Nuclear Materials.*

10. G. R. Odette and C. S. Langley, "Modeling of Synergistic Effects of Displaced Atoms and Transmutant Damage in Fission and Fusion Environments," p. 395 in *Radiation Effects and Tritium Technology* for *Fusion Reactors*, CONF-750989, Vol. 1 (March 1976).

11. L. K. Mansur, M R. Hayns, and E. H. Lee, "Mechanisms Affecting Swelling in Alloys with Precipitates," p. 359–82 in *Phase Stability* Curing *Irradiation*, ed. J. R. Holland, L. K. Mansur and D. I. Potter, The Metallurgical Society of AIME, Warrendale, Pa, 1981.

12. P. J. Maziasz, "Some Effects of Increased Helium Content on Void Formation and Solute Segregation in Neutron-Irradiated Type 316 Stainless Steel," *J. Nucl. Mater.* 108&109, 359–84 (1982).

13. P. J. Maziasz, J. A Horak, and B. L. Cox, "The Influence of Both Helium and Neutron Irradiation on Precipitation in 20%-Cold-Worked Austenitic Stainless Steel," pp. 271–92 in *Phase Stability Curing Irmdiation,* ed. J. R Holland, L. K. Mansur, and D. I. Potter, The Metallurgical Society of AIME, Warrendale, Pa, 1981.

3.2 GRAIN BOUNDARY MICROSTRUCTURAL DEVELOPMENT AND STABILITY FOR VARIOUS PRETREATMENTS OF PATH A PRIME CANDIDATE ALLOY IRRADIATED IN HFIR — P. J. Maziasz and D. N. Braski (Oak Ridge National Laboratory)

3.2.1 ADIP Task

ADIP Task I.C.1, Microstructural Stability, and I.C.2, Microstructure and Swelling in Austenitic Alloys.

3.2.2 Objective

The purpose of this work is to examine and evaluate the effect of thermal-mechanical pretreatments that vary preirradiation grain boundary precipitate structure on grain boundary microstructural development during irradiation in HFIR. The goal is to refine grain boundary cavity structures and thus reduce helium embrittlement.

3.2.3 Summary

Irradiation to 22 dpa in HFIR at 500 and 600°C produced resolvable grain boundary bubbles in Path A PCA and CW 316. PCA-A1 had the coarsest bubble structure at 600°C and no MC precipitate. Medium to coarse distributions of MC developed at the boundaries by heat treatment of PCA-B1 and -B2 were stable under irradiation; very fine bubbles clustered about these particles at 600°C. The PCA also resisted sigma formation, compared with CW 316 (D0 heat) or SA 316 and 316 + Ti (R1 heat) irradiated in HFIR.

3.2.4 Progress and Status

The approach to designing grain boundary MC precipitate structures in the Path A PCA and the microstructure-properties correlations that suggested that helium embittlement resistance can thus be obtained were discussed previously.[1,2] The description of the specimens and the irradiation experiments HFIR-CTR-30 through -32 have also been presented.[3] Relevant compositions, microstructures, and thermal-mechanical pretreatments are given in Sect. 3.1 of this report.

Figure 3.2.1 shows that the increased helium generation *in* HFIR, relative to EBR-II, leads to increased and/or coarser grain boundary bubble structures in 20%-cold-worked type 316 stainless steel (CW 316).

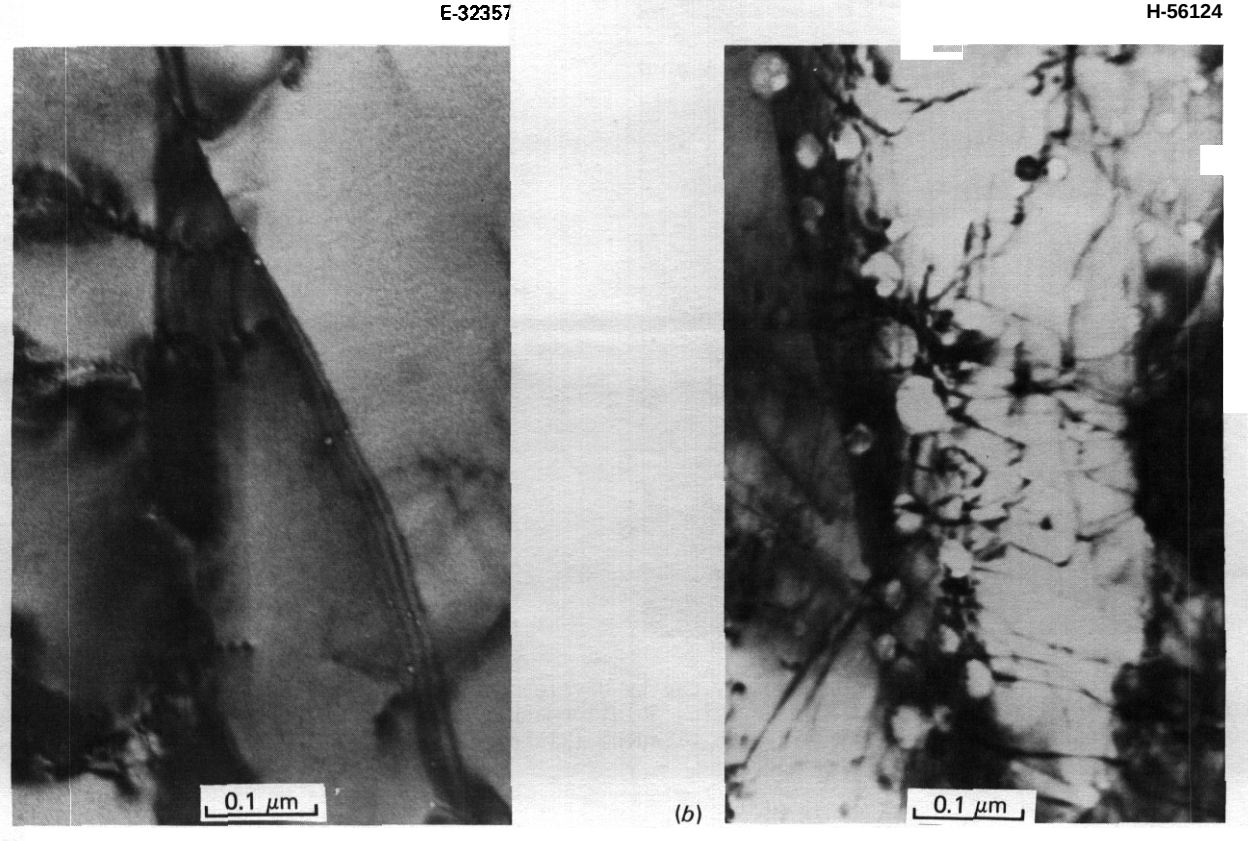

Fig. 3.2.1. Increased helium generation results in increased and coarser grain boundary cavitation in CW 316 (D0 heat). Irradiations were in the temperature range 615 to 640°C. The EBR-II irradiation (*a*) produced 36 dpa and about 22 at. ppm He. HFIR exposure (b) produced 16.6 dpa and 880 at. ppm He.

Reduced postirradiation tensile ductility and intergranular failure were associated with the HFIR microstructure.[2] Contributions to the embrittlement may have resulted from segregation of impurities or from undesirable precipitate phases, in addition to the helium bubble effects.

Grain boundary bubble and precipitate microstructure development under irradiation can be affected by alloying as well as by thermal-mechanical pretreatment. Figure 3.2.2 compares the boundaries in solution-annealed (SA) and CW 316 (00 heat) and 316 + Ti (R1 heat), all irradiated in HFIR to produce 16.6 dpa and 880 at. ppm He at 615 to 640°C (ref. 4). Grain boundary bubbles are roughly similar for SA and CW 316 (D0 heat) and only slightly smaller for SA 316 + Ti (R1 heat) but are considerably smaller for the CW 316 + Ti. Grain boundaries in the same samples are compared in Fig. 3.2.3, at lower magnification, to illustrate

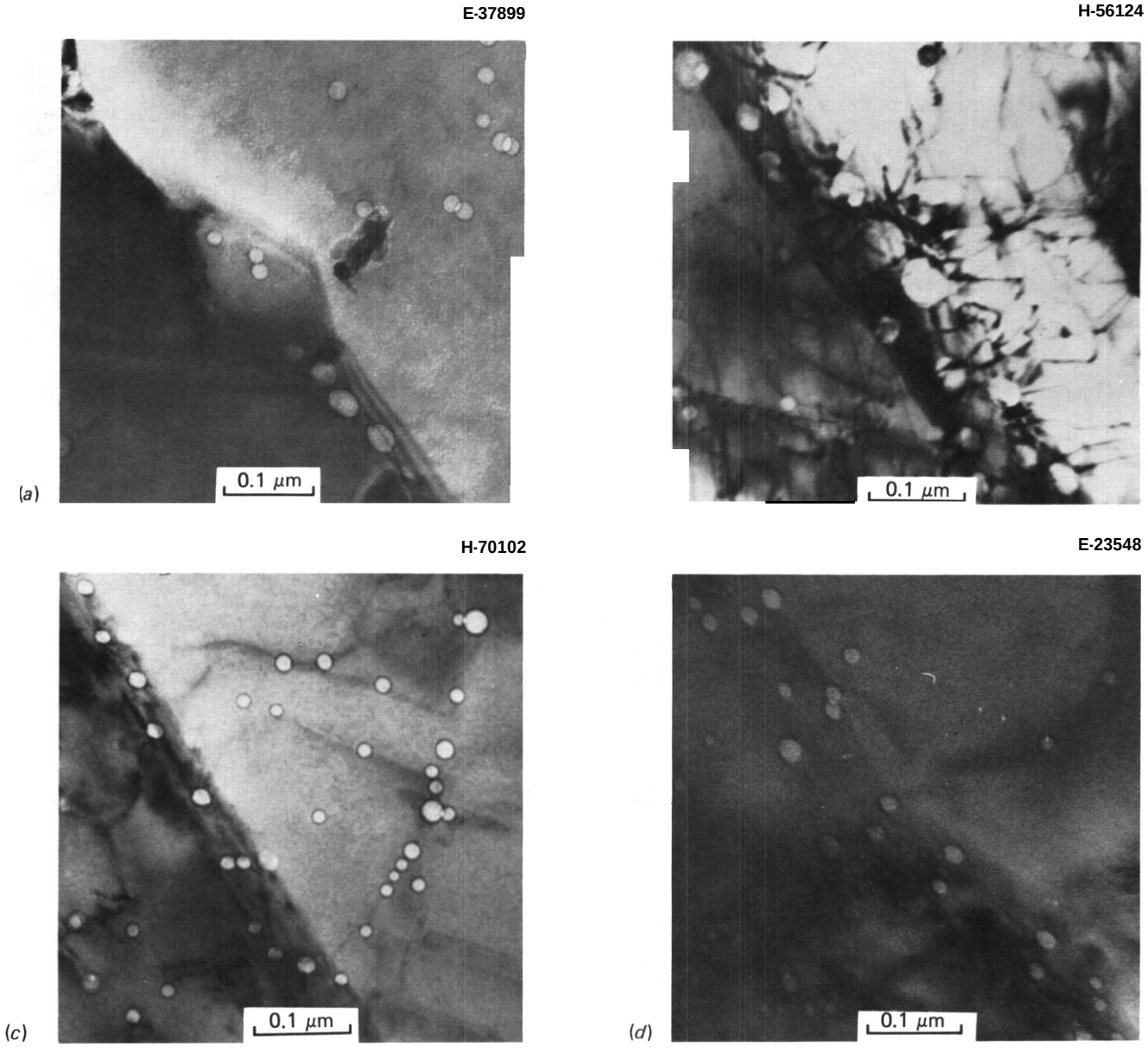

Fig. 3.2.2. Comparison of grain boundary cavity development for stainless steel irradiated in HFIR at 615 to 640°C to 16.6 dpa and 880 at. ppm He. *(a)* Solution-annealed type 316 (D0 heat). (*b*) Cold-worked type 316. (*c*) Solution annealed type 316 with titanium (R1 heat). *(d)* Cold-worked type 316 with titanium.

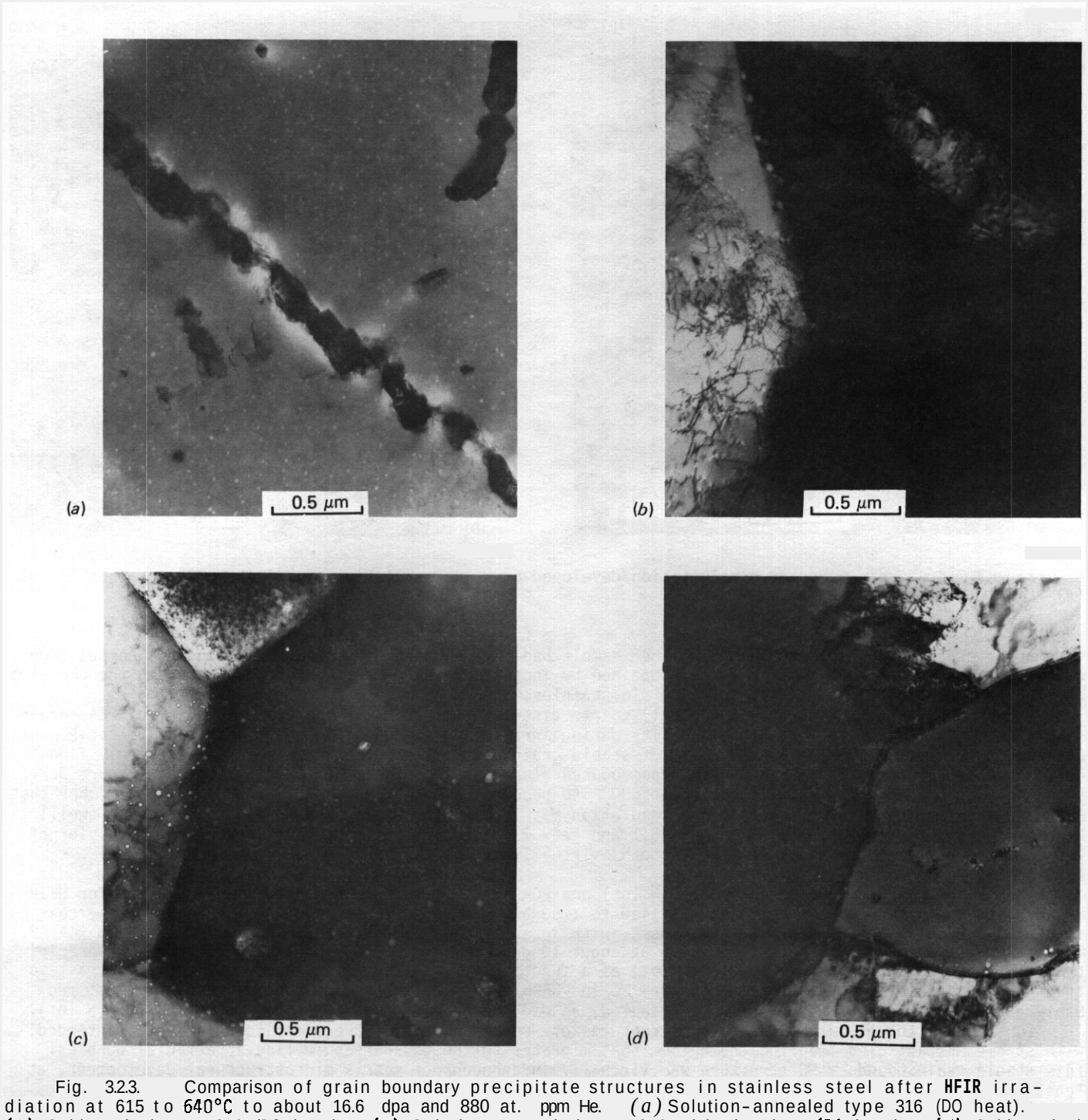

Fig. 3.2.3. Comparison of grain boundary precipitate structures in stainless steel after HFIR irradiation at 615 to 640°C to about 16.6 dpa and 880 at. ppm He. *(a)* Solution-annealed type 316 (DO heat). *(b)* Cold-worked type 316 (DO heat). *(c)* Solution-annealed type 316 with titanium (R1 heat). *(d)* Cold-worked type 316 with titanium (R1 heat).

boundary precipitation differences. The SA 316 (DO heat) shows a coarse dispersion of eta (and/or tau) phase particles in the grain boundaries, but the other materials contain no grain boundary carbides. Instead, the irradiated CW 316 (DO heat) and both SA and CW 316 + Ti (R1 heat) contained grain boundary cavities and massive sigma phase particles. Sigma formation is often greater in titanium-modified austenitic steels. Further, sigma precipitation can be increased by irradiation conditions that result in suppressed swelling and radiation-induced solute segregation (RIS), because such conditions tend to favor thermal phases.[5] Sigma is seldom observed in these steels irradiated in EBR-II below about 700°C (ref. 6).

Grain boundary microstructures of PCA-A1 and PCA-A3 irradiated in HFIR at 600°C to about 22 dpa are compared in Fig. 3.2.4. The cold-worked PCA-A3 had no precipitation, whereas PCA-A1 had a sparse distribution

H-72304

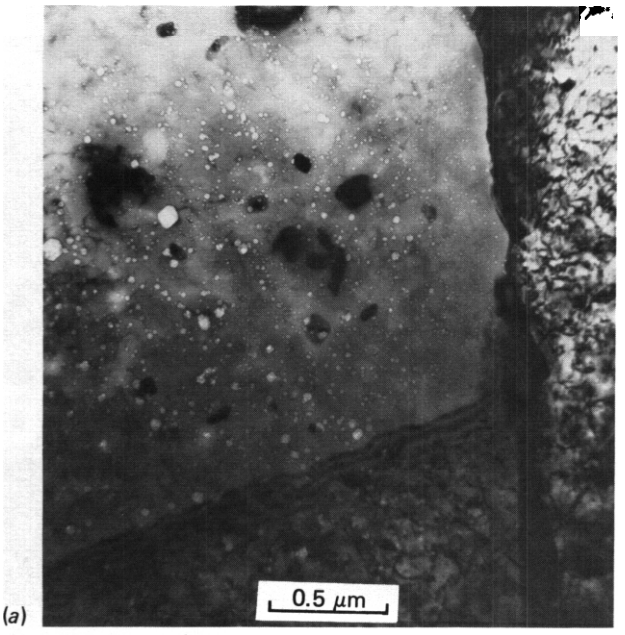

(a)

H-69210

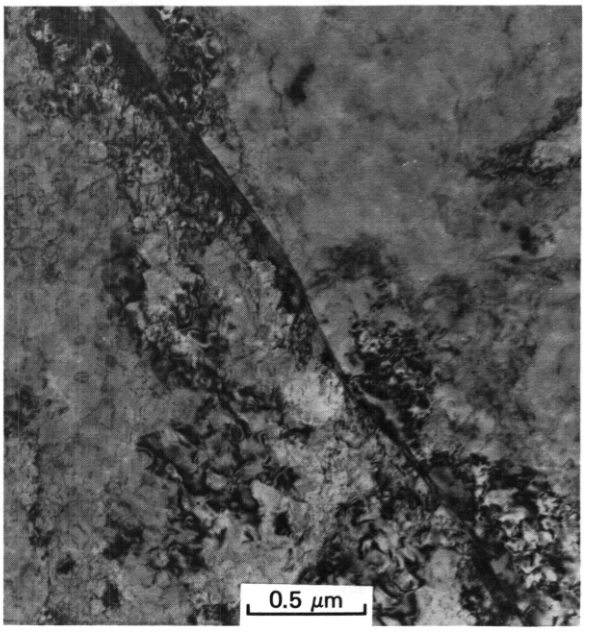

(b)

Fig. 3.2.4. Grain boundary precipitation developed by HFIR irradiation of PCA at 600°C to about 22 dpa. *(a)* PCA-AI. *(b)* PCA-A3.

of coarser eta (and/or tau) carbides. Neither sample had any evidence of sigma phase. The PCA composition was selected for reduced sigma formation, obtained by increasing the nickel content and lowering the chromium content compared to the composition of type 316 stainless steel.

The present results show that moderately coarse distributions of MC in the grain boundary of PCA remain stable during HFIR irradiation. The stability during irradiation at 600°C is shown in Fig. 3.2.5 for PCA-81 and in Fig. 3.2.6 for PCA-B2. The benefit of stable grain boundary precipitates is in the extremely fine helium bubbles distributions that can be accommodated along the interfaces of these particles. Figure 3.2.7 shows such trapping in PCA-B1, irradiated at 600°C to produce about 10 dpa and 550 at. ppm He. Remember that PCA-BI and -82 contain very different preirradiation matrix microstructures' that lead to different swelling behavior under HFIR irradiation (See Sect. 3.1 and ref. 3). In spite of these differences, the behavior of the grain boundary structure is similar in both, virtually independent of the matrix microstructural development.

The grain boundary bubbles in CW 316 (N lot) and PCA-AI, -A3, and -82 are shown in Fig. 3.2.8 for HFIR irradiation that produced about 22 dpa and 1450 to 1750 at. ppm He at 600°C. The PCA-A1 contains the coarsest bubble distribution and PCA-B2 the finest, with intermediate bubble sizes in CW 316 (N lot) and PCA-A3. These trends are similar to those reported2 at about 10 dpa. Figure 3.2.9 shows the development of precipitation and bubble structures in CW 316 (N lot) as a function of increased fluence at 600°C. In contrast to the stability exhibited by the grain boundary MC in PCA-B1 and -82, the grain boundary carbides (most probably eta and/or tau) coarsened and redistributed, as did the bubble microstructure, in the CW 316 (N lot).

In summary, the grain boundary microstructures of PCA-B1 and -B2 behave under irradiation as intended,' with stable MC particles trapping the helium that migrates to the boundaries in fine interfacial bubbles. This stable grain boundary MC structure was virtually independent of matrix microstructural development, at least to 22 dpa at 600°C. The heat treatment to produce it — namely 8 h at 800°C following solution annealing — can be combined with straight 25% cold working (as in PCA-A3) to attempt to impart maximum embrittlement and swelling resistance in the same material (See Sect. 3.1 and ref. 3). Therefore, a new microstructure for the PCA, a combination of PCA-A3 and -B2, has been developed and is referred to as PCA-B3. It is produced by solution annealing, then aging for 8 h at 800°C, followed by 25% cold work.

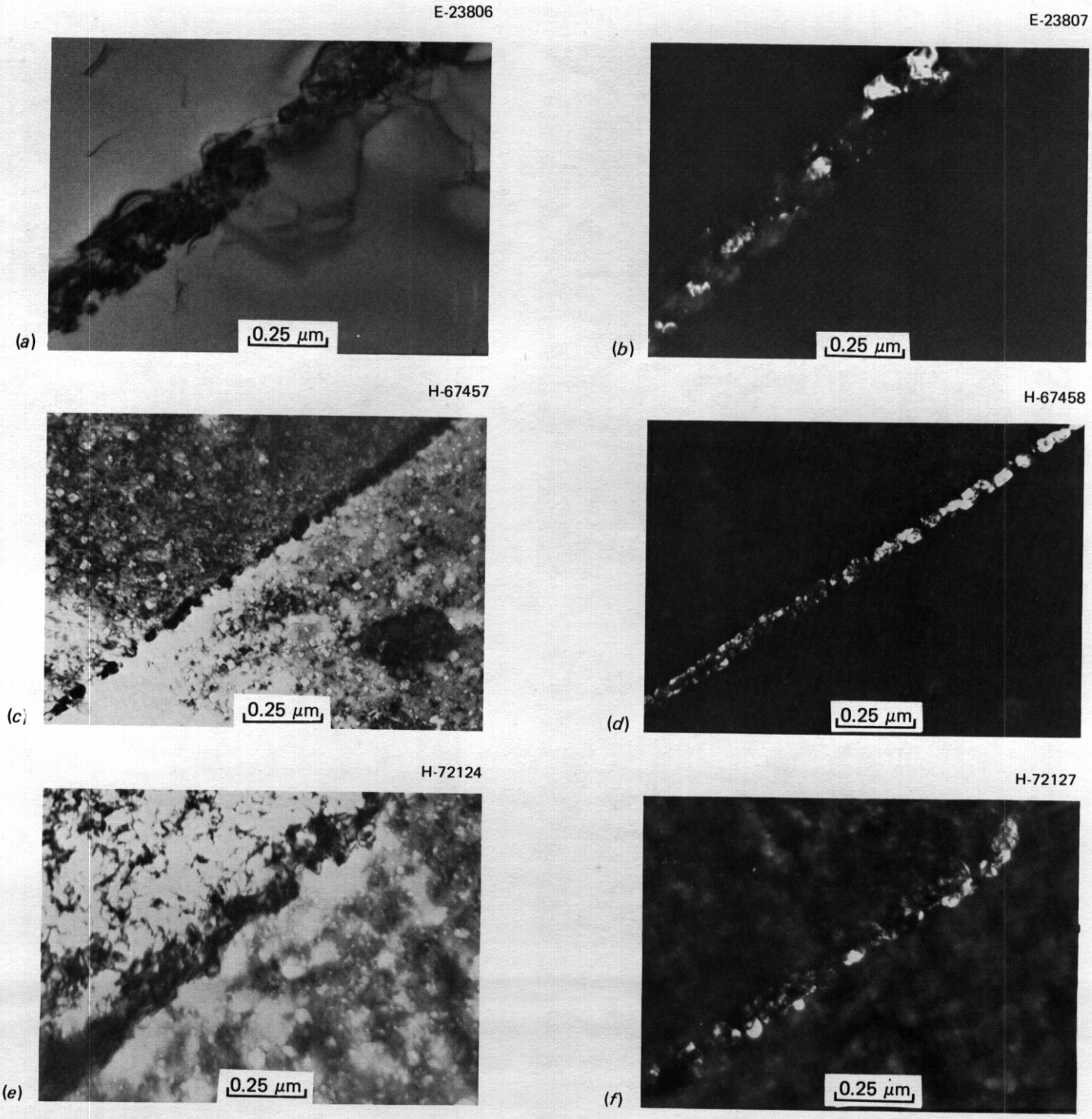

Fig. 3.2.5. Stability of coarse grain boundary MC precipitate in PCA-B1 during HFIR irradiation at 600°C. Dark-field images formed from an MC reflection.

E-23950

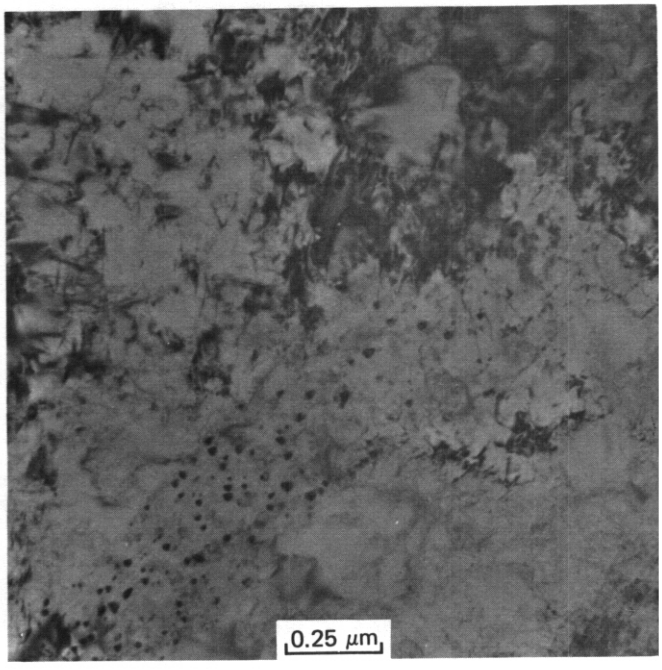

(a)

E-23951

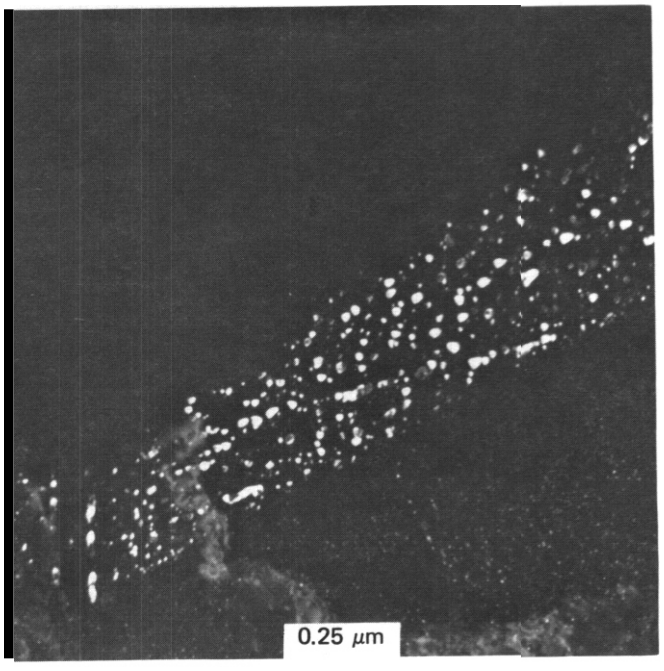

(b)

H-72149

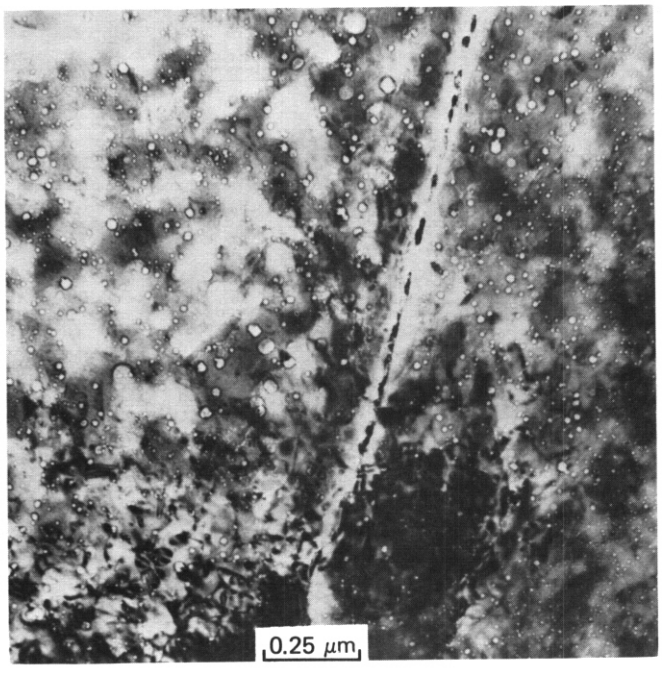

(c)

H-72150

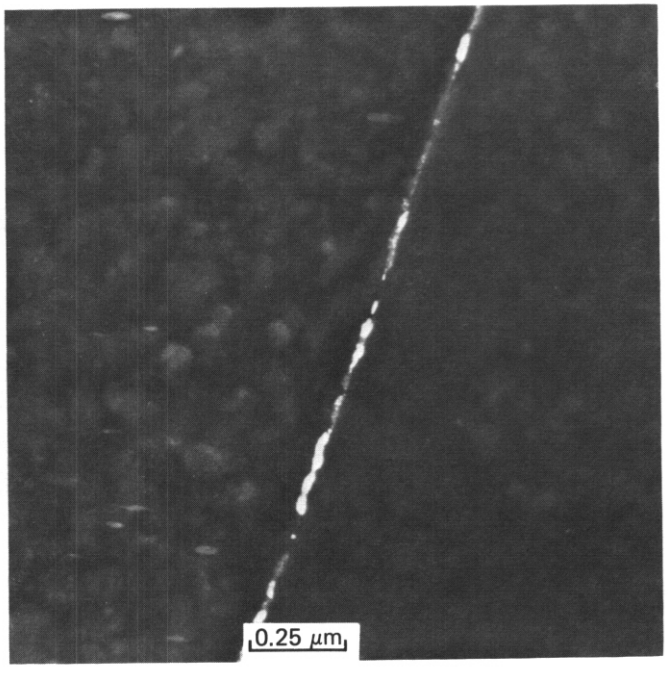

(d)

Fig. 3.2.6. Stability of grain boundary MC precipitate in PCA-B2 during HFIR irradiation at 600°C. Dark-field images formed from an MC reflection.

H-67446

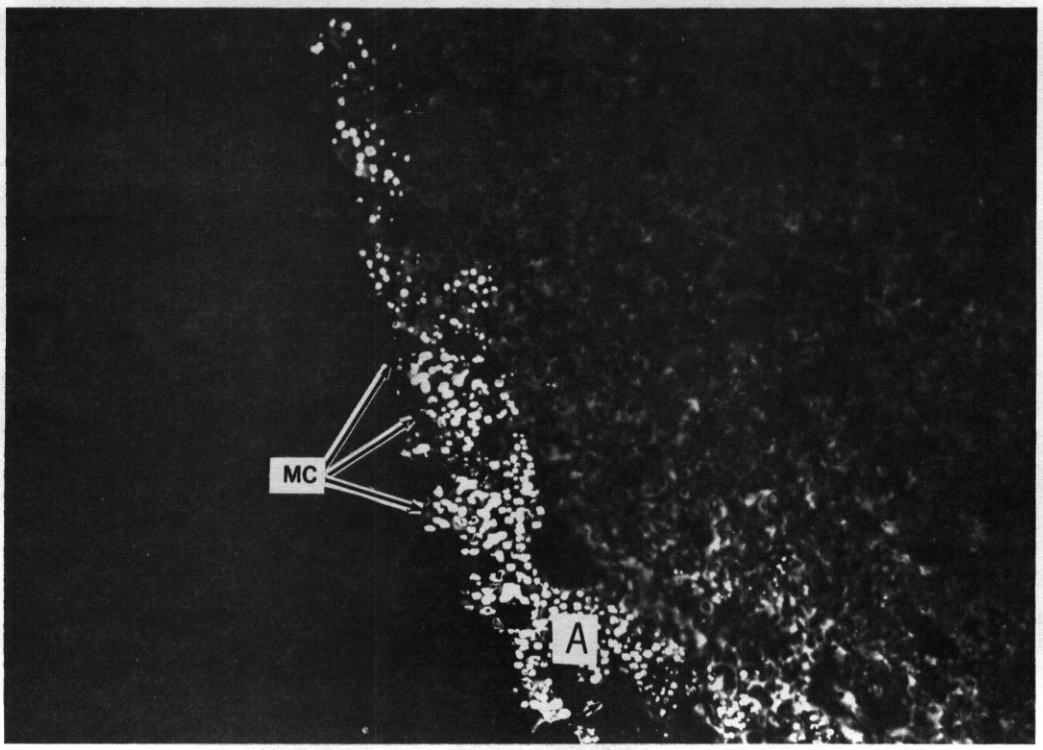

(a)

0.25 μm

H-67449

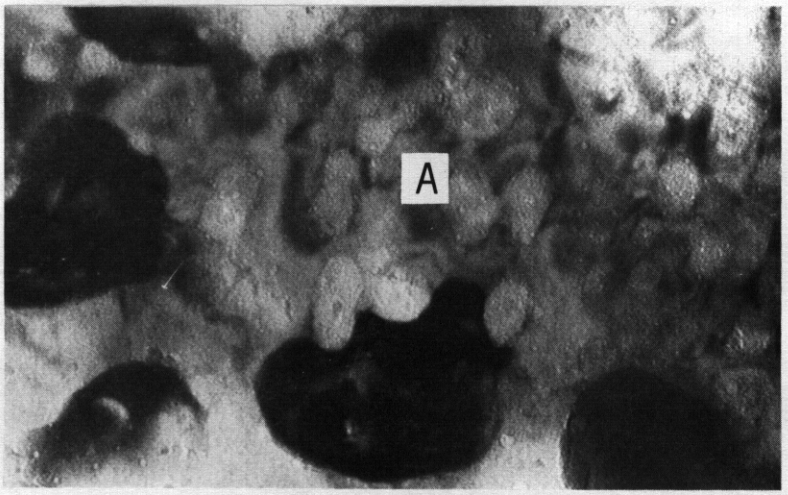

(b)

50 nm

Fig. 3.2.7. Helium trapped in very fine bubbles at the interfaces of grain boundary MC particles in PCA-B1. Irradiation was in HFIR at 600°C to produce 10.5 dpa and 550 at. ppm He. Dark field image is formed from an MC reflection.

H-71460

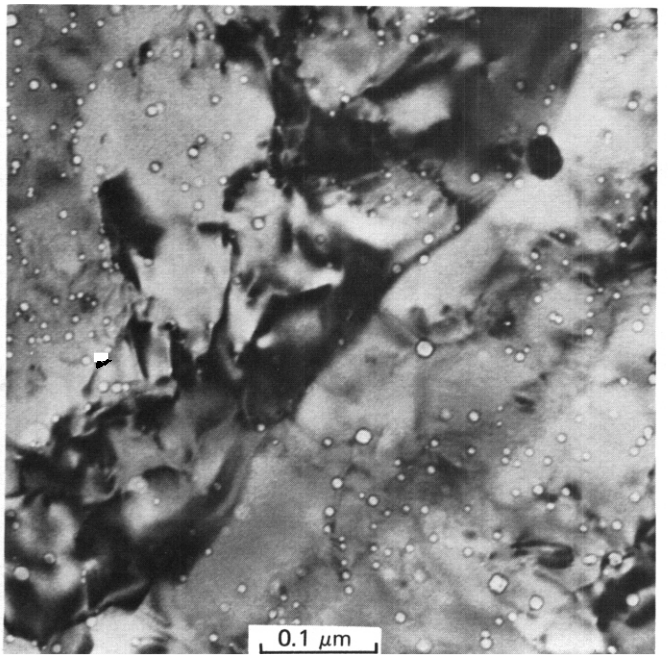

(a)

E 38666

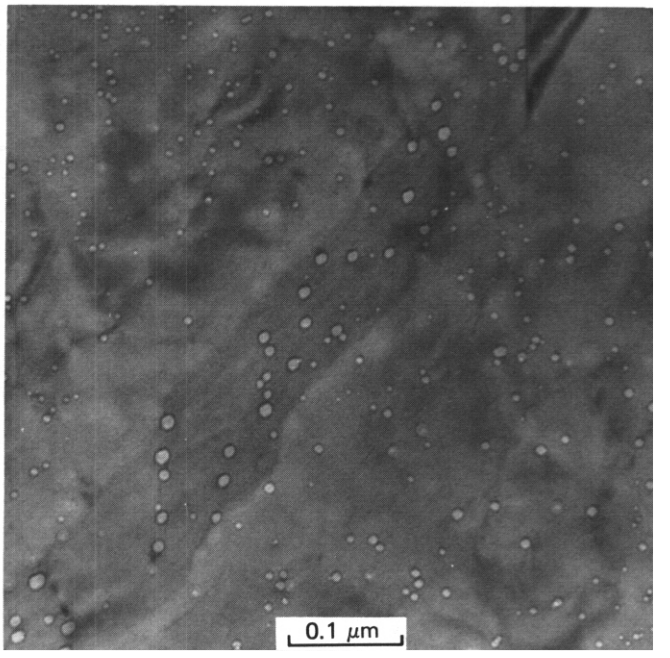

(b)

H-69246

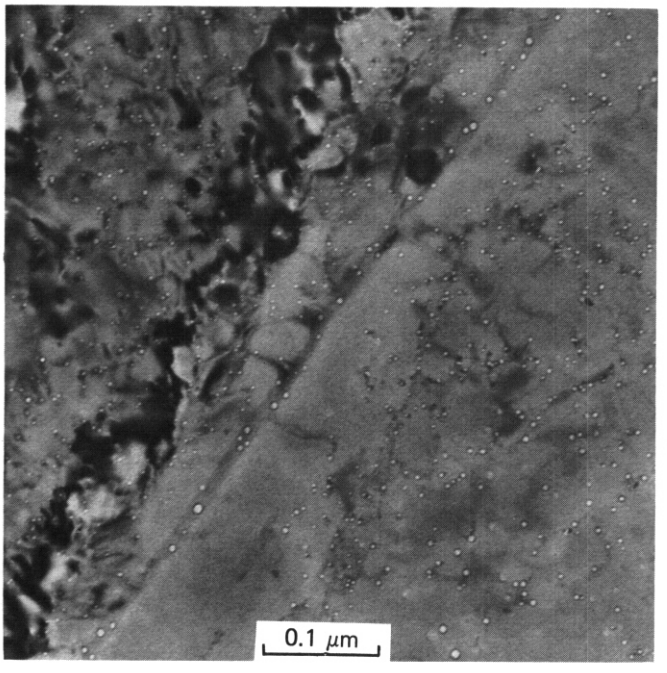

(c)

H-72156

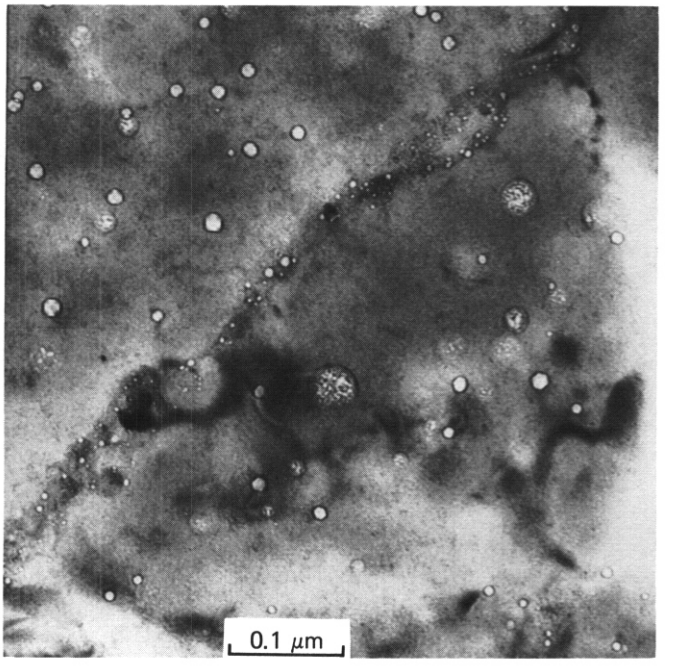

(d)

Fig. 3.2.8. Comparison of grain boundary bubble distributions in (a) CW 316 (N lot), (b) PCA-A1, (c) PCA-A3, and (d) PCA-B2, all irradiated in HFIR to about 22 dpa at 600°C.

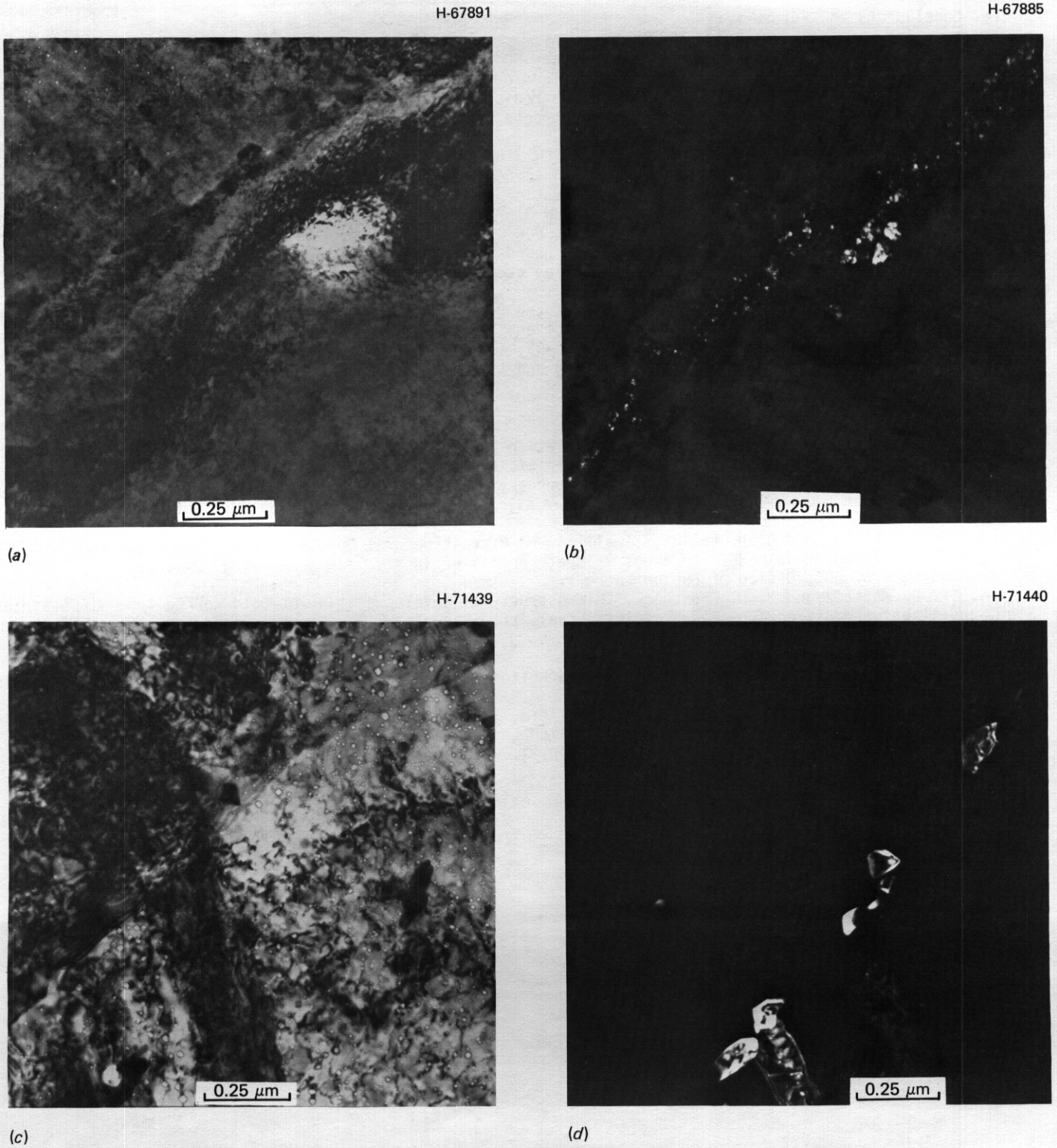

Fig. 3.2.9. The stability of grain boundary carbides in CW 316 (N lot) during HFIR irradiation at 600°C. *Left*, dark field. *Right*, bright field. *Top*, about 10.5 dpa. *Bottom*, about 22 dpa.

3.2.5 Conclusions and Future Work

Neither PCA-A1 nor -A3 developed grain boundary MC during HFIR irradiation at 600°C to about 22 dpa. The PCA-A1 developed sparse, coarse carbides (M_6C and/or $M_{23}C_6$) at the boundaries. In CW 316 (N lot), grain boundary carbides developed and then coarsened and redistributed with increasing fluence at 600°C. Moderate to coarse grain boundary MC, developed by pretreatments before irradiation in PCA-B1 and -B2, remained stable under HFIR irradiation up to about 22 dpa at 600°C.

The CW 316 (DO heat) and particularly SA and CW 316 + Ti (R1 heat) formed massive sigma phase particles at grain boundaries during HFIR irradiation at 615 to 640°C to about 16.6 dpa. In contrast, none of the PCA variants [or CW 316 (N lot)] showed any sigma formation during irradiation to about 22 dpa at 600°C.

Grain boundary bubbles were much smaller in CW 316 (N lot) and the PCA variants than in SA or CW 316 (DO heat) and 316 + Ti (R1 heat) irradiated in HFIR at 600°C to about 22 dpa. Comparison among the PCA variants and CW 316 (N lot) reveals that the largest grain boundary bubbles were seen in PCA-A1 and the smallest in PCA-B2 and -B1. The smallest grain boundary bubbles occurred when the bubbles were dispersed at the interfaces of stable MC particles.

Future work will include disk bend testing of the PCA microstructural variants irradiated in HFIR-CTR-30 through -32. The results may establish the effectiveness of the grain boundary structures in preventing helium embrittlement. The new microstructure, PCA-B3, is currently under irradiation in HFIR-CTR-42 and -43. Postirradiation testing will evaluate the swelling and tensile properties.

3.2.6 References

1. P. J. Maziasz and T. K. Roche, "Preirradiation Microstructural Development Designed to Minimize Properties Degradation During Irradiation in Austenitic Alloys," *J. Nucl. Mater.* 1036104, 797–801 (1981).
2. P. J. Maziasz and D. N. Braski, "Grain Boundary Microstructure in Path A PCA Irradiated to 10 dpa in HFIR," pp. 118–35 in *ADIP Semiannu. Prog. Rep. Mar. 31, 1982,* DOE/ER-0045/8, U.S. DOE, Office of Fusion Energy.
3. P. J. Maziasz and D. N. Braski. "Swelling and Microstructural Development in Path A PCA and Type 316 Stainless Steel Irradiated in HFIR to about 22 dpa," pp. 44–62 in *ADIP Semiannu. Prog. Rep. Sept. 30, 1982*, DOE/ER-0045/9, U.S. DOE, Office of Fusion Energy.
4. P. J. Maziasz and M. L. Grossbeck, "Microstructural Development in POX-Cold-Worked Type 316 Stainless Steel and Titanium-Modified Type 316 Stainless Steel Irradiated in HFIR: Fluence Dependence of the Cavity Component," pp. 28–56 in *ADIP Quart. Prog. Rep. Mar. 31, 1981,* DOE/ER-0045/6, U.S. DOE, Office of Fusion Energy.
5. P. J. Maziasz, "Some Effects of Increased Helium Content on Void Formation and Solute Segregation in Neutron-Irradiated Type 316 Stainless Steel," *J. Nuct. Mater.* 108&109, 359–84 (1982).
6. E. H. Lee, P. J. Maziasz, and A. F. Rowcliffe, "The Structure and Composition of Phases Occurring in Austenitic Stainless Steel in Thermal and Irradiation Environments," pp. 191–218 in *Phase Stability During Irradiation*, ed. J. R. Holland, L. K. Mansur, and D. I. Potter, The Metallurgical Society of AIME, Warrendale, Pa., 1981.

3.3 THE TENSILE PROPERTIES OF UNIRRADIATED PATH A PRIME CANDIDATE ALLOY — D. N. Braski and P. J. Maziasz (Oak Ridge National Laboratory)

3.3.1 ADIP Task

ADIP Task I.B.13, Tensile Properties of Austenitic Alloys

3.3.2 Objective

The objective of this research is to determine the tensile properties of unirradiated PCA in the temperature range room temperature to 700°C.

3.3.3 Summary

The tensile properties of Path A PCA in the A1, A3, and B2 conditions have been determined at temperatures from room temperature to 700°C. The 25%-cold-worked alloy, PCA-A3, showed strength values similar to those of the reference heat of 20%-cold-worked 316 stainless steel but exhibited a lower ductility in the 200–300°C range.

3.3.4 Progress and Status

3.3.4.1 Introduction

The results of tensile tests at 200 and 700°C have been added to the previous results[1] to complete measurements for the range 20 to 700°C. The results are shown graphically for PCA-A1 (solution annealed) in Fig. 3.3.1, PCA-A3 (25%-cold-worked) in Fig. 3.3.2, and PCA-B2 (aged, cold-worked, and reaged) in Fig. 3.3.3. The new tensile results are also listed in Table 3.3.1. Details of the thermomechanical treatments to produce the various microstructures were reported previously.[2] Drops in yield strength, ultimate tensile strength, and uniform elongation were observed for PCA-AI, -A3, and -B2 at 700°C (Figs. 3.3.1 and 3.3.2), but

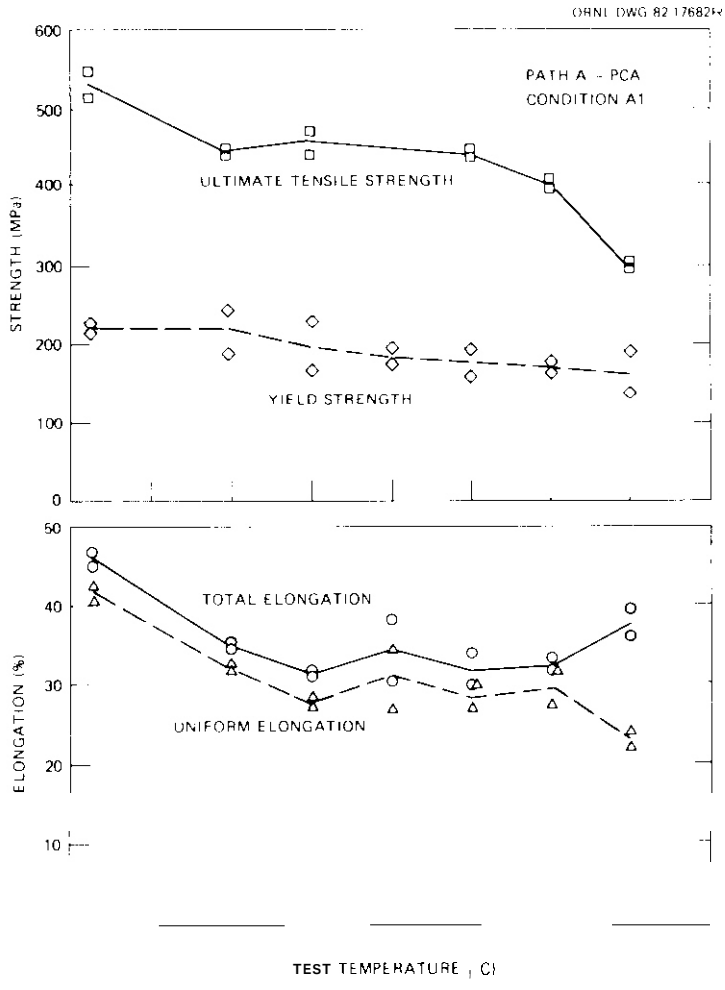

Fig. 3.3.1. Tensile properties of PCA-A1 (solution-annealed) as a function of temperature.

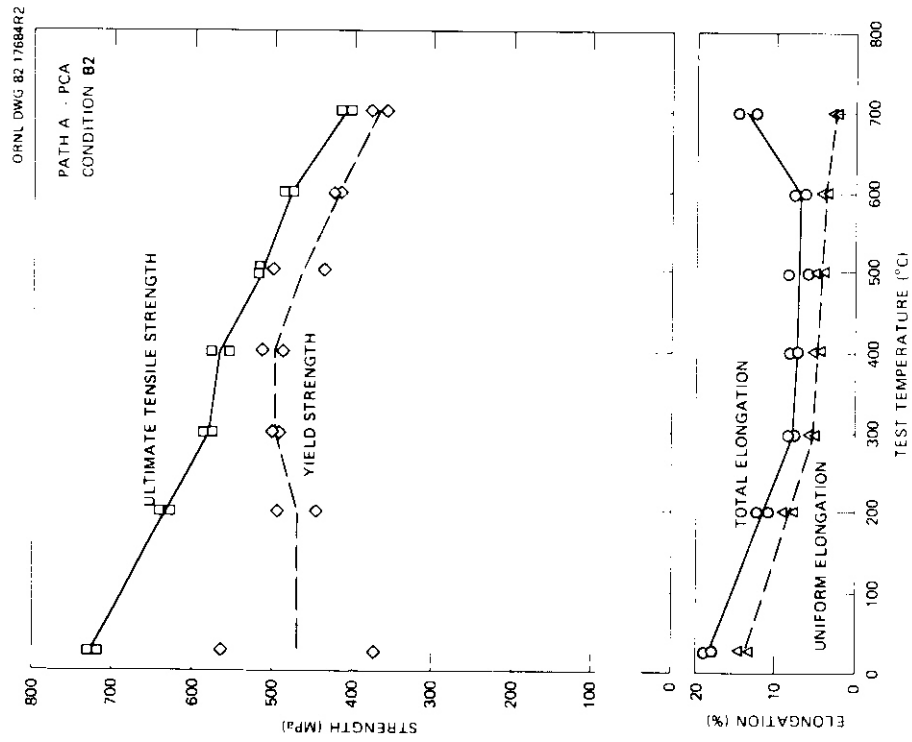

Fig. 3.3.3. Tensile properties of PCA-B2 (aged, 25%-cold-worked, and reaged 15 min at 750°C) as a function of temperature.

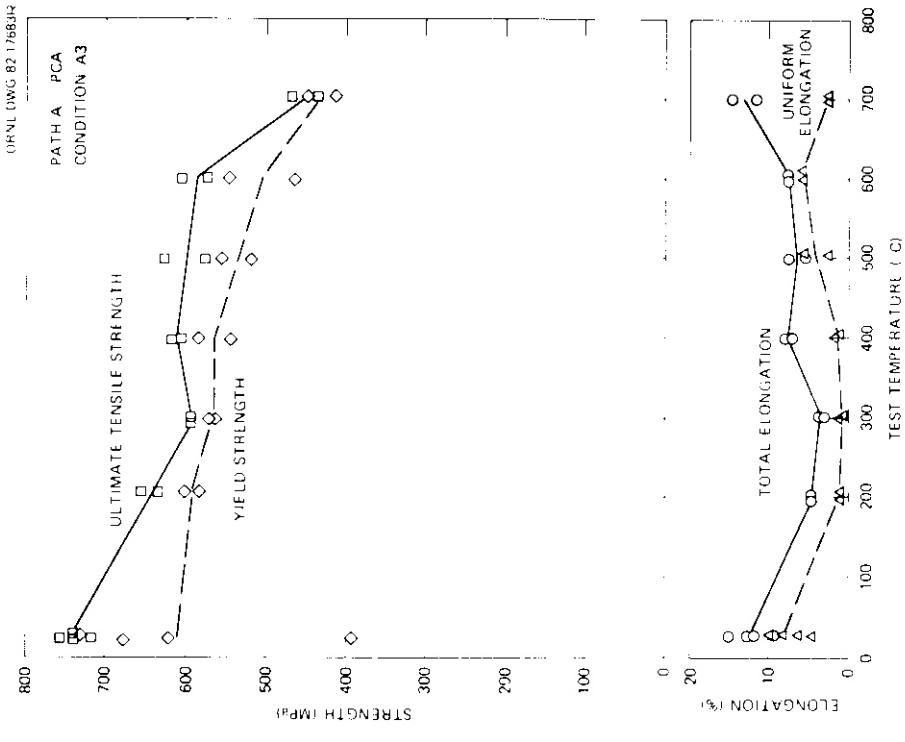

Fig. 3.3.2. Tensile properties of PCA-A3 (25%-cold-worked) as a function of temperature.

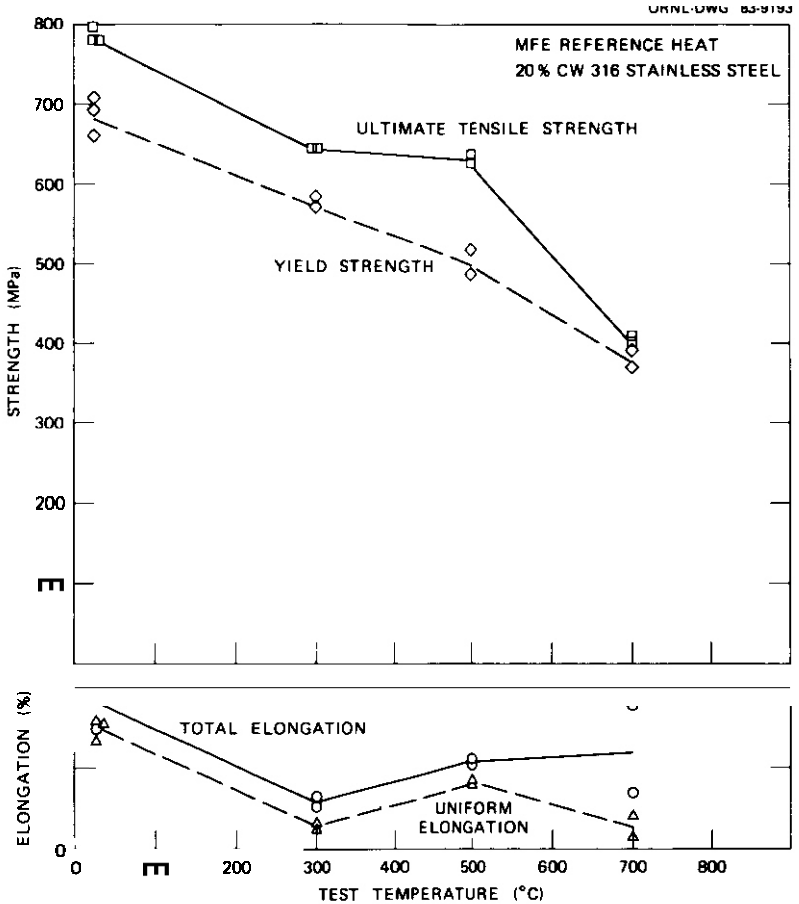

Fig. 3.3.4. Tensile properties of 20%-cold-worked type 316 stainless steel (Magnetic Fusion Energy reference heat) as a function of temperature.

Table 3.3.1. Tensile data for the Path A PCA alloy (heat K-280)

Test temperature (°C)	Yield strength (MPa)	Ultimate tensile strength (MPa)	Uniform elongation (%)	Total elongation (%)
Condition A1 — solution annealed				
200	192.2	444.6	31.8	34.4
200	233.6	437.1	30.6	33.8
700	143.2	297.6	23.6	38.5
700	180.8	302.6	21.0	35.6
Condition A3 — 25% cold worked				
200	594.2	661.4	1.4	5.5
200	619.6	649.7	1.1	5.2
700	446.0	461.2	1.8	11.8
700	410.0	436.3	2.1	14.5
Condition B2 — aged, cold worked, and reaged				
200	534.8	629.6	7.3	10.0
200	485.5	614.4	8.8	12.5
700	364.1	405.8	2.6	14
700	380.9	402.0	2.9	12.6
20%-cold-worked type 316 stainless steel Magnetic Fusion Energy reference heat X-15893				
22	710.0	784.8	16.5	19.1
22	695.1	803.5	13.3	14.8
22	661.4	784.8	15.8	18.4
300	575.5	646.5	2.2	4.9
300	553.1	642.8	3.7	6.7
500	485.8	627.8	7.3	10.6
500	515.7	631.5	7.8	10.3
700	396.1	399.9	0.8	6.3
700	370.0	403.6	3.1	17.8

the total elongation increased for these alloys above the values measured at 600°C. Strength values for PCA-B2 at 600°C are 100 MPa higher in Figure 3.3.3 than reported in a similar figure previously (consistent with the tabular data in ref. 1, however). PCA-A3 is measurably stronger than -82 at 500 and 600°C, but their strengths are similar at 700°C. These alloys also have similar ductility over this same temperature range. The data at 200°C for all three thermomechanical treatments made only slight corrections to the curve reported previously.' However, the relatively low uniform elongation value for PCA-A3 (Fig. 3.3.2) is worth noting. This ductility trough in PCA-A3 between 200 and 300°C warrants further investigation. ?he results for the PCA-A3 from room temperature to 700°C can be compared with those for the reference heat of 20%-cold-worked type 316 stainless steel shown in Fig. 3.3.4 and Table 3.3.1. The results for the two alloys were actually quite similar except that the PCA-A3 exhibited a somewhat deeper ductility trough at 200 to 300°C, and higher yield strength at 500°C and above.

3.3.5 Conclusions and Future Work

The tensile properties of the PCA alloy in three conditions — A1, A3, and B2 — have been determined in the temperature range room temperature to 700°C. The 25%-cold-worked PCA-A3 showed strength values similar to those of the reference heat of 20%-cold-worked type 316 stainless steel but exhibited a deeper ductility trough in the 200–300°C range and higher yield strength at 500°C and above. We will attempt to uncover the reason for the lower ductility by correlating fracture and microstructural information with the properties for these tested samples.

3.3.6 References

1. D. N. Braski and P. J. Maziasz, "The Tensile Properties of Unirradiated Path A PCA," pp. 63–70 in *ADIP Semiannu. Frog. Rep. Sept.* 30, *1982*, DOE/ER-0045/9, U.S. DOE, Office of Fusion Energy.

2. P. J. Maziasr and T. K. Roche, "Design and Fabrication of Preirradiation Microstructures in Path A Prime Candidate Alloy," pp. 25–42 in *ADIP Quart. Prog. Rep. Dec. 31, 1980*, DOE/ER-0045/5, U.S. DOE, Office of Fusion Energy.

3.4 EFFECT OF THE MICROSTRUCTURE ON TENSILE PROPERTIES OF TYPE 316 STAINLESS STEEL — R. L. Klueh (Oak Ridge National Laboratory)

3.4.1 AOIP Task

AOIP Task I.B.13, Tensile Properties of Austenitic Alloys.

3.4.2 Objective

The objective of this study is the determination of the effect of microstructure on the tensile properties of irradiated type 316 stainless steel. The test material is given different levels of cold work and different heat treatments before irradiation in the Oak Ridge Research Reactor (ORR).

3.4.3 Summary

A series of tensile specimens that had been given different thermal and mechanical processing treatments was irradiated in the ORR at 250, 290, 450, and 500°C to a neutron fluence of about 6.8 × 10^{25} neutrons/m^2 (>0.1 MeV)(~5 dpa and 40 at. ppm He). The tensile properties of irradiated and unirradiated steel with 20, 30, and 50% cold work were determined at the irradiation temperatures.

3.4.4 Progress and Status

3.4.4.1 Introduction

Twenty-percent cold-worked type 316 stainless steel has been chosen as the structural material for several core components of first-generation fast breeder reactors. It is also a leading candidate for construction of the first-wall and blanket structure of fusion reactors. The choice of the cold-worked structure followed from the theoretical[1] and experimental[2] observations that high dislocation densities should[1] and did[2] have a favorable effect on the void density, which should and did lead to a decrease in swelling compared with a solution-annealed structure. Several studies have shown that cold working stainless steel leads to a reduction in swelling when the steel is irradiated between $0.3T_m$ and $0.5T_m$ (T_m is the melting point).[3-6] These investigations generally considered cold-work levels up to about 25 or 30%.

Although the reason for the choice of a 20% cold-work level (as opposed to a higher or lower level) does not appear to have been widely discussed in the literature, the choice undoubtedly reflected a consideration of the properties of an unirradiated cold-worked steel as well as the effect of the cold-worked structure on swelling. Brager[6] did show that for type 316 stanless steel, a 10% cold-work level caused nearly as great a suppression of void formation as did 20% cold work. Above about 475°C, he found little difference in the swelling behavior of steels with 10 or 20% cold work: at 420°C (the lowest temperature investigated), there was very little difference between steel cold worked 20 and 30%.

To date, most irradiation studies on the effect of microstructure (cold-work level and solution-anneal heat treatment) on type 316 stainless steel have examined the effect on swelling. Little information appears to be available on the effect of preirradiation microstructure on the irradiated tensile properties.[7-9] On the other hand, considerable information is available on the properties of solution-annealed (1 h at 1050°C) and 20%-cold-worked type 316 stainless steel irradiated in a fast reactor environment.[8-12] These irradiations extend to 8.4 × 10^{26} neutrons/m^2 (>0.1 MeV). In addition to the irradiation in fast reactors, properties of 20%-cold-worked type 316 stainless steel irradiated in the High Flux Isotope Reactor (HFIR), a mixed-spectrum reactor, have been reported.[13-14]

In a fusion reactor, two types of irradiation effects are expected. Displacement damage is produced by high-energy neutrons, and large amounts of transmutation helium are formed by the high-energy neutrons. Thus, it is of interest to determine the effect of both displacement damage and helium on properties. Only displacement damage effects can be studied by irradiation in a fast-spectrum fission reactor. The HFIR studies mentioned above were carried out as part of the fusion reactor materials studies. Irradiation of a nickel-containing alloy in such a mixed-spectrum reactor leads to helium production by a two-step reaction of ^{58}Ni with thermal neutrons. Thus, irradiation of stainless steel in a mixed-spectrum reactor can lead to both displacement damage by the fast neutrons and helium production by the thermal neutrons.

The present study investigated the effects of the preirradiation microstructure of type 316 stainless steel on tensile properties. Specimens with three cold-work levels and three different heat-treated conditions were irradiated in the ORR. The ORR is a mixed-spectrum reactor but has a maximum flux considerably less than that of HFIR.

3.4.4.2 Experimental Procedure

The type 316 stainless steel used in this study was taken from the Magnetic Fusion Energy (MFE) reference heat (X-15893). The chemical composition of this heat is

Element	Composition (wt %)	Element	Composition (wt %)	Element	Composition (wt %)	Element	Composition (wt %)
Cr	17.3	Ni	12.4	Mo	2.2	co	0.35
Mn	1.7	Si	0.7	C	0.05	Fe	Bal
P	0.03	S	0.015	B	0.0004		

Tensile specimens were machined from 0.76-mm-thick sheet. The final thermal and mechanical processing steps used to produce specimen material are given in Table 3.4.1. For the 20-, 30-, and 50%-cold-worked materials, the steel was solution annealed 1 h at 1050°C before the final cold working to 0.76 mn.

Sheet tensile specimens in this experiment were of the SS-1 type with a reduced gage section 20.3 mn long by 1.52 mm wide by 0.76-mm thick (Fig. 3.4.1). Specimens were irradiated in the E-7 position of the ORR in experiment ORR-MFE-2. These specimens were irradiated in holders that contained 22 sheet samples. The cylindrical holders were contained in a water-cooled aluminum block; each holder contained a central hole that contained an electric heater. Temperature was measured and controlled by two thermocouples located at the position of the center of the gage section in two unused sample positions located 180° apart.

Irradiation temperatures obtained in this experiment were approximately 250, 290, 450, and 500°C. The neutron fluence of -6.8×10^{25} neutrons/m^2 (>0.1 MeV) produced -5 dpa and -40 at. ppm He.

Tensile tests were made on unirradiated and irradiated specimens at the irradiation temperatures. Tests were conducted in a vacuum chamber on a 44-kN capacity Instron universal test machine at a strain rate of 4.2×10^{-5}/s.

Table 3.4.1. Heat treatment and cold-work level variations of type 316 stainless steel test specimens

Specimen code	Solution anneal	Anneal	Cold-work level
B4	1 h 1050°C		
B5	1 h 1150°C		
07	1 h 1050°C	10 h 800°C	
A4	1 h 1050°C		20%
C1	1 h 1050°C		30%
B1	1 h 1050°C		50%
A5	1 h 1050°C	10 h 800°C	20%

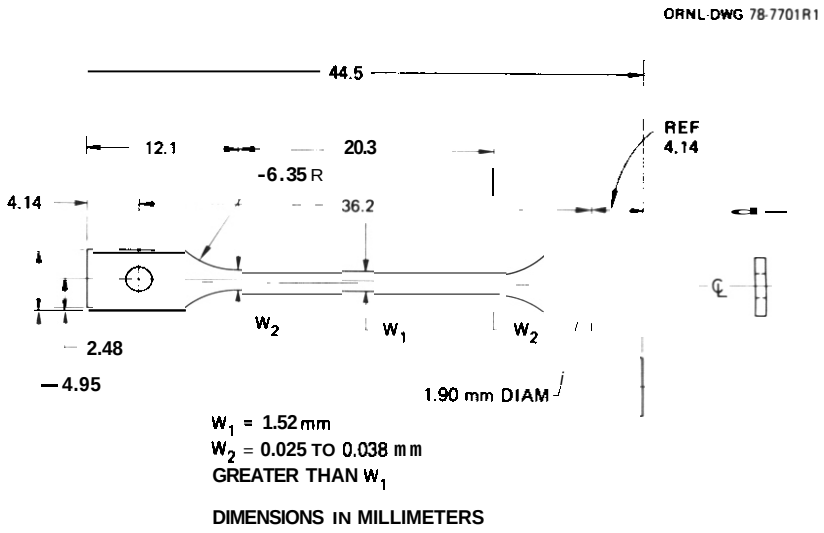

Fig. 3.4.1. The SS-1 type tensile specimen.

3.4.4.3 Results and Discussions

Various types of microstructures were examined (Table 3.4.1): two solution-annealed heat treatments, a solution-anneal heat treatment followed by a low-temperature anneal, three cold-work levels following a common solution-anneal treatment, and a cold-worked structure following the solution anneal and low-temperature anneal. The difference in solution-annealed microstructures was a difference in grain size, with the higher annealing temperature producing the larger grains (Fig. 3.4.2). The appearance of the cold-worked structure depended on the amount of cold work (Fig. 3.4.3); the grain structure was still clearly visible for the material deformed only 20%. When the solution anneal

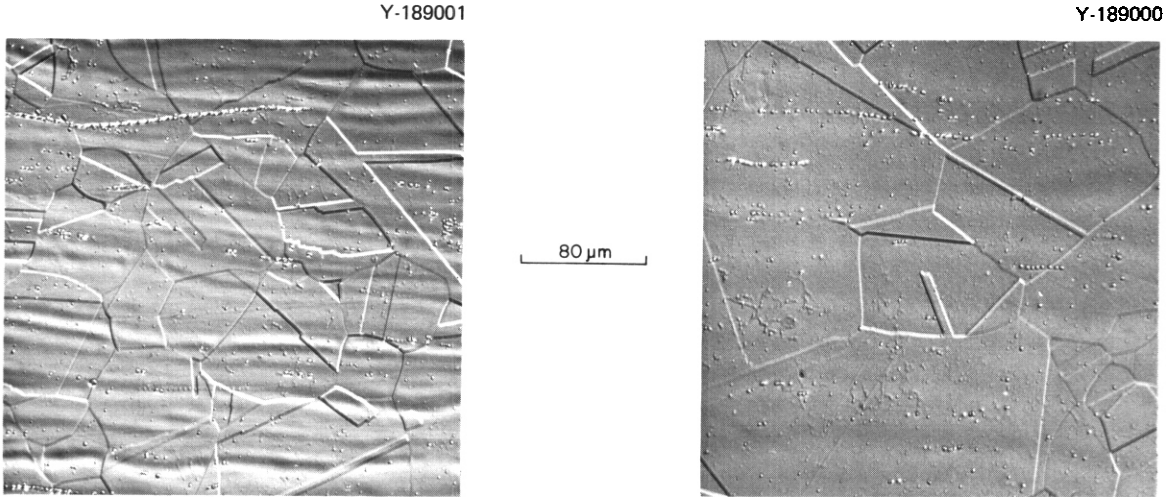

Fig. 3.4.2. Microstructure of type 316 stainless steel solution annealed 1 h at *(a)* 1050°C and *(b)* 1150°C. Differential-interference microscopy was used to show the grain size.

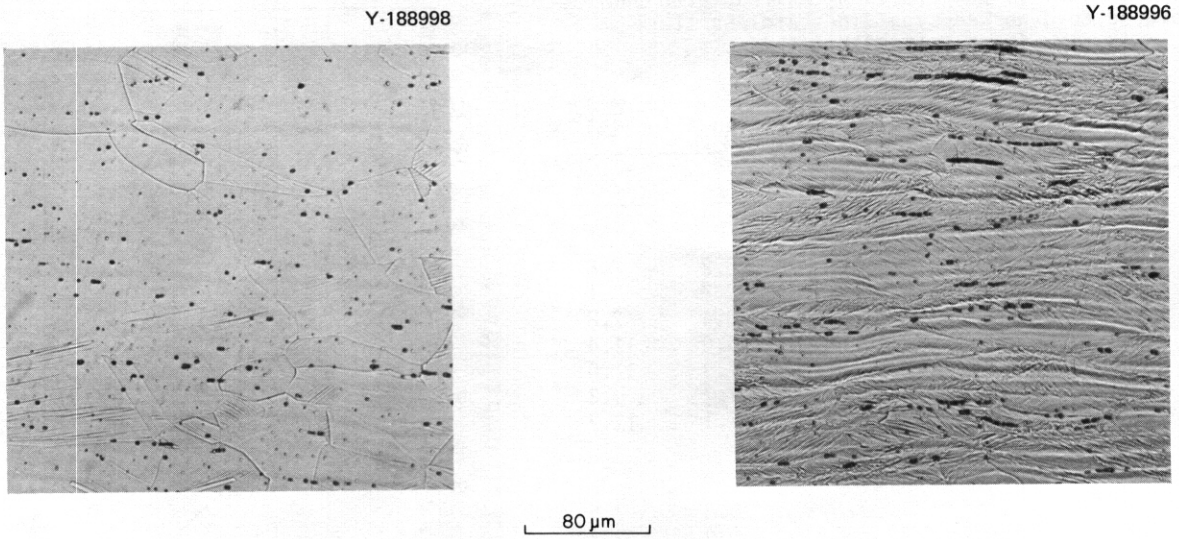

Fig. 3.4.3. Microstructure of type 316 stainless steel cold worked (*a*) 20% and (*b*) 50%.

for 1 h at 1050°C was followed by the anneal for 10 h at 800°C, considerable precipitate formed on grain boundaries and within the matrix (Fig. 3.4.4). After this structure was cold worked 20%, the grain structure was easily seen by optical microscopy.

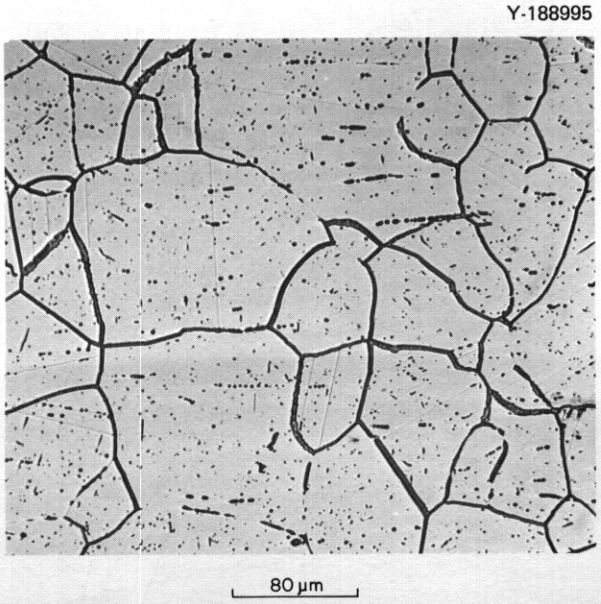

Fig. 3.4.4. Microstructure of type 316 stainless steel solution annealed 1 h at 1050°C and then further annealed 10 h at 800°C.

Tensile data for the specimens with 20, 30, and 50% cold work are presented in Table 3.4.2. Increasing the cold-work level of the unirradiated type 316 stainless steel from 20 to 50% led to a progressive increase in the 0.2%-offset yield stress (YS) (Fig. 3.4.5) and the ultimate tensile strength (UTS) (Fig. 3.4.6). The YS and UTS decreased with increasing temperature; a minimum was observed at 450°C for both the YS and UTS of the 20%-cold-worked steel and a minimum in YS for the 50%-cold-worked steel.

The unirradiated ductility decreased with increasing cold-work levels (Fig. 3.4.7). The uniform and total elongations of the 20%-cold-worked steel were quite high at all temperatures but substantially less for 30% cold work. There was only a slight further decrease for the steel cold worked to 50%. The uniform and total elongations of the unirradiated 20%-cold-worked steel showed a relatively large increase with increasing test temperature, but the steel with 30% and 50% cold work was essentially unaffected by temperature.

Table 3.4.2. Tensile properties of unirradiated and irradiated cold-worked type 316 stainless steel (heat X-15893)

Temperature (°C)		Strength (MPa)		Elongation (%)	
Test	Irradiation**	Yield	ultimate	Uniform	Total
		1 h 1050°C, 20% cold work			
250	2511	965	965	0.2	2.8
250		596	645	2.2	5.1
290	290	983	998	0.4	2.8
4511	450	494	636	10.0	11.4
4511		376	480	7.9	11.0
500	500	437	544	7.7	9.3
500		523	630	7.1	11.7
		1 h 1050°C, 30% cold work			
250		705	770	0.8	3.6
290	290	1027	1035	0.3	2.3
290		663	770	0.9	3.3
4511	4511	634	763	8.5	10.4
450		561	741	1.5	3.7
500	500	476	574	4.3	5.3
500		559	728	2.1	4.1
		1 h 1050°C, 50% cold work			
250	250	1130	1130	0.2	1.9
250		905	960	0.6	2.5
290	290	1128	1161	0.5	2.2
290		912	958	0.6	2.6
450	450	761	860	2.6	3.3
450		785	916	1.0	2.7
500	500	577	637	1.6	1.7
500		805	889	1.2	2.9
		1 h 1050°C, 10 h 800°C, 20% cold work			
250	250	983	983	0.2	1.9
250		617	672	1.1	3.5
290	290	976	995	0.4	2.0
450	450	548	624	3.2	4.0
450		439	512	1.7	3.1
500	500	485	551	3.7	4.1
500		524	636	3.1	4.8

** All irradiated samples were exposed in ORR-MFE-2 to a fluence of 6.8×10^{25} neutrons/m^2, >0.1 MeV, producing approximately 5 dpa and 40 at. ppm He.

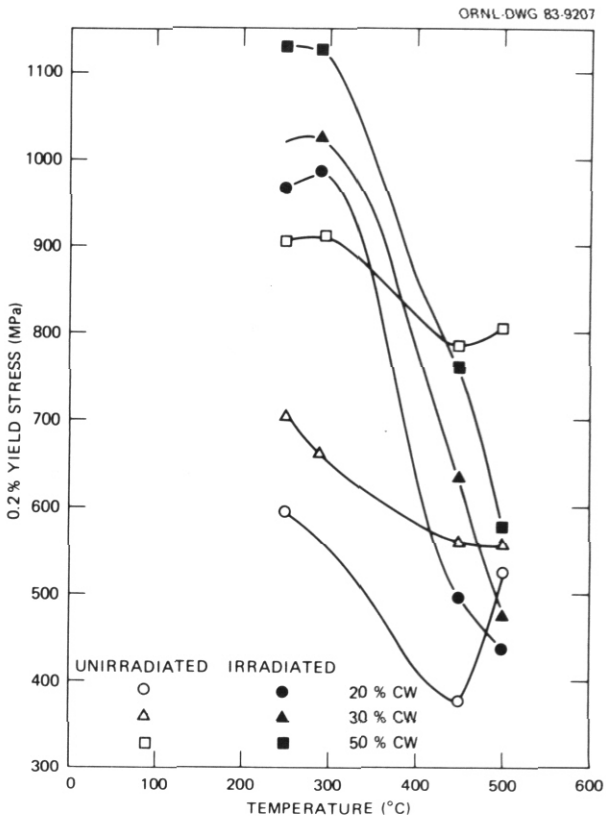

Fig. 3.4.5. The 0.2% yield stress of unirradiated and irradiated cold-worked type 316 stainless steel. Irradiations were at the test temperatures to a fluence producing approximately 5 dpa and 40 at. ppm He.

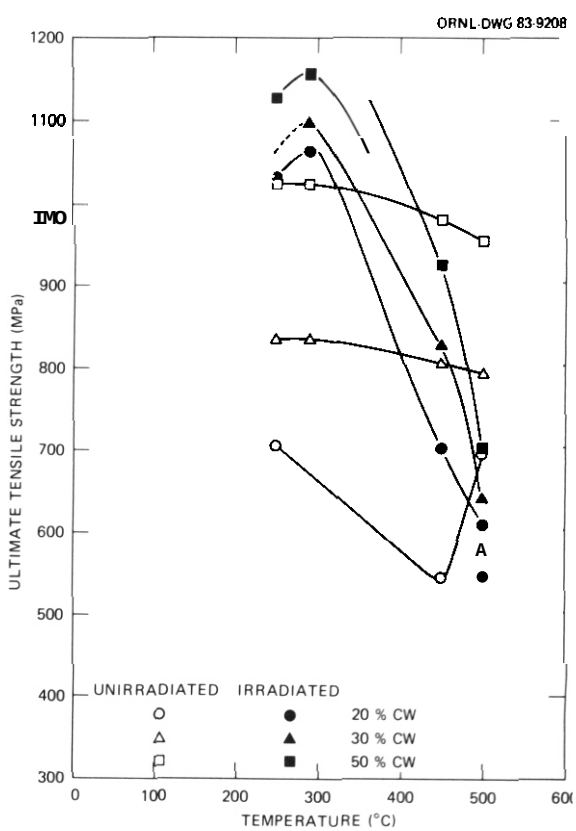

Fig. 3.4.6. The ultimate tensile strength of unirradiated and irradiated type 316 stainless steel. Irradiation conditions as for Fig. 3.4.5.

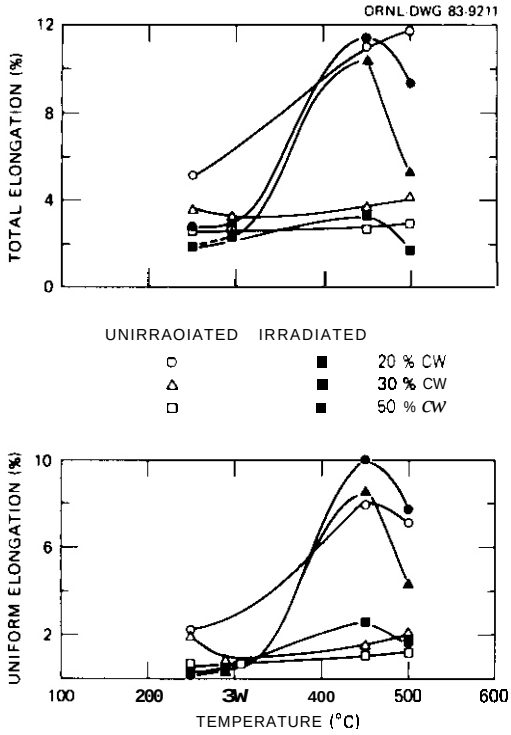

Fig. 3.4.7. The uniform and total elongations of unirradiated and irradiated type 316 stainless steel. Irradiation conditions as for Fig. 3.4.5.

When irradiated, the YS and UTS of all three cold-worked steels increased over the unirradiated values at 250 and 290°C. The relative increase was inversely related to the level of prior cold work. Between 290 and 450°C there was a large decrease in the irradiated strength: at 500°C, the strength of the irradiated steel fell below that of the unirradiated steel. Although the originally strongest 50%-cold-worked steel remained strongest at 500°C, the irradiated strengths for the three cold-work levels appeared to be approaching a common value with increasing temperature.

The ductility of the irradiated cold-worked type 316 stainless steel does not directly reflect the increase in strength (Fig. 3.4.7). Both uniform and total elongations of the irradiated steels increased between 290 and 450°C, but they decreased between 450 and 500°C. The steel with 20 and 30% cold work showed a large increase between 290 and 450°C, whereas a much smaller increase occurred for the steel with *50%* cold work. At 500°C, the total elongation of the steel with 50% cold work actually fell below the value at 250°C. At all temperatures, the reduced ductility of the three steels maintained the inverse relationship with cold-work level that was true for the unirradiated material.

For the three cold-work levels discussed above, deformation followed a 1 h solution anneal at 1050°C. In Figs. 3.4.8 through 3.4.10 the strength and ductility of the type 316 stainless steel cold worked 20% after the 1050°C solution anneal are compared with the steel cold worked *20%* after the 1050°C anneal and a 10-h anneal at 800°C. Both before and after irradiation, there was very little difference in strength for these two steels. The uniform and total elongation values of the steel given the 800°C anneal did not increase between 290 and 450°C nearly as much as did the values for the other steel. This was true for both irradiated and unirradiated

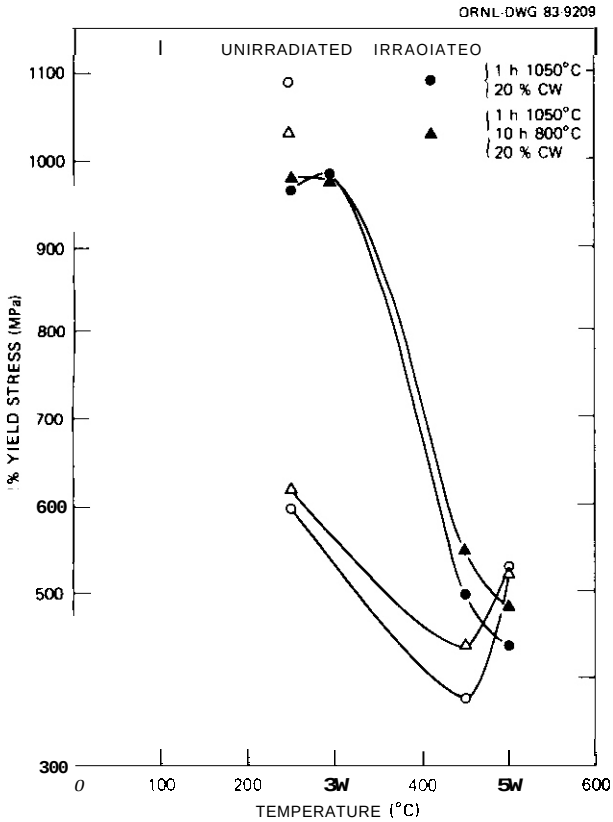

Fig. 3.4.8. The 0.2% yield stress of unirradiated and irradiated 20%-cold-worked type 316 stainless steel; cold work followed two different heat treatments. Irradiations were at the test temperatures to a fluence producing approximately 5 dpa and 40 at. ppm He.

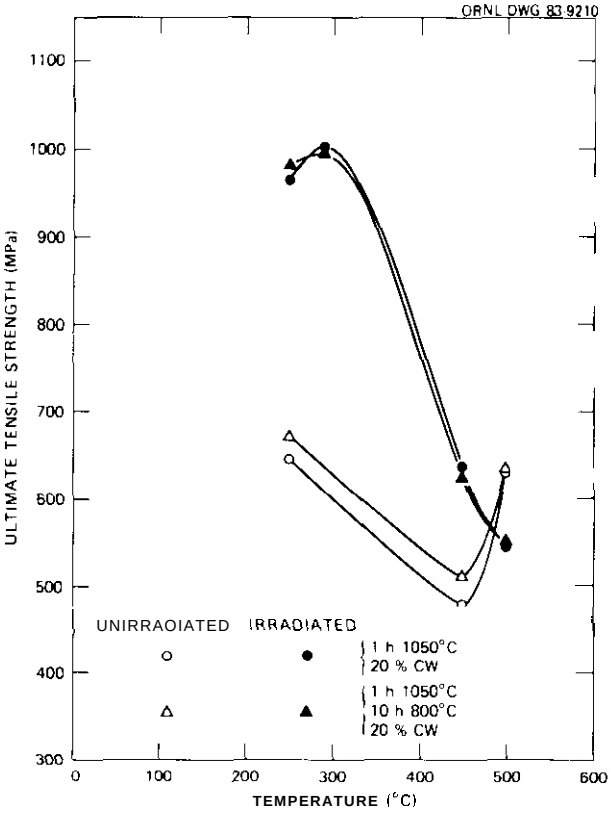

Fig. 3.4.9. The ultimate tensile strength of unirradiated and irradiated 20%-cold-worked type 316 stainless steel; cold work followed two different heat treatments. Irradiation conditions as for Fig. 3.4.8.

steels. However, the irradiated values for both steels approached the unirradiated steels at 450 and 500°C (Fig. 3.4.10).

Because mast irradiation studies on 20%-cold worked type *316* stainless steel have been conducted in conjunction with the fast breeder program and have generally used EBR-II, few irradiations have been below about 370°C (limited by the EBR-II reactor coolant inlet temoerature). Fish et al[11,12] tested 20%-cold-worked type 316 stainless steel irradiated in EBR-II at temperatures between 371 and 816°C. They found an increase in both YS and UTS for material irradiated and tested below about 483°C and only a slight amount of hardening was observed at 483°C. They reported softening for irradiation and testing at 538 and higher. This observation is similar to observations in the present tests on 20%-cold-worked type 316 stainless steel, where softening was observed at 500°C but not at 450°C. A similar observation was made for the steel with 30% cold work; however, the steel with 50% cold work softened at 450°C.

Bloom collected tensile data for 20%-cold-worked type 316 stainless steel irradiated in HFIR and EBR-II (ref. 15). When the YS data were plotted against temperature, Bloom found that the data could be separated according to whether the He:dpa ratio was high (from HFIR irradiation) or low (from EBR-II irradiation). The low He:dpa irradiations in EBR-II resulted in stronger materials than those with a high ratio after irradiation in HFIR.

When the results from the present study are compared with Bloom's collected data, good agreement was observed with the high He:dpa data. This was despite the fact that the HFIR results collected by Bloom were for material that contained several thousand at. ppm He, compared with about 40 at. ppm for the present experiment. Furthermore, the HFIR data were for considerably higher damage levels — up to 50 dpa, compared with about 5 dpa for the present experiments.

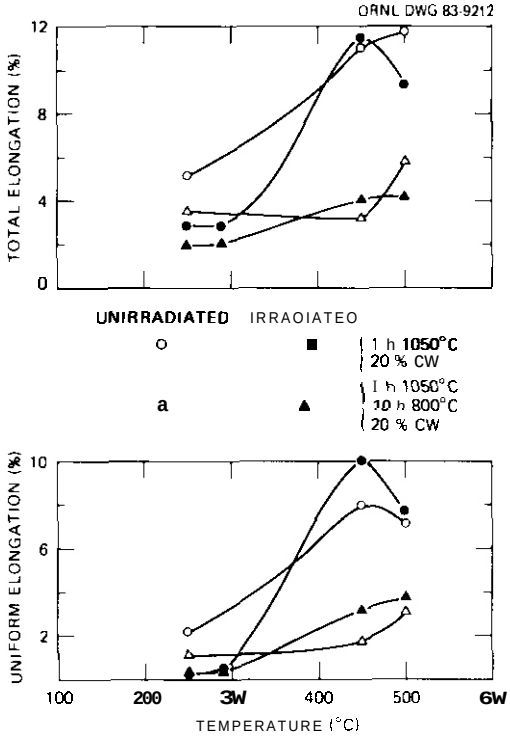

Fig. 3.4.10. The uniform and total elongations of unirradiated and irradiated 20%-cold-worked type *316* stainless steel; cold work followed two different heat treatments. Irradiation conditions as for Fig. 3.4.8.

Because the saturation fluence for irradiation hardening or softening is expected to be much higher than 5 dpa, it is somewhat surprising that the hardening obtained in this study approaches values obtained in studies where irradiation was to considerably higher doses. The only detailed saturation-studies were those of Fish et al.[11,12] in EBR-II (low He:dpa). They found that from 371 to 483°C, where hardening was observed, the hardening increased to about 4-5 × 10^{26} neutrons/m^2; at higher fluences, it remained constant. At 538 to 816°C, where softening occurred, strength decreased to about 2 × 10^{26} neutrons/m^2, after which it became constant.

As stated above, the strength of our irradiated steel fell below the EBR-II data but was similar to that of steels irradiated in HFIR, even though ours contained less helium and displacement damage. A possible interpretation of this observation is that the presence of helium hastens irradiation-damage saturation and also leads to a lower saturation strength.

Exposure of type 316 stainless steel at temperatures of 450 and 500°C can give rise to a loss of strength due to thermal aging effects. For 20%-cold-worked type 316 stainless steel. thermal aging for 4000 h (approximate time of present irradiation) at 450 and 500°C causes only a slight decrease in YS and UTS (ref. 16). In general, the high interstitial and vacancy flux during irradiation *is* expected to accelerate the thermal aging process. Because most of the irradiated strength properties of the present study fell above the values of the unirradiated strengths, irradiation hardening predominated — at least for temperatures up to 450°C. Only at 500°C were some of the strength properties below the unirradiated values. In no case were there large differences, indicating that the loss of strength in this case is due to the processes that occur during thermal aging (i.e., recovery of the cold-worked dislocation structure).

3.4.5 Future Work

The specimens that were solution annealed at 1050 and 1150°C and those that were solution annealed at 1050°C and subsequently heat treated 10 h at 800°C are now being tested. The results of those tests will be presented later.

3.4.6 References

1. R. Bullough, B. L. Eyre, and R. C. Perrin, "The Growth and Stability of Voids in Irradiated Metals," *Nucl. Appl. Technol.* 9, 346–355 (1970).

2. K. Farrell and J. Houston, "Heterogeneous Distribution of Irradiation Voids in Iron," *J. Nucl. Muter.* 35, 352–55 (1970).

3. J. L. Bramman et al., "Density Changes in Cladding Materials Irradiated in DFR," pp. 27–33 in *Voids Formed by Irradiation of Reactor Materials*, British Nuclear Energy Society, London, 1971.

4. C. Cawthorne et al., "Electron Microscope Observations of Voids in Cladding Materials Irradiated in DFR," pp. 35–43 in *Voids Formed by Irradiation of Reactor Materials,* British Nuclear Energy Society, London, 1971.

5. J. O. Stiegler and E. E. Bloom, "The Effect of Thermo-Mechanical Treatments on Void Formation in Irradiated Stainless Steel," **J.** *Nucl. Mater.* 41, 341–44 (1971).

6. H. R. Brager, "The Effects of Cold Working and Preirradiation Heat Treatment on Void Formation in Neutron-Irradiated Type 316 Stainless Steel," *J. Nucl. Mater.* 57, 103–18 (1975).

7. S. Kawasaki, K. Fukaya, and R. Nagasaki, "Effect of Fast Neutron Irradiation on AISI 316 Steel Tube," *Nippon Genshiryoko Gakkaishi* 14, 283–89 (1972).

8. D. Fahr, E. E. Bloom, and J. O. Stiegler, "Post-Irradiation Tensile Properties of Annealed and Cold-Worked Type 316 Stainless Steel," pp. 167–177 in *Irradiation Embrittlement and Creep in Fuel Cladding and Core Components,* British Nuclear Energy Society, London, 1973.

9. K. R. Garr, A. G. Pard, and D. Kramer, "The Effect of Neutron Irradiation on Types 316, 321, and Sandvik 12R72 Stainless Steels," pp. 143–55 in *Properties of Reactor Structural Alloys After Neutron and Particle Irradiation,* ASTM STP *570,* American Society for Testing and Materials, Philadelphia, 1975.

10. K. R. Garr and A. G. Pard, "Swelling and Tensile Property Changes in Neutron-Irradiated Type 316 Stainless Steel," pp. 79–90 in *Irradiation Effects on the Microstructure and Properties of Metals,* ASTM STP 611, American Society for Testing and Materials, Philadelphia, 1976.

11. R. L. Fish and J. O. Waltrous, "Effect of Fast Reactor Irradiation on the Tensile Properties of 20 Percent Cold-Worked Type 316 Stainless Steel," pp. 91–100 in *Irradiation Effects on the Microstructure and Properties of Metals,* ASTM STP 611, Pmerican Society for Testing and Materials, Philadelphia, 1976.

12. R. L. Fish, N. S. Cannon, and G. L. Wire, "Tensile Property Correlations for Highly Irradiated 20 Percent Cold-Worked Type 316 Stainless Steel," pp. 450–65 in *Effects of Radiation on Structural Materials,* ASTM STP 683, Pmerican Society for Testing and Materials, Philadelphia, 1979.

13. E. E. Bloom and F. W. Wiffen, "The Effects of Large Concentrations of Helium on the Mechanical Properties of Neutron-Irradiated Stainless Steel," *J. Nucl. Mater. 58,* 171–84 (1975).

14. M. L. Grossbeck and P. J. Maziasz, "Tensile Properties of Type 316 Stainless Steel Irradiated in a Simulated Fusion Reactor Environment." **J.** *Nuct. Mater. 86.* 883–87 (1979).

15. E. E. Bloom, "Mechanical Properties of Material; in Fusion Reactor First Wall and Blanket Systems," **J.** *Nucl. Mater.* 85&86, 795–804 (1979).

16. D. Fahr, *Analysis of Stress-Stkin Behavior of Type 316 Stainless Steel,* ORNL/TM-4292, November 1973.

3.5 TENSILE PROPERTIES AND SWELLING OF 20%-COLD-WORKED TYPE 316 STAINLESS STEEL IRRADIATED IN HFIR – R. L. Klueh and M. L. Grossbeck (Oak Ridge National laboratory)

3.5.1 ADIP Tasks

ADIP Task I.B.13, Tensile Properties of Austenitic Alloys, and I.C.2, Microstructure and Swelling in Austenitic Alloys.

3.5.2 Objective

The primary goal of the series of experiments HFIR-CTR-26 through -29 is to expand the mechanical property, microstructure, and swelling data base on irradiated 20%-cold-worked type 316 stainless steel. Previous irradiation experiments HFIR-CIR-9 through -13 provided an initial, lower-fluence data base for an understanding of the behavior of the material. Earlier experiments (HFIR-SS-2 through -8) had also provided high-fluence data. However, the previous work was on specimens from an experimental heat of steel. In the present experiinent series, the magnetic fusion energy (MFE) reference heat of type 316 stainless steel (heat X15893) was used. Sufficient overlap with previous irradiation conditions should enable a correlation to be made between the irradiation responses of the two heats of steel.

3.5.3 Summary

immersion density and elevated-temperature tensile properties were determined on 20%-cold-worked type 316 stainless steel irradiated in the HFIR to fluences of I.R to 37 × 10^{26} neutrons/m^2 (>0.1 MeV), which resulted in 16 to 32 dpa and 1250 to 2000 at. ppm He. These data were combined with the data obtained in two previous experiments, one to similar fluences and one to higher fluences (up to 6.3 × 10^{26} neutrons/m^2).

3.5.4 Progress and Status

We previously reported on tensile and immersion density results determined on the MFE reference heat (heat X15893) of type 316 stainless steel irradiated in experiments HFIR-CTR-26 and HFIR-CTR-27 (refs. 1 and 2). The first was to a maximum fluence of 3.9 × 10^{26} neutrons/m^2 (>0.1 MeV), the second to 6.3 × 10^{26} neutrons/m^2. These exposures resulted *in* maximum displacement-damage levels of 29 dpa and about 1900 at. ppm tie in HFIR-CTR-26 and 49 dpa and 3100 at. ppm He in HFIR-CTR-27. Irradiation temperatures ranged from 284 to 620°C. These experiments were from a series of four irradiation experiments, HFIR-CTR-26 through -29. In this report, we present the results from HFIR-CTR-28, which was irradiated to conditions similar to those achieved in HFIR-CTR-26. The HFIR-CTR-29 experiment was planned to obtain data similar to those obtained in HFIR-CTR-27. Unfortunately, that capsule developed a leak during irradiation. Therefore, no data will be obtained from that experiment.

3.5.4.1 Experimental Procedure

Details on the material and test procedure were given previously when the results from HFIR-CTR-26 were discussed.'

Experiment HFIR-CTR-28, like HFIR-CTR-26 and -27, was irradiated in a HFIR peripheral target position with a peak thermal neutron flux of 2.5 × 10^{19} neutrons/(m^2·s) and fast flux of 1.3 × 10^{19} neutrons/(m^2·s) (>0.1 MeV). Irradiation temperatures were approximately 370, 470, and 560°C. Fluences ranged from 1.8 to 3.1 × 10^{26} neutrons/m^2 (>0.1 MeV). The displacement damage and helium production were calculated by the procedures described by Gabriel, Bishop, and Wiffen.3 The calculated displacement damage levels ranged from 16 to 32 dpa, the helium concentrations from 1250 to 2000 at. ppm He.

3.5.4.2 Results and Discussion

The results of the immersion density measurements showed measurable swelling (Table 3.5.1). In all cases there was good agreement with the swelling data obtained in HFIR-CTR-PG, where fluences were Similar. In Fig. 3.5.1, the swelling data from all three experiments are shown as a function of temperature. Curves have been sketched through the two sets of data. The lower curve is for the data obtained from the two low-fluence experiments (HFIR-CTR-26 and -28), where the displacement damage ranged from 16 to 32 dpa with helium concentrations of 900 to 2000 at. ppm. The middle curve is for the high-dose experiment (HFIR-CTR-27), where the displacement damage ranged from 37 to 54 dpa and helium content from 2300 to 3300 at. ppm. Also shown in Fig. 3.5.1 is a curve determined by Maziasz and Grossheck for specimens irradiated in HFIR (ref. 4). The upper end of the fluence range for those irradiations was slightly higher (42–61 dpa, 3000–4200 at. ppm He) than for those of the present study (37–54 dpa, 2300–3300 at. ppm He), although there is an overlap of the data. The Maziasr and Grossbeck swelling values were calculated frorn cavity-volume fraction measurements determined from transmission electron microscopy studies. Finally, the Maziasz and Grossbeck swelling values were for a different heat of steel (the DO heat).

From the present observations, it is obvious that as the fluence was increased the immersion density values began to approach the cavity volume fraction values. The curve shapes are also similar. The present results give an indication of the local minimum observed in the cavity volume fraction measurements.[4,5] Furthermore, a local maximum similar to the one observed in the present study was also previously observed.[4,5]

Table 3.5.1. Swelling behavior and tensile properties of HFIR-irradiated 20%-cold-worked type 316 stainless steel, heat X15893

Temperature (°C)		Fluence[b] >0.1 MeV	Displacement damage	Helium content[c]	Strength (MPa)		Elongation[e] %		Swelling[f]
Test	Irradiation[a]	(neutrons/m²)	(dpa)	(at. ppm)	Yield[d]	Ultimate	Uniform	Total	(%)
350	370	7.6×10^{26}	22	1270	792	901	5.3	8.8	0.05
350	370	3.4	29	1730	723	866	8.3	10.4	0.3
350	370	3.7	31	1910	743	876	6.9	8.7	0.2
450	370	3.7	32	1980	750	854	4.1	6.8	0.2
450	470	1.8	16	880	583	713	6.9	8.9	0.04
450	470	3.4	29	1730	446	615	7.1	8.2	0.4
550	470	1.8	16	880	578	683	3.8	4.6	0.2
575	560	3.1	26	1530	343	539	8.7	9.9	0.3
675	560	3.7	32	1980	317	355	1.0	1.1	0.8

[a] Irradiation temperatures are calculated, ±50°C.

[b] Calculated from dosimetry of previous experiments

[c] Calculated from empirical relationship.

[d] 0.2% offset.

[e] Based On an 18.3-mm gage length.

[f] Immersion density values.

Tensile test results also are tabulated in Table 3.5.1. In Fig. 3.5.2 the 0.2%-offset yield stress is plotted against fluence (and displacement damage) for the test temperatures of 350, 450, and 575°C (for specimens irradiated at 370, 470, and 560°C, respectively). Data are presented from the present experiment as well as from the previous two irradiation capsules.[1,2] Because of the relatively few data obtained, simple straight lines or smoothed curves were drawn through the points to show the trends.

At 350°C the yield stress increases with increasing fluence to a near-constant value. At both 450 and 575°C the yield stress decreases with increasing fluence; eventually, it appears to approach a constant value. Although not shown, the ultimate tensile strength data show trends similar to the yield stress.

The ductility, as expressed by the total elongation, shows relatively little change with increasing fluence (Fig. 3.5.3). The change in uniform elonsation values with fluence generally follows the trend for total elongation (Table 3.5.1).

Figures 3.5.4 and 3.5.5 compare our 350 and 575% results with those of Grossbeck and Maziasz[6] and Bloom and Wiffen.[7] Both those studies were made on the DO heat of type 316 stainless steel (although processed at different times), which was different from the reference heat used in the present study.

The effects of irradiation on the yield stresses show similar trends for all three experiments. The agreement between the yield stress as a function of fluence for the three

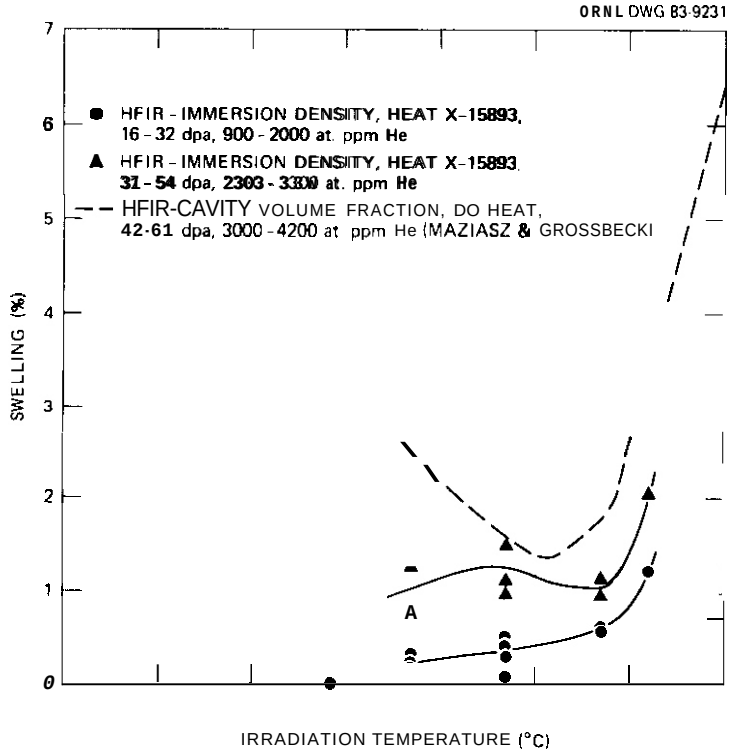

Fig. 3.5.1. Swelling as a function of irradiation temperatures for 20%-cold-worked type 316 stainless steel.

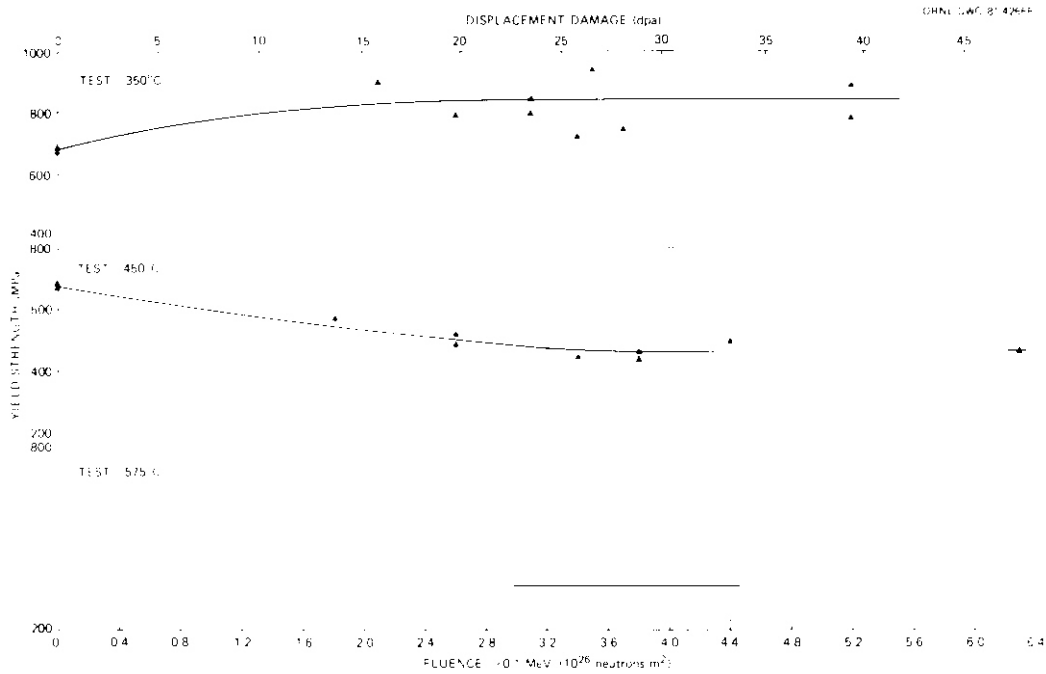

Fig. 3.5.2. The 0.2%-offset yield strength as a function of fluence and displacement damage for irradiated 20%-cold-worked type 316 stainless steel for test temperatures of 350, 450, and 575°C. Calculated HFIR irradiation temperatures were near test temperatures. Steels are further identified in text.

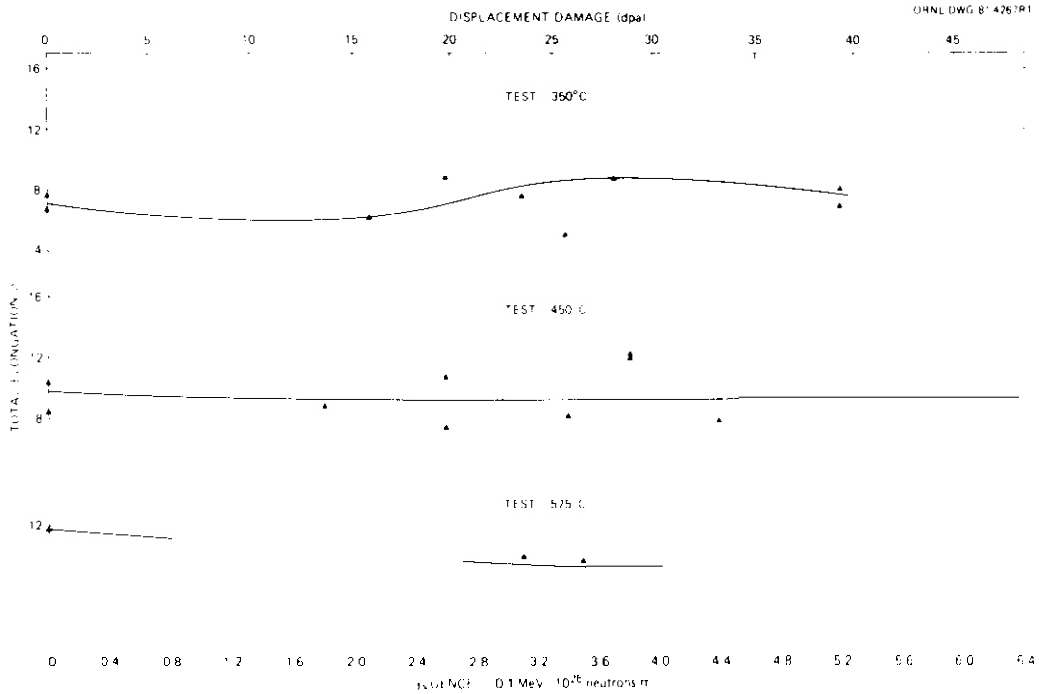

Fig. 3.5.3. Total elongation as a function of fluence and displacement damage for 20%-cold-worked type 31h stainless steel for test temperatures of 350, 450, and 575°C. Irradiation temperatures were near the test temperatures.

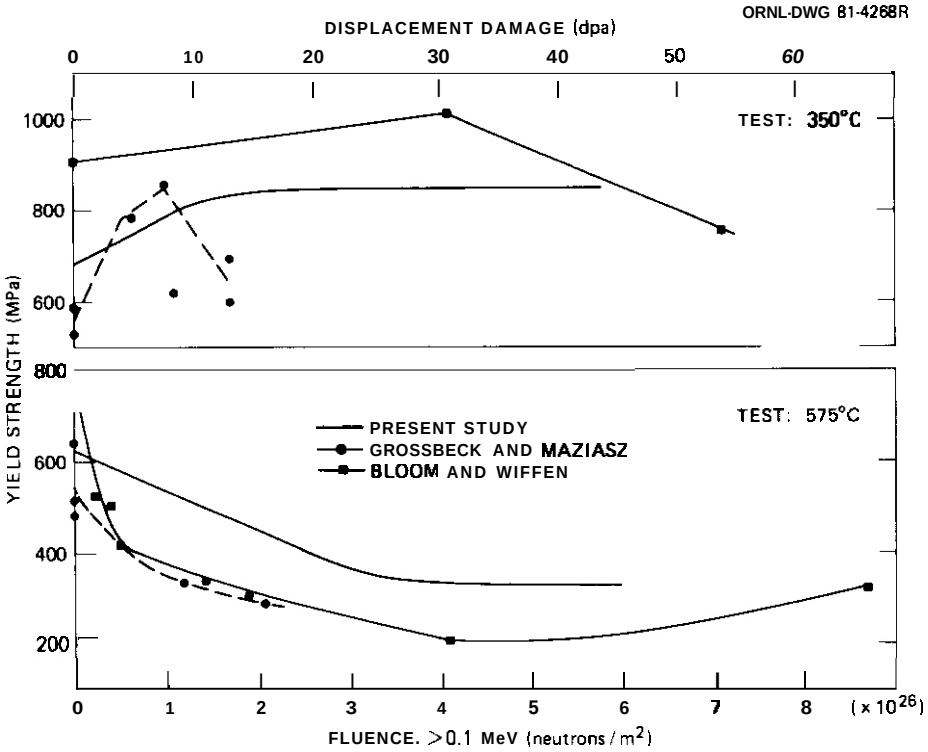

Fig. 3.5.4. Comparison of yield strength as a function of fluence (>0.1 MeV) for irradiated 20%-cold-worked type 316 stainless steel at 350 and 575°C for three experiments. The two curves without data points were taken from Fig. 3.5.2, and the third curve was drawn through data taken from E. E. Bloom and F. W. Wiffen (ref. 7).

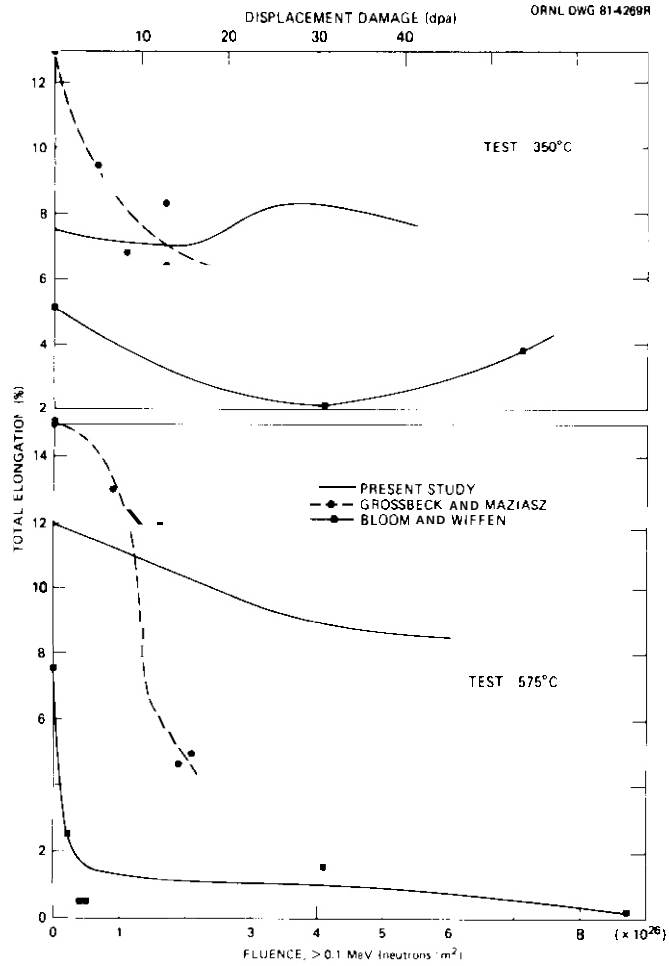

Fig. 3.5.5. Comparison of total elongation as a function of fluence (>0.1 MeV) for irradiated 20%-cold-worked type 316 stainless steel at 350 and 575°C for three experiments. The two curves without data points were taken from Fig. 3.5.3, and the third curve was drawn through data taken from E. E. Bloom and F. W. Wiffen (ref. 7).

studies is quite good. The major difference involves ductility: the values determined by Bloom and Wiffen fall substantially below those determined in the present study and by Grossbeck and Maziasz — especially at 575°C, where Bloom and Wiffen reported a total elongation of 0.5%. No such rapid decrease in ductility was indicated in the other two studies. Grossheck and Maziasz concluded that this difference may have arisen from differences in the fabrication procedures used when the specimen material was cold worked. Such a possibility agrees with the observation that the as-received specimens used by Bloom and Wiffen[7] were stronger and less ductile than those used in the present work and in the work of Grossbeck and Maziasz.[6]

The irradiation temperatures given in Table 3.5.1 are those that were calculated for this experiment and for previous ones.[6,7] Test temperatures are those chosen previously,[6,7] so results can be compared with previous tests. There has been some discussion concerning the accuracy of these calculated irradiation temperatures.[5,6] Indications are that the actual temperatures are 50 to 75°C higher than those calculated and reported here.

To determine the effect of such a temperature difference on the tensile results, specimens irradiated at the calculated temperatures of 370, 470, and 560°C were tested at 450, 550, and 675°C. respectively (instead of the 350, 450, and 575°C temperatures used for the majority of the specimens). The results of these tests are given in Table 3.5.1. For the 370°C-irradiated specimens tested at 450°C and the 470°C specimens tested at 550°C, there was essentially no difference in properties from similarly irradiated specimens tested at 350 and 450°C, respectively. The only major difference occurred for the specimen irradiated at a calculated temperature of 560°C and tested at 675°C instead of 575°C. In this case there was a slight decrease in yield stress and a considerably greater decrease in ultimate tensile strength. Despite the modest decrease in strength properties, however, there was a large decrease in ductility. The total elongation decreased from 9.9% to 1.1%; a similar large decrease in uniform elongation was noted.

These results indicate that even if the calculated irradiation temperatures are 50 to 75°C below actual temperatures,[5,6] there is little difference in tensile properties for specimens irradiated at temperatures up to about 500°C and tested at the corrected temperatures. However, if the calculated temperature of 575°C is lower than the irradiation temperature by 50 to 75°C, a significant difference in tensile properties will occur when the specimens are tested at the higher temperature. At the higher temperatures the large decrease in ultimate tensile strength shows only the normal temperature dependence of strength properties. However, the large decrease in ductility is due to elevated-temuerature helium emhrittlement that occurs in type 316 stainless steel. This latter effect occurs for helium-containing type 316 stainless steel tested at 650 to 700°C and is nearly independent of the irradiation temperature.

3.5.5 References

1. R. L. Klueh and M. L. Grossbeck, "Tensile Properties and Swelling of 20%-Cold-Worked Type 316 Stainless Steel Irradiated in HFIR," pp. 58–69 in *ADIP* mart. *Prog. Rep. Mar. 31, 1981*, DOE/ER-0045/6, U.S. DOE Office of Fusion Energy.

2. R. L. Klueh and M. L. Grossbeck, "Tensile Properties and Swelling of 20%-Cold-Worked Type 316 Stainless Steel Irradiated in HFIR," pp. 71–77 in *ADIP Quart. Prog. Rep. Sept. 30, 1982*, DOE/ER-0045/9, U.S. DOE Office of Fusion Energy.

3. T. A Gabriel, B L. Bishop, and F. W. Wiffen. *Calculated Irradiation Response of Materials Using Fission Reactor (HFIR, ORR, and EBR-II) Neutron Spectra*, ORNL/TM-6361, August 1979.

4. P. J. Maziasz and M. L. Grossheck, "Swelling and Microstructure of HFIR-Irradiated 20%-Cold-Worked Types 316 Stainless Steel and 316 t 0.23 wt % Ti," pp. 43–69 in *ADIP Quart. Prog. Rep. Dec. 31, 1980*, DOE/ER-0045/5, U.S. DOE, Office of Fusion Energy.

5. P. J. Maziasz and M. L. Grossbeck, "Microstructural Development in 20%-Cold-Worked Type 316 Stainless Steel Irradiated in HFIR: Fluence Dependence of the Cavity Component," pp. 28–56 in *ADIP mart. Prog. Rep. Mar. 31, 1981*, DOE/ER-004516, U.S. DOE, Office of Fusion Energy.

6. M. L. Grossbeck and P. J. Maziasz, "Tensile Properties of Type 316 Stainless Steel Irradiated in a Simulated Fusion Reactor Environment," *J. Nucl. Mater.* 85&86, 883–87 (1979).

7. E. E. Bloom and F. W. Wiffen, "The Lffects of Large Concentrations of Helium on the Mechanical Properties of Neutron-Irradiated Stainless Steel," *J. Nucl. Mater.* 58, 171–84 (1975).

3.6 FRACTURE STRAIN OF 20%-COLD-WORKED TYPE 316 STAINLESS STEEL UNDER IRRADIATION IN EBR-II

M. L. Grossbeck and E. E. Bloom (Oak Ridge National Laboratory)

3.6.1 ADIP Task

ADIP Tasks I.B.9, Stress-Rupture Properties of Austenitic Alloys, and I.C.6, Irradiation Creep in Austenitic Alloys.

3.6.2 Objective

This study evaluates the fracture strain of 20%-cold-worked type 316 stainless steel (20% CW 316 SS) under neutron irradiation. Fracture mechanisms and conditions under which irradiation creep relieves stresses and increases plastic flow are to be evaluated. Strain limits determined will establish whether swelling stresses in a fusion reactor first wall can be relieved by irradiation creep.

3.6.3 *Sumnary*

Swelling-driven fracture strain specimens of 20%-cold-worked 316 stainless steel were irradiated to a fluence of 5×10^{26} neutrons/m^2 (>0.1 MeV] in EBR-II at 430, 550, and 625°C. Fracture strain was *not* a function of fluence or strain rate but only of temperature. Fracture strain was found to be 6% at 550°C and 1%at 625°C. All fractures were intergranular, but a notched specimen irradiated at 550°C showed some evidence of ductility.

3.6.4 Progress and Status

3.6.4.1 Introduction

Higher strains are achieved in materials stressed under irradiation than under comparable conditions out-of-reactor.' Irradiation creep results in large strains at temperatures well below the thermal creep regime. It is weakly temperature dependent and often linearly stress dependent. This linear stress dependence results in superplastic or viscoelastic behavior.2 Expressing true stress a as a function of true strain rate $\dot{\varepsilon}$ by

$$\sigma = k\dot{\varepsilon}^m$$

defines the strain-rate sensitivity m:

$$m = \frac{a \ln \sigma}{a \ln \dot{\varepsilon}} .$$

The high values of m associated with irradiation creep led Nichols to suggest superplastic behavior in irradiation creep. 3

Bloom and Wolfer described an experiment to determine fracture strains in types 304 and 316 stainless steels to investigate this behavior.[4] They used swelling-induced force to apply a uniaxial tensile stress to specimens. Although they did not present evidence of superplastic flow, they observed that several specimens that were predicted to fail in-reactor according to postirradiation creep tests did not fail. They concluded, therefore, that in-reactor fracture strains are larger than fracture strains resulting from tests out-of-reactor. Strain in a fractured specimen was estimated to be <3.8% at 550°C, and the specimen failed intergranularly. They concluded that superplastic flow was interrupted by the onset of intergranular fracture.

The present experiment was designed to make more precise measurements of in-reactor fracture strains and to further study the mechanisms *of* in-reactor fracture under conditions of low strain rates.

3.6.4.2 Experiment Description

The material chosen for the investigation was 20%-cold-worked type 316 stainless steel of the composition given in Table 3.6.1. The material was swaged from rod with intermediate annealing ending with an anneal for 15 min at 1150°C followed by swaging to a 20% reduction in area.

The specimens were loaded by the method of differential swelling. The specimens were machined into a configuration similar to a bolt (Fig. 3.6.1) and placed inside tubes of high-swelling material. The high-swelling material was a high-purity laboratory heat of type 316 stainless steel of composition also presented in Table 3.6.1. This was the same material used by Bloom and Wolfer. It had a swelling threshold *of* about 0.5×10^{26} neutrons/m^2 (>0.1 MeV) and a swelling rate 5%/(10^{26} neutrons/m^2) at 550°C (ref. 5). The specimen was designed with the area of the driver tube 8 times the gage area of the specimen. This would permit minimal deformation in the driver but would still fulfill the constraints of irradiation space.

	Content (wt %)			Content (wt %)	
	Specimen	Driver		Specimen	Driver
Cr	17.3	17.0	Al	<0.005	0.02
co	0.011	0.03	Nb	<0.01	0.02
Ni	13.1	16.7	V	0.01	<0.001
Mn	1.51	0.03	Cu	<0.01	0.02
Mo	2.26	2.5	N	0.002	0.004
Si	0.54	0.10	Fe	bal	bal
C	0.056	0.001			

ORNL-DWG 76-2154

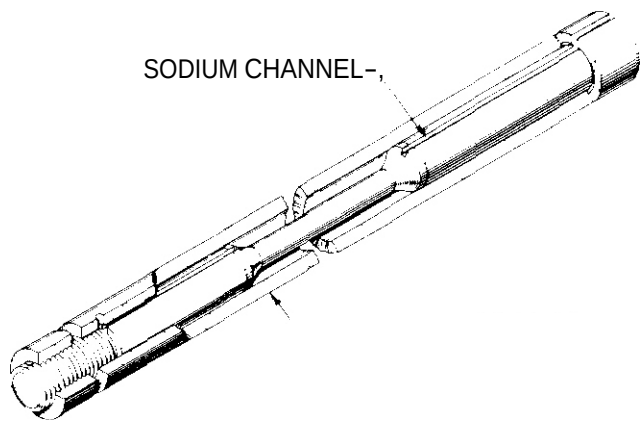

10^{26}

Table 3.6.2. Results of swelling and strain measurements

Specimen	Irrad. temp. (°C)	Specimen type	Gage length (mm)	Strain rate [%/(10^{26} neutrons/m²)]		Actual average strain rate (10^{-10}/s)	Swelling (density decrease) (%)		Strain (%)		Fluence[a] (10^{26} neutrons/m²)	
				Design	Actual		Driver	specimen	Specimen	Fracture	At stress initiation	Estimated at fracture
1	430	1	11.9	2	0.49	5.79	5.65	0.013	2.43			
2		1	11.7	2	0.59	7.05	6.56	–0.095	2.96			
3		2	11.7	0.2	0.070	0.83		0.018	0.35			
4		3	12.1	2 delay	1.1	13.1	7.48	0.16	1.87		3.3	
5		4	6.58	4 delay	1.9	22.5	6.01	0.077	1.70		4.1	
21		5	11.6	2 delay, notch	1.3	15.0	5.97	0.028	1.64		3.7	
6	550	1	31.5	2	1.7[b]	19.4[b]	22.4	1.08		4.5		3
7		1	30.7	2	1.5	17.1	21.9	1.3	7.17			
10		2	30.7	0.2	0.13	1.1		0.58	0.47			
12		3	33.8	2 delay	1.3	15.8	22.3	0.72	2.93		2.8	
14		4	15.6	4 delay	3.5[b]	41.6[b]	25.4	1.15		5.1	2.6	4
22		5	31.0	2 delay, notch	2.0[b]	23.3[b]	25.0	0.89		0.44	2.2	2.2
16	625	1	27.2	2	0.64[b]	7.64[b]	9.4	0.48		1.1		1.7–5
17		1	30.2		0.61[b]	7.246	9.3	–0.024				
18		2	30.5	0.2	0.058	0.69			0.29			
19		3	27.7	2 delay	1.05	12.6	11.8	0.21	1.37		3.7	
20		4	13.7	4 delay	1.9[b]	22.6[b]	10.1	0.20		1.3	4.3	5
24		5	27.4	2 delay, notch	0.89[b]	10.5[b]	10.2	0.18		0.0n	4.3	<1

[a]Total exposure was 30.496 MWd, resulting in a fluence of 5×10^{26} neutrons/m² (>0.1 MeV).

[b]Calculated from change in length of driver. Other Strain values calculated from final length.

[c]Damaged in disassembly.

The specimens were irradiated in sodium in the Experimental Breeder Reactor-I1 (EBR-II) to a fluence of 5.0 × 10^{26} neutrons/m^2 (>0.1 MeV) (24 dpa). The specimens were enclosed in sodium-filled capsules containing zirconium getters. The capsule that operated at 625°C was heat pipe controlled, those at 550°C gas gap controlled, and those at 430°C were in thermal contact with reactor coolant, but sealed. All capsules contained thermal expansion temperature monitors, although the monitor in the 625°C capsule failed.

Following irradiation, the lengths of the specimens and the driver tubes were measured. The elongations of the fractured specimens were determined by measuring from matching identifiable features on the fracture surfaces to fiducial marks on the shoulders. Scanning electron microscope (SEM) fractography was then performed on the fractured specimens. Following this destructive exami'nation, immersion densities of driver tubes and specimens were determined.

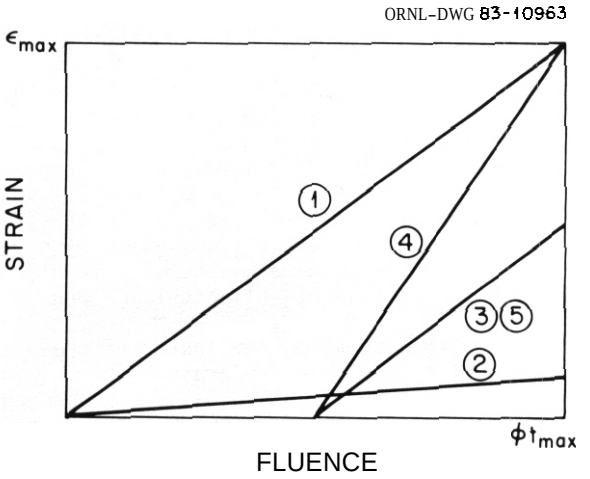

Fig. 3.6.2. Strain versus fluence to illustrate the differences in types of specimens employed.

3.6.4.3 Results and Discussion

The results are summarized in Table 3.6.2. Although the gage lengths were adjusted to achieve constant strain rates at all temperatures, deviations from design temperature and uncertainties in swelling rates resulted in different strain rates. As can be seen from comparing design strain rates with actual strain rates, the design values were approximately achieved at 550°C. Comparison of immersion density of driver tubes with driver tube lengths indicates that despite the 8:1 ratio of driver cross-sectional area to specimen cross section, significant irradiation creep occurred in the tubes. Nevertheless, the stress in the specimens resulted in irradiation creep in the specimens and in some cases fracture. Significant swelling was observed in the specimens only at 550°C, where it was subtracted from driver swelling in the strain calculations. Although data are very limited, an accelerating effect of stress on swelling is apparent at 550°C. This is apparent from the specimen swelling data, where the low-strain-rate (low-stress) specimens, type 2, had only half the swelling of type 1, and the delayed-stress specimens also exhibited lower swelling than type 1 specimens. A similar effect was observed by Bates and Gilbert in pressurized tubes.6

Seven specimens fractured in-reactor, none at 430°C. At 550°C the specimen with a strain rate of 2.0 × 10^{-9}/s (type 1) and the specimen with twice this strain rate but with stress delayed until a fluence of 2.6 × 10^{26} neutrons/m^2 (type 4) both fractured with about 5% strain. Since the driver continued to swell to an effective specimen strain of about 8.5%, the fracture probably occurred at approximately 50% of the irradiation or at a fluence of 3 × 10^{26} neutrons/m^2 for the type 1 specimen and 4 × 10^{26} neutrons/m^2 for the type 4 specimen. However, specimen 7, a twin to specimen 6, failed to fracture even at a strain of 7.6%. Therefore, the average fracture strain is greater than 6%. The lack of fracture in specimen 7 also might lead one to conclude that specimen 6 fractured near the end of the irradiation. At 625°C the two corresponding specimens fractured with slightly greater than 1% elongation, consistent with results of Fish[7] at 650°C. Swelling measurements seem to indicate that the type 1 specimen might have fractured (at 1.7 × 10^{26} neutrons/m^2) before the type 4 specimen initiated strain, but both fractured at approximately the same strain level despite different fluences at the time of fracture. The specimens that were notched failed at much lower strains, 0.74% for 550°C and 0.00% for 625°C, but the notched specimen at 430°C sustained 1.6% strain without failure. This result is expected because of the stress concentration at the notch root. It is perhaps encouraging that a strain of almost 1% was achieved at 550°C despite such adverse conditions.

All fractures were intergranular, as expected for such a low strain rate at elevated temperatures from postirradiation data.[8] A larger grain size is evident at 625°C than at 550°C, ASTM 4.5 and 6, respectively. The recrystallization temperature had been previously observed to fall between 550 and 625°C for this heat of steel.[9] Details of the fracture surfaces may be seen in Fig. 3.6.3. Here the grain boundary surfaces appear to become more complex as the estimated fluence before fracture increases. At 625°C the grain boundaries of all these specimens had precipitates. Specimen 20 shows a structure of microdimples, many of which contain precipitates. Although corrosion cannot be discounted, there is no evidence of such a surface morphology on the lateral surfaces of the specimens. The structure probably resulted from creep cavities on the grain boundaries. At 550°C the increase in complexity as the estimated fluence before fracture increased is more dramatic. In specimen 22, which was notched and probably fractured soon after stress was applied at a calculated fluence of 2.2 × 10^{26} neutrons/m^2, the grain boundaries are clean and smooth. Evidence of slip bands with cross slip appears on specimen 6. However, specimen 14, which is estimated to have fractured near the end of the irradiation, shows prominent features aligned with crystallographic planes. Since the grain boundaries and even slip bands are often heavily decorated with carbide precipitation at these temperatures, the sheet features may be continuous precipitates. However, since they appear

to be ductile, they could be a result of irradiation creep, in contrast with the notched specimen, which was likely to have fractured rapidly. Following nucleation of a crack on the grain boundaries, a very high stress concentration arises at the crack tip. At strain rates on the order of 10^{-9}/s the crack perhaps grows sufficiently slowly to allow plastic flow along the slip bands at the crack tip by irradiation creep. This plastic flow, which might be nearly superplastic on a microscopic level, could result in the sheets of material along slip bands.

Figure 3.6.4 shows a compilation of creep rate curves for the three temperatures of interest: 430, 550, and 625°C. The curves were plotted from an equation for irradiation creep for a similar heat of type 316 stainless steel given by Puigh.[10] Also drawn on the same axes is the specimen strain rate imposed by the swelling of the driver. The creep curves, which are plots of $\dot{\varepsilon} = f(\sigma, \phi t)$, give the creep rate for a given stress at a desired fluence or they give the stress level in the specimen forced to strain at a given rate (assumed constant) at a desired fluence. Thus, the curves provide the stress sustained in the specimens.

Since few in-reactor stress-rupture data are available, data for onirradiated specimens of another heat of type 316 stainless steel will be used as a rough guide to understanding the fracture behavior.7 For 430°C, curves are plotted far types 1 and 4 specimens. As can be seen from the intersections of the type 1 curve with the constant stress curves, maximum stress of about 500 MPa is reached imnediately following the completion of transient creep, and with increasing fluence the irradiation creep rate increases, reducing the stress in the specimen. A stress level of 500 MPa is significantly below the ultimate tensile stress for irradiated materials7 as well as below the predicted (from data from unirradiated specimens[11]) creep rupture stress for failure in 4.2 × 10^7 s, the duration of the irradiation. The type 4 specimen attained a stress level about equal to the creep rupture stress but within the error limits for survival.

For 550°C a similar plot is shown with curves for types 1, 3, and 4 specimens. Here, the type 1 specimen is predicted to reach a stress level of 350 MPa, and the type 4 specimen, a level of 450 MPa. The value of 350 MPa is above the creep rupture stress, and 450 MPa is above the yield stress far 550°C. Therefore, fracture is expected in the type 1 specimen (one failed and one did not), and fracture is predicted in the type 4 specimen soon after application of the stress. However, the completely brittle intergranular nature of the fracture with no apparent reduction of area shows that the intergranular fracture mechanism intervened before the yield stress was reached. The fact that about 5% strain was present supports the theory that superplastic flow (no necking) occurred until the intervention of the brittle fracture. The type 3 specimen is predicted to have reached a maximum stress level of 200 MPa; thus, fracture was not expected on the basis of postirradiation data, and fracture was not observed.

ORNL-PHOTO 1576-83

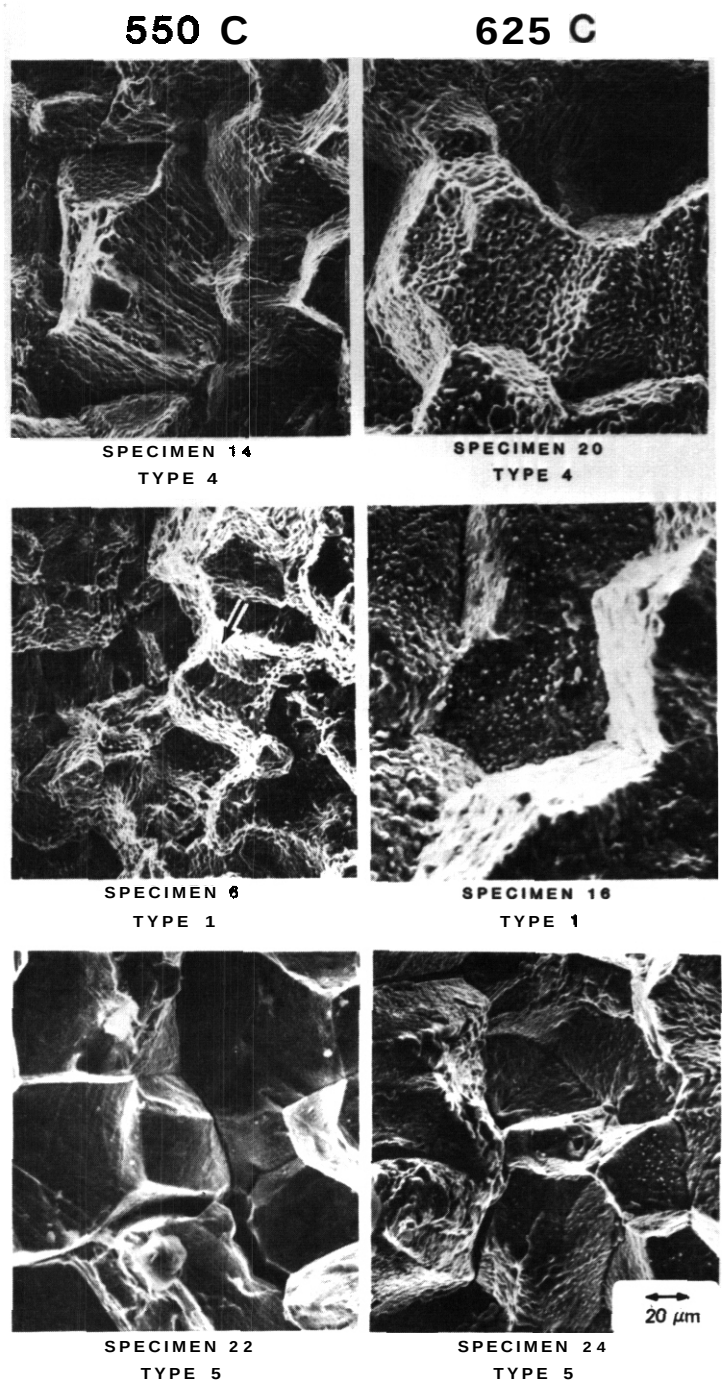

Fig. 3.6.3. Scanning electron micrographs of fracture surfaces of specimens that failed under irradiation. The arrow for specimen 6 indicates a region of slip bands.

For 625°C, curves for types 1, 3, and 4 specimens are again plotted. The type 1 specimen is predicted to have sustained a stress level of slightly greater than 100 MPa, and the type 4 specimen, a stress of about 130 MPa; both fractured. The type 3 specimen was predicted to incur a maximum stress of less than 100 MPa and did not fracture. Although the specimens with the highest predicted stresses failed and those with the lowert did not, the stresses are too close to predict failure from previous creep rupture data.

3.6.5 Conclusions

1. The fracture strain clearly decreases with increasing temperature in the range 550 to 625°C for a fluence of 5×10^{26} neutrons/m^2; it is 6% at 550°C and 1% at 625°C.
2. The strain to fracture does not appear to be a function of fluence or strain rate in the range 2 to 5×10^{26} neutrons/m^2 but depends only on temperature.
3. The presence of a notch reduces fracture strain to <1% at 550°C and ≈0 at 625°C, but the strain is <1.6% at 430°C.
4. All fractures were intergranular, with some evidence of ductility for a notched specimen at 550°C, where fracture probably occurred rapidly and at a low fluence.

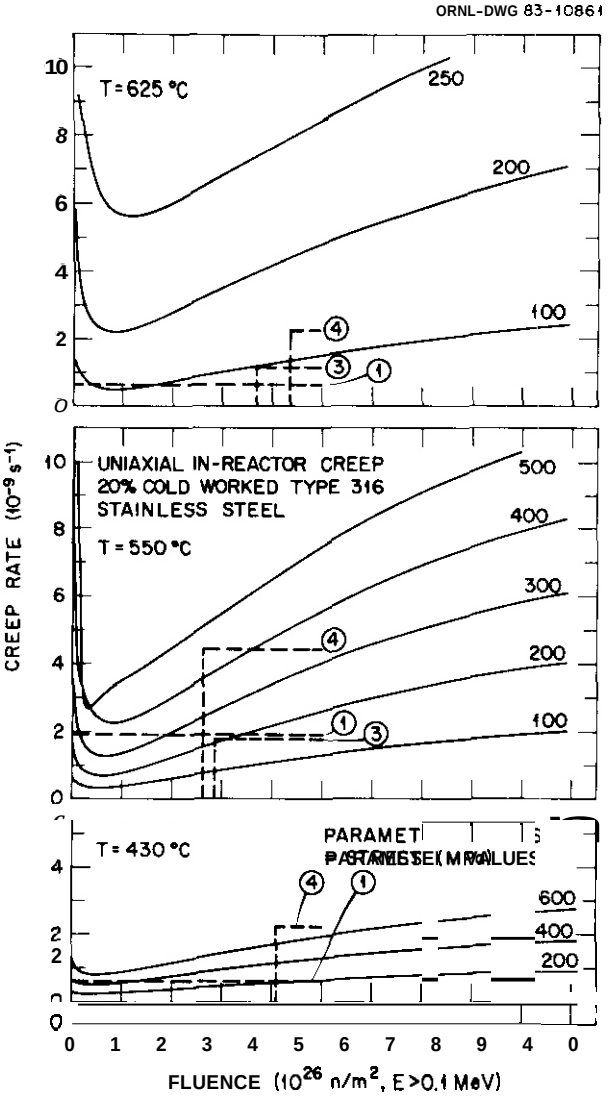

Fig. 3.6.4. Uniaxial irradiation creep rate as a function of fluence for type 316 stainless steel with specimen creep curves superimposed to predict specimen stress levels. Circled numbers refer to specimen types.

3.6.6 References

1. E. R. Gilbert and B. A Chin, "Irradiated Materials Measurement Technology," pp. 665–79 in Effects of Radiation *on* Materials, *ASTM STP* 725, American Society for Testing and Materials, Philadelphia, 1981.
2. W. A. Rackofen, I. R. Turner, and D. H. Avery, "Superplasticity in Al-Zn Alloy" in *ASM Trans.* Q. 57, 980–90, (1964).
3. 'F. A. Nichols, "Evidences for Enhanced Ductility During Irradiation Creep," *Mater. Sci. Eng.* 6, 167–75, (1970).
4. E. E. Bloom and W. G. Wolfer, "In-Reactor Deformation and Fracture of Austenitic Stainless Steels," pp. 656–72 in *Effects* of Radiation *on* structural *Materials*, ASTM STP 683, ed. J. A. Sprague and 0. Kramer. American Society for Testing and Materials. Philadelphia, 1979.
5. J. M. Leitnaker, E. E. Bloom, and J. O. Stiegler, "The Effect of Minor Constituents on Swelling in Stainless Steel," *J.* Nucl. Mater. 49(1), 57–66 (November 1973).
6. J. F. Bates and E. R. Gilbert, "Experimental Evidence for Stress Enhanced Swelling," *J. Nucl.* Mater. 59, 95–102, (1976)
7. R. L. Fish, N. S. Cannon, and G. L. Wire, "Tensile Property Correlations for Highly Irradiated 20 percent Cold-Worked Type 316 Stainless Steel," pp. 450–465 in Effects of Radiation *on Structural* ,Materials, ASTM STP 683, American Society for Testing and Materials, Philadelphia, 1979.
8. M L. Grossbeck, J. O. Stiegler, and J. J. Holmes, "The Effects of Irradiation on the Fracture Behavior of Austenitic Stainless Steels," pp. 95–116 in *Radiation* Effects *in Breeder Reactor Structural Materials*, ed. M. L. Bleiberg and J. W. Bennett, the Metallurgical Society of AIME, New York, 1977.
9. H. R. Brager, HEDL, private communication, March 1983.
10. R. J. Puigh, E. R. Gilbert, and B. A Chin, "An In-Reactor Creep Correlation for 20 Percent Cold-Worked AISI 316 Stainless Steel," pp. 108–121, in Effects of *Radiation on Materials*, ASTM STP 782, American Society for Testing and Materials, Philadelphia, 1982.
11. C. D. Johnson, J. L. Straalsund, and G. L. Wire, "A New Approach to Stress-Rupture Data Correlation," *Mater. Sci. Eng.* 28, 69–75, (1977).

4. PATH B: ALLOY DEVELOPMENT — HIGHER STRENGTH Fe-Ni-Cr ALLOYS

No contributions.

5.1 MECHANICAL PROPERTY EVALUATIONS OF PATH C VANADIUM SCOPING ALLOYS -

R. Bajaj and R. E. Gold (Westinghouse Electric Corporation)

5.1.1 ADIP Tasks

I.B.ll. Stress-Rupture Properties of Reactive/Refractory Metal Alloys (Path C)
I.B.15. Tensile Properties of Reactive/Refractory Metal Alloys (Path C)

5.1.2 Objective

The objective of this program is to develop creep/stress rupture data for the unirradiated Path C Vanadlum Scoping Alloys doped with controlled amounts of non-metallic impurity, namely oxygen.

5.1.3 *Sumnary*

Thls report updates the data on the creep/stress rupture of the vanadium-base scoping alloys containing zero, 600 wppm and 1200 wppm additional oxygen. The conclusions drawn earlier that V-15Cr-5Tl shows superior creep/stress rupture properties to V-20Tl and VANSTAR-7 alloys and that addition of 1200 wppm oxygen has no major effect on the creep rupture propertles remain valid. The additional fractography presented here confirms the ductile nature of these alloys.

5.1.4 Progress and Status

The Path C Vanadium-Base Scoping Alloys, which were prepared for the ETM Research Materials Inventory, sited at the Oak Ridge National Laboratory, are the subject of this evaluation. These include:

V-201i
V-15Cr-5Ti
VANSTAR-7 (V-9Cr-3.3Fe-1.2Zr-0.054C)

Efforts during the preceding fiscal year (FY 82) focused on establishing the tensile and stress rupture behavlor of lntentlonally contaminated alloys. Controlled amounts of oxygen contaminations (up to 1200 wppm additional) were introduced by gas metal reaction prior to testing. The results of these efforts were reported previously.[1,2] The activities for the current fiscal year are focused on completion of the stress rupture testing and evaluation of the fracture behavior of these specimens.

Tasks associated with these efforts are: [from the FY'82 scope]

Task 5. Completlon of Creep/Stress-Rupture Testing of Contaminated Specimens
Task 6. Microstructural Characterization

The results of creep/rupture testing and post-test microstructural analysis (fractography) of specimens completed during FY'82 have been reported. The present report updates the results of creep/stress rupture tests in progress at the time of the last report. Additional post-test fractography results are also presented.

5.1.4.1 Material Identification and Condition

The chemical analysis of the three Path C Vanadium Scoping Alloys, the heat treatments, contamination exposures, specimen designations and the oxygen analyses of the contaminated specimen have been reported previously.[1,2]

5.1.4.2 Creep/Stress Rupture Evaluations

Creep/stress rupture tests on sheet specimens of the three alloys containing three levels of oxygen (base composition plus two levels of contamination), were conducted in high vacuum ($<10^{-8}$ torr) with a dead-weight load system. The temperatures and stress levels for the experiments were chosen, based on the creep/stress rupture data for the non-contaminated alloys, to cause fracture in 1000-2000 hours. In the following the results of all the tests completed to this date are presented in tabular and graphical form.

Table 5.1.1 presents the creep/stress rupture data for this alloy in the non-contaminated and contaminated conditions. This table updates the data collected thus far and represents a maximum rupture time of ~3000 hours. At 650°C, the alloy shows increased rupture time with Increasing oxygen content. with a concomitant decrease in failure straln. The alloy exhlbits a ductlle behavlor at all contamination levels (up to 1200 wppm additional) with failure strains >28%. The creep straln vs time curves for the alloy are shown in Figure 5.1.1.

TABLE 5.1.1 Creep/Stress-Rupture Test Data for V-20Ti

Specimen Ident. No.	Nominal[a] O_2 Content (wppm)	Test Temp. (°C)	Stress (MPa)	Stress (ksi)	Time (hrs)	Cumul. Strain (%)	Comment
15	0	650	148	21.5	1158	(0.02)	No Rupture
15(Cont'd.)	0	650	218	31.5	2968	50.7	
16	0	650	276	40	800	34.5	
82-18	600	650	276	40	1006.6	32.2	
82-28	1200	650	276	40	1158.4	28.5	
82-38	600	700	207	30	14		Controller Malfunction
82-48	1200	100	207	30	732.3	43.7	

[a]Additional oxygen content; i.e. above the initial concentration of 450 wppm

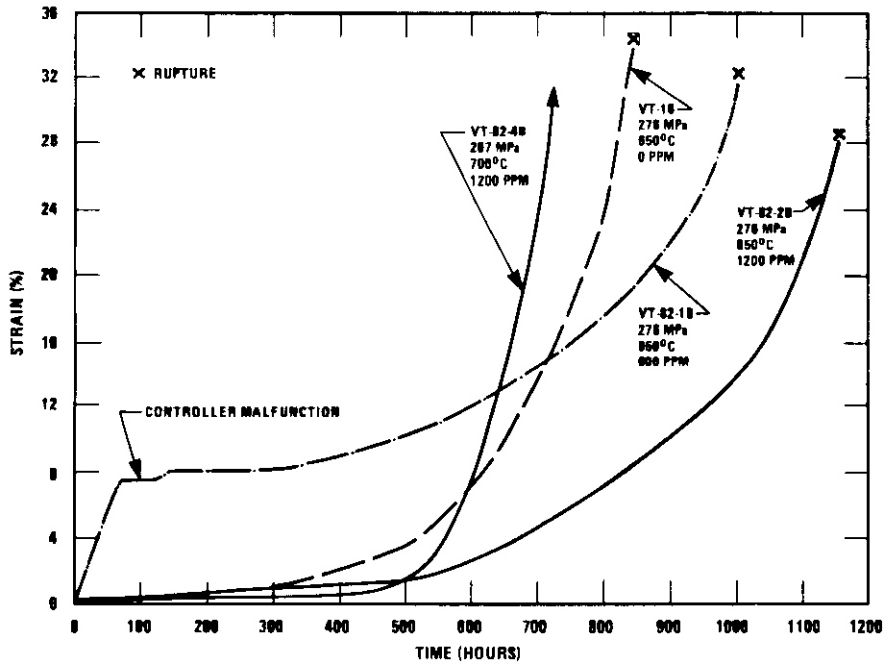

Figure 5.1.1 Effect of Oxygen on the Creep Properties of V-20Ti

V-15Cr-5Ti

The updated creep/stress rupture data for V-15Cr-5Ti are presented in Table 5.1.2 and the creep strain vs time curves are shown In Figure 5.1.2. A contamlnatlon level of 1200 wppm (addltlonal) does not appear to have a significant affect on the failure straln of thls alloy. The effect of contamlnatlon levels on the time to rupture was not monotonic at all temperatures; for example, at 750°C, a saturation tendency was apparent above 600 wppm and Increased thereafter. Addltlonal testlng Is requlred to clearly deflne the effects of contamlnatlon on the creep/stress rupture propertles of thls alloy.

TABLE 5.1.2 Creep/Stress-Rupture Test Data for V-15Cr-5Ti

Specimen Ident. No.	Nominal[a] O_2 Content (wppm)	Test Temp. (°C)	Stress (MPa)	Stress (ksi)	Time (hrs)	Cumul. Strain (%)	Comment
15	0	650	414	60	1055	(0.5)	No Rupture
82-58	600	700	414	60	11.1	33.1	
17	0	150	368	53.5	115	13.8	
18	0	750	345	50	321	22.4	
82-16	600	750	345	50	791.9	11.4	
82-28	1200	150	345	50	780.0	14.6	
16	0	800	216	40	629.0	22.5	
82-36	600	800	216	40	547.8	13.1	
82-48	1200	800	216	40	1543.3	15.2	

[a] Additional oxygen content; i.e. above the Initial concentration of 230 wppm

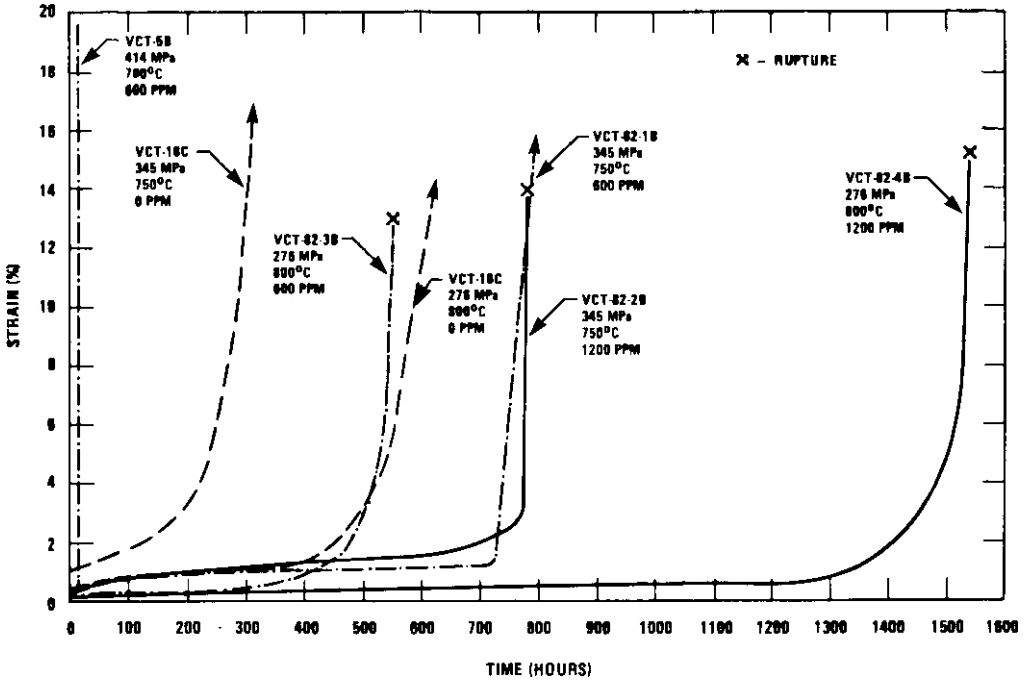

Figure 5.1.2 Effect of Oxygen on the Creep Properties of V-15Cr-5Ti

VANSTAR-1

The updated creep/stress rupture data for VANSTAR-1 are shown in Table 5.1.3. Specimen 82-48 accumulated a total of 4935.8 hours at 700°C, when the test was terminated. This test represents the longest creep/rupture test on any vanadium alloy at 100°C. The creep strain at this point was −0.2% Indicating that the specimen is still in the second stage of creep and rupture life may be significantly longer. No definite conclusions can be drawn regarding the effect of oxygen contamination on the stress rupture properties, although it appears to increase the rupture life at 700°C. The updated creep straln vs time curves for VANSTAR-1 are shown in Flgure 5.1.3.

TABLE 5.1.3 Creep/Stress-Rupture Test Oata for VANSTAR-?

Specimen Ident. No.	Nominal[a] O_2 Content (wppm)	Test Temp. (°C)	Stress (MPa)	Stress (ksi)	Time (hrs)	Cumul. Strain (%)	Comment
15	0	650	216	40	1261	(0.11)	No Rupture
15 (Cont'd.)	0	650	331	48	1611	(0.52)	No Rupture
17	0	100	216	40	1200	(0.12)	No Rupture
11 (Cont'd.)	0	150	276	40	1733	14.8	
82-38	600	700	276	40	3579.3	10.1	
82-40	1200	700	216	40	4935.8	0.19+	
16	0	150	201	30	2192.0	(1.02)	No Rupture
16 (Cont'd.)	0	750	241	35	2428	19.3	
82-18	600	750	216	40	139.6	11.4	
82-28	1200	150	216	40	10.2	16.1	Controller Malfunction
82-68	1200	150	276	40	439.8	8.5	Repeat of Previour Test

[a]Additional oxygen content; i.e. above the initial concentration of 280 wppm.

+Test terminated before rupture.

5.1.4.3 Fractoqraphy of Contaminated Creep Specimens

In the previous report[2] fractographs of three specimens each of V-20Ti and V-15Cr-5Ti and two VANSTAR-1 specimens were presented. All specimens, wlth the exception of one V-15Cr-5Ti specimen, showed ductile, dlmpled rupture. Four additional specimens, one of V-20Ti, one of V-15Cr-5Ti, and two of VANSTAR-1 were examined by SEM. Representative micrographs are presented in Figures 5.1.4 through 5.1.1 and are dlscussed below.

The fracture in specimen VT-82-10 (600 wppm) tested at 650°C/276 MPa occurred by a ductile shear mechanism; two different dimple sizes are evident on the micrograph (figure 5.1.4). A companion specimen VT-82-28 (1200 wppm) tested under the identical condltlon (650°C/276 MPa), which showed comparable failure strain (32% vs. 29%) had also shown a bimodal dimple size distribution.[2] However, the large dimples were larger in VT-82-10 than in VT-82-20. The smaller dimples were comparable in size in the two specimens. No variation was found in the fracture mode from the surface to the interior of the specimens.

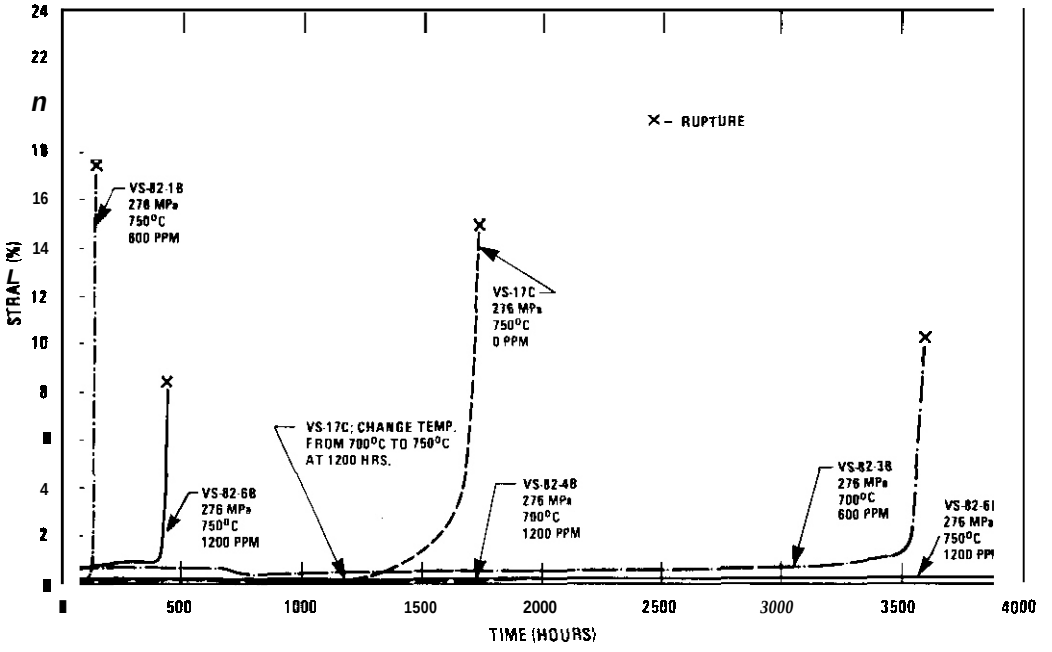

Figure 5.1.3 Effect of Oxygen on the Creep Properties of VANSTAR-7

V-15Cr-5Ti

The fracture surface of specimen VCT-82-5E (600 wppm) tested at 700°C/414 MPa displayed ductile, dimpled rupture with a uniform size distribution (Figure 5.1.5). This specimen was tested at the highest stress (414 MPa) and lowest temperature used for this alloy. Although this specimen fractured in relatively short time (17.1 hours), no variation was found in the rupture mode from the surface to the interior of the specimen.

VANSTAR-7

Specimen VS-82-38, which failed after 3580 hours, showed dimpled rupture, Figure 5.1.6. The large precipitates seen in the micrograph were analyzed by EDX analysis and found to be rich in Zr and are believed to be ZrC. The dimples presumably nucleate at these precipitates during deformation.

Specimen VS-82-6B also showed a dimpled rupture. This rupture was very similar to the ductile rupture in another specimen. VS-82-6B, tested under identical conditions but which contained 600 wppm oxygen as compared to 1200 wppm oxygen (VS-82-1B).[2]

5.1.5 Discussion of Results

This is a wrap-up report on the creep of vanadium alloys and thereby presents only limited additional data on creep rupture. The additional data presented here only support the conclusions drawn earlier.[2] An updated plot of the Larson-Miller parameter for the three vanadium alloys and for Type 316 SS is presented in Figure 5.1.8. No additional comment on the creep properties of these alloys is deemed necessary.

It was reported previously that the fracture mode observed for the contaminated creep specimens was different from that observed for similarly contaminated tensile Specimens. Some of the tensile specimens, tested at RT and 500°C, displayed cleavage fracture in the near-surface regions although final fracture was by ductile shear. The creep fracture of the specimens tested in the temperature range of 650 to 800°C. almost always occurred totally by ductile shear. It was concluded that the difference in the fracture mode was due to variation in oxygen concentration from the surface to the bulk which was alleviated by long term exposure to high temperatures during creep testing. The fractography presented here confirms the observation of uniform fracture mode in creep specimens.

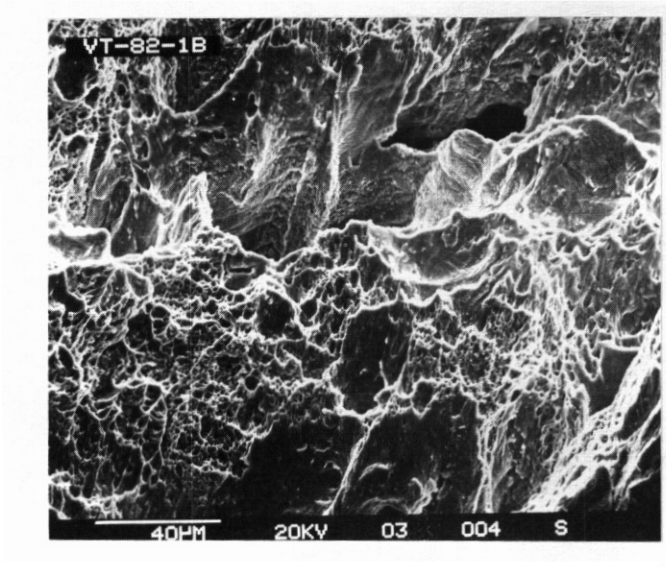

Figure 5.1.4 Scanning Electron Micrograph of a V-20Ti Creep Specimen [600 wppm Oxygen; 650°C; 276 MPa]

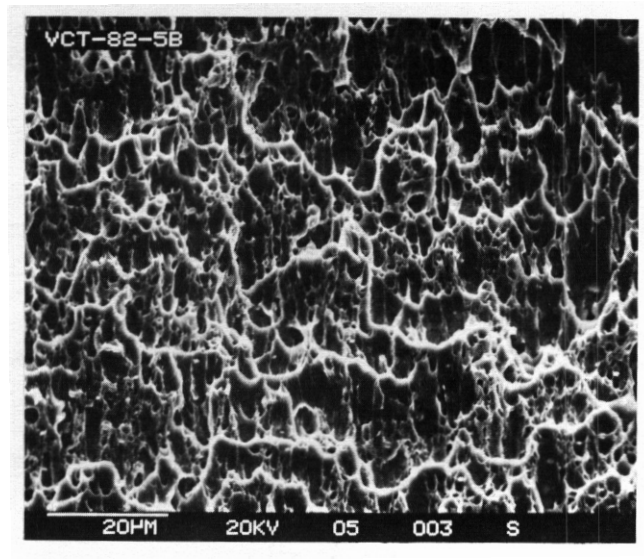

Figure 5.1.5 Scanning Electron Micrograph of a V-15Cr-5Ti Creep Specimen [600 wppm Oxygen; 700°C; 414 MPa]

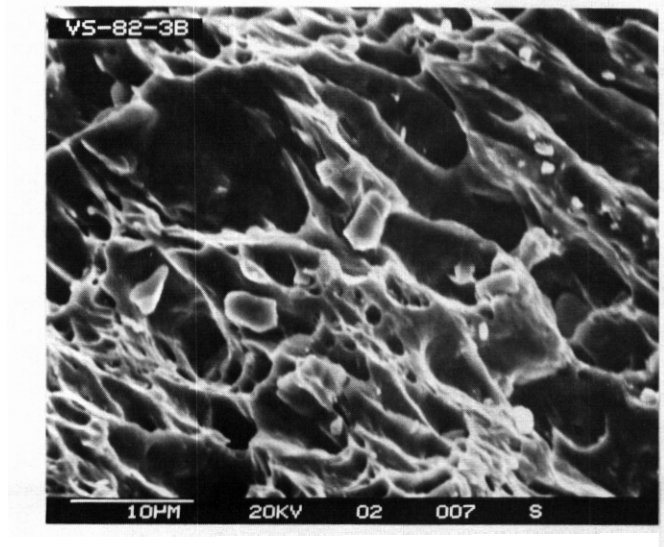

Figure 5.1.6 Scanning Electron Micrograph of a VANSTAR-7 Creep Specimen [600 wppm Oxygen; 700°C; 276 MPa]

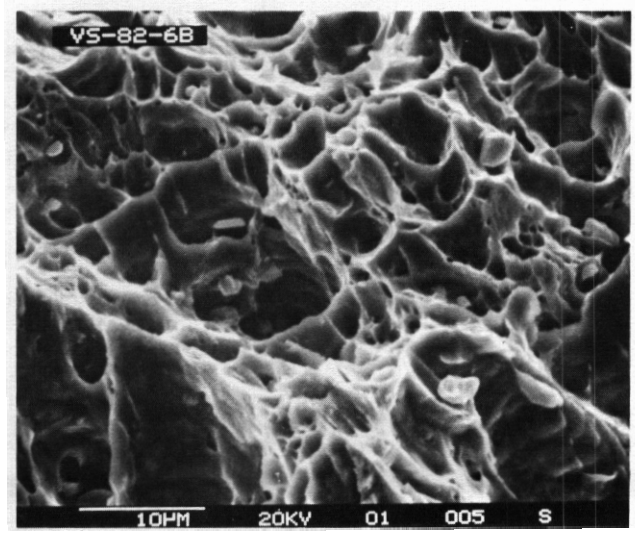

Figure 5.1.7 Scanning Electron Micrograph of a VANSTAR-7 Creep Specimen [1200 wppm Oxygen; 750°C; 276 MPa]

5.1.6 References

1. R. E. Gold, "Mechanical Property Evaluations of Path C Vanadium Scoping Alloys," Alloy Development for Irradiation Performance, Progress Report for Period Ending March 31, 1982, DOE/ER-0045/8, p. 281 (September 1982).

2. R. E. Gold and R. Bajaj, "Mechanical Property Evaluations of Path C Vanadium Scoping Alloys," Alloy Development for Irradiation Performance, Progress Report for Period Ending Sept. 30, 1982, DOE/ER-0045/9, p. 122 (March 1983).

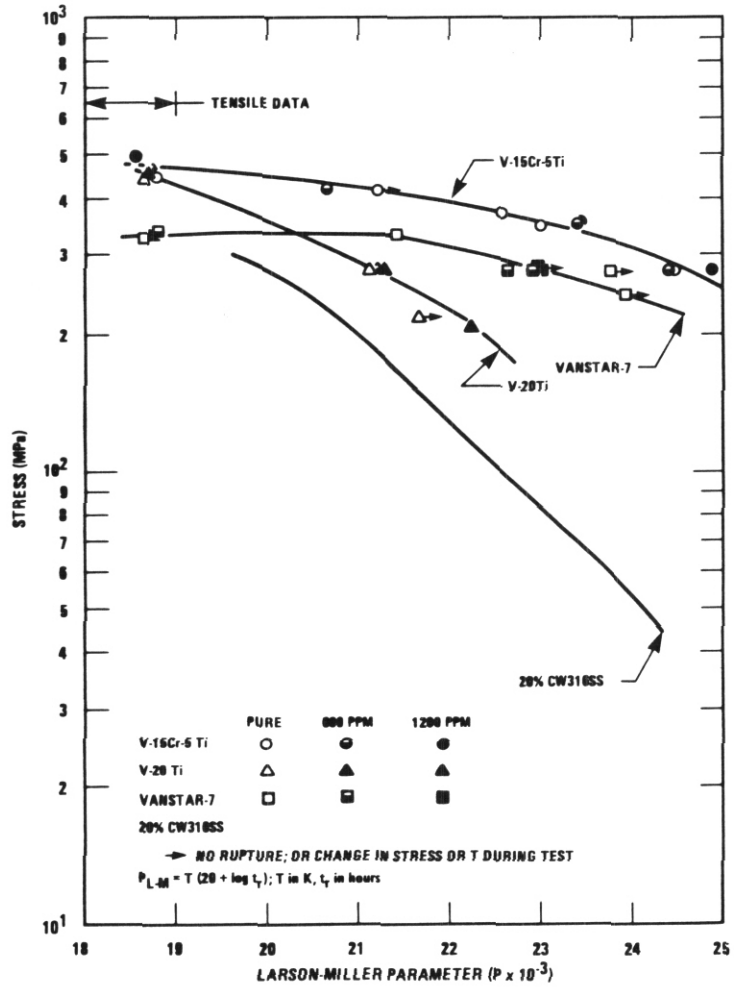

Figure 5.1.8 A Larson-Miller Plot of Tensile and Creep Data for the Vanadium-Base Scoping Alloys and 20% CW 316 SS

Acknowledgments

The authors acknowledge the support of G. O. Yatsko and R. L. Ammon of the Westinghouse Advanced Energy Systems Division (Large Site) for the creep testing and T. Mullen of the W R&D Center for SEM fractography work. The cooperation and general support of Drs. E. E. Bloom, F. W. Wiffen, and J. L. Scott of the Metals and Ceramics Division of the Oak Ridge National Laboratory are also gratefully acknowledged.

5.2 WELDABILITY OF PATH C VANADIUM ALLOYS -

R. E. Gold and R. Bajaj (Westinghouse Electric Corporation)

5.2.1 ADIP Tasks

I.A.5. Fabrication and Welding of Path C Metal Alloys

5.2.2 Objective

The objective of this effort was to examine the basic weldability of the Path C Vanadium-Base Scoping Alloys and to determine the bend ductile-brittle transition temperatures of base metal and weld specimens of each alloy.

5.2.3 Summary

Gas tungsten arc welds were prepared for each of the three vanadium-base (Path C) scoping alloys using semi-automatic, full penetration, bead-on-sheet welds. The bend ductile-brittle transition temperatures (DBTTs) of these welds and base metal specimens were determined. In terms of weldability the alloys were ranked: (best) V-20Ti, V-15Cr-5Ti, VANSTAR-7. The bend DBTT values for weld specimens were: V-20Ti, -196/-150°C; V-15Cr-5Ti, -20/+50°C; VANSTAR-7, -75/-50°C, for longitudinal/transverse bend tests.

5.2.4 Progress and Status

The Path C Vanadium-base Scoping Alloys are the subject of this evaluation. These are: V-20Ti, V-15Cr-5Ti, and VANSTAR-7 (V-9Cr-3.3 Fe-1.2 Zr-0.054C). These alloys have been the subject of a series of test programs aimed at the characterization of their tensile and stress rupture properties [see preceding section, 5.1, this Semiannual Report]. Activities reported here are those associated with the FY'83 continuation of the evaluation of the unirradiated properties of the subject alloys. Specific tasks are:

Task 7. Material Procurement, Specimen Preparation, and Heat Treatments
Task 8. Gas Tungsten Arc Welding
Task 9. Bend Ductile-Brittle Transition Temperature Determinations
Task 10. Post-test Examinations

Tasks 7, 8 and 9 have been completed and Task 10 is partially completed. The results of these activities are presented in the following subsections in the appropriate task sequence.

5.2.4.1 Material Procurement, Specimen Preparation, and Heat Treatments

Material for these investigations was procured from the ETM Research Materials Inventory in the form of 0.76 mm thick sheet. The material identifications and chemical analyses are provided in Table 5.2.1. Upon receipt the alloy sheet was cold-sheared into pieces approximately 2.5 x 15 cm.; the longitudinal (rolling) direction of the sheet was always maintained parallel with the 15 cm. dimension.

TABLE 5.2.1 Chemical Analysis of Vanadium Alloy Sheet

	Elemental Analysis (w/o)	
		Zr

After shearing, all alloys were heat treated in vacuum for one hour at previously determined recrystallization temperatures. These temperatures, which produce an equiaxed (~30 to 35 μm) microstructure, are 1100, 1200, and 1350°C for the V-20Ti, V-15Cr-5Ti, and VANSTAR-7 alloys, respectively.

5.2.4.2 Gas Tungsten Arc Welding

All gas tungsten arc (GTA) welding was carried out in an argon atmosphere in a glove box used extensively for the preparation of high quality weldments in refractory metal alloys. During welding operations, continuous monitoring of oxygen and water vapor was carried out. All welds were full penetration, bead-on-sheet (to avoid edge preparation variables) welds performed semiautomatically with nonconsumable thoriated tungsten electrodes. Owing to the limited availability of sheet material, preliminary weld parameter screening was performed to identify a common set of welding conditions for all three alloys. These conditions were:

Welding Speed	38.1 cm/min.
Current	70 Amperes
Voltage	10.5 V (dc)
Gap (electrode to sheet)	1.52 mm

Eight welds were prepared for each of the alloys.

During welding, the sheet specimens were held in a clamping fixture which provided mechanical restraint to avoid buckling or bowing of the thin sheet. Molybdenum chill/clamp plates were used, with a clamp spacing of 9.5 mm. The tungsten electrodes were changed after every fourth weld. The oxygen level in the argon atmosphere was maintained between 5.2 and 7 ppm (by volume), and the water vapor content was below 5.4 ppm (by volume) throughout the welding operations.

After welding, the specimens were examined visually as-welded and following dye penetrant inspection. Except for an occasional, small transverse crack near the weld termination point, the welds in V-20Ti and V-15Cr-5Ti were crack-free. In VANSTAR-7, however, in addition to cracks at the weld termination point, dye penetrant inspection revealed irregular cracking in the weld fusion zones of several, but not all, of the welds. Photographs of typical specimens of each alloy are shown in Figure 5.2.1. Note the general curvature which resulted when the specimens were removed from the welding fixture.

Before shearing the bend test blanks, each alloy was given a one hour post weld anneal in vacuum at the recrystallization temperatures noted previously. Post weld anneals are used routinely in refractory metal alloy welding studies for the purpose of chemically combining any oxygen and/or nitrogen picked up in welding with the reactive metal solute - e.g. Ti or Zr - in the subject alloys. This is considered particularly important for applications involving exposure of the welds to liquid alkali metals. In the current program, the post weld anneal appeared to have little affect on V-20Ti, but caused considerable grain growth in both the V-15Cr-5Ti and VANSTAR-7 alloys (metallography incomplete at present). Grain growth was particularly significant in the heat-affected-zones of the VANSTAR-7 specimens, Figure 5.2.2.

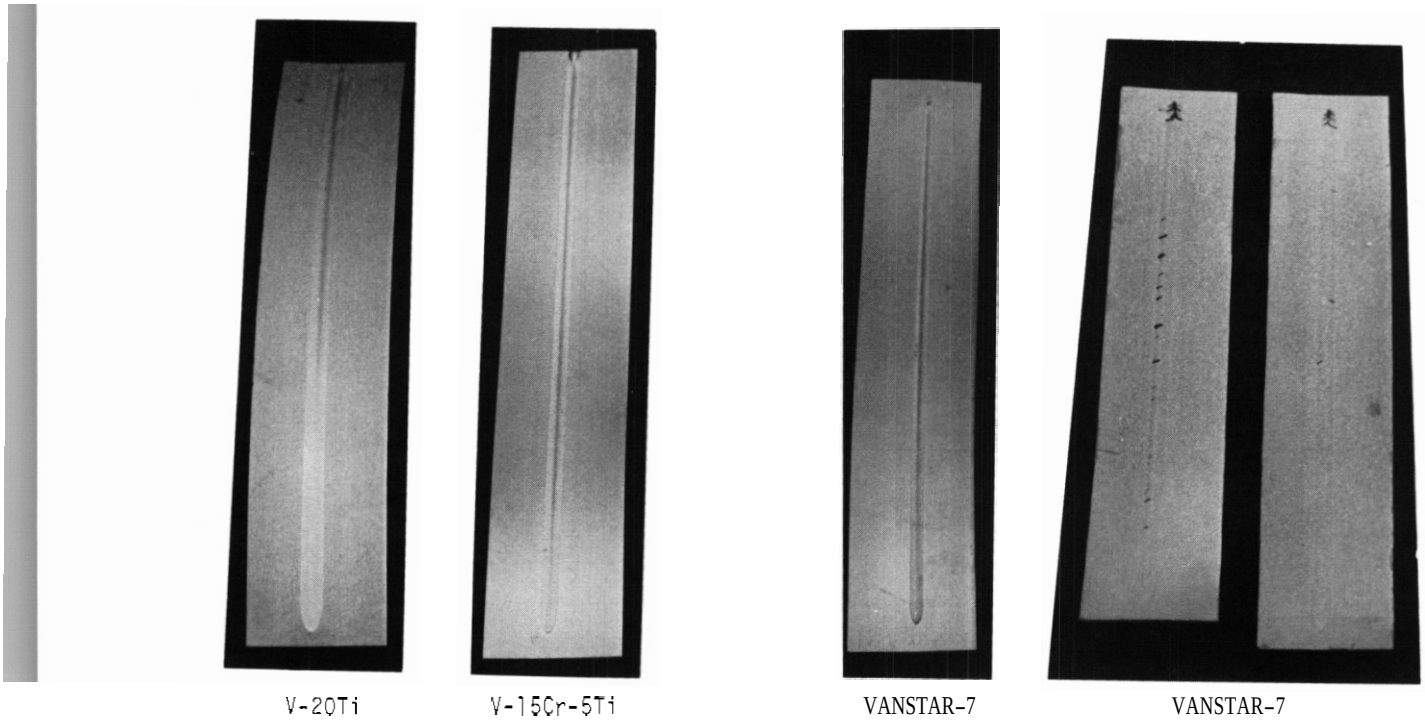

Figure 5.2.1 Typical GTA Weld Specimens in Vanadium Alloys.

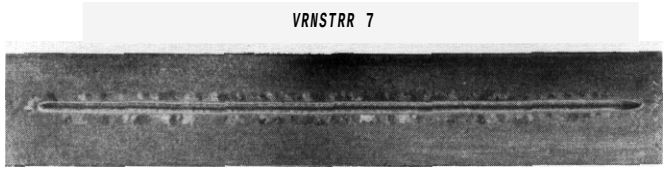

Figure 5.2.2 VANSTAR-7 Weld Specimen Showing Coarse Grains in the Heat Affected Zone.

If this phenomenon had been limited to only the weld specimens it might have been possible to explain the behavior in terms of dissolution or coarsening of grain boundary - stabilizing precipitates during the welding; it was, however, also observed, although to a lesser degree, in the base metal specimens given identical heat treatments. Additional heat treatment - metallographic analyses will be carried out to explore this behavior.

5.2.4.3 Bend Ductile-Brittle Transition Temperature Determinations

The eight welds and two base metal specimens, each 2.5 x 15 cm, of each of the vanadium alloys were sheared to yield specimens for three point bend testing. Approximately four transverse and five longitudinal test specimens were prepared from each weld. The bend test parameters and specimen orientations are defined in Figure 5.2.3. All testing was carried out using a punch speed of 0.04 cm/s (1 inch/min) with the top surface of the weld in tension. Most tests were conducted using a 1t punch radius; this bend radius produces an outer fiber strain of approximately 30% on the tension side of the specimen.

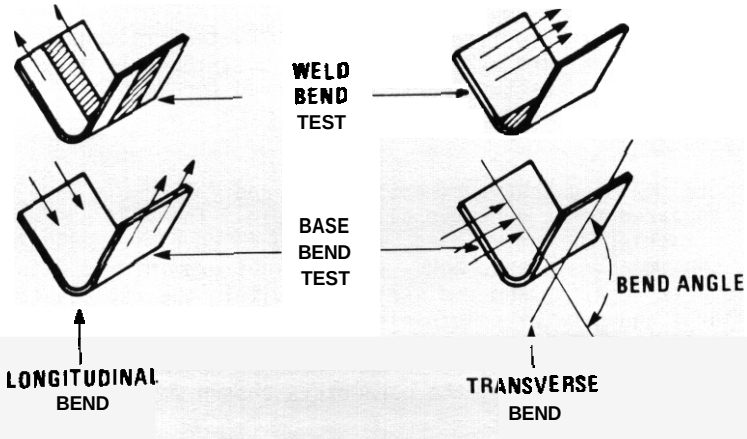

NOTE: Arrow indicate the sheet rolling direction

Specimen Width	12 t (t= sheet thickness)
Specimen Length	24 t
Test Span	15 t
Punch Speed	0.04 cm/s
Temperature	Variable
Punch Radius	Variable, generally 1t, 2t, or 4t

FIGURE 5.2.3 Test Parameters and Specimen Orientations Used for Three Point Bend Tests on Vanadium Allny Sheet.

The bend testing procedure provides for immediate withdrawal of the mechanical load at the first sign of load drop; this is normally observed to indicate the onset of cracking. In this way it is often possible to locate and examine the fracture initiation site without continuing to total destruction of the specimen. For tests at other than room temperature, the specimens are permitted to equilibrate at the test temperature for a minimum of ten minutes prior to testing.

The average values of the 1t bend DBTT s are summarized in Table 5.2.2. Typical plots of the bend angle vs. test temperature for each of the three alloys are presented in Figure 5.2.4. The crack locations and orientations are indicated for specimens which fractured during testing.

TABLE 5.2.2 Summary of Bend DBTTs for the Vanadium-Base Scoping Alloys

Alloy	Specimen Type	1t Bend DBTT (°C) Longitudinal	Transverse
V-20Ti	Base Metal	-196	-150
	Weld	-125	-125
V-15Cr-5Ti	Base Metal	-20	50
	Weld	+50/+100	50
VANSTAR-7	Base Metal	-75	-50
	Weld	20	20

All values for welds are the average of bend tests on at least five welds.

Base metal values are the average of tests on two specimens.

5.2.4.4 Post-Test Examinations

Selected bend specimens were examined by scanning electron microscopy in order to characterize the fracture surfaces. For V-20Ti, even for fractures at -196°C, the fractographs indicated ductile tearing to be the predominate failure mode, Figure 5.2.5. Fractures in V-15Cr-5Ti were almost totally characteristic of cleavage, Figure 5.2.6, as were fracture surfaces observed for VANSTAR-7 bend specimens, Figure 5.2.7.

5.2.5 Discussion of Results

In terms of the general welding behavior, both V-20Ti and V-15Cr-5Ti were welded without difficulty; V-20Ti, in particular, appeared to be exceptionally weldable. The VANSTAR-7 alloy, while not prone to obvious or catastrophic cracking during welding, was found to develop small cracks in the weld fusion zones of several of the weld specimens. These cracks, although not examined in detail, are probably hot cracks and are related to solute segregation and redistribution within the rapidly cooled fusion zone. In view of the more complex metallurgy and greater solute element variation in this alloy, this is not altogether surprising. Neither should it be interpreted to mean VANSTAR-7 can not be satisfactorily welded by the GTA process. In the limited evaluation described here no attempt was possible to develop optimum welding parameters for each of the alloys. Hence, the parameters chosen may very well be near-optimum for V-20Ti but much less so for the other two alloys.

There is no immediately apparent reason for the considerable grain growth observed in the V-15Cr-5Ti and VANSTAR-7 alloys following the post weld anneals at their respective recrystallization temperatures. This issue will be examined more closely in the next several months.

For all of the alloys the bend DBTTs of the welds were higher than for the corresponding base metal; this is as expected. Interestingly, despite the presence of small cracks in several of the bend specimens the bend DBTT of VANSTAR-7 was lower than that of the V-15Cr-5Ti alloy which welded without incident. The bend DBTTs of both VANSTAR-7 and V-15Cr-5Ti were higher than would be expected from the high ductilities exhibited by these alloys in tension tests at room temperature. Part of the reason for this might be the higher loading rate used for the bend tests. There is also a strong possibility that the large (duplex) grain size which developed in these alloys during the post weld anneal is a major contributing factor. Additional base metal bend testing and heat treating/microstructural response studies are currently underway to explore these issues.

Based on these preliminary evaluations the alloy weldability rankings appear to be: (best) V-20Ti, V-15Cr-5Ti, VANSTAR-7. In terms of the bend DBTTs, the rankings would be: (best - or lowest DBTT) V-20Ti, VANSTAR-7, V-15Cr-5Ti.

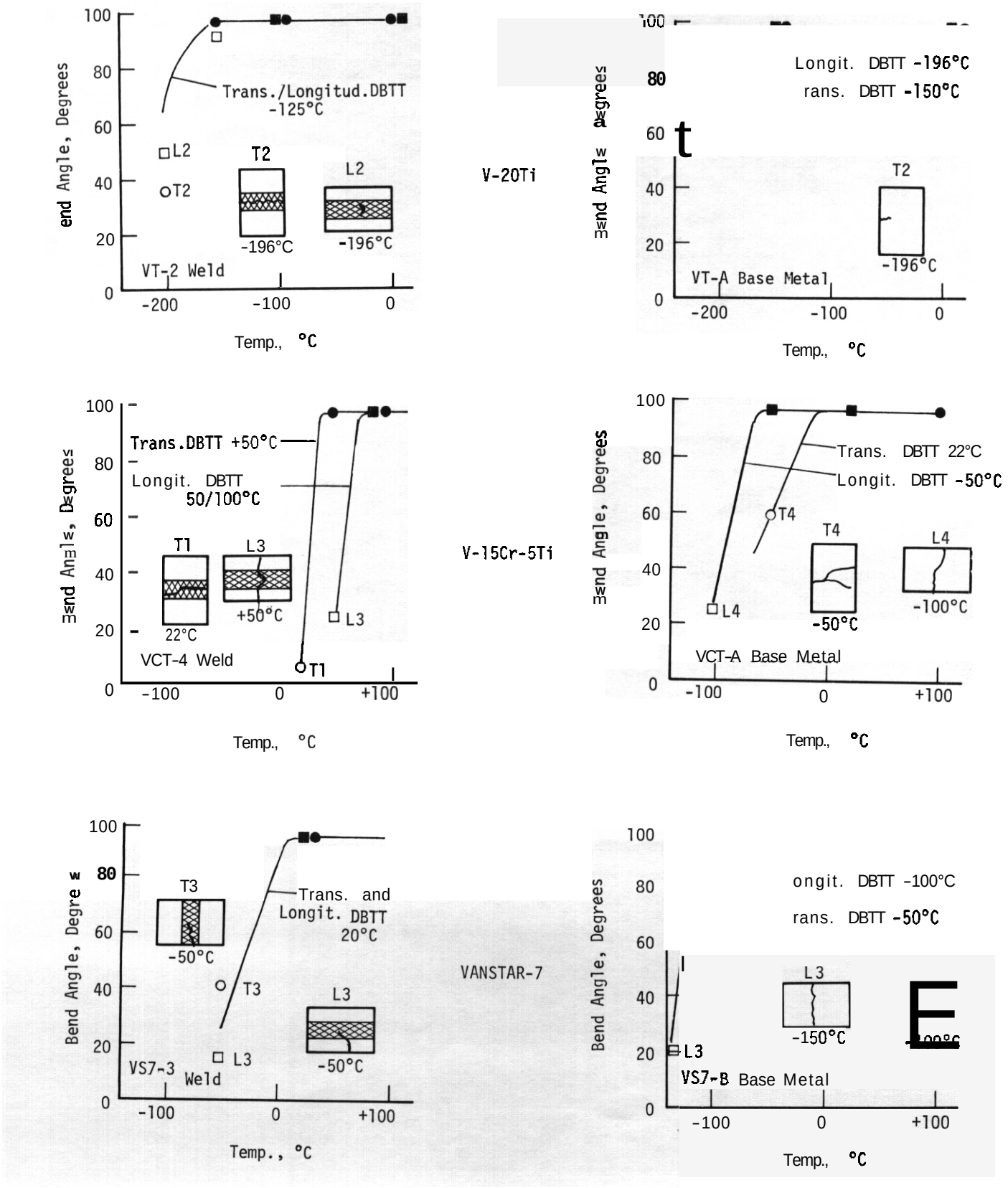

Figure 5.2.4 Typical Bend Angles vs. Test Temperature Plots for Vanadium Alloy Tests [Open Symbols = Fractures].

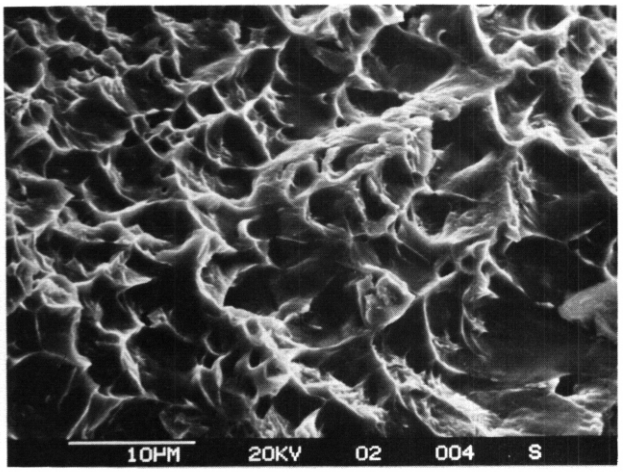

Base Metal

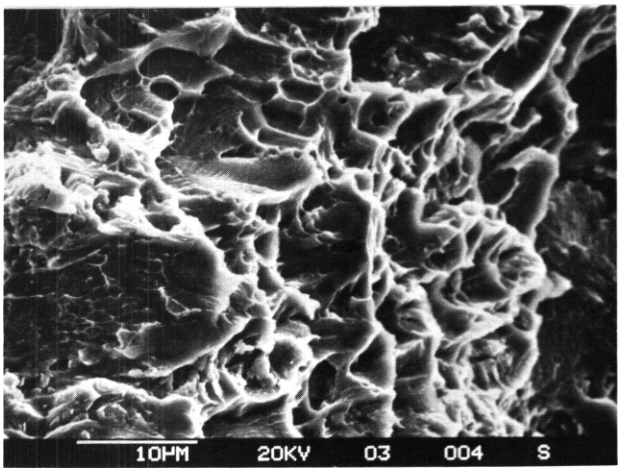

Weld Specimen

Figure 5.2.5 Fractographs of V-20Ti Bend Specimens Tested at -196°C

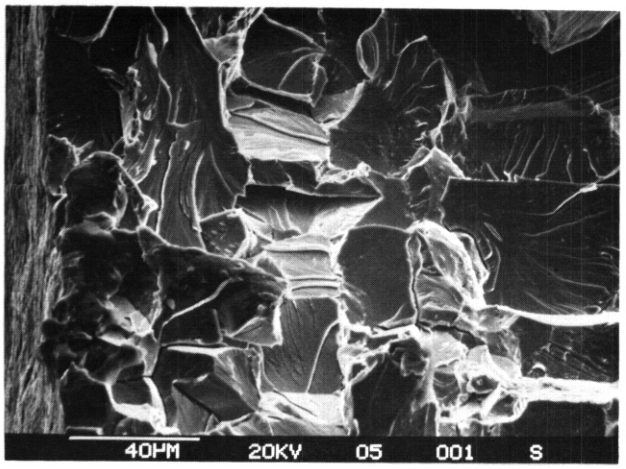

Base Metal; 22°C

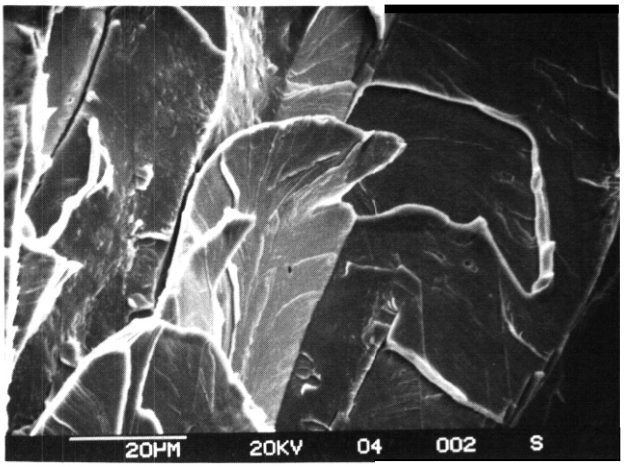

Weld; -50°C

Figure 5.2.6 Fractographs of V-15Cr-5Ti Bend Specimens

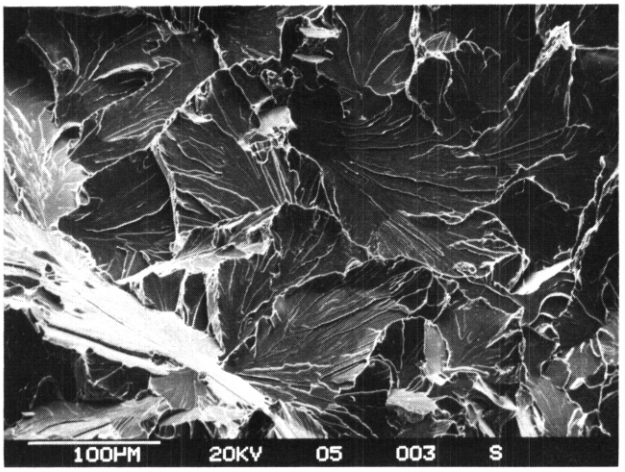

Figure 5.2.7 Fractograph of VANSTAR-7 Weld Metal Bend Specimen Tested at -100°C

5.3 EVALUATION AND DEVELOPMENT OF VANADIUM-BASE ALLOYS FOR FUSION REACTOR APPLICATIONS - B. A. Loomis and D. L. Smith (Argonne National Laboratory)

5.3.1 ADIP Task

I.A.3. Perform Chemical and Metallurgical Compatibility Analyses.

5.3.2 Objective

This research program provides the necessary data that are required for the evaluation and development of vanadium-base alloys for first-wall and blanket structures in fusion reactors. The research effort is focused on (1) the corrosion and compatibility of selected vanadium-base alloys in the environments projected for fusion reactors, (2) investigations of the pertinent environmental effects on the mechanical properties of the selected alloys, (3) evaluation of the effect of vanadium alloy composition on weld microstructure and mechanical properties, and on secondary fabrication processes, and (4) determination of environmental effects of the integrity and mechanical properties of weldments.

5.3.3 *Summary*

The corrosion of "pure" V and V-5Ti, V-15Cr and V-15Cr-5Ti alloys at 725 K and 825 K in flowing helium containing 10 ppm water was determined for exposure times that yielded a steady-state corrosion rate. The experimentally determined corrosion rates for the V and V-base alloys were compared with the corrosion rate obtained for PCA stainless steel under the same environmental conditions. These results showed that the steady-state corrosion rates for the V-15Cr alloy and V-15Cr-5Ti alloy were low but approximately one order of magnitude greater than the steady-state corrosion rate determined for the PCA stainless steel. Also, the temperature dependence of the electrical resistivity for V and V-15Cr-5Ti alloy was determined for temperatures ranging from *17* K to 1000 K.

5.3.4 Progress and Status

5.3.4 .1 Introduction

Vanadium-base alloys offer potentially significant advantages over other candidate alloys as fusion reactor structural materials. High fluence irradiations under LMFBR conditions and high-damage-level ion irradiations have demonstrated an inherent resistance of certain vanadium alloys to void swelling in comparison to most other candidate alloys. Of particular importance in projecting the potential radiation-damage resistance of vanadium alloys to fusion reactor conditions is their apparent insensitivity to moderate compositional and microstructural variations. Such insensitivity may make special treatments, such as cold-work and post-weld heat treatment, unnecessary. The relatively high thermal conductivity and low thermal expansion coefficient of vanadium alloys result in lower thermal stresses for a given heat flux compared to *most* other candidate alloys and should allow an increased thermal loading and lifetime of structural components. Since the mechanical strength of vanadium alloys is retained at relatively high temperatures, higher operating temperatures are projected for vanadium alloys than for austenitic or ferritic steels. Vanadium alloys produce the least impact of the primary candidate alloys on tritium breeding, and selected vanadium alloys offer the potential for the lowest long-term (> 30 y) activation of the candidate alloys presently considered. Under controlled conditions, vanadium alloys are among the most corrosion-resistant alloys in high-temperature (725 K) lithium.

The major concerns regarding the use of vanadium alloys relate to their reactivity with air (primarily oxygen and nitrogen), which may lead to embrittlement or oxidation effects when exposed to even fairly low oxygen or nitrogen partial pressures. In this report we present some initial results on the corrosion of pure V and V-5Ti, V-15Cr and V-15Cr-5Ti alloys at 725 K and 825 K in helium containing 10 ppm water. The corrosion rates for these materials are compared with the corrosion rate for PCA stainless steel under identical environmental conditions. Also, we present in this report the electrical resistivity for pure V and V-15Cr-5Ti alloy at temperatures between 77 K and 1000 K.

5.3.4.2 Experimental Procedure

The "pure" V and V-base alloy specimens for these experiments were prepared from stock that contained ~900 appm O. The V-15Cr-5Ti alloy was obtained from the Fusion Program Research Materials Inventory at Oak Ridge National Laboratory. The "pure" V and V alloys were annealed for one hour at 1475 K prior to initiation of the experimental studies. The PCA stainless steel with B2 microstructure was also obtained from the Fusion Program Research Materials Inventory.

For the corrosion studies, sheet specimens (0.01 m x 0.01 m x 0.0002-0.0008 m) of "pure" V, V-5 w/o Ti, V-15 w/o Cr, V-15 w/o Cr-5 w/o Ti, and PCA stainless steel at *725* ± 5 K and 825 ± 5 K were exposed for increasing periods of time to flowing He that contained 10 ppm by volume of water. The flow rate of the gas was 8.3 x 10^{-7} m^3/s. The increase in weight of the specimens was determined with an accuracy of 2 x 10^{-9} kg at time intervals of ~5 x 10^5 s (140 h).

The electrical resistivity of the "pure" V and V-15Cr-5Ti alloy was determined at temperatures ranging from 77 K to 1000 K. The specimens were mounted in a system evacuated to 10^{-3} Pa for the electrical resistance measurements at temperatures above 300 K. The electrical resistance of the sheet specimens (0.04 m x 0.04 m x 0.0001 m) was determined with a precision of 0.02 μΩ by the four-point potentiometric method. Copper wires of 0.0004-m diameter were spot welded to the specimens to provide electrical contact. The electrical resistivity of the specimens was calculated from the resistance data with appropriate correction for the dimensional change.

5.3.4.3 Experimental results

Corrosion

The corrosion rates for the V, V-base alloys and the PCA stainless steel at 725 K and 825 K on exposure for increasing periods of time to flowing helium containing 10 ppm water are shown in Fig. 1 and Fig. 2, respectively. In Fig. 1 and Fig. 2, a plotted corrosion rate value (data point) is computed from the increase of specimen weight per unit area for the interval of exposure time between a data point and the preceding data point. On the basis of these limited studies, the steady-state corrosion rates for these materials are shown below for an exposure time of ≥ 15 x 10 s (417 h).

Corrosion Rate ($kg/m^2 \cdot s$)

Material	725 K	825 K
V	1.2×10^{-9}	1.1×10^{-8}
V-5Ti	0.9×10^{-9}	0.7×10^{-8}
V-15Cr	0.2×10^{-9}	0.4×10^{-8}
V-15Cr+5Ti	0.4×10^{-9}	0.5×10^{-8}
PCA SS	0.5×10^{-10}	0.5×10^{-9}

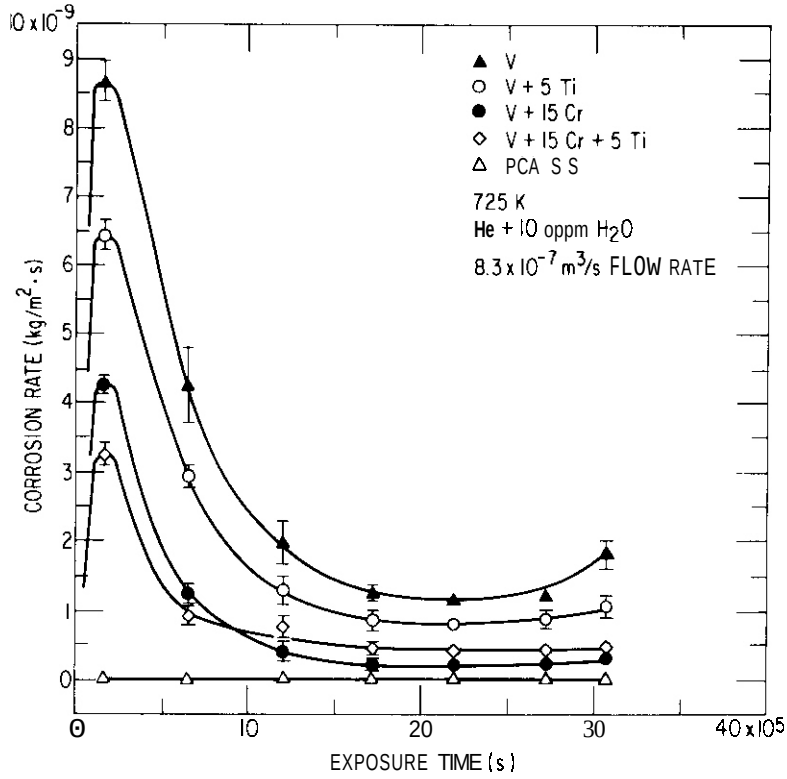

Fig. 1 Corrosion rates for V, V-base alloys and PCA stainless steel at 725 K.

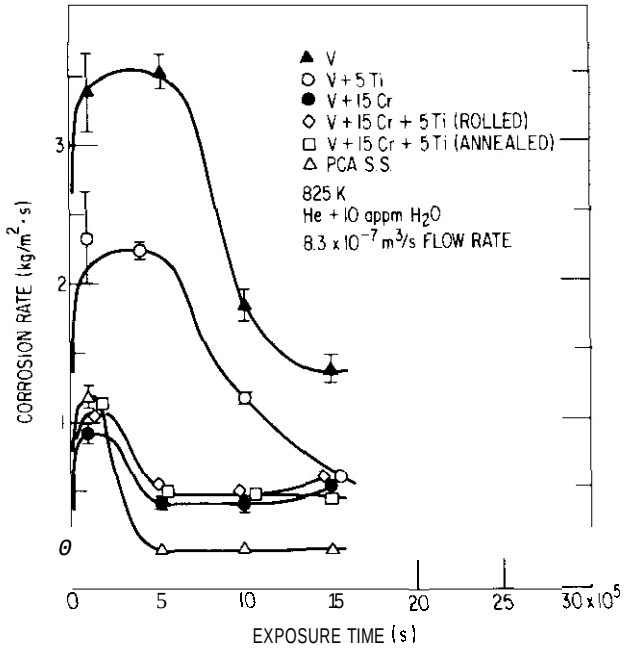

Fig. 2. Corrosion Rates for V, V-base alloys and PCA stainless steel at 825 K.

It can be observed in Figs. 1 and 2 that the V and V-base alloys have corrosion rates (weight gains) approximately an order of magnitude greater than for austenitic steel during the initial exposure time of $\lesssim 10 \times 10^5$ s. Also, these experimental results show that the presence of Cr solute in the V alloys is essential for minimum corrosion in flowing helium containing 10 ppm water.

Electrical Resistivity

The electrical resistivity of V and the V-15Cr-5Ti alloy at temperatures between 77 K and 100 K is shown in Fig. 3. On the basis of these experimental data an equation which yields the temperature dependence of the electrical resistivity (ρ) for V is

$$\rho_V(T) = 25.63 + 0.087 \times T - 1.06 \times 10^{-5} T^2$$

and the equation for the V-15Cr-5Ti alloy is

$$\rho_{V\text{-}15Cr\text{-}5Ti}(T) = 37.75 + 0.077\ T - 8.62 \times 10^{-6} \times T^2$$

In these equations, the electrical resistivity is in units of $\mu\Omega$-cm and the temperature is in degrees Celsius.

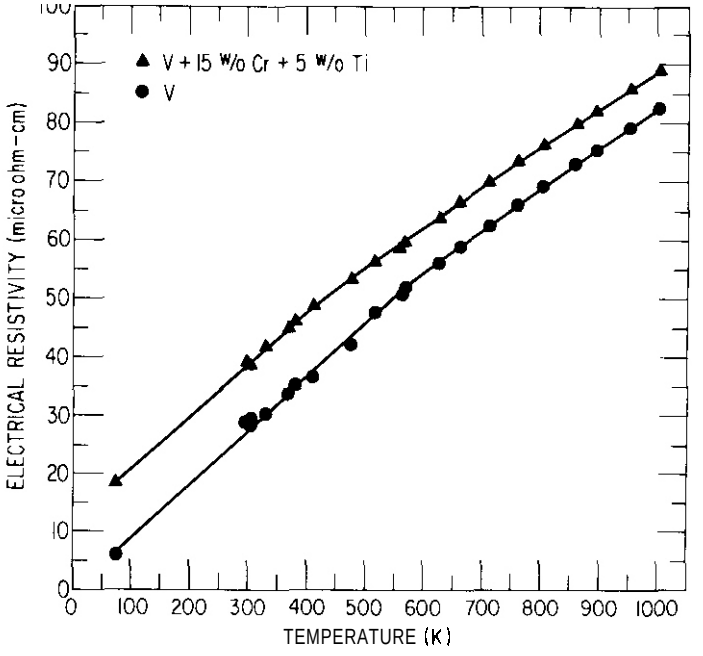

Fig. 3. Temperature Dependence of the Electrical Resistivity for V and V-15Cr-5Ti Alloy.

5.5.5 Discussion of Results

Investigations on the swelling of V-base alloys during heavy-ion irradiation have shown that r additions to V result in substantial swelling whereas Ti additions effectively suppress swelling.! These swelling studies have also shown that the effectiveness of Ti solute for the suppression of swelling of V is not significantly altered by the addition *of* Cr solute to form a ternary alloy, **e.g.,** V-15Cr-5Ti alloy.

The experimental results obtained in the present study on the corrosion of V-base alloys show that a Cr addition to V to form a binary V alloy results in a maximum corrosion resistance for V. The addition of Ti solute (5 w/o) to V is much less effective than the addition of Cr solute for maximum corrosion resistance of V. However, the addition of Ti solute to a V-Cr alloy, **e.g.** V-15Cr-5Ti alloy, does not significantly increase the minimum corrosion rate determined for a V-15Cr alloy. The experimental results obtained in this study suggest that the corrosion rate of PCA stainless steel at 725 K and 825 K in flowing helium with 10 ppm water is approximately an order of magnitude less than the corrosion rate for V-15Cr and V-15Cr-5Ti alloys.

5.3.6 References

1. Cavity Formation in Single- and Dual-Ion Irradiated V-15Cr-5Ti Alloy, B. A. Loomis and G. Ayrault, Damage Analysis and Fundamental Studies Quarterly Progress Report, DOE/ER-0046/12, October-December 1982, p. 194.

6.1 STATUS OF SCALEUP OF AN IRON-BASE LONG-RANGE-ORDERED ALLOY — T. K. Roche, D. N. Braski, and C. T. Liu (Oak Ridge National Laboratory)

6.1.1 ADIP Task

ADIP Tasks I.A.5, Perform Fabrication Analyses, and I.D.1, Materials Stockpile for MFE programs.

6.1.2 Objective

The objective of this work is to perform semiproduction scaleup of an iron-base long-range-ordered (LRO) alloy to gain some commercial experience with this class of developmental alloy. The activity will provide material for irradiation, mechanical property, compatibility, and other property tests to evaluate the potential of the alloy class for use in fusion energy systems.

6.1.3 Sumnary

Semiproduction scaleup of the iron-base alloy LRO-37 has been successfully completed. Three ingots of the alloy were produced by a commercial source, hot forged to slab, then rolled to 3.3-, 1.6-, and 0.8-mm sheet stock. The high-purity material contained MC-type carbides, and $M_2(C,N)$-type carbides were observed in commercial-grade alloy.

6.1.4 Progress and Status

Long-range-ordered alloys of the system $(Fe,Ni)_3(V,Ti)$ have been developed on a laboratory scale at ORNL. These alloys have unique properties that make them attractive as structural materials for advanced energy systems. This alloy development program has reached the important phase of alloy scaleup.

Semiproduction scaleup of the alloy LRO-37 (Fe–39.4 Ni–22.4 W.43 Ti, wt %) has been completed at the facilities of High Technology Materials Division, Cabot Corporation. Three ingots, each weighing approximately 18 kg (40 lb), were produced by two different melt practices — vacuum induction melting plus electron beam remelting using high-purity materials (one ingot, LRO-37-HP), and vacuum induction melting plus electroslag remelting using commercial grade materials (two ingots, LRO-37-CG). The principal difference between the HP and CG ingots, other than melt practice, was the grade of vanadium melt stock. Very high-purity vanadium was used for making the HP alloy, and more economical, but lower purity, ferrovanadium was used for the CG alloy. Melt stock for the other additions was the same for all ingots. A small amount of cerium was added to the alloys to improve their high-temperature properties. The previously reported chemical analyses showed the composition of the ingots to be reasonably close to the alloy specification. Three-fourths of the ingot stock of each of the two alloy grades, HP and CG, was easily press forged from 102-mm-diam (4.0-in.) round to aooroximately 35-mm-thick (1.4-in.) slab at 1150°C. The unforged ingot stock will be retained for future studies.

The final stage of the program, production of sheet stock by hot and cold rolling of the forged slab, was Completed with no difficulty during the present reporting period. The forged slab was hot rolled to 6.35 mm (0.25 in.) in ten passes at a reduction in thickness of 15% per pass. Initial heating and all reheating was at 1100°C in an argon-atmosphere furnace. The material was reheated 15 min between passes and annealed at the rolling temperature for 20 min after the last pass.

Following sandblasting, pickling, and conditioning, the material was cold rolled to finish thicknesses of 3.3, 1.6, and 0.8 mm (0.131, 0.065, and 0.031 in.). Total reduction of 50% in thickness, using a schedule of 5 to 10% reduction per pass, was easily accomplished before intermediate annealing at 1100°C. The yield of sheet stock listed in Table 6.1.1 was received with approximately 50% cold work following the final in-process anneal.

Table 6.1.1. Sheet stock produced from semiproduction scaleup of alloy LRO-37 (Fe–39.4 Ni–22.4 W.43 Ti, wt %)

Thickness		Width		Length		Pieces	Total weight	
(mn)	(in.)	(mm)	(in.)	(mm)	(in.)		(kg)	(lb)
Alloy LRO-37-HP (high purity), Heat EB11581-2-1630								
3.3	0.131	165.1	6.5	609.6	24	1	2.7	6
1.6	0.065	165.1	6.5	558.8	22	2	2.7	6
0.8	0.031	152.4	6.0	584.2	23	1	1.4	3
0.8	0.031	165.1	6.5	762.0	30	1		
Alloy LRO-37-CG (commercial grade), Heat EB11681-2-0735								
3.3	0.131	165.1	6.5	558.8	22	2	7.7	17
3.3	0.131	165.1	6.5	660.4	26	1		
1.6	0.065	165.1	6.5	482.6	19	4	4.5	10
0.8	0.031	139.7	5.5	381.0	15	1	5.9	13
0.8	0.031	165.1	6.5	660.4	26	4		
0.8	0.031	139.7	5.5	787.4	31	1		
0.8	0.031	165.1	6.5	914.4	36	2		

The second phase found[2] in the microstructure of LRO-37-CG contains the following metal elements as determined by x-ray fluorescence analysis (in order of decreasing amounts): V, Ni, and Fe. The peak previously identified as Cr $K\alpha$ is now believed to be the V $K\beta$, and Cr is no longer believed to be part of the phase. Vacuum fusion analyses showed that the phase also contained (by weight percent) 0.043 H, 6.9 N, 2.3 O, and 4.45 C. Therefore, the second phase appears to be a vanadium-rich carbonitride with the general formula $M_2(C,N)$. This phase has not been observed in other $(Ni,Fe)_3V$ ordered alloys, where the carbon has been invariably tied up in the cubic MC-type carbide. The reason why $M_2(C,N)$ formed instead of MC in LRO-37-CG is not clear at the present time, but it is probably related to the higher impurity level of the CG feedstock. The $M_2(C,N)$ phase was not found in the "high-purity" LRO-37-HP ingot that was prepared by the same vendor.

6.1.5 Reference

1. T. K. Roche and C. T. Liu, "Status of Scale-up of an Iron-Base Long-Range-Ordered Alloy," pp. 321–26 in *ADIP Semiannu. Prog. Rep. Mar. 32, 2982,* DOE/ER-0045/8, U.S. DOE, Office of Fusion Energy.

2. T. K. Roche, D. N. Braski, and C. T. Liu, "Status of Scale-up of an Iron-Base Long-Range-Ordered Alloy," pp. 158–59 in *ADIP Semiannu. Prog. Rep. Sept. 30, 1982,* DOE/ER-0045/9, U.S. DOE, Office of Fusion Energy.

6.2 BEND DUCTILITY OF IRON-BASE LONG-RANGE-ORDERED ALLOYS AFTER IRRADIATION IN HIIR — D. N. Braski (Oak Ridge National Laboratory)

6.2.1 ADIP Task

ADIP Task I.B.16, Tensile Properties of Special and Innovative Materials

6.2.2 Objective

The objective of this research is to define the response of $(Fe,Ni)_3V$ long-range-ordered (LRO) alloys to neutron irradiation. The overall goal is to determine the potential use of this alloy class as a structural material for fusion energy systems.

5.2.3 Summary

Three iron-base LRO alloys with base composition $(Fe,Ni)_3V$ tested at 600°C exhibited intergranular fracture and reduced bend ductilities after irradiation to 10 dpa at 600°C in HIIR. The embrittlement extended to lower temperatures as the damage level increased. The weakness of the grain boundaries may be caused by the presence of helium, segregating elements, VC particles, or a combination of these factors.

6.2.4 Progress and Status

6.2.4.1 Experimental Procedure

Disks (3 mm diam × 0.25 mm thick) of the alloys LRO-16, -20, and -37 were irradiated in HFIR at 300, 400, 500, and 600°C. The alloy compositions and heat treatments used are given in Table 6.2.1. Irradiation was accomplished in the disk irradiation experiments HFIR-CTR-30, -31, and -32. Displacement damage levels of 10, 21, and 42 dpa were attained, with approximate helium generation levels of 1000, 2000, and 6000 at. ppm, respectively. Some of the disks were subsequently tested in bending at the irradiation temperatures, with the technique developed by HEDL.[1] In our bend test the ram speed was 0.51 mm/min (0.02 in./min). Other disks were examined by transmission electron microscopy, and the results of some of these examinations have been reported.[2]

Table 6.2.1. Long-range-ordered alloy cornpositions and heat treatments

Alloy	Composition (wt %)				Heat treatment
	Fe	Ni	V	Ti	
LRO-16	46.0	31.0	23.0		10 min at 1170°C, water quenched, aged at 640°C for 4 d, 600°C for 12 d, and 500°C for 6 d.
LRO-20	37.6	39.5	22.9		15 min at 1200°C, water quenched, aged at 650°C for 4 d, 600°C for 1 d, and 500°C for 2 d.
LRO-37	37.6	39.5	22.4	0.4	15 min at 1200°C, water quenched, aged at 650°C for 4 d, 600°C for 1 d, and 500°C for 2 d.

6.2.4.2 Results

Figure 6.2.1 shows a typical load-deflection curve for an LRO disk that did not fracture and was bent to the maximum for the disk bend rig (–0.5 mm). The initial portion of the curve can be approximated by a straight line and is analogous to the elastic portion of a tensile stress-strain curve. As bending continued the curve changed slope and produced the characteristic shape shown in the figure. Sharp deviations from this curve shape were indicative of crack initiation and propagation in the disk. The occurrence of such changes was used to calculate the bend deflection ω for a particular disk. The strain at fracture ϵ was then estimated by the approximation[1]

$$\epsilon = t\omega/(a^2 + \omega^2)$$

where t = disk thickness and a = disk radius.

The results of the postirradiation bend tests on the three alloys LRO-16, -20, and -37 are given in Fig. 6.2.2. Bend ductility is plotted as a function of damage level. All the disks irradiated to 10 dpa at 300 to 500°C and then tested at the irradiation temperature passed the bend test without failing, but all those irradiated and tested at 600°C fractured at strains less than 1.5%. Disks irradiated to 21 dpa failed after irradiation and testing at 500°C, and disks irradiated to 42 dpa failed for irradiation and test temperatures as low as 400°C. In all cases of failures, the bend ductility was less than 2%. Huang, Hamilton, and Wire showed that at low bend fracture strains the bend ductility very closely approximates the tensile ductility of the material.[1]

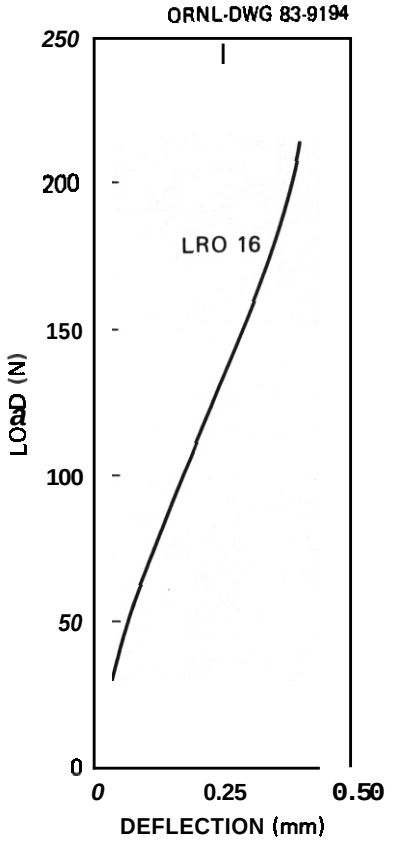

Fig. 6.2.1. Typical load-deflection curve for LRO disk that does not fracture during the test.

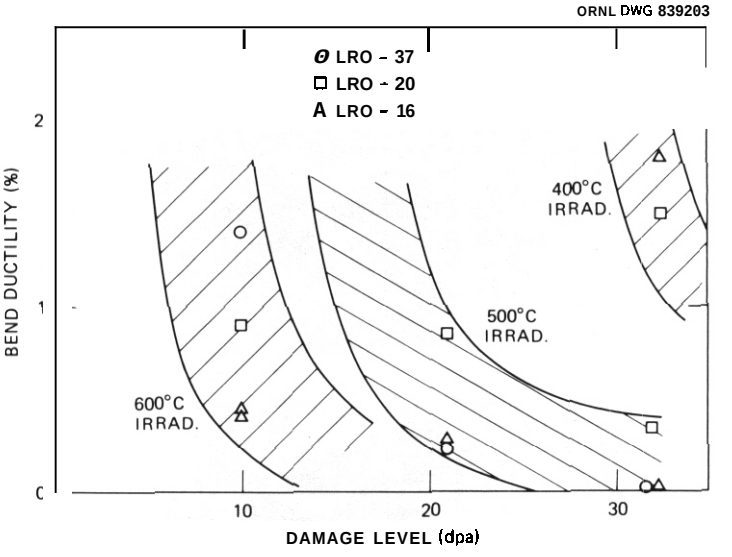

Fig. 6.2.2. Bend ductility of LRO disks after irradiation in HFIR shown as a function of damage level. The disks were tested at the irradiation temperatures.

Figures 6.2.3 through 6.2.5 show the load-deflection curves and the corresponding scanning electron micrographs for disks of each-alloy irradiated to 10 dpa at 600°C and tested at 600°C. In each case the disk fractured intergranularly after relatively little deflection. In one case (Fig. 6.2.3), the ram motion was continued after fracture to better expose the fracture surface. This fracture surface. of the LRO-16 disk. exhibited features that are believed to be associated with VC particles and also sigma phase in the grain boundaries. The other two alloys (Figs. 6.2.4 and 6.2.5) had fracture surfaces in which the exposed grain boundaries were very clean and smooth.

Examinations of the microstructures of the irradiated alloys showed that the grain boundaries contained a moderate number of helium bubbles, which could have a weakening effect.[2] Previous irradiation experiments with the LRO-16 alloy also indicated that sulfur and perhaps boron segregated in the grain houndaries.[3] Thus we suspect that elemental segregation also took place in the present HFIR irradiations and contributed to the weakness of the grain boundaries. Finally, recent transmission electron microscopy has shown that extensive precipitation of VC in the grain boundaries occurred for irradiation at 500°C to damage levels above 10 dpa. The precipitation was so extensive that the grain boundaries were completely lined with thin VC platelets, shown in the bright field–dark field pair in Fig. 6.2.6. In these cases, many tiny helium bubbles were also observed along the VC particleinatrix interface. It is not known whether the VC precipitation was induced or aided by the irradiation or caused by simple thermal aging.

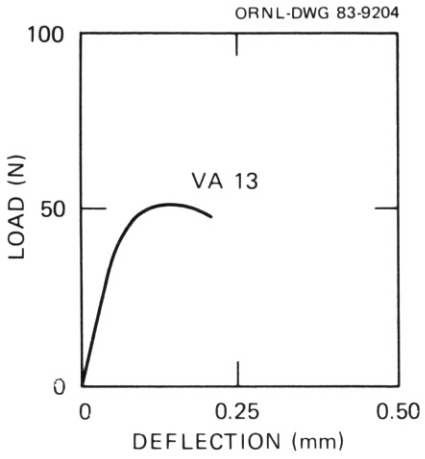

(a)

M-14983

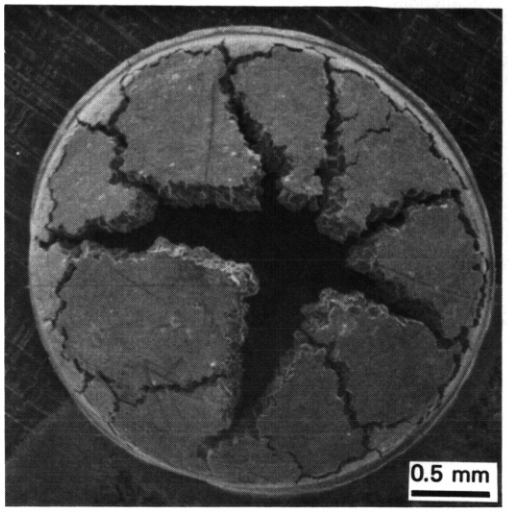

(b)

M-14987

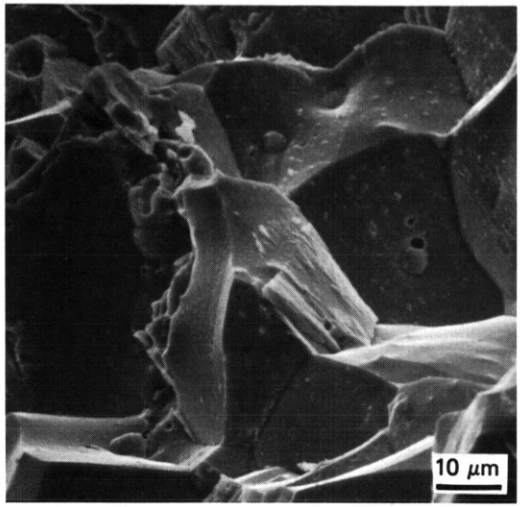

(c)

Fig. 6.2.3. (a) Load-deflection curve for LRO-16 disk irradiated in HFIR to 10 dpa at 600°C and bend tested at 600°C. (b) Low-magnification scanning electron micrograph of disk after testing. (c) Higher magnification micrograph showing intergranular fracture.

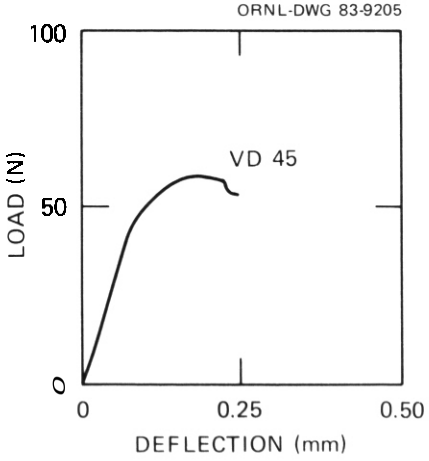

(a)

M-14998

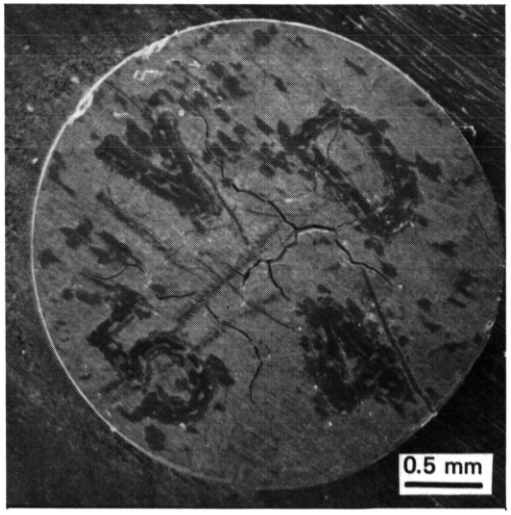

(b)

M-15002

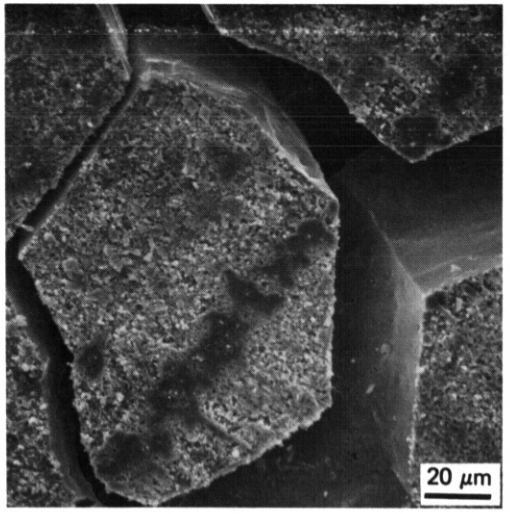

(c)

Fig. 6.2.4. (a) Load-deflection curve for LRO-20 disk irradiated in HFIR to 10 dpa at 600°C and bend tested at 600°C. (b) Low-magnification scanning electron micrograph of disk after testing. (c) Higher magnification micrograph showing intergranular fracture.

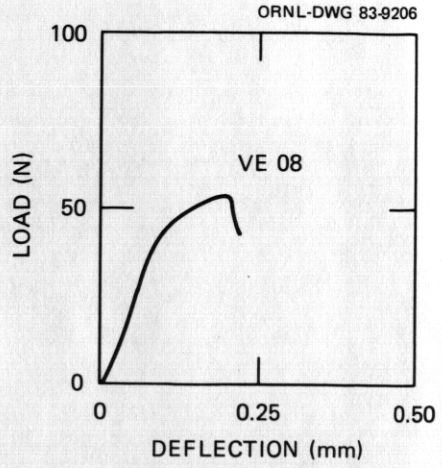

(a)

M-14990

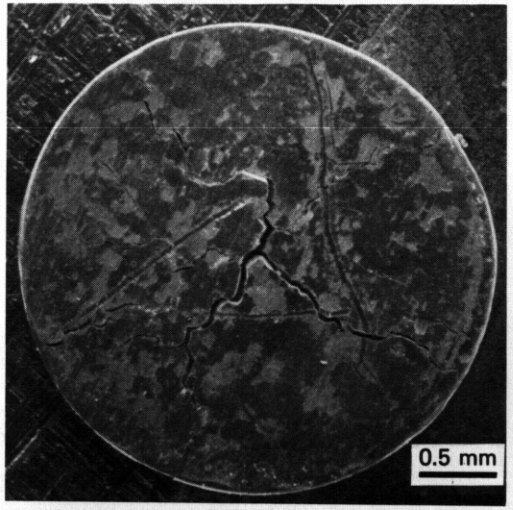

(b)

M-14992

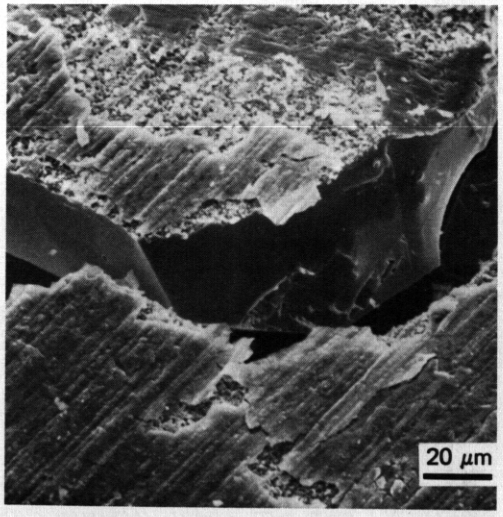

(c)

Fig. 6.2.5. (*a*) Load-deflection curve for LRO-37 disk irradiated in HFIR to 10 dpa at 600°C and bend tested at 600°C. (*b*) Low-magnification scanning electron micrograph of disk after testing. (*c*) Higher magnification micrograph showing intergranular fracture.

H-73761

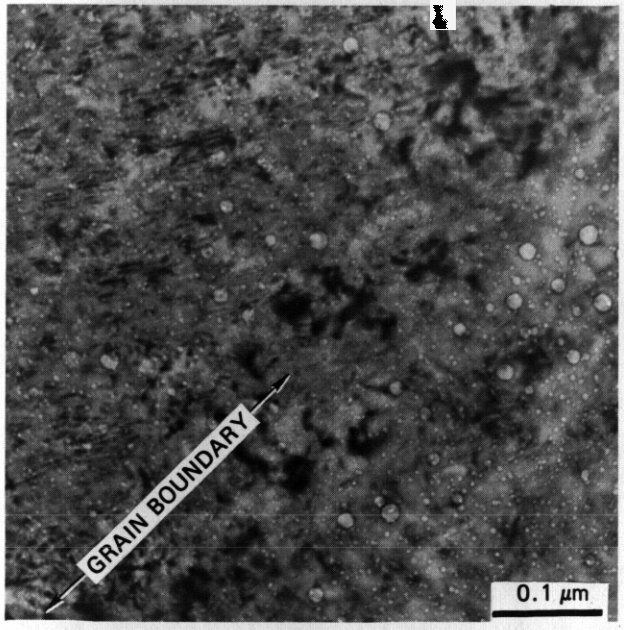

(a)

H-73760

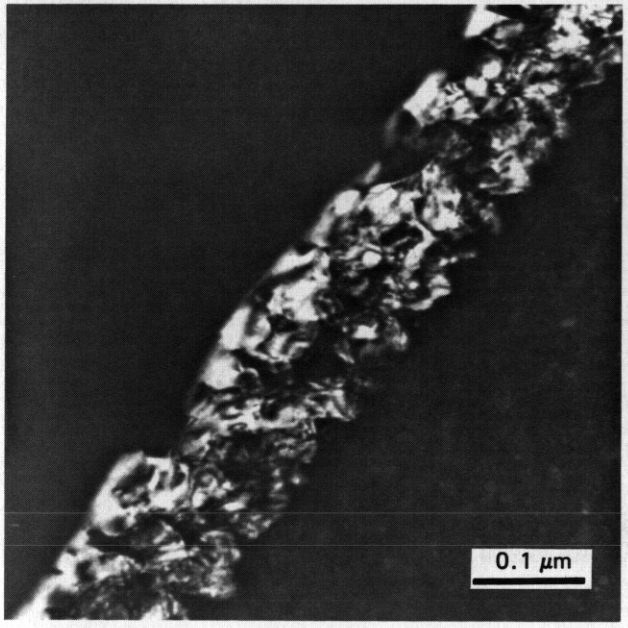

(b)

Fig. 6.2.6. (*a*) Bright field and (*b*) dark-field transmission electron micrographs using a precipitate reflection to show continuous layer of thin VC platelets in high-angle grain boundary. The LRO-37 disk had been irradiated to 21 dpa in HFIR at 500°C.

6.2.5 Conclusions and Future Work

1. After a 10-dpa irradiation in HFIR at 600°C, disks of the iron-base LRO alloys LRO-16, -20, and -37 all failed the bend tests at 600°C and exhibited bend ductilities less than 1.5%. At higher damage levels LRO disks also failed for irradiation and test temperatures below 600°C, indicating that the embrittlement was becoming more extensive.
2. All three LRO alloys fractured intergranularly.
3. The weakness of the grain boundaries may be caused by the presence of helium, segregating elements such as sulfur, VC particles, or a combination of these factors.

Future work on the LRO alloys will attempt to establish the relative importance of the several factors (i.e., helium, segregation, VC) that possibly contribute to the grain boundary embrittlement. Once this is known, compositional and/or microstructural adjustments of the alloy can be investigated for possible improvement of ductility after irradiation.

6.2.6 References

1. F. H Huang, M L. Hamilton, and G. L. Wire, "Bend Testing for Miniature Disks," *Nuct. Technol.* 57(2), 234–42 (May 1982).
2. D. N Braski, "Microstructures of Iron-Ease Long-Range-Ordered Alloys Irradiated to 10 dpa in HFIR," pp. 327–33 in *ADIP Semiannu. Prog. Rep. Mar. 31, 1982,* DOE/ER-0045/8, U.S. DOE, Office of Fusion Energy.
3. O. N Braski, "Microstructure and Tensile Properties of Neutron-Irradiated $(Fe_{0.61}Ni_{0.39})_3V$ Ordered Alloy," pp. 325–40 in *Effects of Radiation a Materials,* proceedings of the Eleventh International Symposium, Scottsdale, Arizona, June 28–30, 1982, ed. H. R. Brager and J. S. Perrin, ASTM STP 782, American Society for Testing and Materials, Philadelphia, 1982.

7. PATH E ALLOY DEVELOPMENT — FERRITIC STEELS

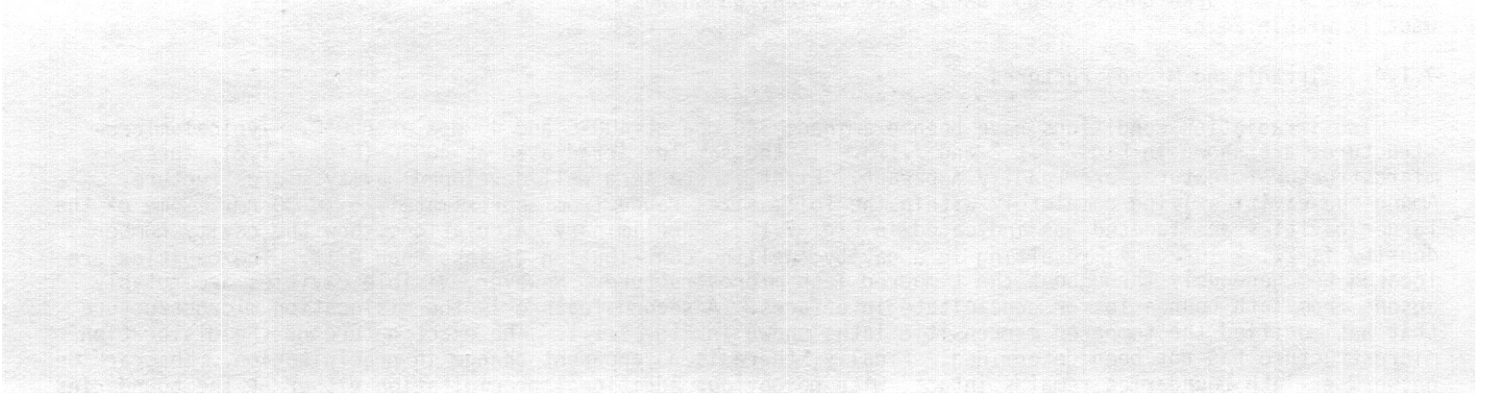

7.1 PRELIMINARY TRANSMISSION ELECTRON MICROSCOPY OF 12 Cr-1 MoVW IRRADIATED TO 40 dpa IN HFIR — J. M. Vitek and R. L. Klueh (Oak Ridge National Laboratory)

7.1.1 ADIP Task

ADIP Tasks are not defined for Path E, Ferritic Steels, in the 1978 program plan.

7.1.2 Objective

The objective of this work is to evaluate the microstructural response of 12 Cr-1 MoVW steels to HFIR irradiation. Since a transmutation reaction of nickel produces helium, the effect of helium and displacement damage on the microstructure can be ascertained.

7.1.3 Summary

Specimens of 12 Cr-1 MoVW steel were irradiated in HFIR to 40 dpa at 400 and 600°C. Preliminary microstructural examination indicates significant cavity formation in this steel, and this is attributed in part to the helium produced during irradiation.

7.1.4 Progress and Status

7.1.4.1 Introduction

Disks of 12 Cr-1 MoVW steel were included in the irradiation experiments HFIR-CTR-30, -31, and -32 (ref. 1). These experiments were conducted at 300, 400, 500, and 600°C to displacement damage levels (at the capsule midplane) of 40, 20, and 10 dpa.

During HFIR irradiation nickel undergoes a transmutation reaction that results in helium production. Thus, helium is generated along with displacement damage during irradiation. By including alloys with different nickel concentrations, the effect of helium on the irradiated microstructure can be ascertained. Therefore, a series of nickel-doped ferritic steels[2] were included in the HFIR-CTR-30, -31, and -32 experiments. This report presents early results on the undoped 12 Cr-1 MoVW alloy irradiated to produce 40 dpa and approximately 85 at. ppm He.

7.1.4.2 Specimen Preparation

The 12 Cr-1 MoVW alloy is from a Combustion Engineering heat, XAA-3587. The alloy chemistry is given in Table 7.1.1. The disks were irradiated in the normalized-and-tempered condition, produced by the following heat treatment: 1050°C/0.5 h/air cool + 780°C/2.5 h/air cool. This heat treatment resulted in a tempered lath martensite structure. The recovered lath martensite network has chromium-rich $M_{23}C_6$ located preferentially at lath boundaries and prior-austenite grain boundaries. In addition, the structure contains some finer vanadium-rich precipitates. The normalized-and-tempered microstructure has been described in detail elsewhere,[2,3] and a typical microstructure is shown in Fig. 7.1.1.

The irradiated samples were electropolished in a hot cell twin-jet electropolisher. A 7:1 solution of methanol and sulfuric acid was

Table 7.1.1. Composition of 12 Cr-1 MoVW heat XAA-3587

Element	Content (wt %)	Element	Content (wt %)
Cr	11.99	W	0.54
Mo	0.93	Nb	0.018
Ni	0.43	C	0.21
V	0.27	N	0.020
Mn	0.50	Si	0.18

ORNL-PHOTO 6105-81

Fig. 7.1.1. Typical normalized-and-tempered microstructure of unirradiated 12 Cr-1 MoVW.

E-39592

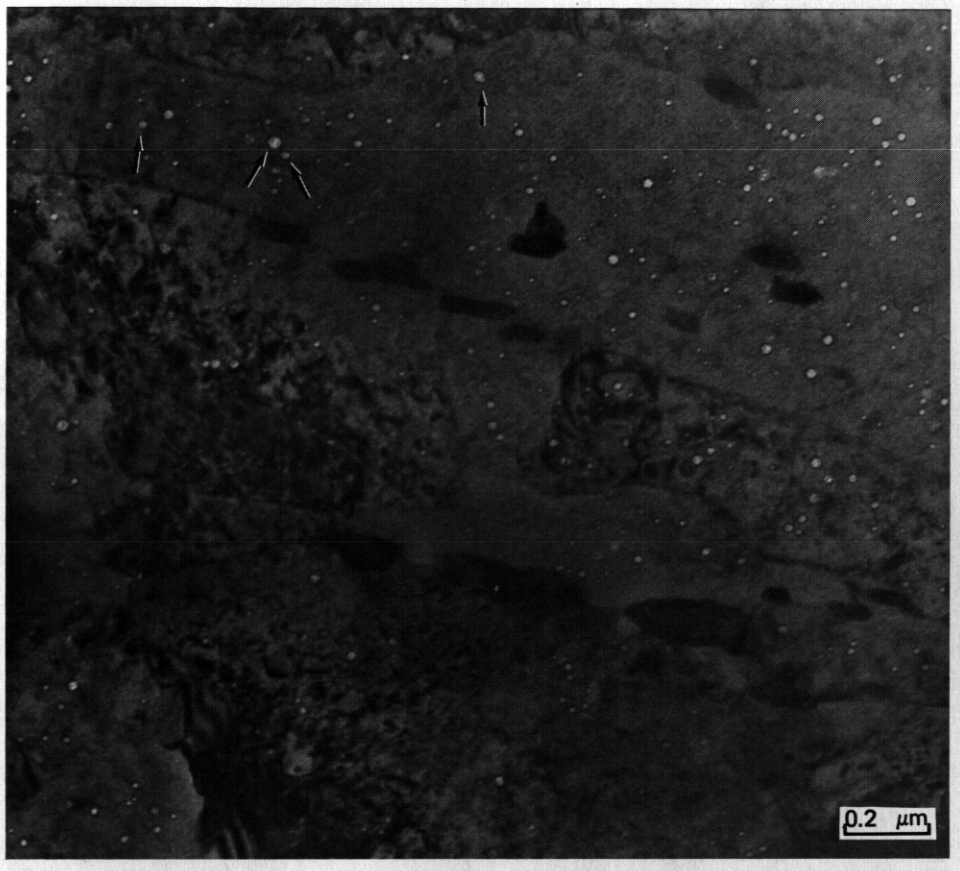

Fig. 7.1.2. Microstructure of 12 Cr-1 MoVW irradiated in HFIR to produce 40 dpa at 400°C. Arrows identify a few of the faceted cavities.

[redacted]

E-41561

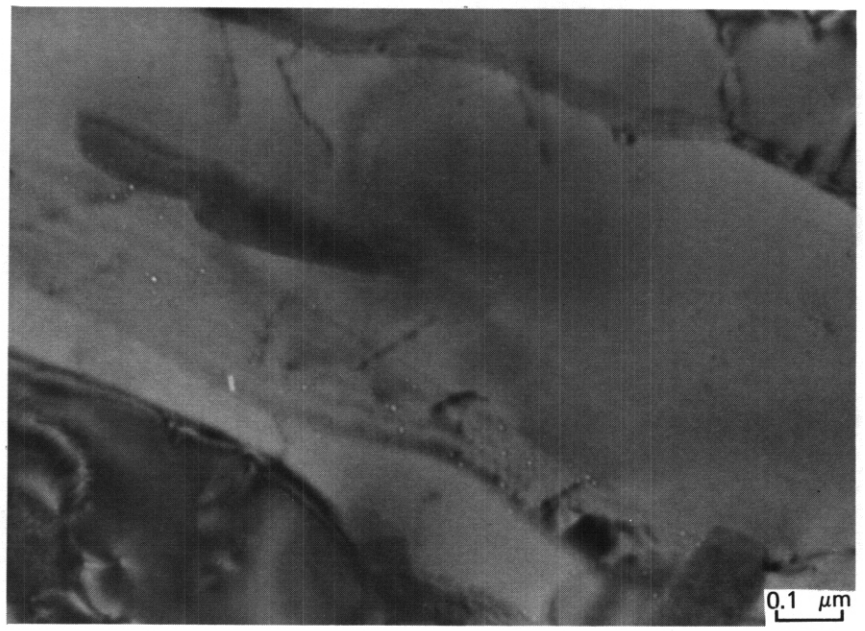

(a)

E-41563

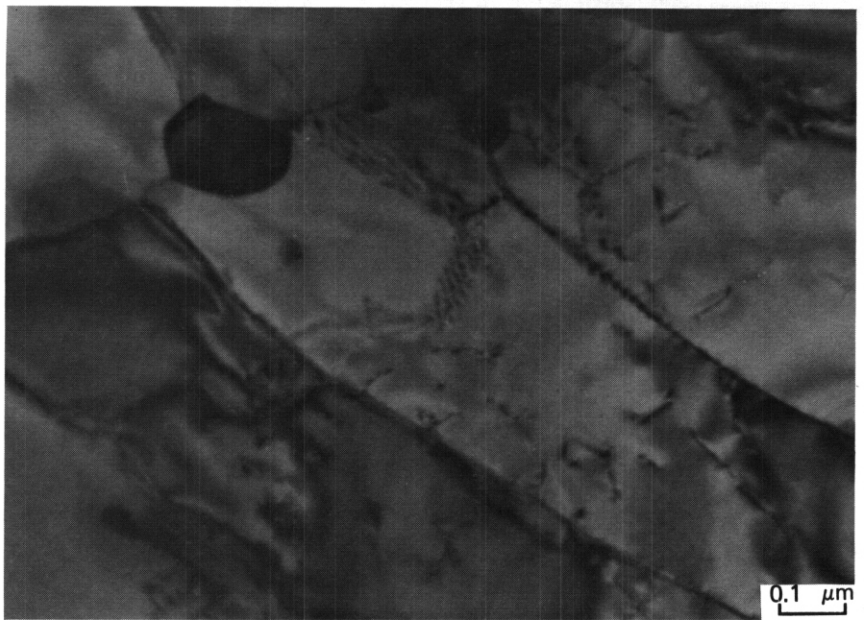

(b)

Fig. 7.1.3. *(a)* **Cavity microstructure of 12 Cr-1 MoVW irradiated in HFIR to 40 dpa at 600°C.** *(b)* **Essentially dislocation-free microstructure in the same sample.**

As found after irradiation at 400°C, cavities are absent from precipitate interfaces. The cavities observed ranged in size from 3 to 9 nm, a considerably smaller range than found after the 400°C irradiation. Further work is currently in progress to determine the cavity size distribution, the cavity concentration, and the corresponding volume swelling contribution. Also, in contrast to results of the 400°C irradiation, the tempered martensite structure remained intact with little change in the lath substructure [Fig. 7.1.3(*b*)]. Finally, there was no obvious additional precipitation during irradiation. The large carbides at lath boundaries have remained in place, and no additional precipitation was observed. Positive identification of precipitates by examination of carbon extraction replicas is forthcoming.

7.1.5 Discussion

An extensive discussion of the results is premature because the results presented are limited and preliminary. However, a few interesting features are noteworthy and are in contrast with the results of reported work on fast-spectrum neutron-irradiated ferritic steels.

The greatest difference found is the cavity distribution observed in the HFIR-irradiated specimens. Previous results on similar steels irradiated over the temperature range 400 to 615°C to fluences producing up to 30 dpa have shown no homogeneous distribution of cavities and no swelling.[4-6] These irradiations were in fast reactors, where much lower helium production results. Studies on other ferritic alloys in which a limited number of cavities were produced by fast reactor irradiation showed cavities only at irradiation temperatures of 450°C and lower.[6,7] These latter studies included work on 9 Cr-1 MoVNb and 2 1/4 Cr-1 Mo steels. Density measurements also showed no swelling above 450°C (ref. 8). In contrast, we have observed cavities at both 400 and 600°C. Thus the preliminary results presented here seem to show an influence of simultaneous helium production on the irradiated cavity microstructure. However, the higher fluences of this work could also be a contributing factor.

As for precipitation reactions that may occur during irradiation, no evidence of large precipitate particles was found. This contrasts with chi, sigma,[5] and G phase[6] precipitation reported for fast-reactor irradiation. However, the possibility of a fine distribution of precipitates cannot be discounted, and ongoing work should clarify this point.

7.1.6 Future Work

Future analysis will complete the matrix on 12 Cr-1 MoVW steel irradiated to *10,* 20, and 40 dpa at temperatures from 300 to 600°C. The studies will quantify the microstructural observations including cavity size distributions, concentration, and swelling. Extraction replica examination will provide more information on the precipitation response of the alloys. Following work on the 12 Cr-1 MoVW alloys, a similar study will be undertaken to evaluate the microstructures of HFIR-irradiated 9 Cr-1 MoVNb.

7.1.7. References

1. M. L. Grossbeck. J. W. Woods. and G. A. Potter. "Experiments HFIR-CTR-30, -31, and -32 for Irradiation of Transmission Electron Microscopy Disk Specimens," pp. 36–44 in *ADIP Quart. Prog. Rep. Sept. 30, 1980*, DOE/ER-0045/4, U.S. DOE, Office of Fusion Energy.

2. R. L. Klueh and J. M. Vitek. "Characterization of Ferritic Steels for HFIR Irradiation." pp. 294–308 in *ADIP Quart. Prog. Rep. June 30, 1980,* DOE/ER-0045/3, U.S. DOE, Office of Fusion Energy.

3. J. M. Vitek and R. L. Klueh, "Effect of Heat Treatment Variations on 9 Cr-1 MoVNb and 12 Cr-1 MoVW Ferritic Steels," pp. 263–74 in *ADIP Semiannu. Prog. Rep. Sept. 30, 1981*, DOE/ER-0045/7, U.S. DOE, Office of Fusion Energy.

4. E. A Little and D. A. Stow, "Void-Swelling in Irons and Ferritic Steels. II. An Experimental Survey of Materials Irradiated in a Fast Reactor," *J. Nuct. Mater.* 87, 25-39 (1979).

5. E. A. Little and L. P. Stoter. "Microstructural Stability of Fast Reactor Irradiated 10–12% Cr Ferritic-Martensitic Stainless Steels,' pp. 207–33 in *Effects of Radiation on Materials*, ed. H. R. Brager and J. S. Perrin, ASTM-STP 782, American Society for Testing and Materials, Philadelphia, 1982.

6. D. S. Gelles and L. E. Thomas, "Microstructural Examination of HT-9 and 9 Cr-1 Mo Contained in the AD-2 Experiment," pp. 343–61 in *ADIP Semiannu. Prog. Rep. Mar. 31, 1982*, DOE/ER-0045/8, U.S. DOE, Office of Fusion Energy.

7. D. S. Gelles, "Microstructural Examination of a Series of Commercial Ferritic Alloys Irradiated to Very High Fluence," pp. 187–211 in *ADIP Quart. Prog. Rep. Dec. 31, 1980,* DOE/ER-0045/5, U.S. DOE, Office of Fusion Energy.

8. M. K. Zimmerschied, D. T. Peterson, R. W. Powell, and J. F. Bates, "Immersion Density Analysis of Commercial Alloys Irradiated to Very High Fluence," pp. 226–34 in *ADIP Quart. Prog. Rep. Dec. 31, 1980*, DOE/ER-0045/5, U.S. DOE, Office of Fusion Energy.

7.2 ELEVATED-TEMPERATURE TENSILE PROPERTIES OF 12 Cr-1 MoVW STEEL IRRADIATED IN THE EBR-II, AD-2 EXPERIMENT

— R. L. Klueh and J. M. Vitek (Oak Ridge National Laboratory)

7.2.1 ADIP Task

ADIP Tasks are not defined for Path E, Ferritic Steels, in the 1978 program plan.

7.2.2 Objective

The goal of this project is to measure the tensile properties of 12 Cr-1 MoVW steels irradiated at elevated temperatures in EBR-II. In the future, the results from this work will be compared with elevated-temperature irradiations of this steel in HFIR, where much more helium is produced in irradiations to the same dpa level.

7.2.3 *Summary*

The effect of irradiation on the tensile properties of 12 Cr-1 MoVW steel in two normalized-and-tempered conditions was determined for specimens irradiated in EBR-II at 390 to 550°C. Tests were conducted at room temperature and at the irradiation temperature. Irradiation to approximately 11 dpa increased the ultimate tensile strength for each irradiation temperature; an increased yield stress was noted only at the lowest temperature.

7.2.4 Progress and Status

The tensile specimens described in this report were irradiated in EBR-II as part of the large AD-2 experiment conducted by HEDL.[1] The experiment includes 12 Cr-1 MoVW, 9 Cr-1 MoVNb, and 2 1/4 Cr-1 Mo steels, with specimens for the determination of tensile properties, impact properties, fracture toughness, fatigue, and crack growth. Disks of each material are also included to determine microstructural effects of irradiation.

7.2.4.1 Experimental Procedure

The 12 Cr-1 MoVW steel used in this experiment was obtained from the Carpenter Technology Corporation and had the composition of the commercial Sandvik alloy, HT9. The vendor-certified chemical composition and the HEDL overchecks for heat 91354 are given in Table 7.2.1. The steel was obtained as 33.3-mm-diam bar that had been hot and cold rolled to 0.76-mm sheet, from which the tensile specimens were fabricated.

Two different heat treatments were used to produce normalized-and-tempered microstructures: The first, referred to as HT-1, was 0.07 h (4 min) at 1038°C, air cooled, then tempered 0.5 h at 760°C; the second, hereafter referred to as HT-2, was 0.5 h at 1038°C, air cooled, then tempered 2.5 h at 760°C. These heat treatments resulted in prior austenite grain sizes of ASTM 7 and 5 for HT-1 and HT-2, respectively.

Table 7.2.1. Chemical composition of 12 Cr-1 MoVW steel (heat 91354)

Element	Composition (wt %)		Element	Composition (wt %)	
	Carpenter Technology	HEDL overcheck		Carpenter Technology	HEDL overcheck
C	0.21	0.20	co	0.01	
Mn	0.50	0.39	cu	0.04	0.07
P	0.008		Al	0.034	
S	0.003		B	0.0007	
Si	0.21	0.14	As	<0.005	
Ni	0.58	0.49	N	0.004	
Cr	12.11	12.39	Ta	<0.01	
Mo	1.03	0.99	W	0.53	
V	0.33	0.45	Fe	Balance	Balance
Ti	0.002				

Sheet tensile specimens in this experiment were of an SS-1 type, with a reduced gage section 20.3 mm long by 1.52 mm wide by 0.76 mm thick (Fig. 7.2.1). The specimen design was in accordance with ASTM Specification E 8. All specimens were machined with their gage lengths perpendicular to the rolling direction of the sheet.

Specimens were irradiated in capsules designed to maintain temperatures of 390, 450, 500, and 550°C. Irradiation was in row 4 of EBR-II to a fluence of 2.3–2.5 × 10^{26} neutrons/m^2 ($E > 0.1$ MeV), which produced approximately 11 dpa in the steel.

After irradiation, tensile tests were conducted at room temperature and at the irradiation temperature. As-heat-treated and thermally aged samples were also tested to separate the effect of irradiation from thermal aging effects. Thermal aging was at the irradiation temperatures for 5000 h — the approximate time of the irradiation. The tensile tests were conducted in a vacuum chamber on a 44-kN-capacity Instron universal testing machine at a crosshead speed of 8.5 μm/s, which results in a nominal strain rate of 4.2 × 10^{-4}/s.

ORNL-DWG 78-7701R1

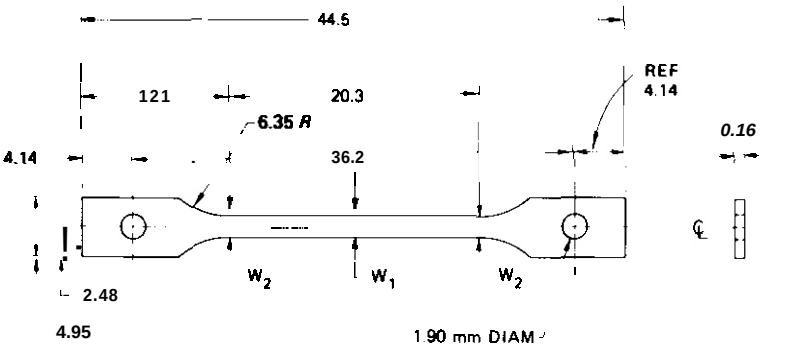

Fig. 7.2.1. The SS-1 tensile specimen.

7.2.4.2 Results

The tensile results for the unirradiated and irradiated 12 Cr-1 MoVW steel are given in Tables 7.2.2 and 7.2.3. In Figs. 7.2.2–7.2.4, the tensile properties of the irradiated steels tested at the irradiation temperatures are compared with unirradiated specimens tested at the same temperatures. Figures 7.2.5 and 7.2.6 show tensile properties determined in room-temperature tests plotted against irradiation temperature.

The tensile properties of the steel in the unirradiated condition show a definite effect of heat treatment. The specimens with HT-1 had a considerably higher 0.2%-offset yield stress (YS) (Fig. 7.2.2) and ultimate tensile strength (UTS) (Fig. 7.2.3) at a given temperature than HT-2, although the differences in ductility were relatively minor (Fig. 7.2.4).

When the irradiated results for the tests at the irradiation temperatures are considered (Figs. 7.2.2–7.2.4), it is seen that irradiation at 390°C increased the YS and UTS for both heat treatments. The relative increase for HT-1 was somewhat larger than that for HT-2. A slight decrease in ductility accompanied the increase in strength.

Table 7.2.2. Tensile properties of unirradiated 12 Cr-1 MoVW steel

Test temperature (°C)	Strength (MPa)		Elongation (%)	
	Yield	Ultimate	Uniform	Total
HT-1 (0.07 h/1038°C/air cooled+0.5 h/760°C)				
22	693	862	4.6	5.8
200	670	852	5.7	8.6
400	641	786	2.9	5.6
450	586	722	3.9	6.3
500	532	645	3.9	8.2
550	471	550	2.5	12.5
HT-2 (0.05 h/1038°C/air cooled+2.5 h/760°C)				
22	636	805	6.8	10.2
400	548	677	3.5	6.1
450	503	623	4.0	6.7
500	499	598	4.6	10.9
550	423	486	2.4	9.8

Table 7.2.3. Tensile properties of irradiated 12 Cr-1 MoVW steel. Irradiation in ERR-11. row 4, in the AD-2 experiment to a fluence producing approximately 11 dpa.

Temperature (°C)		Strength (MPa)		Elongation (%)	
Test	Irradiation	Yield	Ultimate	Uniform	Total
HT-1 (0.07 h/1038°C/air cooled+0.5 h/760°C)					
22	390	1017	1081	3.0	5.2
400	390	872	916	1.3	3.4
22	450	651	842	7.5	9.8
450	450	599	74s	3.9	6.6
22	500	670	862	6.3	9.5
500	500	543	705	3.3	5.9
22	550	622	R17	6.3	8.9
550	550	474	521	3.3	12.2
HT-2 (0.05 h/1038°C/air cooled+2.5 h/760°C)					
22	390	795	931	6.4	9.4
400	390	673	745	2.5	4.8
22	450	735	874	7.5	10.8
450	450	515	644	5.1	8.9
22	500	578	756	6.6	10.0
500	500	509	646	3.8	6.9
22	550	562	769	7.2	10.0
550	550	434	529	3.6	12.9

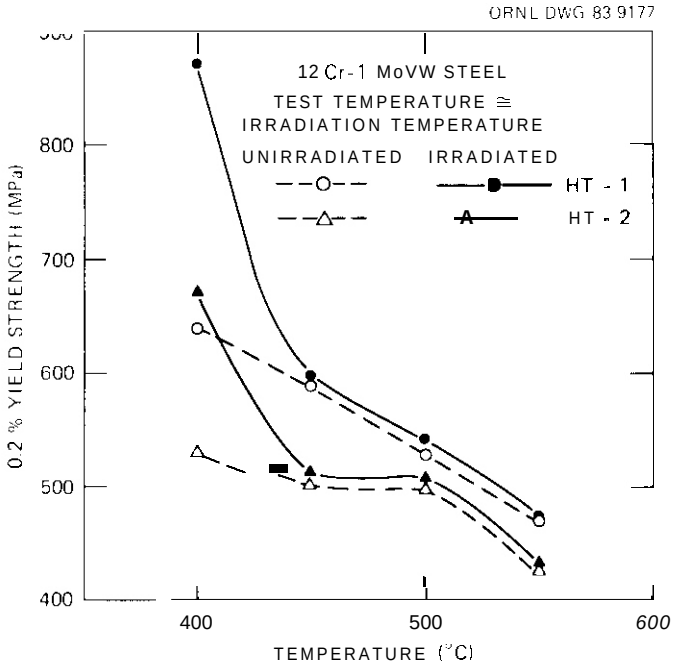

Fig. 7.2.2. The 0.2% yield stress plotted against test temperature (approximate irradiation temperature) for unirradiated and irradiated 12 Cr-1 MoVW steel in two heat-treated conditions. Irradiation in EBR-II experiment AD-2 to 11 dpa.

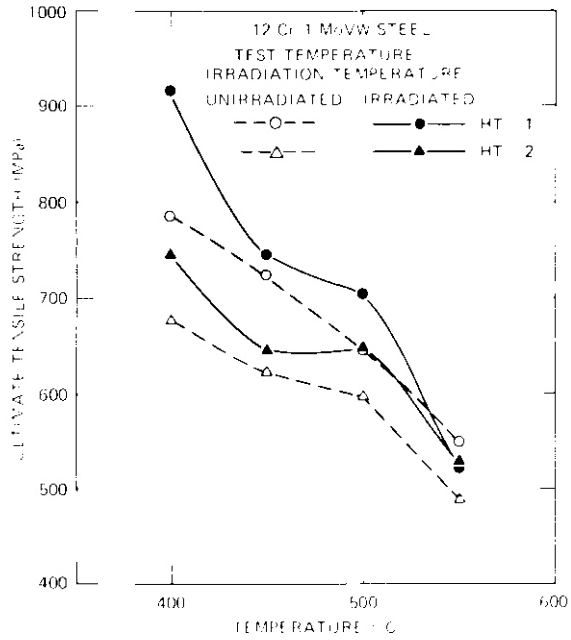

Fig. 7.2.3. The ultimate tensile strength plotted against test temperature (approximate irradiation temperature) for unirradiated and irradiated 12 Cr-1 MoVW steel in two heat-treated conditions.

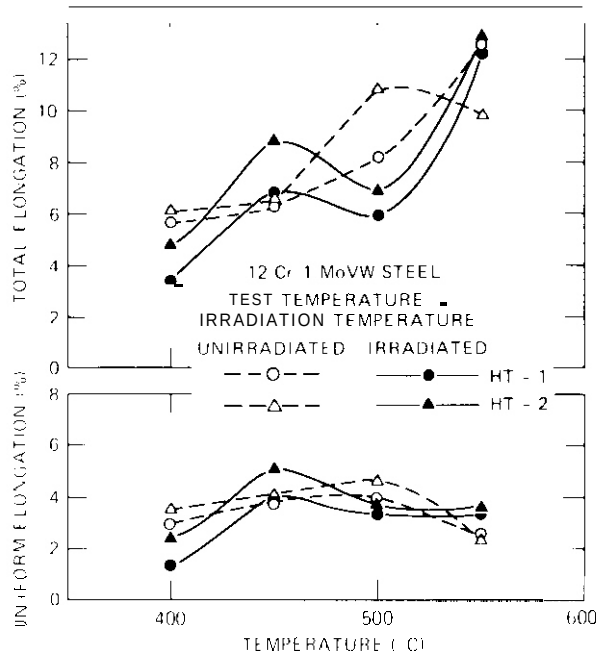

Fig. 7.2.4. The uniform and total elongation plotted against test temperature (approximate irradiation temperature) for unirradiated and irradiated 12 Cr-1 MoVW steel in two heat-treated conditions.

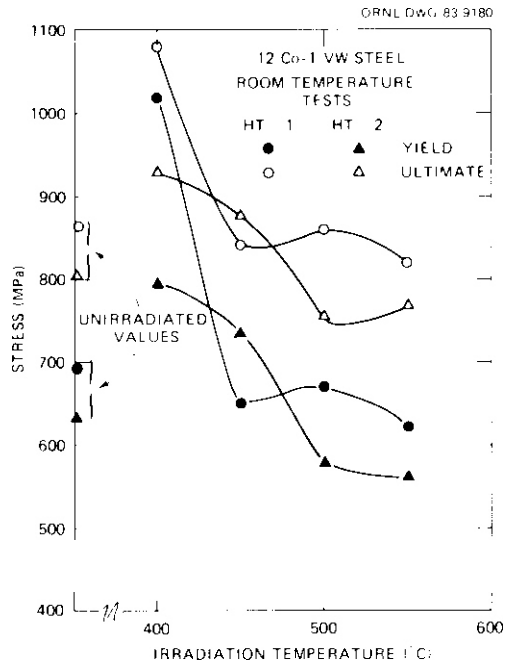

Fig. 7.2.5. The 0.2% yield stress and ultimate tensile strength plotted against irradiation temperature for unirradiated and irradiated 12 Cr-1 MoVW steel in two heat-treated conditions. All tests at room temperature. Irradiation to 11 dpa in the AD-2 experiment.

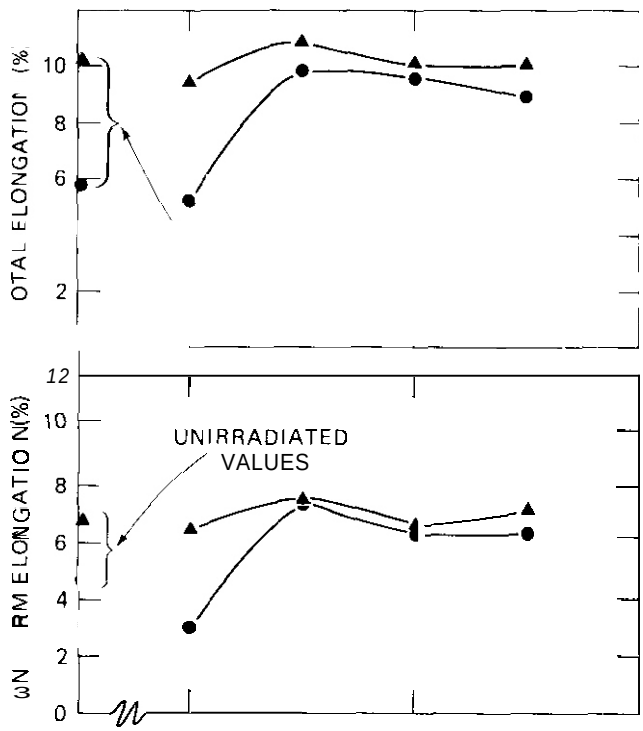

steel at 550°C.

There is very little difference in uniform or total elongation between unirradiated and irradiated steel, regardless of heat treatment (Fig. 7.2.4). The greatest difference between irradiated and unirradiated steels occurs at 400°C, the lowest test temperature, where the total elongation of HT-1 is only a little more than 3%, and at 500°C, where the total elongation of the irradiated steel goes through a local minimum. Ductility increases with temperature, and total elongation of the irradiated steels at 550°C exceeds 12%.

When the results of the room-temperature

1. R. J. Puigh and N. F. Panayotou, "Specimen Preparation and Loading for AD-2 Ferritics Experiment," pp. 260–93 in *ADIP Quart. Frog. Rep. June* 30, 1980, DOE/ER-0045/3, U.S. DOE, Office of Fusion Energy.

7.3 FATIGUE CRACK GROWTH IN PATH E ALLOYS - A. M. Ermi (Westinghouse Hanford Company)

7.3.1 ADIP Task

The Department of Energy (DOE)/Office of Fusion Energy (OFE) has cited the need for these data under the ADIP Program Task, Ferritic Steels Development (Path E).

7.3.2 Objective

The objective of this study is to provide fatigue crack growth data on candidate ferritic alloys and to establish a base for the evaluation of the effects of irradiation on fatigue crack growth.

7.3.3 *Summary*

Fatigue crack growth tests on unirradiated HT-9, HT-9 weldments and 9Cr-1Mo have been conducted in helium at temperatures up to 550°C and at cyclic frequencies of 6.67 and 0.667 s^{-1}. Little differences in crack growth behavior between the three materials were observed at any single condition. However, higher crack growth rates were evident at the lower stress intensity factors at 0.667 s^{-1} on specimens tested at 300°C compared to 550°C. No effect of irradiation was observed on HT-9 irradiated to 13 dpa at 550°C and tested at 550°C at 6.67 s^{-1}.

7.3.4 Progress and Status

7.3.4.1 Introduction

The fatigue crack growth behavior of materials being considered for fusion reactor first wall application must be characterized in order to evaluate the integrity of potentially flawed structures. This study investigates the crack growth behavior of two ferritic alloys, HT-9 and 9Cr-1Mo, and of one ferritic weldment, HT-9, in order to provide baseline information from which effects of more hostile environments can be determined.

7.3.4.2 Materials and Experimental Procedures

The chemical compositions and complete thermal-mechanical processing for the materials were described previously in the report detailing specimen preparation for the ferritics AD-2 experiment in EBR-II.[1] The final thermal-mechanical treatments are repeated in Table 7.3.1. (NOTE: Four room temperature tests on Hi-9 were conducted on a different heat of material and *used* slightly different final heat treatments.[2])

Table 7.3.1. Final Thermal-Mechanical Processing of Ferritic Materials

Material	Processing
HT-9 (Ht. 91354):	40% CW to 0.610 mm (0.024"); 1038°C/4 min./AC + 760°C/30 min./AC
9Cr-1Mo (Ht. 30182):	77% CW to 0.635 mm (0.024"); 1038°C/1 hr./AC + 760°C/1 hr./AC
HT-9 Weldrnent:	6.35 mm (0.250") HT-9 (Ht. 91353) base metal; 1050°C/30 min./AC + 760°C/2.5 hr./AC; 93°C Preheat, Gas-lungsten Arc Welded Between 93°C-143°C; Post-Weld Temper: 780°C/1 hr.; Machined to 0.813 mm (0.032")

Miniature center-cracked-tension specimens were used for the fatigue testing.[3] The stress cycling was accomplished using feedback-controlled servo-hydraulic miniature fatigue machines operated in load control.[4] A sinusoidal waveform with a stress ratio (minimum load/maximum load) of 0.05 was used for all tests. Cyclic frequencies of 6.67 and 0.667 s^{-1} (400 and 40 cpm) were used, except for some room temperature tests where 15.0 s^{-1} was used.

Tests were conducted at 25, 300, 390, 450, 500 and 550°C. The latter four temperatures were chosen to match those of the AD-2 irradiations. The elevated temperature tests were conducted in flowing, high purity helium (99.99%) with <0.01% oxygen. The temperatures of the furnaces were controlled to ±1.5°C. The test parameters of all of the specimens in this study are listed in Table 7.3.2.

The crack lenqths were monitored continuously durinq the stress cycling by using an electrical potential technique,[5] and this information along with the cycle counts and temperatures were automatically recorded by computer. Fatigue crack growth rates (da/dN) were calculated using the secant method,[6] and the corresponding stress intensity factor ranges (ΔK) were calculated using:[7]

Table 7.3.2. Fatigue Crack Growth Test Parameters

Material	Spec. No.	Freq. (s^{-1})	Temp. (°C)	Maximum Load (N)	Maximum Load (lbs.)
HT-9 (0.610 mm)	Ea01	15.0	25	2113	475
	Ea02	15.0	25	2113	475
	Ea03	15.0	25	2113	475
	Ea04	15.0	25	2113	475
	Ea25	6.67	300	1779	400
	Ea32	6.67	300	1557	350
	Ea38	6.67	390	1890	425
	Ea41	6.67	390	1904	428
	Ea34	6.67	450	2211	497
	Ea35	6.67	450	1890	425
	Ea36	6.67	450	1890	425
	Ea37	6.67	500	1890	425
	Ea40	6.67	500	1890	425
	Ea29	6.67	550	1557	350
	Ea31	6.67	550	1557	350
	Ea66*	6.67	550	2046	460
	Ea26	0.667	300	1779	400
	Ea28	0.667	300	1557	350
	Ea81	0.667	300	1890	425
	Ea30	0.667	450	2202	495
	Ea33	0.667	450	2202	495
	Ea80	0.667	450	2891	650
	Ea24	0.667	550	1668	375
	Ea42	0.667	550	2335	525
9Cr-1Mo (0.635 mm)	Eb20	6.67	300	2113	475
	Eb25	6.67	300	2002	450
	Eb27	6.67	550	2002	450
	Eb28	6.67	550	2113	475
	Eb21	0.667	300	2122	477
	Eb24	0.667	300	2002	450
	Eb18	0.667	550	2576	579
	Eb31	0.667	550	2366	532
HT-9 Weldment (0.813 mm)	Ec14	6.67	75	2447	550
	Ec07	6.67	300	2558	575
	Ec08	6.67	300	2558	575
	Ec04	6.67	390	2598	584
	Ec05	6.67	390	2558	515
	Ec03	6.67	550	2558	575
	Ec12	6.67	550	2558	575
	Ec09	0.667	300	2669	600
	Ec10	0.667	300	2669	600
	Ec02	0.667	550	3114	700
	Ec13	0.667	550	3114	700

R = Min. load/max. load = 0.05.
Waveform = Sinusoidal.

Environment = Helium (except 25°C).
*Irrad. at 550°C to 13 dpa.

$$\Delta K = (1-R)(P\sqrt{\pi a}/Wt)[\sec(\pi a/W)]^{1/2} \times [a-0.025(2a/W)^2 + 0.06(2a/W)^4]$$

where R is the load ratio, P is the maximum applied load, W is the specimen width (nominally 25.4 mm), t is the specimen thickness, and a is the half-crank length.

7.3.4.3 Results and Discussion

Results of the individual tests for each temperature-frequency combination are given in Figs. 7.3.1 through 7.3.9 for HT-9, in Figs. 7.3.10 through 7.3.13 for 9Cr-1Mo and in Figs. 7.3.14 through 7.3.19 for HT-9 weldments. Linear least-squares regression analyses were performed for each material-temperature-frequency combination, and are included on the plots. The results of these analyses are summarized in Table 7.3.3. The data were fit to the Paris equation:[8]

$$da/dN = C(\Delta K)^n$$

where C and n are dependent on the material and experimental condition.

The regression lines are replotted in Figures 7.3.20 through 7.3.25, showing the temperature dependence of crack growth for the various material-frequency combinations. At a cyclic frequency of 6.67 s^{-1}, there are insignificant differences in crack growth behavior (less than a factor of 2) between HT-9, 9Cr-1Mo and HT-9 weldments over the temperature range from 25°C to 550°C. When the frequency is reduced by an order of magnitude to 0.667 s^{-1}, little differences were again observed between the materials, although at 550°C the HT-9 exhibited a slightly higher growth rate at lower stress intensity factors. However, at this lower frequency, higher crack growth rates at lower stress intensity factors were observed at 300°C for all three materials compared to the crack growth rates at 500°C.

Tests at additional temperatures as well as at lower cyclic frequencies are planned to further characterize this behavior. Scanning electron microscope of selected specimen fracture surfaces is also planned.

Weld development of irradiated specimen gauges to the specimen end grips using a newly developed tungsten inert gas (TIG) welder is underway. The new TIG welder incorporates a feature for preheating the specimen prior to welding, thus eliminating the weld zone failures observed in a number of specimens welded on the prototypic welder. Results of one test on HT-9 irradiated at 550°C to 13 dpa in the EBR-II AD-2 ferritics experiment is given in Fig. 7.3.6. For the range of stress intensity factor investigated, there is little effect of irradiation on crack growth of HT-9 tested at 550°C at a cyclic frequency of 6.67 s^{-1}.

7.3.5 Conclusions and Future Work

Baseline data on the fatigue crack growth behavior of HT-9, 9Cr-1Mo, and HT-9 weldments were reported. Little differences in the crack growth behavior were observed between the materials tested from 25 to 550°C in helium at cyclic frequencies of 6.67 and 0.667 s^{-1}. However, crack growth rates far all three materials tested at a frequency of 0.667 s^{-1} were higher at 300°C than at 550°C. Additional testing and post-test fracture surface examinations are planned. One test on HT-9 irradiated at 550°C to 13 dpa and tested at 550°C at 6.67 s^{-1} exhibited little difference in crack growth behavior compared to the control tests. Tests on additional ferritics irradiated in the AD-2 experiment (13 dpa), the AD-2 reconstitution experiment (~30 dpa) and the HFIR-RB1 experiment (10 dpa) are planned during FY83.

7.3.6 References

1. R. J. Puigh and N. F. Panayotou, "Specimen Preparation and Loading for the AD-2 Ferritics Experiment", pp. 260-293 in *ADIP Quart. Prog. Rep. June 30, 1980*, DOE/ER-0045/3.

2. D. A. Mervyn, D. T. Peterson and F. H. Huang, "Microstructural and Fatigue Crack Growth Characterization of HT-9", pp. 132-155 in *ADIP Quart. Prog. Rep. March 31, 1980*, DOE/ER-0045/2.

3. L. A. James, R. E. Bauer and J. L. Straalsund, "Development of Small Fatigue Crack Growth Specimens for In-Reactor and Postirradiation Testing", pp. 36-40 in *ADIP Quart. Prog. Rep. June 30, 1978*, DOE/ET-0058/7.

4. D. A. Mervyn, M. M. Paxton and A. M. Ermi, "Development of the Miniature Fatigue Crack Growth Machine", pp. 29-42 in *ADIP Quart. Prog. Rep. September 30, 1979*, DOE/ET-0058/7.

5. J. L. Straalsund and D. A. Mervyn, "Adaptation of an Electrical Potential Technique to Measure Fatigue Crack Growth", pp. 4-9 in *ADIP Quart. Prog. Rep. December 31, 1978*, DOE/ET-0058/4.

6. W. G. Clark, Jr., and S. J. Hudak, Jr., "Variability in Fatigue Crack Growth Rate Testing". *Journal of Testing and Evaluation* 3(6), 454-476 (1975).

7. H. Tada, P. C. Paris and G. R. Irwin, The Stress Analysis Handbook, Del Research Corp. St. Louis, MO, P. 22, 1973.

8. P. Paris and F. Erdogen, "A Critical Analysis of Crack Propagation Laws", *Journal of Basic Engineering* 85(4) 528-534 (1963).

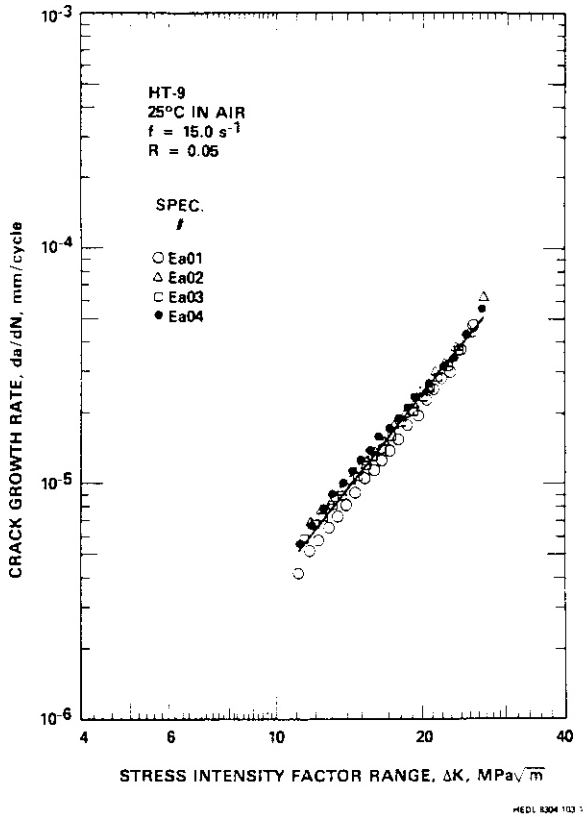

Fig. 7.3.1. Fatigue crack growth of HT-9 tested in air at 25°C and 15 s^{-1}.

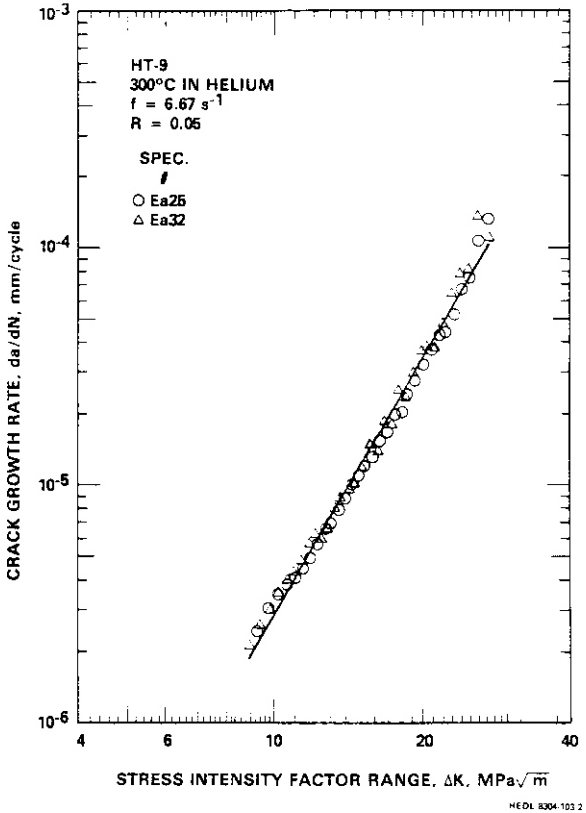

Figure 7.3.2. Fatigue crack of HT-9 in helium at 300°C and 6.67 s^{-1}.

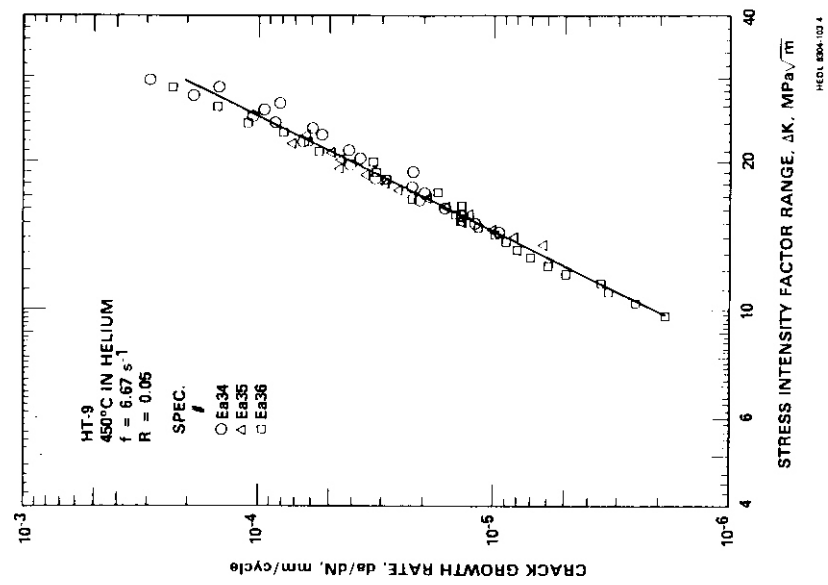

Fig. 7.3.4. Fatigue crack growth behavior of HT 9 in helium at 450°C and 6.67 s^{-1}.

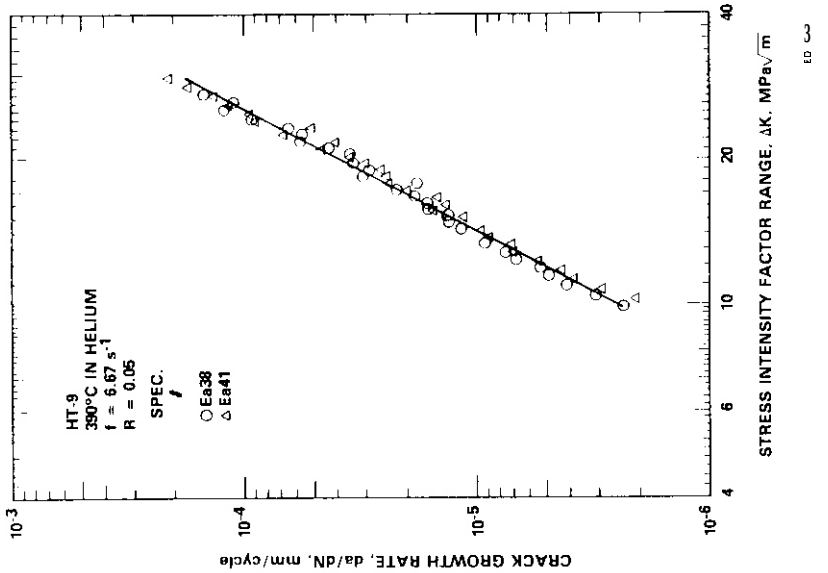

Fig. 7.3.3. Fatigue crack growth behavior of HT 9 tested in helium at 390°C and 6.67 s^{-1}.

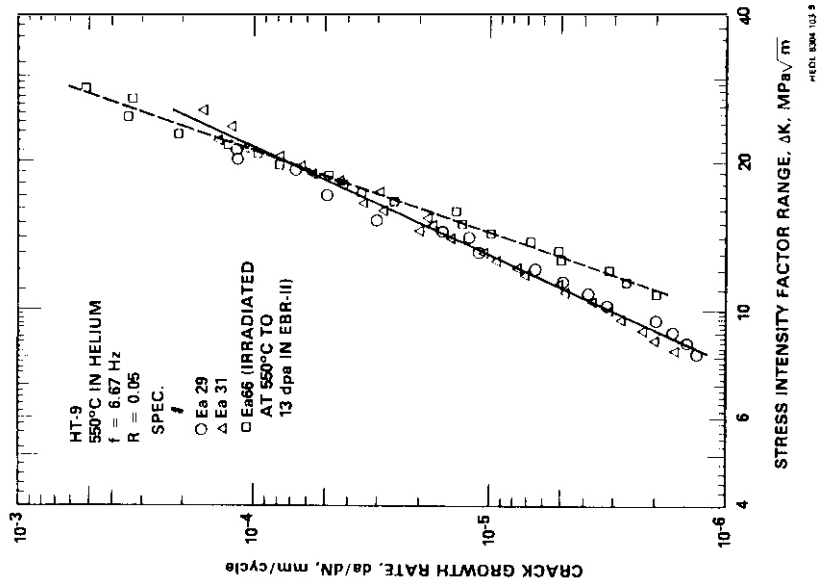

Fig. 7.3.6. Fatigue crack growth behavior of HT-9 tested in helium at 550°C and 6.67 s^{-1}.

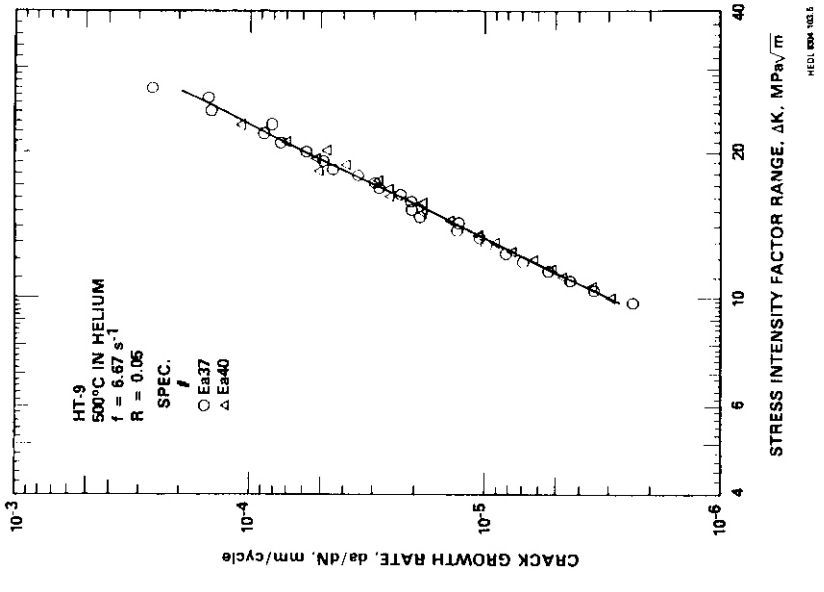

Fig. 7.3.5. Fatigue crack growth behavior of HT-9 tested in helium at 500°C and 6.67 s^{-1}.

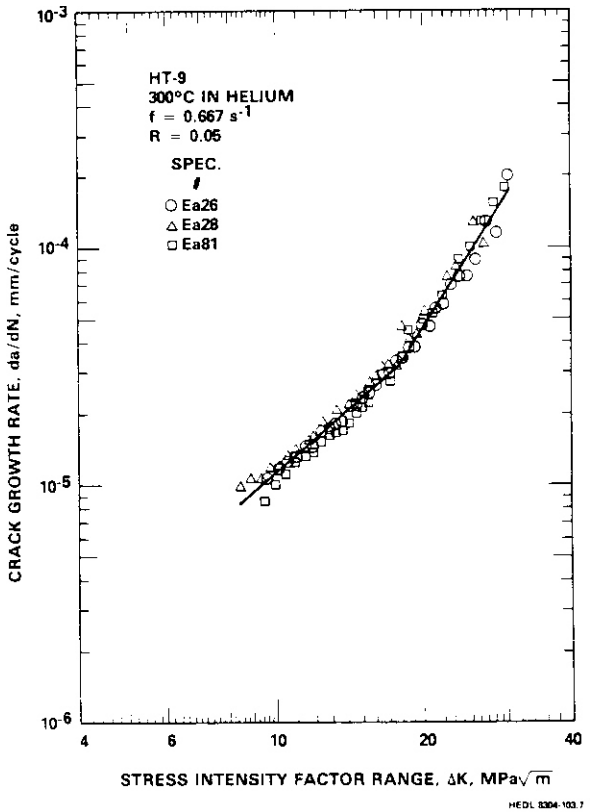

Fig. 7.3.7. Fatigue crack growth behavior of HT-9 tested in helium at 300°C and 0.667 s^{-1}.

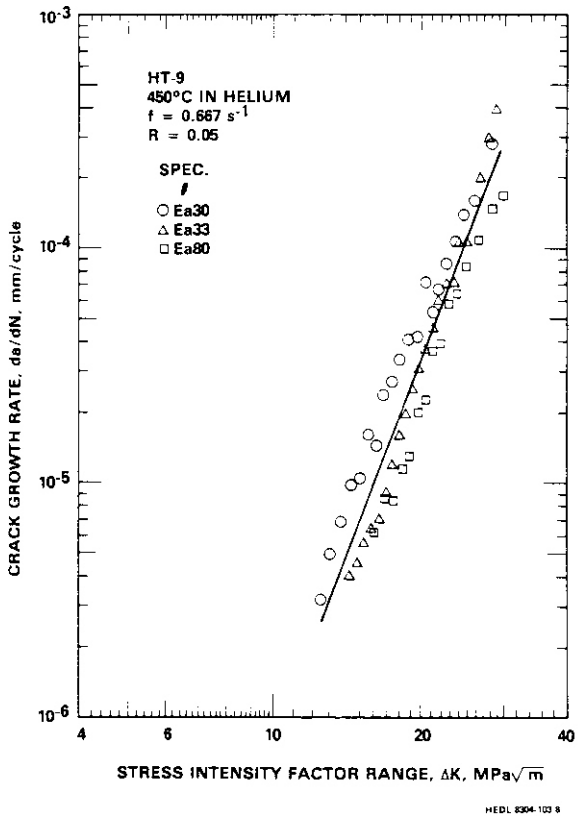

Fig. 7.3.8. Fatigue crack growth behavior of HT 9 in helium at 450°C and 0.667 s^{-1}.

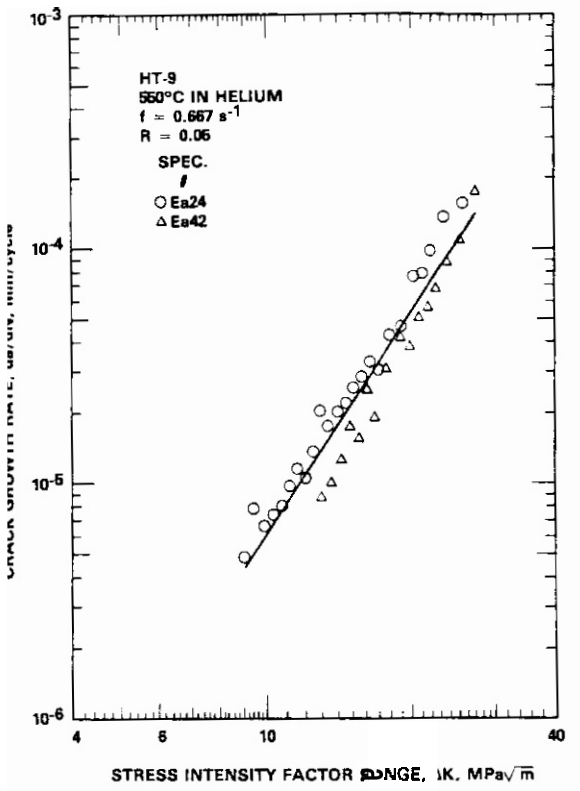

Fig. 7.3.9. Fatigue crack ... of HT 9 in helium at 550°C and 0.667 s^{-1}

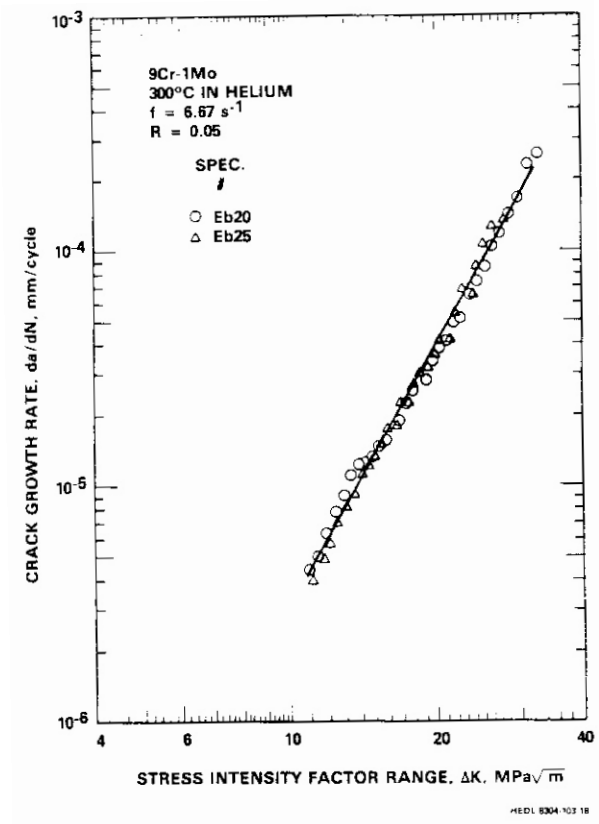

7.3.10. Fatigue crack growth ... of helium at 300°C and 6.67 s^{-1}.

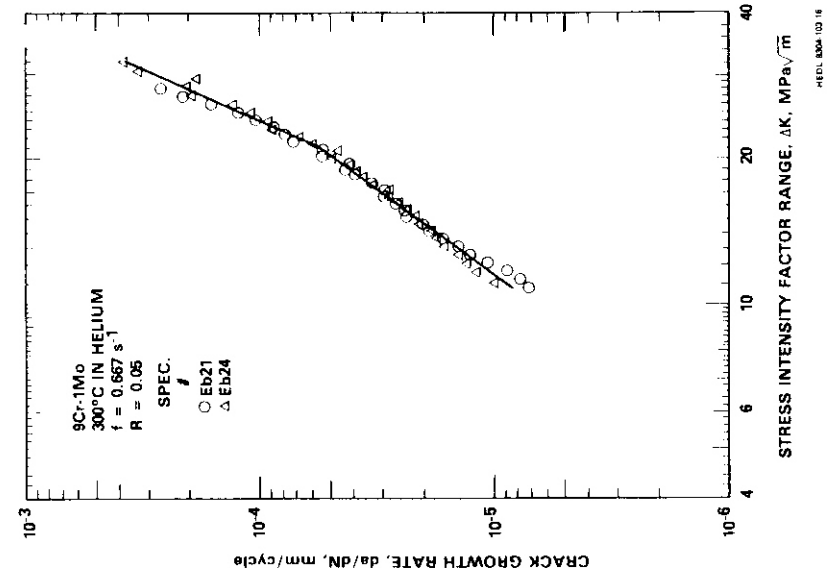

Fig. 7.3.12. Fatigue crack behavior of 9Cr-1Mo Tested in helium at 300°C and 0.667 s^{-1}.

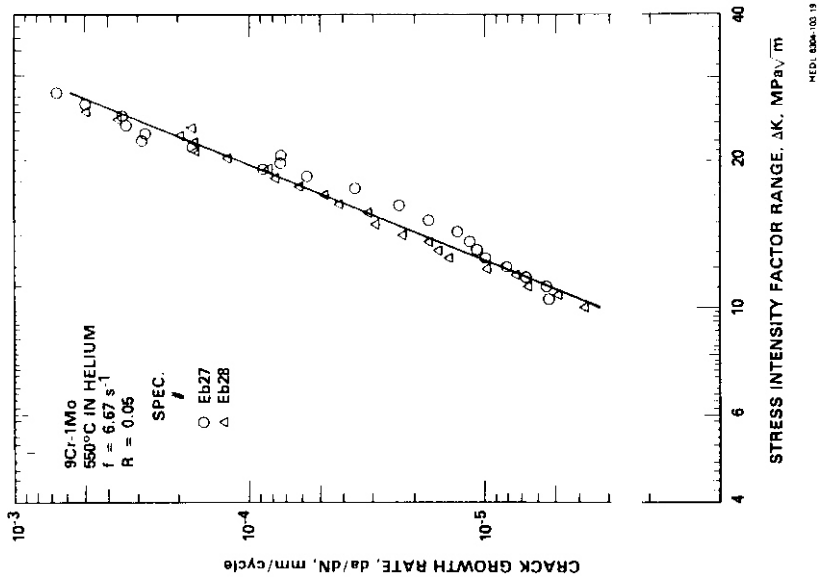

Fig. 7.3.11. Fatigue crack of Tested in helium at 550°C and 6.67 s^{-1}.

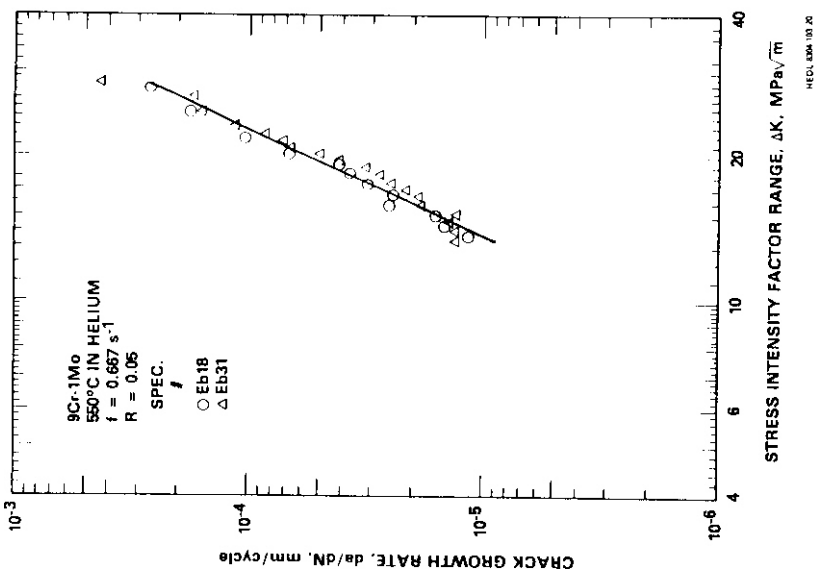

Fig. 7.3.13. Fatigue crack growth behavior of 9 Cr-1 Mo tested in helium at 550°C and 0.667 s^{-1}.

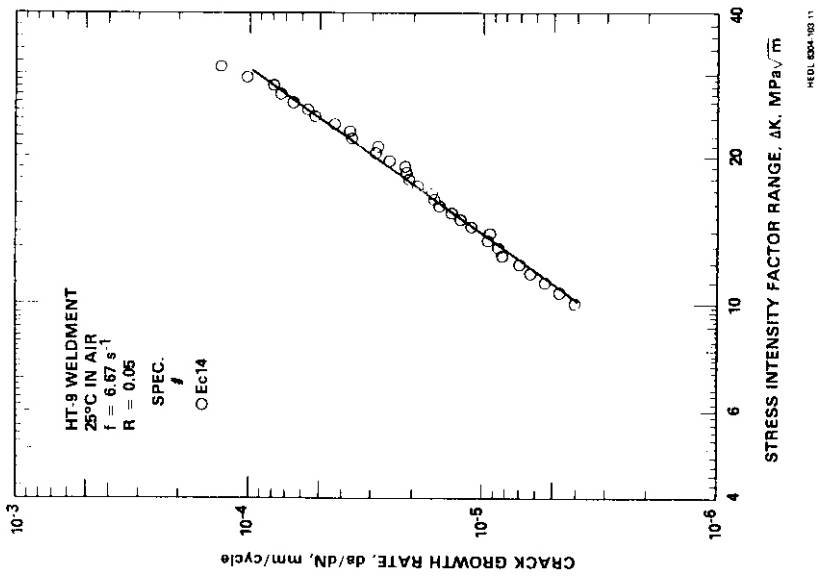

Fig. 7.3.14. Fatigue crack growth behavior of HT-9 weldment tested in air at 25°C and 6.67 s^{-1}.

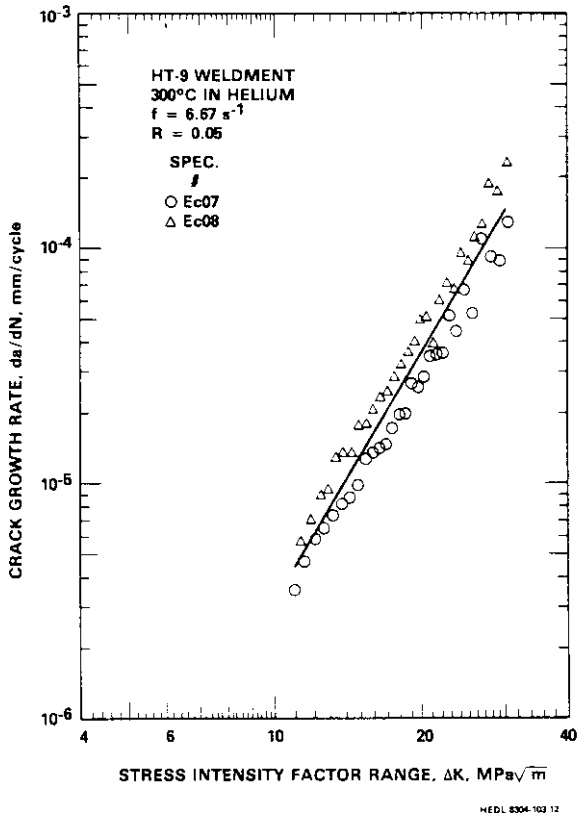

Fig. 7.3.15. Fatigue crack growth of HT 9 tested in helium at 300°C and 6.67 s^{-1}.

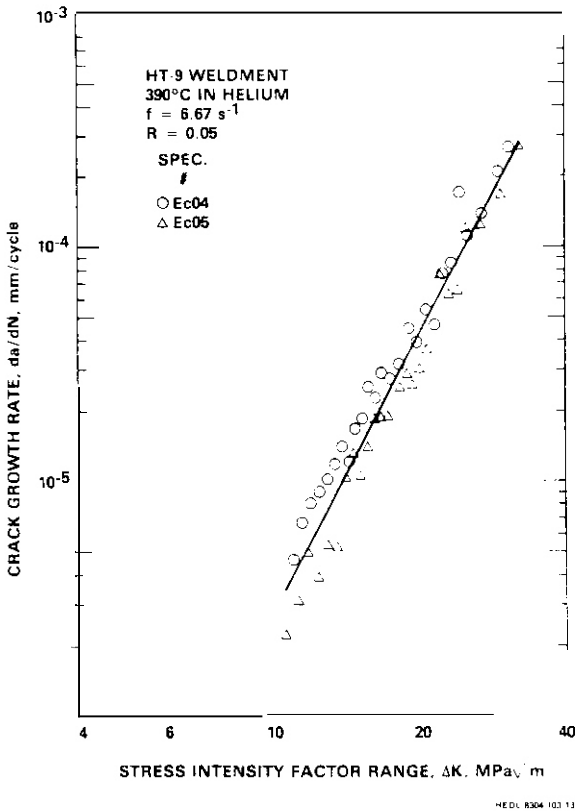

Fig. 7.3.16. Fatigue crack growth of HT 9 tested in helium at 390°C and 6.67 s^{-1}.

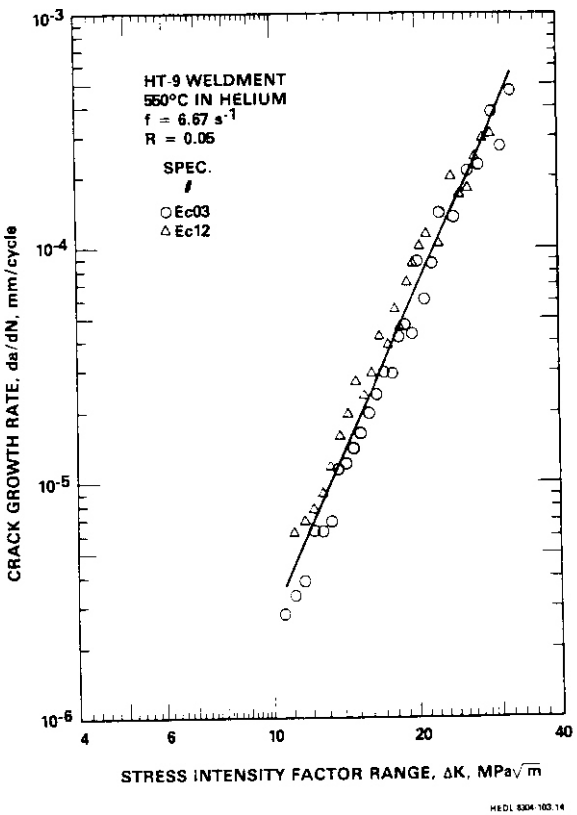

Fig. 7.3.17. Fatigue crack growth of HT-9 tested in helium at 550°C and 6.67 s^{-1}.

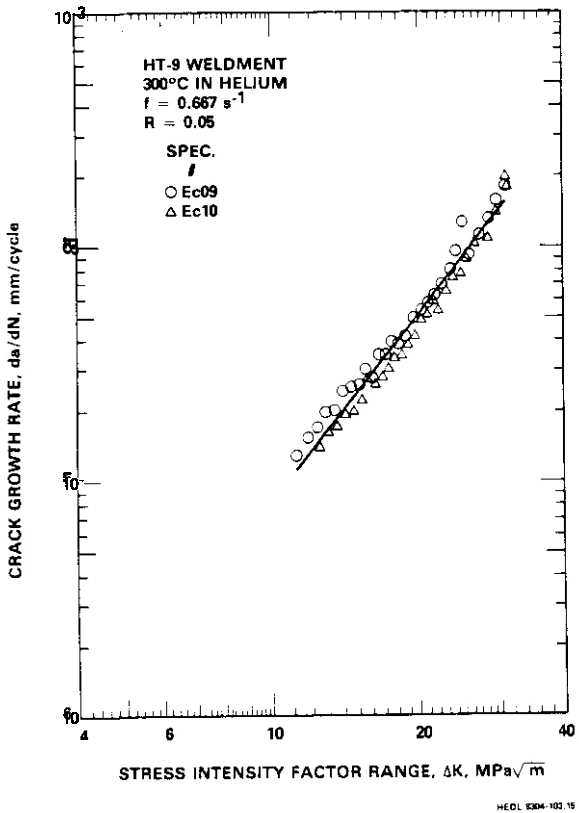

Fig. 7.3.18. Fatigue crack growth of HT-9 weldment tested in helium at 300°C and 0.667 s^{-1}.

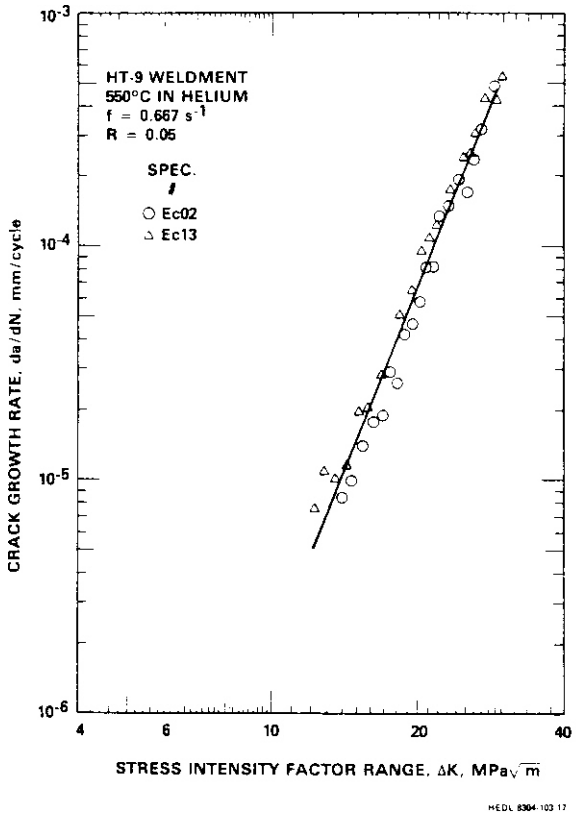

Fig. 7.3.19. Fatigue crack growth behavior of HT-9 tested in helium at 550°C and 0.667 s^{-1}.

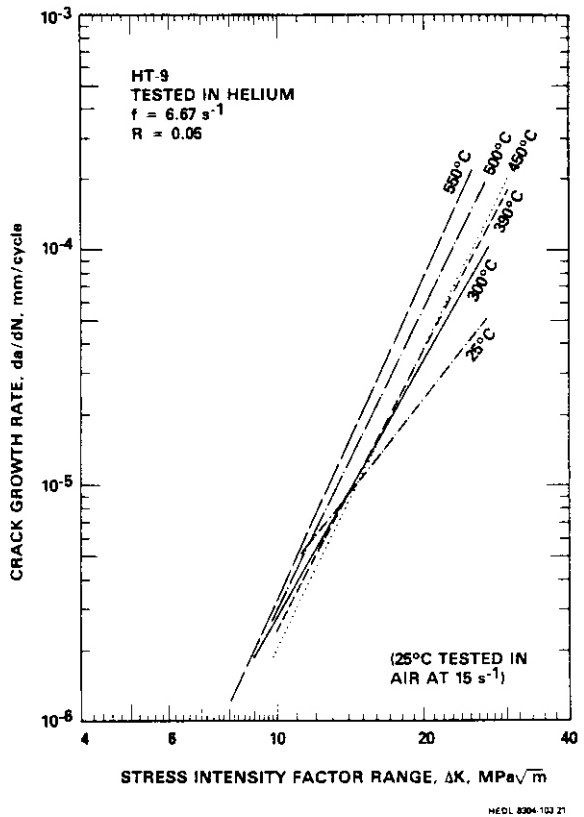

Fig. 7.3.20. Fatigue crack growth behavior of HT-9 tested at 6.67 s^{-1}.

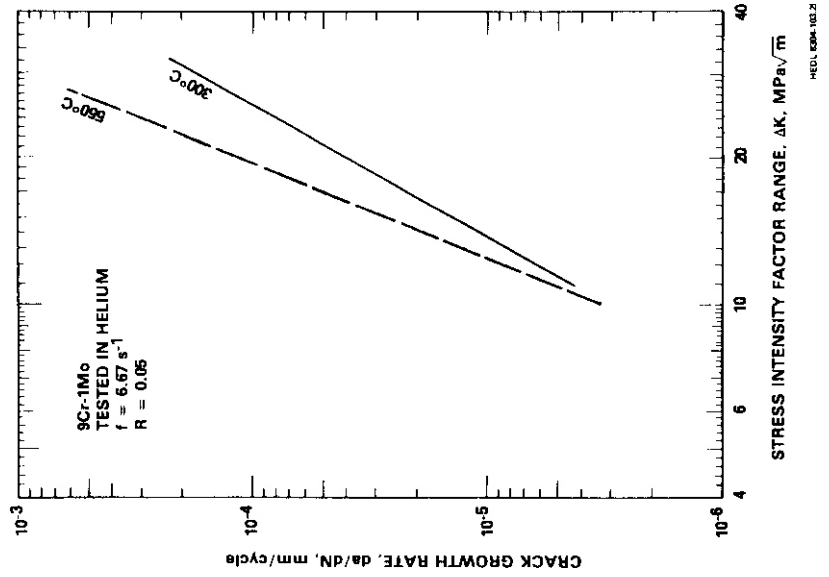

Fig. 7.3.21. Fatigue growth behavior of HT-9 tested at 0.667 s^{-1}.

Fig. 7.3.22. Fatigue growth behavior of 9Cr-1Mo tested at 6.67 s^{-1}.

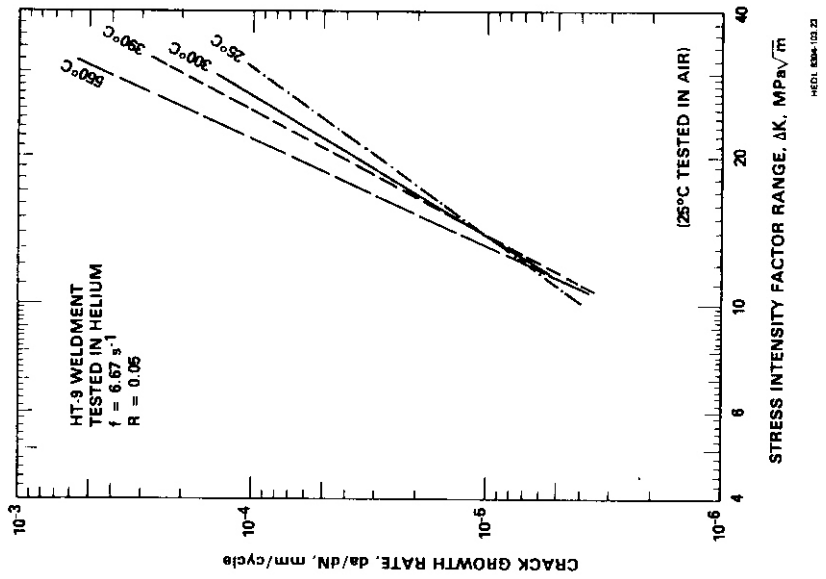

Fig. 7.3.23. Fatigue crack growth behavior of 9Cr-1Mo tested at 0.667 s^{-1}.

Fig. 7.3.24. Fatigue crack growth behavior of HT-9 weldment at 6.67 s^{-1}.

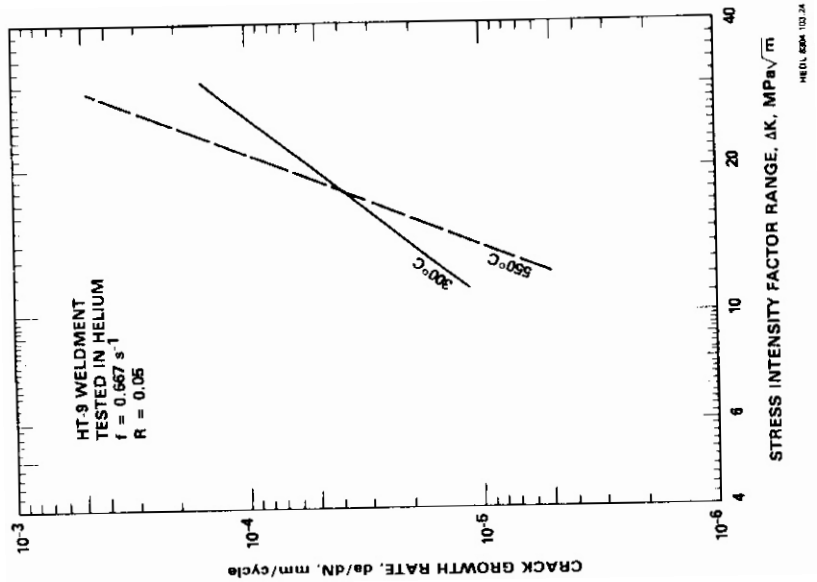

Fig. 7.3.25. Fatigue crack growth behavior of HT-9 weldment tested at 0.667 s^{-1}.

Table 7.3.3. Fatigue Crack Growth Equations Analyses[a]

	# of Spec.	Data Pairs	Temp. (°C)	Freq. (s^{-1})	C	n	Correlation Coefficient	Scatter Factor[b]	ΔK Data Range
	4	78	25	15.0	9.62×10^{-9}	2.60	0.9901	1.486	11.1-27.4
	2	63	300	6.67	7.01×10^{-10}	3.59	0.9942	1.892	8.9-27.6
	2	59	390	6.67	2.84×10^{-10}	3.93	0.9940	1.701	9.9-30.0
	3	64	450	6.67	1.26×10^{-10}	4.20	0.9903	2.224	9.7-30.2
	2	47	500	6.67	1.64×10^{-10}	4.25	0.9960	1.667	9.7-27.5
	2	44	550	6.67	8.91×10^{-11}	4.56	0.9934	2.061	8.0-25.5
	1[c]	20	550	6.67	9.36×10^{-13}	6.08	0.9960	1.764	10.0-28.4
	3[d]	57	300	0.667	1.99×10^{-7}	1.75	0.9767	1.414	8.4-18.0
		38			3.96×10^{-9}	3-13	0.9701	1.664	18.0-30.4
	3	57	450	0.667	2.77×10^{-12}	5.41	0.9525	3.873	12.7-30.4
	2	40	550	0.667	4.70×10^{-9}	3.11	0.9669	2.503	8.9-27.5
9Cr-1Mo	2	58	300	6.67	6.72×10^{-10}	3.65	0.9967	1.455	10.9-33.0
	2	45	550	6.67	2.34×10^{-11}	5.12	0.9870	2.791	10.1-27.9
	2[d]	35	300	0.667	1.09×10^{-8}	2.78	0.9861	1.423	10.9-20.0
		23			4.74×10^{-11}	4.57	0.9823	1.715	20.0-32.4
	2	31	550	0.667	5.49×10^{-11}	4.61	0.9801	2.230	13.4-28.5
HT-9 Weldment	1	32	25	6.67	4.84×10^{-9}	2.89	0.9958	1.549	10.0-31.6
	2	58	300	6.67	1.08×10^{-9}	3.47	0.9668	2.784	11.0-30.7
	2	53	390	6.67	3.28×10^{-10}	3.91	0.9764	3.228	10.6-32.9
	2	52	550	6.67	7.47×10^{-11}	4.57	0.9951	2.497	10.5-32.2
	2	55	300	0.667	2.01×10^{-8}	2.61	0.9860	1.777	11.3-31.2
	2	38	550	0.667	1.15×10^{-11}	5.19	0.9863	2.575	12.2-30.2

[a] $da/dN = C(\Delta K)^n$ where da/dN = [mm/cycle] and ΔK = [MPa$\sqrt{m}$].

[b] Total scatter factor of extreme points about regression line on da/dN.

[c] Irradiated at 550°C to 13 dpa in EBR-II.

[d] Bi-linear behavior.

7.4 FRACTURE TOUGHNESS OF IRRADIATED HT-9 WELD METAL - F. H. Huang and D. S. Gelles (Westinghouse Hanford Company)

7.4.1 ADIP Task

The Department of Energy/Office of Fusion Energy (DOE/OFE) has cited the need to investigate ferritic alloys under the ADIP program task Ferritic Steels Development (Path E).

7.4.2 Objective

The objective of this work is to evaluate the effects of neutron irradiation on the fracture toughness of HT-9 weld metal. The goal is to characterize the post-irradiation fracture behavior of welded ferritic materials for fusion reactor applications.

7.4.3 Summary

Fracture toughness tests uslng electropotential techniques on HT-9 weld material Irradiated to a fiuence of 2.8 x 10^{22} n/cm^2 (E >0.1 MeV) at 390°C were performed at 93, 205, 316 and 427°C. Testing of HT-9 welds irradiated at 450, 500 and 550°C was performed at 205°C. The test results were analyzed using the J-integral approach. After the test, the specimens were examined by scanning electron mlcroscopy in order to understand the fracture process in this weld material. The test results show that irradiation temperature has little effect on the fracture toughness of HT-9 weld metal. In addition, it was found that for the 390°C irradiation condition, testing at 93 and 427°C showed little change in fracture toughness after irradiatlon. However, testing at 200 to 300°C resulted In higher toughness, higher than that of unirradlated material.

7.4.4 Progress and Status

7.4.4.1 Experimental Procedure

2.54 mm thick circular compact tension specimens were fabrlcated from HT-9 weld metal and were irradiated in EBR-II to a fiuence of 2.8 x 10^{22} n/cm^2 (E >0.1 MeV). The configuration of the specimen is shown in Fig. 7.4.1a. The notch orientation of the weld specimen is parallel to the fuslon line of the HT-9 welded material. Details of specimen fabrication were reported in Reference 1. The single specimen electropotential technique was used to obtain J versus Aa curves. Fig. 7.4.1b shows the lead positions for power supply and potential output. To produce a sharp crack tip, all specimens were remotely fatigue precracked with a hydraulic testing system at a maximum stress intensity factor of 30 MPa$\sqrt{m}$. After the fatigue crack was initiated, the load was reduced. The test procedure was described in Reference 2. Following the test, the fracture surfaces of two irradiated HT-9 weld specimens (T727 and T730) irradiated at 390°C and tested at 205°C were examlned using a scanning electron microscope.

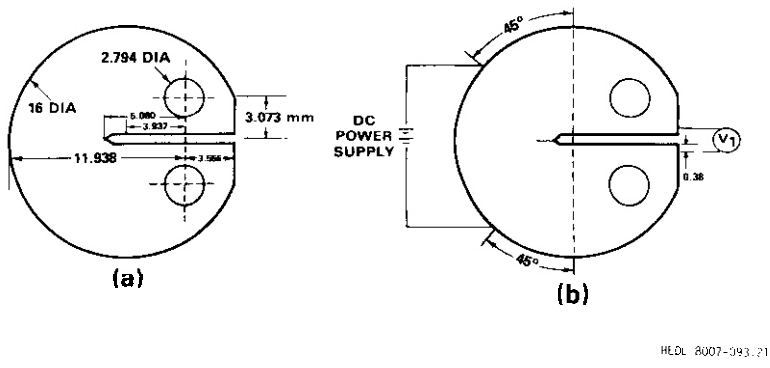

Fig. 7.4.1. (a) Circular compact tension specimen dimensions. (b) Schematic drawing of electropotential technique.

7.4.4.2 Results and Discussions

Fracture toughness measurements

The potential output versus crack extension as revealed by heat tinting is plotted in Fig. 7.4.2. A calibration curve for irradiated HT-9 weld was established following the procedure described in Reference 3. The continuous crack extensions can be obtained from electropotential output via this calibration curve. The values of J were calculated from load versus displacement curves. Figure 7.4.3 shows J versus Δa curves for irradiated HT-9 welds tested at elevated temperatures. The fracture toughness values at

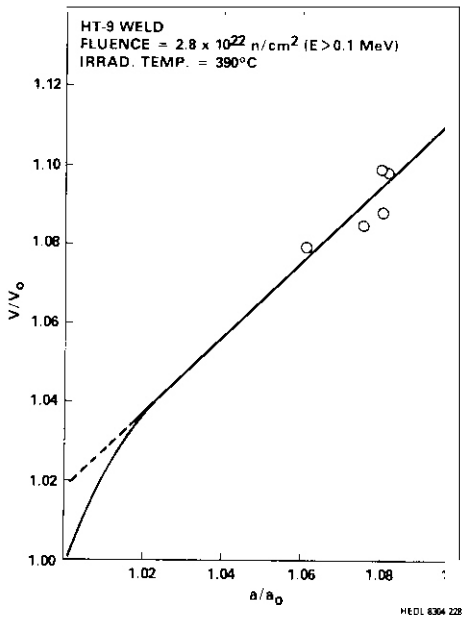

Fig. 7.4.2. Electropotentiai calibration curve for irradiated HT-9 weld.

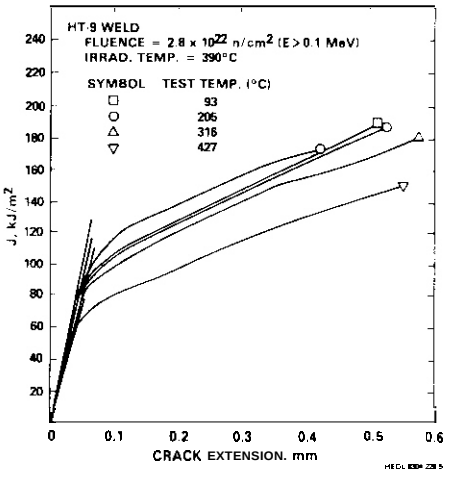

Fig. 7.4.3. J versus △a curves obtained via an electropotential calibration curve for irradiated HT-9 weld tested at elevated temperatures.

crack initiation, J_{1C}, were determined from these J versus *'a* curves and the blunting lines and are listed in Table 7.4.1. **Also** listed *in* **Table** 7.4.1 is the **tearing** modulus (T). The test and irradiation temperature dependences of J_{1C} for irradiated HT-9 weld **are** plotted in Figs. 1.4.4 and 7.4.5, respectively. **As** shown in Fig. 7.4.4, the fracture toughness of HT-9 weld metai surprisingly increases after irradiation. Anaiysis of the results also shows that HT-9 weld metal exhibits similar trends in which the fracture toughness decreases with increasing test temperature before as weii as after irradiation. In contrast to fracture toughness, the tearing modulus of HT-9 weld was degraded significantly by irradiation. As shown in Fig. 7.4.6, the tearing modulus of HT-9 was reduced 35% due to welding, and was further reduced by a factor of 2 as a result of irradiation.

The effects of irradiation on the fracture toughness and tearing modulus of HT-9 weld are shown in Fig. 7.4.5. Overall, the test results show that neutron irradiation has little effect on the fracture toughness of HT-9 weld but severely reduces the ability of HT-9 weld to resist crack propagation after the crack is initiated.

Tabie 7.4.1. Fracture Toughness Test Results of irradiated HT-9 Weld Metal

Irradiation Temperature (°C)	Test Temperature (°C)	(in-lb/in 2		Modulus
390	93	586.0	102.6	36.4
390	205	591.5	103.5	39.6
390	316	575.1	100.6	43.3
390	421	440.7	77.1	46.1
450	205	451.1	80.0	35.1
500	205	467.9	81.9	32.0
550	205	499.6	87.4	65.3

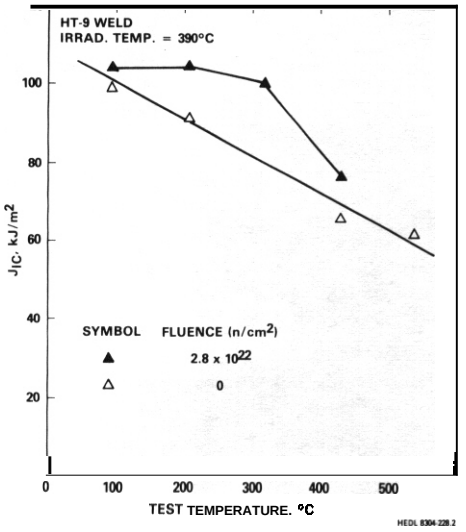

Fig. 7.4.4. Temperature dependence of fracture toughness for irradiated and unirradiated HT-9 weld metal.

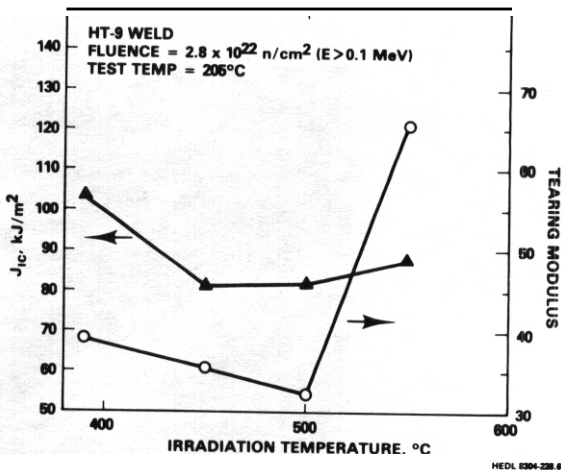

Fig. 7.4.5. Irradiation temperature dependence of fracture toughness and tearing modulus for irradiated HT-9 weld metal tested at 205°C.

Fractography

Examples of the fracture appearances for two specimens which were irradiated at 390°C and tested at 205°C are shown in Figs. 7.4.7 and 7.4.8. The fracture surfaces are rough and failure is by dimple rupture tending to follow microstructural features such as grain boundaries, martensite lath boundaries and delta ferrite features. At low magnification the structures appear quite different. However, at higher magnification, the fracture surfaces of the two specimens in the vicinity of the fatigue crack are found to be quite similar, and as can be shown from Fig. 7.4.3, the toughness measurements from these specimens are similar. In comparison with behavior in an unirradiated specimen.' irradiation at 390°C has not affected the fracture mode on a coarse scale, but it has resulted in less pronounced dimple rupture on a fine scale, probably as a consequence of irradiation hardening. This change in fracture mode probably arises from the reduction in tearing modulus which results from irradiation.

7.4.5 Conclusions

Test results show that the fracture toughness of HT-9 weld metal increases after Irradiation. Like unirradiated weld metal the fracture of irradiated welds decreases with increasing temperature. In addition, it was found that welding. as well as irradiation, has little effect on the fracture toughness of HT-9. However, the tearing modulus of HT-9 is significantly reduced as a result of welding and irradiation.

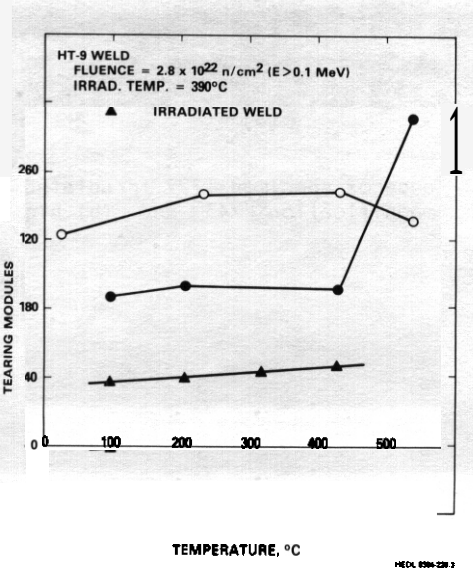

Fig. 7.4.6. Temperature dependence of tearing modulus for irradiated and unirradiated HT-9 weld metal.

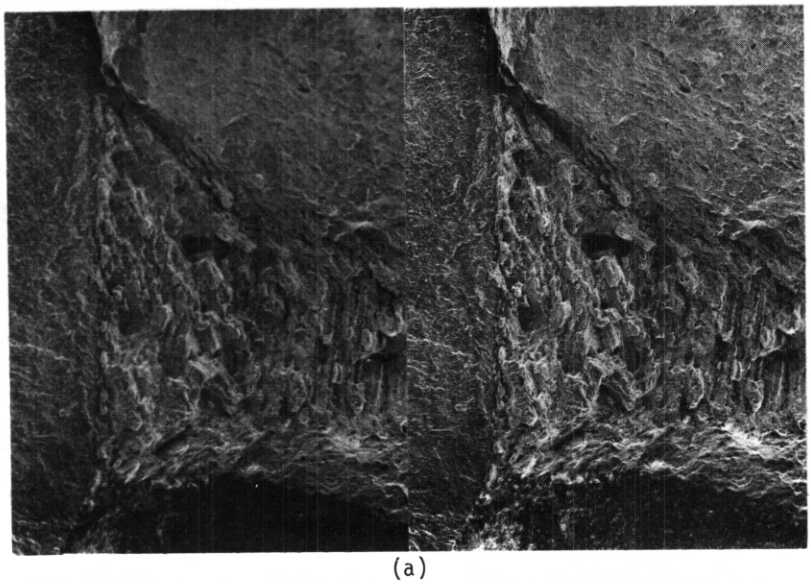

(a)

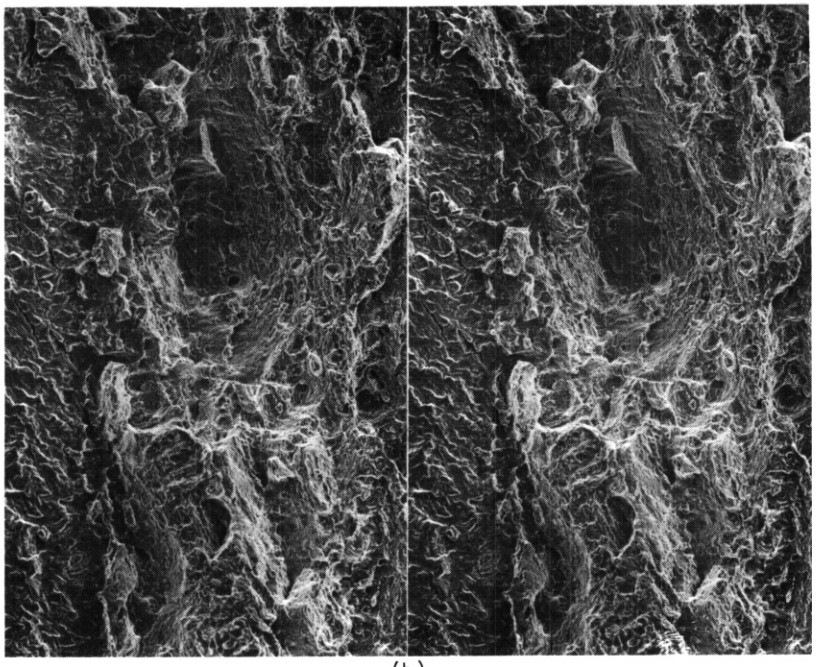

(b)

Fig. 7.4.7. The fracture appearance of specimen T727 irradiated at 390°C and tested at 205°C presented as stereopairs at (a) low magnification [X43] and (b) higher magnification [X200].

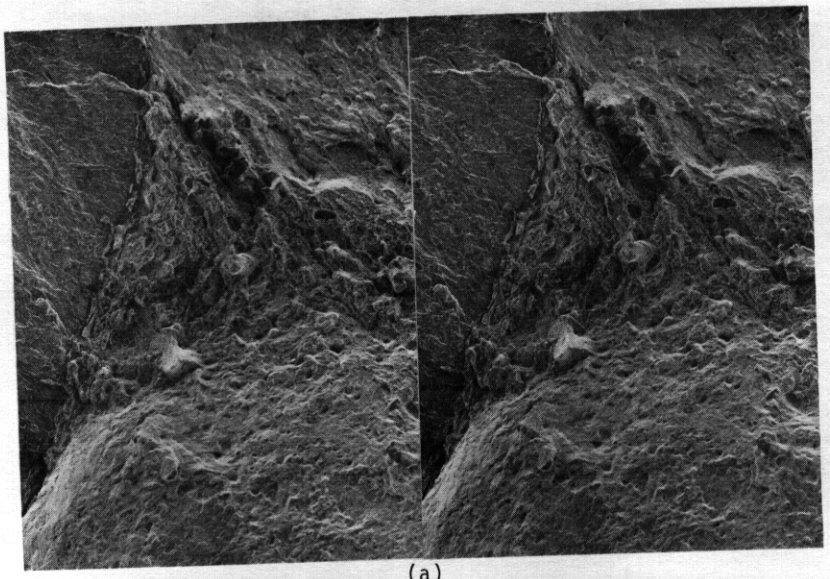

(a)

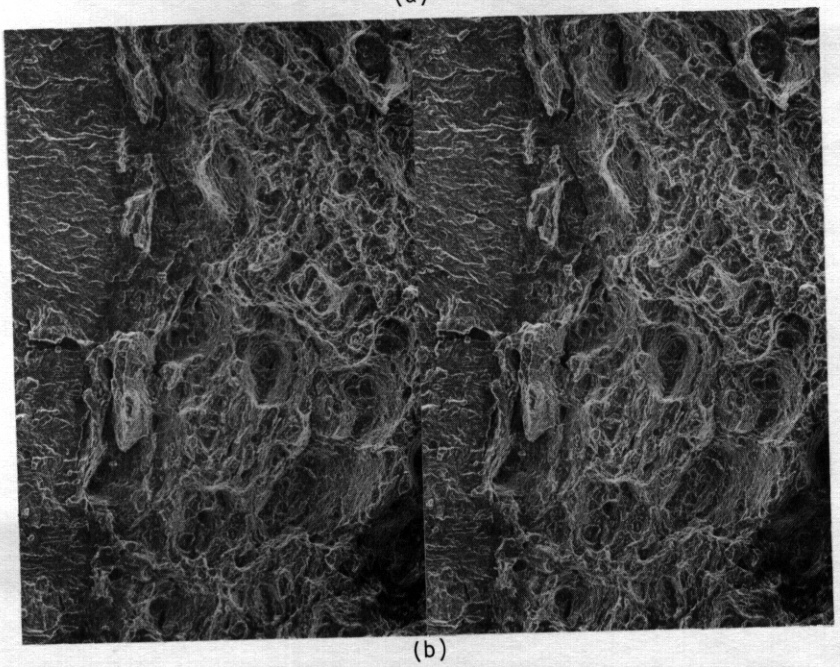

(b)

Fig. 7.4.8. The fracture appearance of specimen T730 irradiated at 390°C and tested at 205°C presented as stereopairs at (a) low magnification [X43] and (b) higher magnification [X200].

7.4.6 References

1. R. J. Puigh and N. F. Panayotou, "Specimen Preparation and Loading for the AD-2 Ferritics Experiment," ADIP Quart. Prog. Rep. Sept. 30, 1980, DOE/ER-0045/3, pp. 260-293.

2. F. H. Huang. "Fracture Toughness of Unirradiated HT-9 and Modified 9Cr-1Mo Welds," ADIP Semiannual Proa. Rep. Sept. 30. 1982. DOE/ER-0045/9, pp. 221-229.

3. F. H. Huang and G. L. Wire, "Analysis of Single Specimen Tests on HT-9 for J_{1c} Determination,' ADIP Quart. Prog. Rep. Sept. 30. 1980, DOE/ER-0045/3, pp. 236-254.

4. D. S. Gelles, F. H. Huang and N. F. Panayotou, "Fractographic Examination of Compact Tension Specimens of Unirradiated HT-9 and Modified 9Cr-1Mo Welds," ADIP Semiannual Prog. Rep. March 31, 1982, DOE/ER-0045/8, pp. 442-459.

7.5 EFFECT OF SPECIMEN SIZE AND MATERIAL CONDITION ON CHARPY IMPACT PROPERTIES OF 9 Cr-1 MoVNb — W. R. Corwin and A. M. Hougland (Oak Ridge National Laboratory)

7.5.1 ADIP Task

ADIP tasks are not defined for Path E, Ferritic Steels, in the 1978 program plan.

7.5.2 Objective

Radiation-induced degradation of the impact properties of ferritic steels is a major concern in determining their suitability for first-wall and blanket structure use in magnetic fusion reactors. To evaluate these properties, it is necessary to reduce the size of standard impact specimens for irradiation experiments in existing high-flux reactors. The objective of this study was to investigate the effect of specimen size reduction on measured impact properties. Full- and subsize specimens of normalized-and-tempered and quench-embrittled 9 Cr-1 MoVNb steel were used in these tests.

7.5.3 *Summary*

Charpy-impact properties were determined on full- and subsize specimens of normalized-and-tempered as well as quenched-only 9 Cr-1 MoVNb steel. The subsize specimen produced consistently smaller fractional drops in the upper-shelf energy and larger shifts in the transition temperature than did the full-size specimen. Area and volumetric normalizations of the specimen size effect were also performed.

7.5.4 Progress and Status

7.5.4.1 Introduction

The degradation of fracture resistance of ferritic steels subjected to neutron irradiation can be qualitatively evaluated by examining the shift in the ductile-to-brittle transition temperature and the drop in the upper-shelf energy determined in the Charpy impact test. However, the Charpy test is empirical, and its primary usefulness is derived from either correlation with more quantitative measures of fracture toughness or by comparison with other Charpy test results for different materials or conditions of interest. Any departures from the standard testing procedures' will yield results that will vary in some degree from those of a standard test.

In examining the effects of neutron irradiation on the high-chromium ferritic steels 9 Cr-1 MoVNb and 12 Cr-1 MoVW, which are candidates for the first wall of magnetic fusion reactors, it is necessary to severely limit the size of test specimens to accommodate irradiation in available high-flux test reactors. Impact specimens with a cross section of 5 by 5 mm are employed instead of the 10 by 10-mm cross section of standard size Charpy impact specimens. To evaluate the effectiveness of the smaller specimen in measuring the relative shift in transition temperature and drop in upper-shelf energy, compared with a standard Charpy specimen, a study of impact properties of 9 Cr-1 MoVNb steel in both the normalized-and-tempered (N&T) and quenched-only (Q) conditions was conducted. Full-size Charpy V-notch specimens and subsize specimens of both V-notch and precracked types were taken from both material conditions in both the longitudinal and transverse orientations.

7.5.4.2 Experimental Procedure

All impact specimens in the study were taken from plate material of an electroslag remelt heat of 9 Cr-1 MoVNb steel, heat 30176. The steel was given a standard normalizing and tempering treatment of 1038°C for 1 h and 760°C for 1 h. Details on the mechanical properties of this material are available elsewhere.[2,3] A portion of the material was then reaustenitized and quenched in water *to* approximate the effects of irradiation embrittlement. Standard Charpy and subsize Charpy impact specimens were taken from each material condition in two orientations: the WR orientation (transverse), in which the axis of the specimen is parallel to the width of the plate and the crack propagates in the rolling direction, and the RW orientation (longitudinal), in which the axis of the specimen lies in the rolling direction and the crack propagates across the plate width.

The full-size Charpy specimens (the ASTM standard specimens') had dimensions of 10 by 10 by 55 mm and a 2-mm-deep 45" notch with a 0.25-mm root radius. The subsize specimens had dimensions of 5 by 5 by 55 mm and a 0.76-mm-deep 30" notch with a 0.05- to 0.10-mm root radius. A limited number of the subsize specimens were precracked to a relative crack length a/w of about 0.5 for comparative testing. (For a/w of 0.5, the precrack extends to within 2.5 mm of the unnotched surface.) The subsize specimens correspond exactly to those being used in the ADIP subsize Charpy irradiation experiments[4,5] except in length. The 55 mm length of the specimens in this study and the resultant span-to-width ratio of 8:1 (compared with 4:1 for the irradiation experiment specimens) was used to allow testing on an existing Charpy impact test machine. Complementary studies using a 4:1 span subsize specimen are planned once the new impact machine to be used in testing the irradiated specimens is operational.

7.5.4.3 Results and Discussion

The results of the impact tests in both orientations for the full-size specimens in the N&T and Q conditions and the subsize specimens in the N&T and Q conditions (Figs. 7.5.1 through 7.5.4), show that the same trends are followed for both size specimens. The upper shelf is higher and the ductile-to-brittle transition temperature is lower for the RW orientation in the N&T condition regardless of the specimen used. For the Q condition, the RW orientation has a higher upper shelf and transition temperature in both specimen sizes.

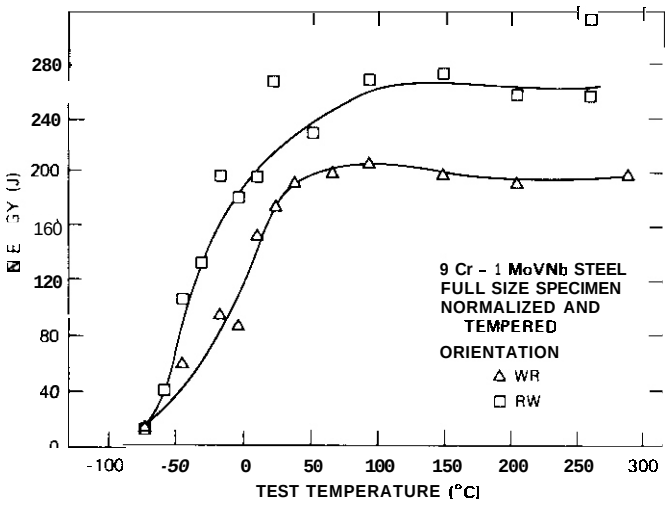

Fig. 7.5.1. Effect of orientation on the full-size V-notch Charpy impact energy of normalized and tempered 9 Cr-1 MoVNb steel (heat 30176).

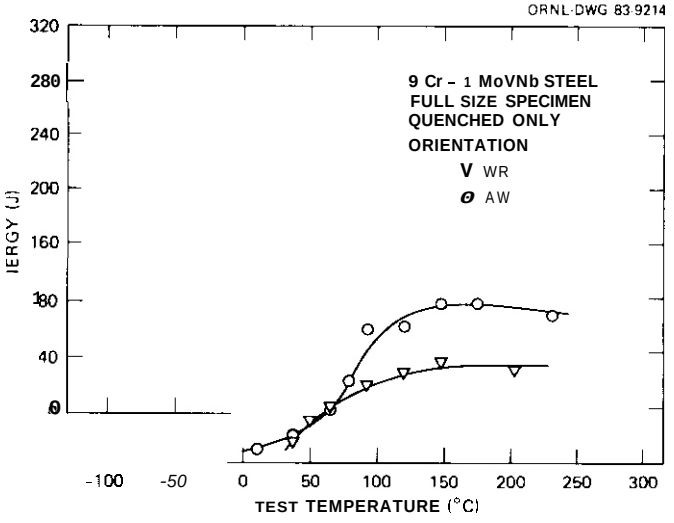

Fig. 7.5.2. Effect of orientation on the full-size V-notch Charpy impact energy of quenched 9 Cr-1 MoVNb steel (heat 30176).

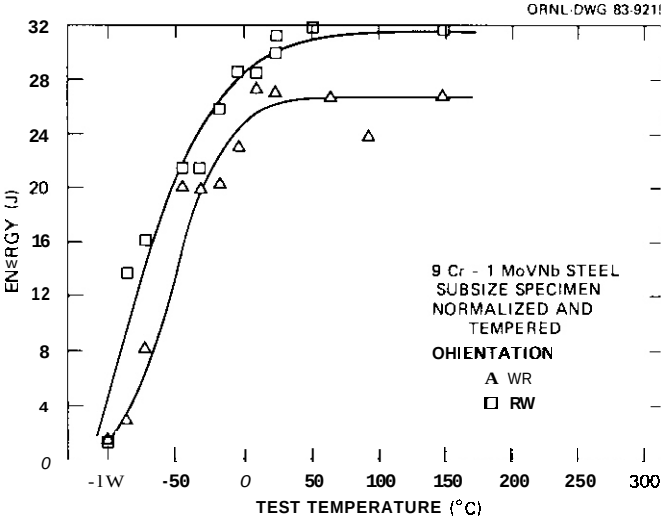

Fig. 7.5.3. Effect of orientation on the subsize V-notch Charpy impact energy of normalized and tempered 9 Cr-1 MoVNb steel (heat 30176).

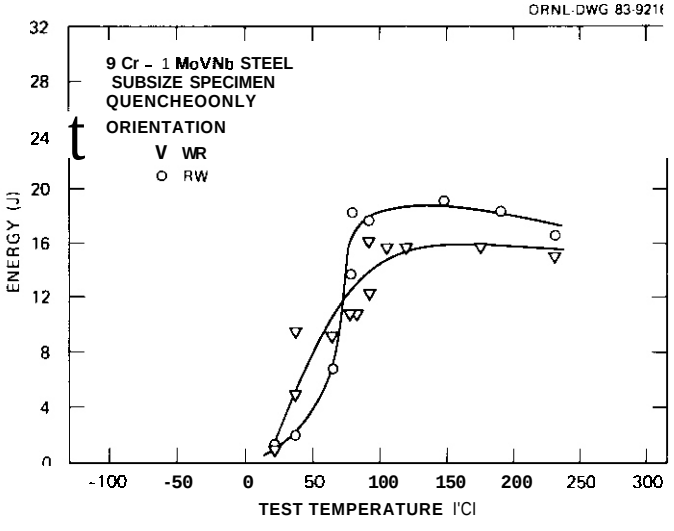

Fig. 7.5.4. Effect of orientation on the subsize V-notch Charpy impact energy of quenched 9 Cr-1 MoVNb steel (heat 30176).

It should be noted that the temperature representing the ductile-to-brittle transition needs to be explicitly defined for nonstandard specimens. The traditional method of defining the transition temperature at a given energy (e.g., 68 or 41 J) cannot apply to the subsize specimen. Fracture surface appearance could be used but is complicated to use inasmuch as the relative amount of plasticity increases with decreasing specimen size because of a lack of constraint. In this study the transition temperature is arbitrarily defined at one-half the average upper-shelf energy. This is subjective but is at least consistent regardless of specimen size.

The effect of specimen size and type on the impact energy of the full-size and subsize V-notch and precracked specimens can be exam-ined separately for the WR orientation in the N&T and Q conditions and for RW orientation in the N&T and Q conditions (Figs. 7.5.5 through 7.5.8). Other than the general reduction in impact energy in going from the full-size V-notch to the subsize V-notch to the subsize precracked specimen, little can be said about the upper-shelf properties for all material conditions and orientations examined. However, the effect on transition temperature is noticeably different for the N&T material than for the Q material. Although the transition temperature for the subsize V-notch specimen is lower than that for the corresponding full-size specimen in all cases, it is less than 10°C lower for the Q material, whereas it is about 40°C lower for the N&T condition. In contrast, the limited data on the precracked subsize specimen yielded a transition temperature about 35 to 40°C higher than that of the corresponding full-size specimen and 45 to 75°C higher than the corresponding subsize V-notched (uncracked) specimen. The behavior of the precracked specimens can be at least partially accounted for by the rate sensitivity of the impact properties of ferritic steel and the higher effective strain rate at the tip of the fatigue crack in the specimen.

To investigate the embrittlement due to the Q heat treatment (which is qualitatively similar to the effect of irradiation), the data were examined separately for each Specimen type — full- and subsize specimens in each of the WR and RW orientations (Figs. 7.5.9 through 7.5.12). Consistent trends of greater transition temperature and lower upper-shelf energy for the Q material compared to the N&T material were noted for both specimen types and both orientations.

Methods are needed to improve agreement between the two specimen types for the transition temperature shifts and upper-shelf energy drops caused by the quenching. To achieve this, the impact energy for each specimen was normalized on both an area and a volumetric basis. In the area normalization, the impact energy for each test was divided by the nominal fracture area. This is net area below the notch, 0.8 cm^2 for the full-size specimens and 0.21 cm^2 for the subsize specimens. The results of area normalization for all specimens

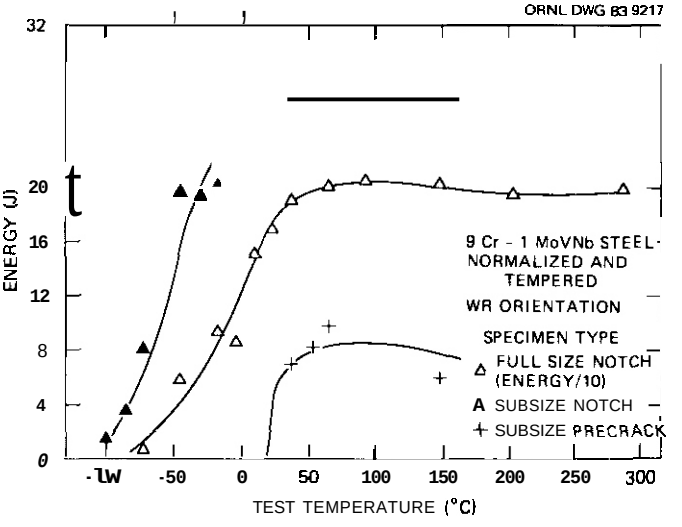

Fig. 7.5.5. Effect of specimen type on the Charpy impact energy of normalized and tempered 9 Cr-1 MoVNb steel (heat 30176) in the WR orientation.

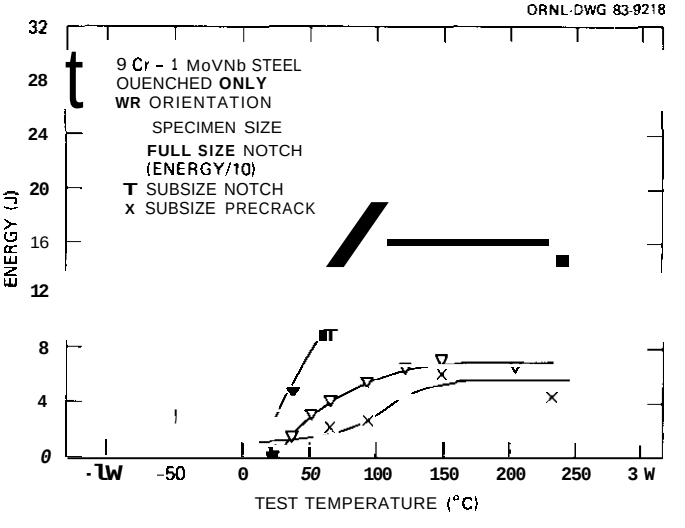

Fig. 7.5.6. Effect of specimen type on the Charpy impact energy of quenched 9 Cr-1 MoVNb steel (heat 30176) in the WR orientation.

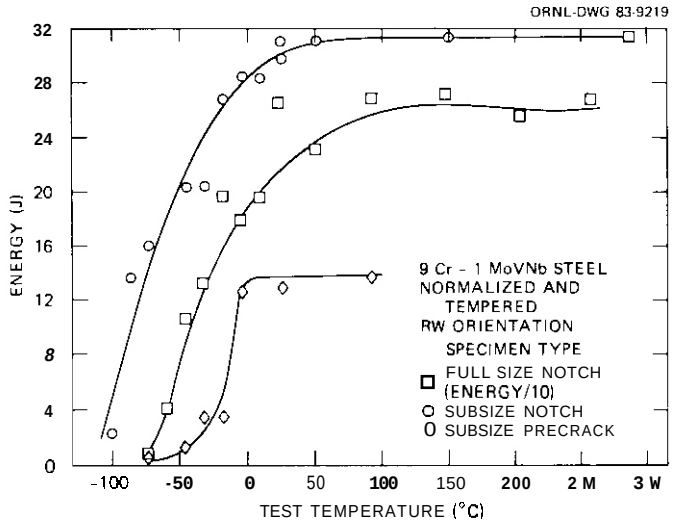

Fig. 7.5.7. Effect of specimen type on the Charpy impact energy of normalized and tempered 9 Cr-1 MoVNb steel (heat 30176) in the RW orientation.

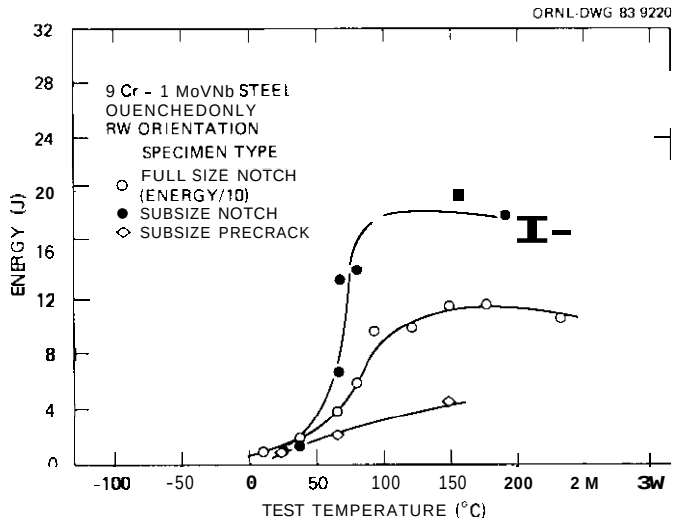

Fig. 7.5.8. Effect of specimen type on the Charpy impact energy of quenched 9 Cr-1 MoVNb steel (heat 30176) in the RW orientation.

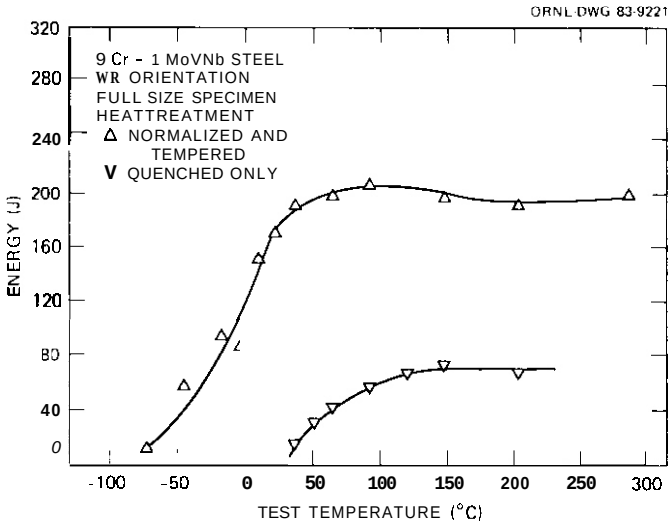

Fig. 7.5.9. Effect of heat treatment on the Charpy impact energy of full-size V-notch specimens of 9 Cr-1 MoVNb steel (heat 30176) in the WR orientation.

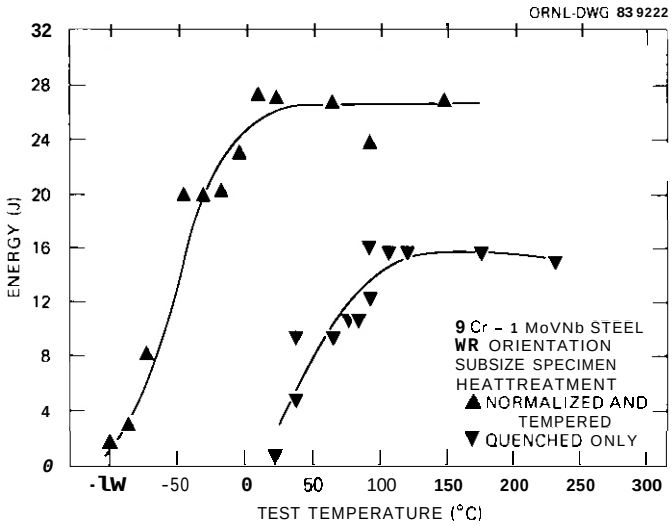

Fig. 7.5.10. Effect of heat treatment on the Charpy impact energy of subsize V-notch specimens of 9 Cr-1 MoVNb steel (heat 30176) in the WR orientation.

in the RW and WR orientations (Figs. 7.5.13 and 7.5.14, respectively) show that only a poor match of the full- and subsize specimens exists for either the N&T or Q condition. The best match is seen at the low test energies, as expected because the fracture event is more confined to a fracture plane with little or no plasticity. At the relatively higher energy levels, where shear lips develop and more material away from the fracture face is plastically deformed, normalization based on area is clearly inadequate. A normalization based on a fracture volume was attempted. The fracture volume was taken to be a rectangular prism with a cross-sectional area equal to the area below the V-notch and a length, parallel to the specimen axis, equal to the average of the two sides of the rectangular area below the notch. For the full-size, 10 by 10-mm specimen with a 2-mm-deep notch, this is 10 by 8 by 9 mm or 720 mm^3, while, for the subsize 5 by 5-mm specimen with a 0.76-mm-deep notch, it is 5 by 4.24 by 4.62 mm or 98 mm^3. The results of the volumetric normalization for the WR and RW orientations (Figs. 7.5.15 and 7.5.16, respectively) show that the

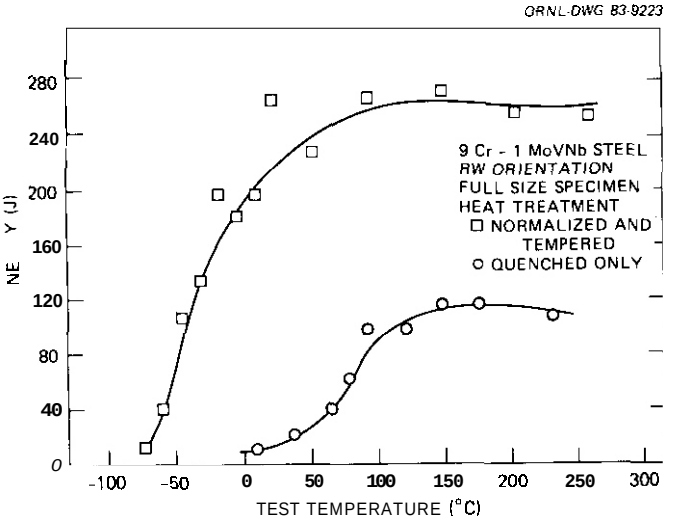

Fig. 7.5.11. Effect of heat treatment on the Charpy impact energy of full-size V-notch specimens of 9 Cr-1 Mo VNb steel (heat 30176) in the RW orientation.

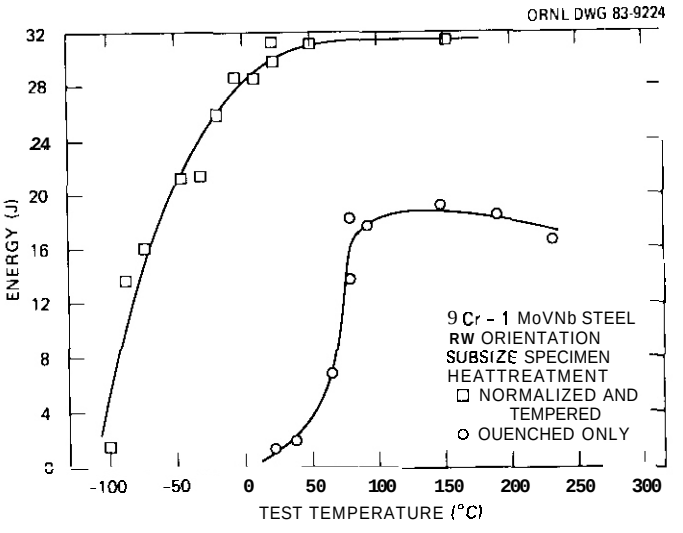

Fig. 7.5.12. Effect of heat treatment on the Charpy impact energy of subsize V-notch specimens of 9 Cr-1 Mo VNb steel (heat 30176) in the RW orientation.

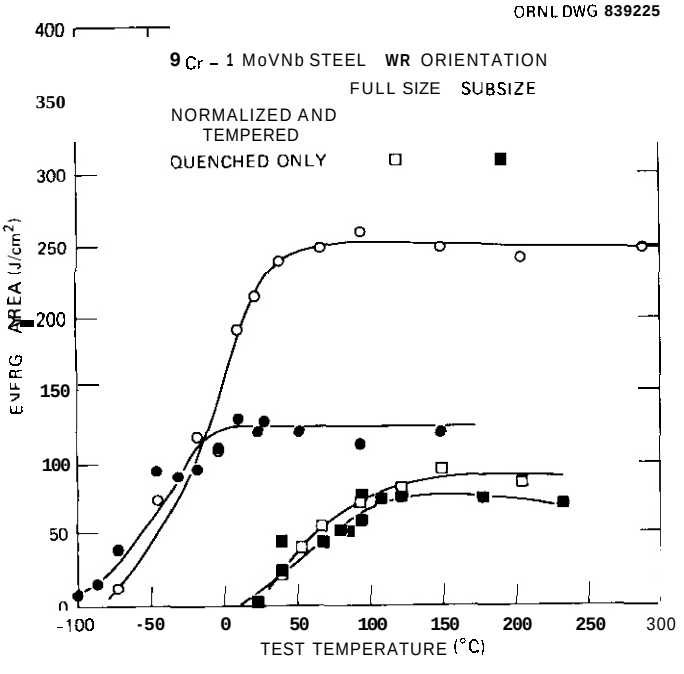

Fig. 7.5.13. Normalization of Charpy impact energy data using the nominal fracture area. WR orientation of the 9 CR-1 MoVNb steel (heat 30176).

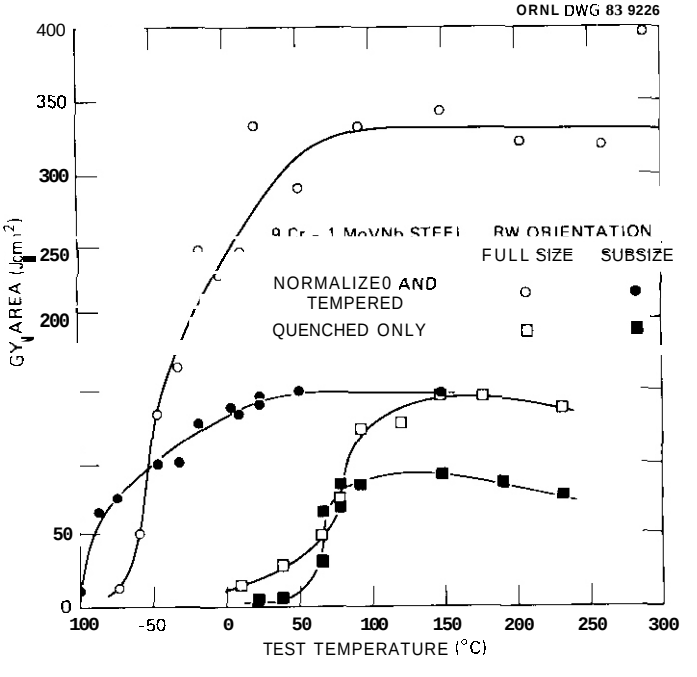

Fig. 7.5.14. Normalization of Charpy impact energy data using the nominal fracture area. RW orientation of the 9 Cr-1 MoVNb steel (heat 30176).

agreement at relatively high energy levels between the full- and subsize specimens is much better than for the data normalized on an area basis. However, the overall coincidence of the data sets is still small.

All the values for upper-shelf energy and transition temperature for each material condition, specimen size, orientation, and basis of analysis are compiled in Table 7.5.1. To facilitate comparison of the various parameters examined, a histogram of the fractional upper-shelf drops and transition-temperature shifts between the N&T and Q material was constructed (Fig. 7.5.17). From this it can readily be seen that the subsize V-notch specimen consistently yields a smaller fractional drop in upper shelf and a larger transition-temperature shift than the full-size specimen for all conditions examined and all bases of analysis employed. These effects are most pronounced in the precracked subsize specimens.

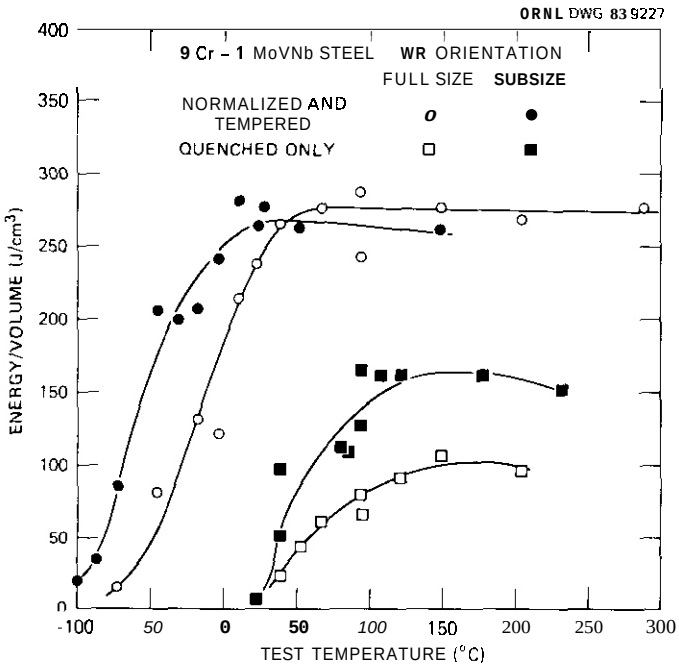

Fig. 7.5.15. Normalization of Charpy impact energy data using the nominal fracture volume. WR orientation of the 9 Cr-1 MoVNb steel (heat 30176).

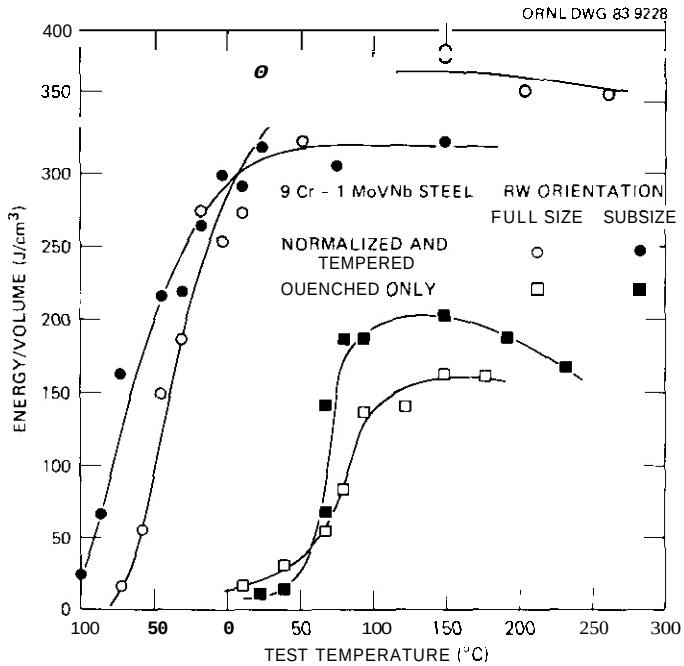

Fig. 7.5.16. Normalization of Charpy impact energy data using the nominal fracture volume. RW orientation of the 9 Cr-1 MoVNb steel (heat 30176).

Table 7.5.1. Upper shelf energy and transition temperature for 9 Cr-1 MoVNb steel HT 30176

Orientation	Basis[a] and (units for upper-shelf energy)	Upper-shelf energy			Transition temperature[d] (°C)		
		N&T[b]	Q[c]	Drop (%)	N&T[b]	Q[c]	Shift
	Size, 10 by 10 by ***55 mm; notch mdius, 0.25 mm***						
WR	E (J)	202	76	62	−8	53	61
WR	A (J/cm²)	250	90	64	−11	55	66
WR	V (J/cm³)	275	98	58	−18	56	74
RW	E (J)	264	117	56	−31	79	110
RW	A (J/cm²)	332	143	57	−38	78	116
RW	V (J/cm³)	372	162	56	−33	77	110
	Size, 5 by 5 by ***55 mm; notch mdius,*** 0.05–0.10 mm						
WR	E (J)	26.6	15.7	41	−51	51	102
WR	A (J/cm²)	124	74	40	−47	57	104
WR	V (J/cm³)	267	163	39	−60	50	110
RW	E (J)	31.3	18.4	41	−68	71	139
RW	A (J/cm²)	148	89	40	−87	67	154
RW	V (J/cm³)	320	190	41	−65	68	133
	Size, 5 by 5 by ***55 mm; precracked***						
WR	E (J)	8.5	5.4	36	−25	96	121
RW	E (J)	10.0	*e*	*e*	−13	*e*	*e*

[a]Basis for Charpy energy used in upper-shelf and transition-temperature determinations are E = energy; A = energy/fracture area; V = energy/nominal fracture volume.

[b]Normalized and tempered condition.

[c]Quenched-only condition.

[d]Determined at 50% of upper shelf.

[e]Insufficient data.

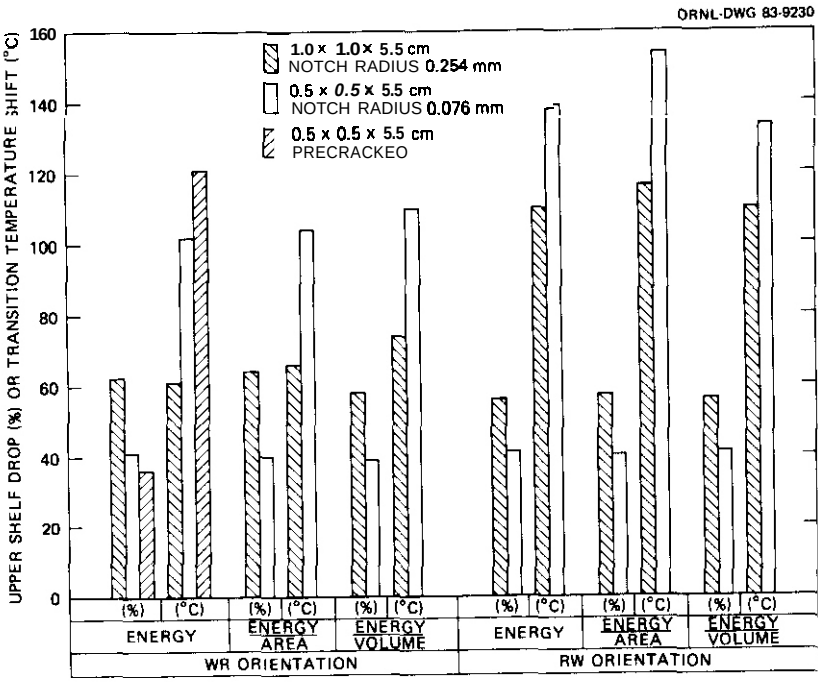

Fig. 7.5.17. Summary of the effects of specimen type, orientation, and normalization basis on the drop in upper shelf energy and shift in transition temperature. Property changes **are** for quenched compared to normalized-and-tempered 9 Cr-1 MoVNb steel.

1.5.5 Conclusions and Future Work

In examining the impact energy of full- and subsize specimens of 9 Cr-1 MoVNb steel in two orientations in both the N&T and Q conditions, the following was determined:

1. For the given material condition, the subsize V-notch specimen yielded a lower transition temperature in all cases than did the full-size specimen, with the greater differences for the N&T material. In contrast, the precracked subsize specimen yielded a higher transition temperature.
2. The Q material exhibited a decreased upper-shelf and a higher transition temperature than did the NT material for all specimen types. This heat treatment was useful for evaluating the effect of specimen size on measurement of the degree of material embrittlement that may be typical of radiation effects.
3. Normalizing the impact energy to fracture area or fracture volume showed that the low-energy tests with little plastic deformation were better correlated on an area basis and that the higher energy tests gave better agreement after volumetric normalization. Neither method was particularly successful; therefore, a more sophisticated treatment is required.
4. For all conditions examined and bases of analysis used, the subsize V-notch specimens produced a greater transition-temoerature shift and a lower percentage reduction of upper-shelf energy than did the full-size V-notch specimen.

Future work will include examination of other subsize specimens, including those with the same span-to-width ratio of 4:1 that will be used with the irradiated specimens. More sophisticated correlation and comparison methods for data generated with the different size specimens will also be investigated.

7.5.6 References

1. "Standard Methods for Notched Bar Impact Testing of Metallic Materials, E 23," *1982 Annual Book of ASTM Standards, Part 1o,* herican Society far Testing and Materials, Philadelphia, *1982.*

2. V. K. Sikka and R. H. Baldwin, "Tensile Testing," *Advanced Alloy Technology Program Semiannu. Prog. Rep. Mar. 31, 1981,* ORNL/MSP/1.7-81/1, pp. 2-73–2-135.

3. W. J. Stelzman and D. A. Canonico, "Charpy V-Notch Toughness Studies," *Advanced Alloy Technology Program Semiannu. Prog. Rep.* Mar. *31, 1981,* ORNL/MSP/1.7-81/1, pp. 2-135–2-140.

4. J. M. Vitek and J. W. Woods, "Experiments HFIR-MFE-RB1, -RB2, and RB3 for Low Temperature Irradiation of Path E Ferritic Steels," pp. 3C–35 in *ADIP Semiannu. Prog. Rep. Sept. 30, 1981,* DOE/ER-0045/7, U.S. DOE, Office of Fusion Energy.

5. W. L. Hu and N. f. Panayotou, "Miniature Charpy Test Device Development and Impact Test Results for the ferritic Alloy HT9," pp. 235–62 in *ADIP Semiannu. Prog. Rep. Sept. 30, 1981,* DOE/ER-0045/7, U.S. DOE, Office of Fusion Energy.

7.b The Toughness of Simulated Heat-Affected Zone Microstructures in HT-Y (ESR Melt Practice) - J. C Lippold (Sandia National Laboratories, Livermore)

7.6.1 AUIP Task

The Department *of* Energy (UOE)/Office of Fusion Energy (OFE) has stated the need for these data under ADIP program task, Ferritic Steels Uevelopment (Path El.

7.6.2 Objective

Several distinct microstructural regions have been identified in the HAZ of 12Cr-1Mo-U.3V steels (HT9). The purpose of this investigation is to evaluate the toughness of two of these regions in the electroslag remelted (ESR) National Fusion Heat. The toughness properties of these regions following postweld heat treatment (PWHT) will be compared to the properties of HAZ microstructures from the AOO-processed reference heat which have experienced identical thermal histories.

7.6.3 Summary

The toughness behavior of the heat-affected zone in the ESR National Fusion Heat was determined using Gleeble-simulated microstructures. Two regions of the HAZ were evaluated; one region represents the portion of the HAZ nearest the fusion zone, the other corresponds to a region which is heated only slightly above the upper critical temperature. Charpy V-notch results indicated that following a PWHT at 760°C for 1 hour both regions of the HAZ exhibit superior toughness behavior to that of the quench-and-tempered base material. The upper shelf toughness increased 20-40 Joules and the DBTT decreased nearly 20°C relative to the base metal. The toughness of both the ESR base material and HAL microstructures was superior to that of the AOD-processed National Fusion Heat, which had been previously tested in a similar manner.

7.6.4 Progress and Status

7.6.4.1 Introduction

The heat-affected zone (HAZ) in 12Cr-1Mo-U.3V martensitic stainless steels, such as HTY, can exhibit a variety of microstructures whose mechanical properties differ significantly fran those of the base material. Evaluation of *HAL* microstructures from welds in the AOD-processed National Fusion Heat revealed that at least four distinct regions are present in the as-welded condition.[1-3] These microstructures and their relation to the Fe-Cr-C pseudo-binary phase diagram are summarized in Figure *1.* Note that regions 1-3 are reaustenitized during welding and subsequently transform to untempered martensite upon cooling below the inartensite start temperature (M_s). A postweld heat treatment (PWHT) is necessary to reduce the hardness and provide a microstructure whose properties are comparable to the quench-and-tempered base metal.

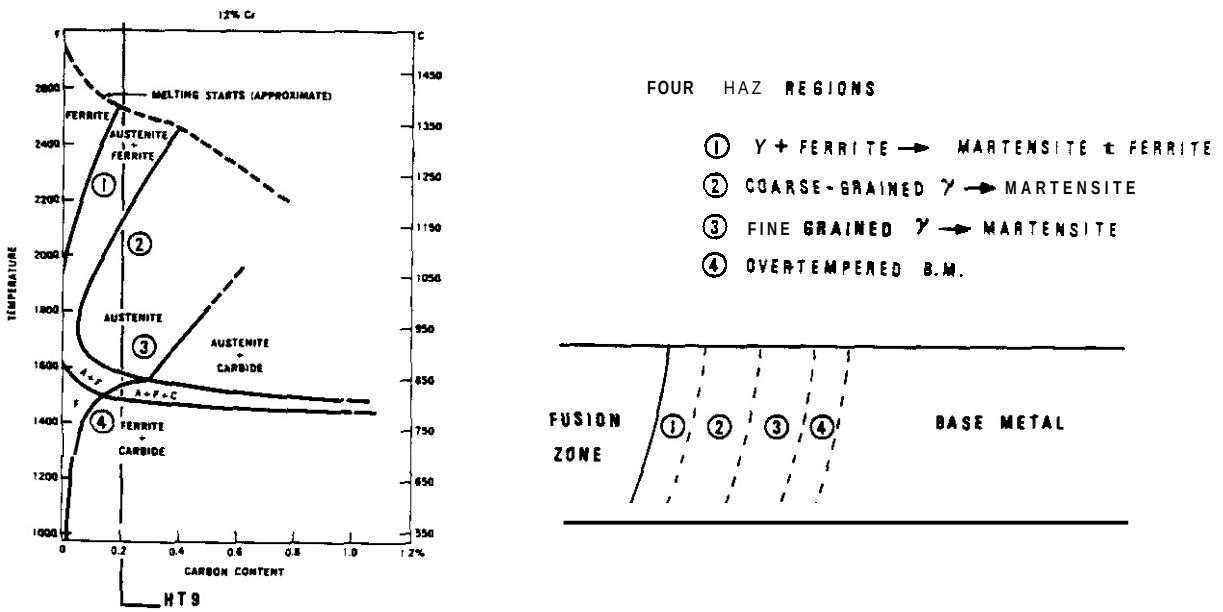

Figure 1. Relationship between the Fe-Cr-C pseudo-binary phase diagram and the four HAZ regions observed in HT9 weldments.

Previous investigations have shown the effect of PWHT on the toughness of the four HAZ regions in AOO-processed HT9. [4-6] It was shown that PWHT temperatures below 600°C for 1 hour resulted in only a slight softening of the as-welded structure. A PWHT at 600°C provided some recovery of toughness properties, but, in general, the HAZ properties were inferior to those of the base metal. Finally, a PWHT at 760°C for 1 hour resulted in toughness properties throughout the HAZ which were at least equivalent to the base metal toughness. The toughness properties of the HAZ microstructures from the AOD-processed National Fusion Heat are sumnarized in Table 1.

Sumnary of Charpy Results (AOD)

HAZ Regio	PWHT*	DBTT (K)	Lower Shelf (J)	Upper Shelf (J)
	High	288	15	80
	Low	318	7	42
	High	275	15	65
	Low	313	5	45
	High	273	27	90
	Low	303	10	45
4	High	275	15	60
	Low	273	15	60
Base meta	Q/T**	266	15	61

*High: 1033K/1 hi tow: 873K/1 hr
**Q/T : 1323K/0.5 /AC, 1033K/1 hr

7.6.4.2 Experimental Procedure

The material evaluated in this investigation was an electroslag remelted (ESR) heat originally produced by the argon-oxygen decarburization (AOD) melting process. The details of the melting and breakdown procedure were previously reported by GA Technologies, San Diego.[7] The compositions of the ESR heat and the starting AOD heat are listed in Table 2. Material was provided as 15mm thick plate in the stress relieved condition. The plate was sectioned and given the standard quench-and-tempered (Q/T) heat treatment consisting of austenitizing at 1050°C for 30 minutes air cooling, and then tempering at 760°C for 1 hour. The hardness of the Q/T base material was R_C 24-26.

CHEMICAL COMPOSITON LIMITS

HEAT	C	Si	Mn	P	S	Cr	Mo	Ni	V	W	N	Al	Ti	other (Max.)
DIN. SPEC (1.4935)	.17/ .23	.1/ .50	.3/ .80	0.035 (max)	0.035 (max)	11.0/ 12.5	0.8/ 1.20	.3/ .80	.25/ .35	.4/ .6				
AOD (9607)		.24	.57	0.018	0.007	11.64	1.01	.52	.30	.57	.044	.009	<.01	O_2 .013, Co 0.01
ESR (9607R2)	.20	.17	.57	0.016	0.003	12.1	1.04	.51	.28	.45	.027	.008 .007	.001	Cu .07, Co <0.05, As 0.003 O_2 .002, B <.001, Bi <.001 Pb <.0001, Sb 0.0005 Sn 0.004, Q <.001

The presence of four separate and distinct microstructural regions within the HAZ of 12Cr-1Mo-0.3V welds poses the problem of unambiguously evaluating the HAZ. Rather, it would be desirable to evaluate each region individually in order to determine its unique properties. To accomplish this task, the Gleeble®, a highly precise thenno-mechanical simulator, was utilized to synthetically produce the microstructures in bulk samples. Gleeble blanks 11 x 11 x 100mm were machined with the 100mm dimension either transverse or longitudinal to the rolling direction (R.D.). The blanks were

then thermally cycled in the Gleeble to simulate Regions 1 and 3 in the HAZ (Figure 1). The temperature-time history of the Gleeble heat treatments is shown in Figure 2. Following the Gleeble simulation, the blanks were tempered at 760°C for 1 hour. This tempering treatment represents the PWHT.

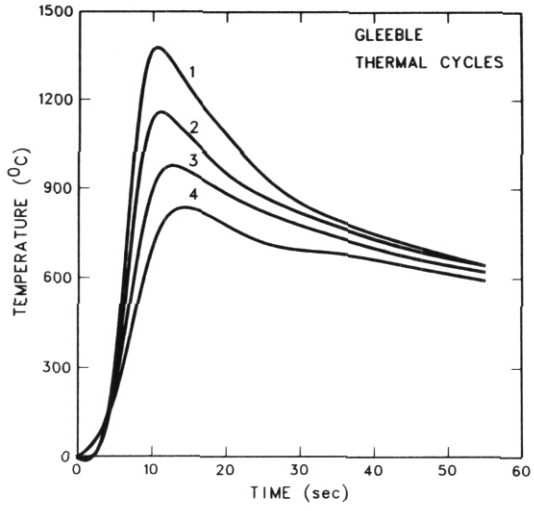

Figure 2. Gleeble thermal cycles used to simulate the four HAZ microstructures.

Standard Charpy V-notch samples 10 x 10 x 55mm were machined from the Gleeble-treated and tempered blanks such that the notch was located within the uniform microstructural region produced during the Gleeble thermal cycle. Toughness values measured in terms of absorbed enegy (Joules) were determined in the range fran -b0 to 100°C.

7.6.4.3 Results

The microstructures of HAZ Region 1 and Region 3 samples following the PWHT at 760°C/1 hr are shown in Figure 3. Region 1 exhibits a relatively coarse prior austenite grainsize resulting from heating to an extremely high austenization temperature. Careful examination of this microstructure revealed the presence of a small mount of delta ferrite (high temperature ferrite) along prior austenite grain boundaries. This ferrite forms during heating into the two-phase delta ferrite plus austenite region (Figure 1) and does not completely dissolve during cooling after welding or during the PWHT. The Region 3 microstructure contains a very fine prior austenite grain size. The grain refinement in this HA2 region results from reaustenization at a temperature only slightly above the upper critical temperature (Ac_3). In this temperature regime there is little thermal driving force for grain growth; in addition, base metal carbides which do not completely dissolve in this temperature range tend to retard the movement of the austenite grain boundaries.

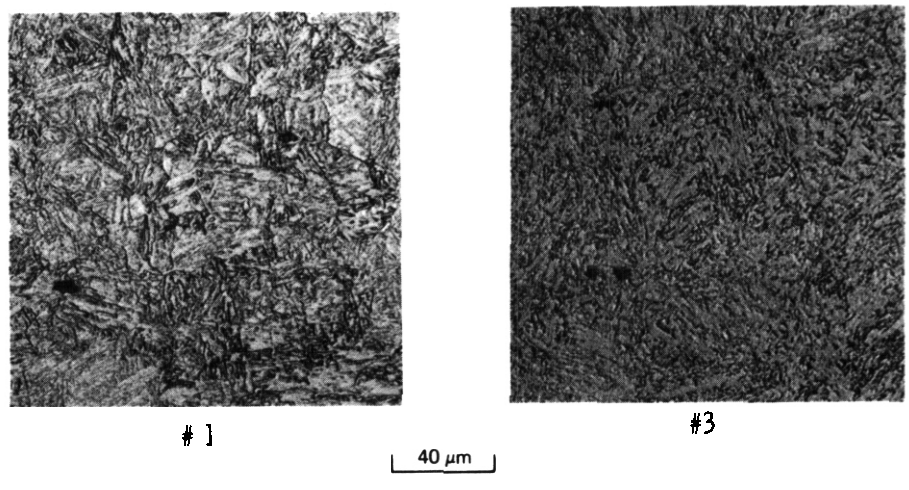

Figure 3. The microstructure of simulated HAZ regions after PWHT at 760°C/1 hr, a) Region 1; b) Region 3.

The microstructures simulated in the Gleeble were metallographically identical to the actual HAZ microstructures produced in the welded HT9/ESR plate. In addition, the Gleeble heat treated and tempered microstructures were similar to AOD-processed material subjected to the same thermal history. The ferrite stringers observed in the AOD plate were not present in the ESR plate.

7.6.4.3.1 Charpy V-notch Results

Charpy V-notch toughness plotted in terms of energy absorbed (Joules) versus temperature for the two ESR HAZ regions tested in both the T-L and L-T orientation is presented in Figure 4. Samples oriented parallel to the rolling direction (R.D.), the L-T orientation, exhibited superior toughness behavior to companion samples tested in the T-L orientation.

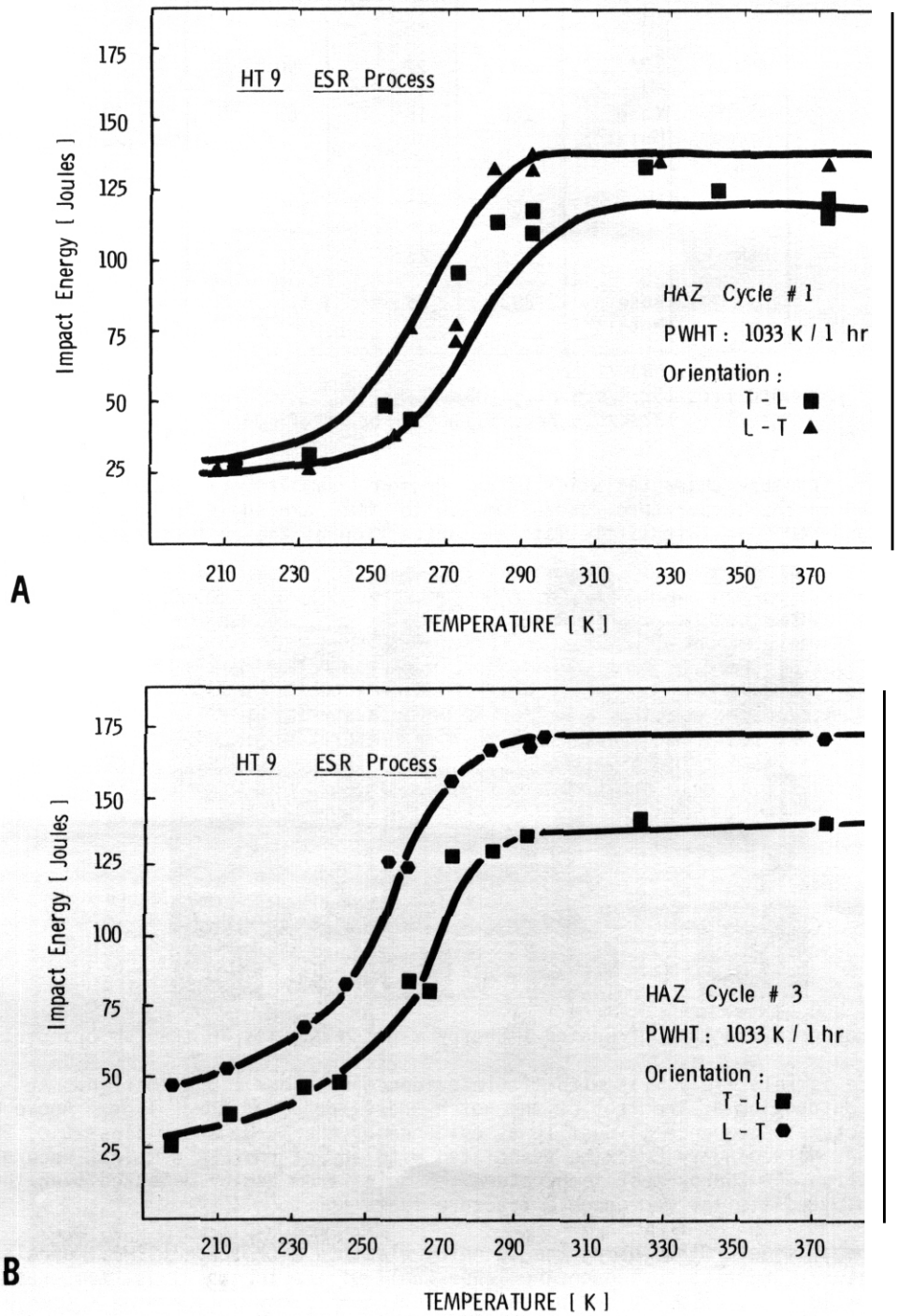

Figure 4. Charpy V-notch results for samples in the L-T and T-L orientation after PWHT at 760°C/1 hr, a) Region 1, b) Region 3.

Table 3 summarizes the toughness behavior of the ESR material and compares this behavior with that of the AOD material subjected to the identical Gleeble simulations and PWHT. The base metal toughness of both the AOD and ESR material is listed for reference. Note that the upper shelf toughness of Regions 1 and 3 after PWHT is superior to that of the base metal for both melt practices. In addition, the HAZ of the ESR material exhibits a reduction in DBTT relative to the base metal. In contrast, the simulated HAZ microstructures fran the AOD material exhibit an increase in DBTT relative to the base metal.

Effect of Melt Practice on HAZ Toughness

Melt Practice	HAZ Region	DBTT (K)	Lower Shelf (J)	Upper Shelf (J)
AOD	1*	288	15	80
	3*	273	27	90
	Base Metal**	266	15	61
ESR	1*	268	27	122
	3*	263	27	142
	Base Metal***	283	25	110

*PWHT: 1033K/1 hr.
**Q/T : 1323K/0.5 hr., 1033K/1 hr.
***Q/T : 1323K/0.5 hr., 1033K/2.5 hr. (Ref. 7)

7.6.4.3.2 Fracture Behavior

The macroscopic fracture characteristics of HAZ Region 1 samples oriented transverse to the R.D. (T-L) and tested in the temperature range fran -60 to 100°C are shown in Figure 5. The samples broken at -60 and -40°C exhibit little lateral contraction at the root of the notch. The overall

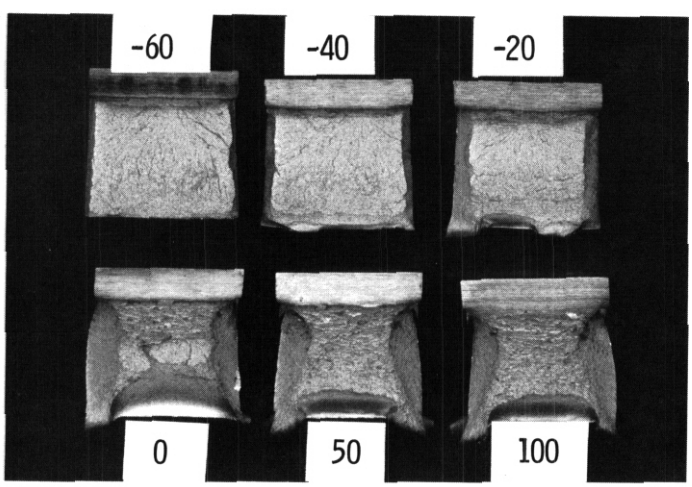

Figure 5. Macroscopic fracture of Region 1 Charpy V-notch samples in the T-L orientation.

fracture surface is relatively flat with little evidence of shear lip formation. At -20°C there is noticeable contraction at the root of the notch and evidence of shear lips. Above 0°C the macroscopic fracture appearance is ductile as evidence by the large shear lips at 0, 50, and 100°C. There was no secondary cracking associated with any of the ESR samples, regardless of HAZ region, orientation, or Charpy test temperature. Samples from Region 3 tested over the same temperature exhibited similar macroscopic fracture features.

The fracture mode, as determined using the scanning electron microscope (SEM), was also a function of test temperature. Samples tested on the lower shelf of the toughness vs. temperature curve failed by quasi-cleavage, as evidenced by the fracture morphology of a Region 1 sample tested at -40°C and shown in Figure ba. On the upper shelf the failure mode was predominantly ductile rupture (Figure 6b). The dimple size was generally bimodal; small dimples nucleate at carbides

along prior austenite and martensite lath boundaries while the large dimples (Figure 6b) nucleate at Al-rich inclusions.

In general, the simulated HAZ #3 samples exhibited superior toughness relative to HAZ #1 samples which experienced identical thermal histories. As an example, a HAZ #1 sample tested at 0°C failed at 72 Joules and a HAZ #3 sample tested at -12°C failed at 125 Joules (both were in the L-T orientation). Despite the lower test temperature the HAZ #3 sample failed in a ductile manner while the HAZ #1 sample exhibited a mixed ductile dimple/cleavage failure mode (Figure 7).

7.6.4.4 Discussion

Simulated HAZ microstructures fran the ESR National Fusion Heat of 12Cr-1Mo-0.3V steel exhibited superior toughness relative to both the quench-and-tempered ESR base material and the original AOD-processed material. Reference to Table 3 indicates that although the absolute value of the ESR upper shelf impact energy for both HAZ #1 and HAZ #3 is greater than the corresponding AOD value, the percentage increase above the base metal level is actually less. Thus, the intrinsic toughness of the quench-and-tempered base material is the most significant factor affecting the toughness of the HAZ after tempering at 760°C.

The increase in the base metal toughness of the ESR-processed material relative to the AOD reference heat probably results from a combination of factors including microstructural refinement, absence of ferrite stringers, and reduction in the overall inclusion content. These factors result in a "cleaner", more homogeneous microstructure which generally results in higher upper shelf toughness levels. The benefits of the ESR processing carries over into the HAZ when

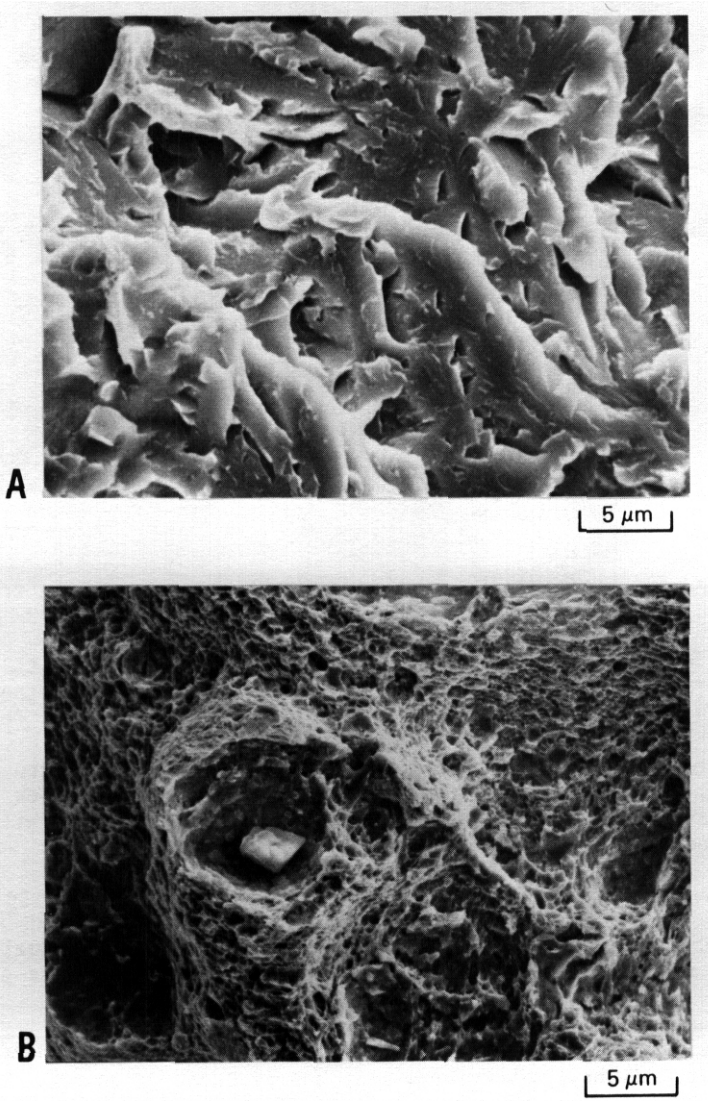

Figure 6. Fractographs of Region 1 Charpy V-notch samples tested at a) -10°C, b) 25°C.

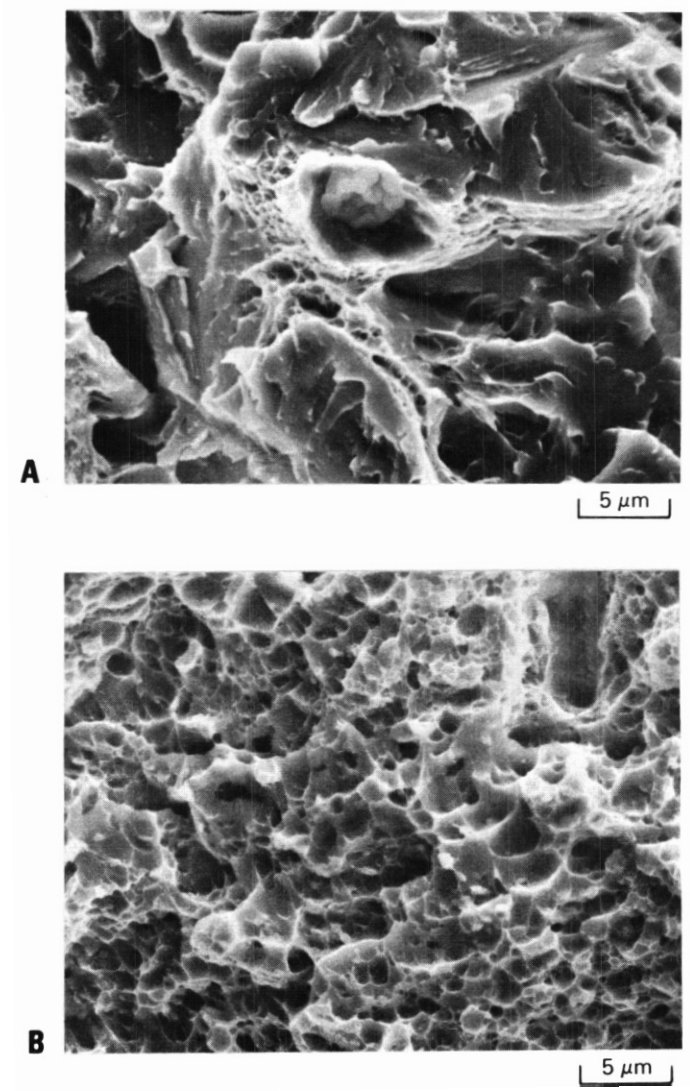

Figure 7. Fractographs of Charpy V-notch samples tested in the transition region, a) Region 1, 0°C, b) Region 3, -12°C.

the material is welded and a further increase in toughness results due to the double kat treatment which the HAZ experiences. In Region 3 particularly, the refinement of the prior austenite grain size provides the greatest increase in toughness relative to the base material.

In addition to an increase in upper shelf toughness, the HAZ microstructures exhibited a decrease in the DBTT. The shift in DBTT to a temperature nearly 40°C below ambient temperature provides an additional safety margin when designing welded structures which will experience a wide range of operating conditions.

7.6.5 Conclusions

1. Simulated HAZ microstructures fran the ESR National Fusion Heat exhibit superior toughness relative to both the base metal and identical microstructures produced from the AOD reference heat.

2. Upper shelf toughness of the HAZ increases 20-40 Joules over the base metal value following at PWHT at 760°C/1 hr.

3. The DBTT of the HAZ decreases nearly 20°C below the base metal DETT following a PWHT at 760°C.

7.6.6 References

1. J. C. Lippold, "Weldability of HT-9: The Autogenous GTA Process", ADIP Quarterly Report, DOE/ER-0045-2, July 1980, pp. 98-108.

2. J. C. Lippold, "Tempering and Transformation Behavior of HT9 Weldments", ADIP Quarterly Report, DOE/ER-0045-3, October 1980, pp. 216-225.

3. J. C. Lippold, "Transformatin and Temperiang Behavior of 12Cr-1Mo-0.3V Martensitic Stainless Steel Weldments," Proceedings of the Second Topical Meeting on Fusion Reactor Mateials, Seattle, WA August 1981, pp. 1127-1133.

4. J. C. Lippola, "THe Effect of Postweld Heat Treatment on the Toughness of the Heat-Affected Zone in 12Cr-1Mo-0.3 V Steel (HT9)," ADIP Quarterly Report, DOE/ER-0045-8, March 1982, pp. 388-398.

5. J. C. Lippold, "The Toughness of Simulated Heat-Affected Zone Microstructures in a 12Cr-1Mo-0.3V Martensitic Stainless Steel," ADIP Quarterly Report, DOE/ER-0045-8, March 1982, pp. 371-387.

6. J. C. Lippold, "The Effect of Postweld Heat Treatment on the Microstructure and Properties of the Heat-Affected Zone in 12Cr-1Mo-0.3V (HT9) Weldments," presented at the conference Ferritic Alloys for Use in Nuclear Energy Technologies, Snowbird, Utah, June 1983.

7. T. A. Lechtenberg, "The Procurement and Characteization of the ESR National Fusion Program Heat of 12Cr-1Mo Steel", ADIP Semiannual Report DOE/ER-0045/8, March 1982, pp. 363-369.

1.7 Fractographic Examination of Cracking in HT-9 Multipass **Welds** — (Sandia National Laboratories, Livermore)

To be reported in the next semiannual report.

7.8 The Influence of Prior Cold Work on the Hydrogen Charged Tensile Fracture of a 12Cr-1Mo Steel - W. M. Garrison, Jr. and J. M. Hyzak, Sandia National Laboratories, Livermore.

7.8.1 AOIP Task

The Department of Energy (DOE) Office of Fusion Energy (OFE) has cited the need for these data under the AOIP Program Task, Ferritic Alloy Development (Path E).

7.8.2 Objective

The goal of this study is to evaluate the hydrogen compatibility of 12Cr-1Mo ferritic/martensitic steel for use in first wall and blanket structures. This report summarizes data on the effect of internal hydrogen on the room temperature tensile properties of ESR processed 12Cr-1Mo steel.

7.8.3 Summary

Prior research on the tensile behavior of quenched-and-tempered 12Cr-1Mo steel has shown that the alloy is susceptible to grain boundary cracking in both the hydrogen charged and uncharged conditions [1,2]. In the present study, the quenched-and-tempered material has been cold worked by swaging to determine how distortion of the prior austenite grain boundaries affects the hydrogen charged fracture process. quenched-and-tempered bar stock was swaged to one of three different final reductions and tested in both the cold worked condition and after retempering to reduce the strength to the original quenched-and-tempered level. Tensile tests were performed on the specimens in both the hydrogen Charged and uncharged conditions.

Swaging and retempering improved both the uncharged and hydroyen charged tensile ductilities compared to the original quenched-and-tempered properties. For the largest swaging reduction, the uncharged tensile ductility (R_A) increased by 13%, and the hydrogen charged tensile ductility was 55% compared to 18% for the quenched-and-tempered specimens. The improvement in tensile ductility for the swaged-and-retempered specimens was associated with changes in fracture mode compared to the quenched-and-tempered material. The most noteworthy difference was that even after hydrogen charging the swaged-and-retempered specimens exhibited no intergranular cracking which was present in both the uncharged and hydrogen charged quenched-and-tempered specimens.

7.8.4 Progress and Status

7.8.4.1 Introduction

Studies of the hydrogen compatibility of a 12Cr-Mo steel (HT-9) have focused on the effect of internal hydrogen introduced by cathodic charging on its tensile ductility [1,2]. In the uncharged condition, tensile fracture of HT-Y was characterized by a dimpled rupture fracture mode primarily along prior austenite grain boundaries. Introducing 6-8 wppm internal hydrogen by cathodic charging reduced the ductility by 73% and changed the fracture mode to intergranular brittle fracture. These prior austenite grain boundaries contained high levels of phosphrous and were covered by a nearly continuous array of plate-like Carbides. While segregated impurities and carbides are believed to enhance decohesion along prior austenite grain boundaries [3,4], their relative importance in promoting the intergranular fracture in hydrogen charged HT-Y remains to be determined. However, sensitization of these boundaries appears to be the most important factor promoting the low ductility of hydrogen charged HT-Y. Cold work by swaging has been introduced in this study for two reasons: to increase the surface area of the prior austenite grain boundaries, effectively reducing the phosphorous concentration and carbide area fraction, and to provide boundaries less favorably oriented for intergranular fracture.

7.8.4.2 Experimental Procedure

The 12Cr-1Mo steel used in this study was 1.59 cm thick ESR processed plate with chemical composition:

C	Cr	Mo	V	W	Si	Mn	S	P
0.20	12.1	1.04	0.28	0.45	0.17	0.57	.003	.016

The transverse tensile properties of the unswaged material were determined using specimens machined from blanks austenitzed at 1050°C for 30 minutes, air cooled, tempered at 750°C for one hour and then water quenched. Round bars 1.59 cm in diameter were machined from the plate stock with their length transverse to the rolling direction. These bars were austenitzed and tempered as above, and then swaged at room temperature to final diameters of 1.27 cm, 0.97 cm and 0.63 cm. These diameters correspond to reductions in area by swaging of 36%, 63% and 84%, respectively. For each swaging condition some material was retempered at 730°C for two hours to

reduce the yield strength to that of the original quenched-and-tempered condition (≈725 MN/M^2). Round tensile specimens were then machined from the swaged, ana swaged-and-retemperea material. The tensile specimens had a gage diameter ana lenyth of 0.28 an, and 2.0 cm respectively.

Tensile specimens were cathodically chargea with hydrogen at room temperature at a current density of 0.006 A/cm^2 for either 2.5 or 24 hours in a 4% sulphuric acid solution containing 5 mg/ℓ of sodium arsenate as a recoiiibination poison. when charged for 2.5 hours the quenched-and-tempered plate material containea 6-8 wppm of hydrogen as measured by a LECO hydrogen aeterminator. After charging, the specimens were immediately plated with 0.004 cm of copper and then equilibrated 24 hours oefore testing. All tensile tests were run at room temperature at an initial strain rate of u.025/min.

7.8.4.3 Microstructure

The quenched-and-tempered microstructure had an equiaxed prior austenite grain size ot ASTM 3 (Figure 1a). The martensite was in the overtempered conditon with carbide precipitation at both martensite lath boundaries and prior austenite grain boundaries. The carbides precipitated at the grain boundaries were the larger of the two and were identified as the $M_{23}C_6$ type. These grain ooundary carbides which had a maximum lenyth of approximately 0.7μm were plate-line in shape and tormed a closely spaced but noncontinuous network along the boundaries (Figure 1b).

The swaged-ana-retempered microstructure was severely distorted along the swaging axis as shown in Figure 2 tor the 84% swaging reduction. The grain boundaries were no longer easily identifiable although estimates from measurements of the martensite packets indicated an aspect ratio of approxiinately 10. TEM replica examination of the carbide morphology revealed a slight coarsening of the precipitates in the swaged-and-retempered microstructure compared to the quenched-and-tempered structure.

7.U.4.4 Tensile Test Results - Swaged Microstructure

The yield strength of HT-Y. 74u MN/M^2 prior *to* swaging, increased with the degree of swaging and reached 1422 MN/M^2 after the 84% reduction (Figure 3). Subsequent annealing at 730°C for 2 hours reauced the yield strengths of all swaged material to that of the quenched-and-temperea structure (Figure 3). The tensile ductility, measured by reduction in area (R_A), decreased witn the mount of swaging (Figure 4). After the swaging reauction of 84%, the R_A decreased from 59% to 43%. However, the swayed-and-retempered material was more ductile than the original quenched-and-tempered structure. The swaying reduction of 84% when retemperea increased the ductility by 13% (Figure 4) compared to the unswayed specimens.

The introduction of hydroyen oy cathodic charginy reauced the tensile ductility for all material conditions (Figure 5). For all reductions, the swayed specimens had slightly lower ductility after charging for 2.5 hours than did the quenched-and-tempered specimens (Figure 5a). However, swaying followed by the retemper at 730°C resultea in substantial improvements in the hydrogen charged ductility of HT-Y; the two largest swaging reductions were the most eftective (Figure 5b). For example, charging at 0.006 A/cm^2 tor 2.5 hours reauced the R_A of the quenched-and-tempered HT-9 to 18%, while the ductilities ot the swaged-ana-retempered specimens decreased to only 55.9%, 56.7% ana 41.6% for swaying reduction of 84%, 63% and 36%, respectively. The same effect was seen after charging for 24 hours; the original material had a ductility of 10% while the structures swaged 84%, 63% and 36% ana then retempered had R_A values of 39%, 45.7%, and 17%, respectively.

The improved ductiiity of the swaged-and-retemperea specimens in both the uncharged and hydrogen charged conditions was associated with a change in fracture mode compared to the original quenched-and-tempered specimens. The tensile fracture of the quenched-and-temperea uncharged specimens was characterized by a microvoid coalescence and secondary cracking often along prior austenite grain boundaries [1,2] (Figure 6). However, secondary cracking along grain boundaries was not observed for the swayed-and-retemperea specimens with the two largest reductions (Figure 7). The material swaged only 36% before annealing exhibited some intergranular secondary cracking.

The differences in tracture behavior between the quenchea-ana-tempered and swaged-and-retempered specimens were more dramatic after hydrogen charging. Cathodic charging at 0.006 A/cm^2 for 2.5 hrs resulted in intergranular brittle fracture for the quenched-and-tempered specimens (Figure 8) and a dimpled rupture fracture mode for swaged-and-retempered specimens with the two 1argest reductions (Figure 9). While the uncharged and chargea specimens with the swagea-and-retemperea structures both failed by void coalescence, the mechanisms differed. In the uncharged conaition the tracture surface was rather tlat and failure occurred primarily by the coalescence of voids nucleated at carbiae precipitates (Figure 7). After hyarogen charging, the fracture surface was no longer flat but was characterizea by large conical mounds ana cavities with large inclusions at their center (Figure 9). Apparently, internal hydrogen caused preferential nucleation of voids at the larger inclusions. These initiation sites subsequently linked up by the nucleation ana growth of voids

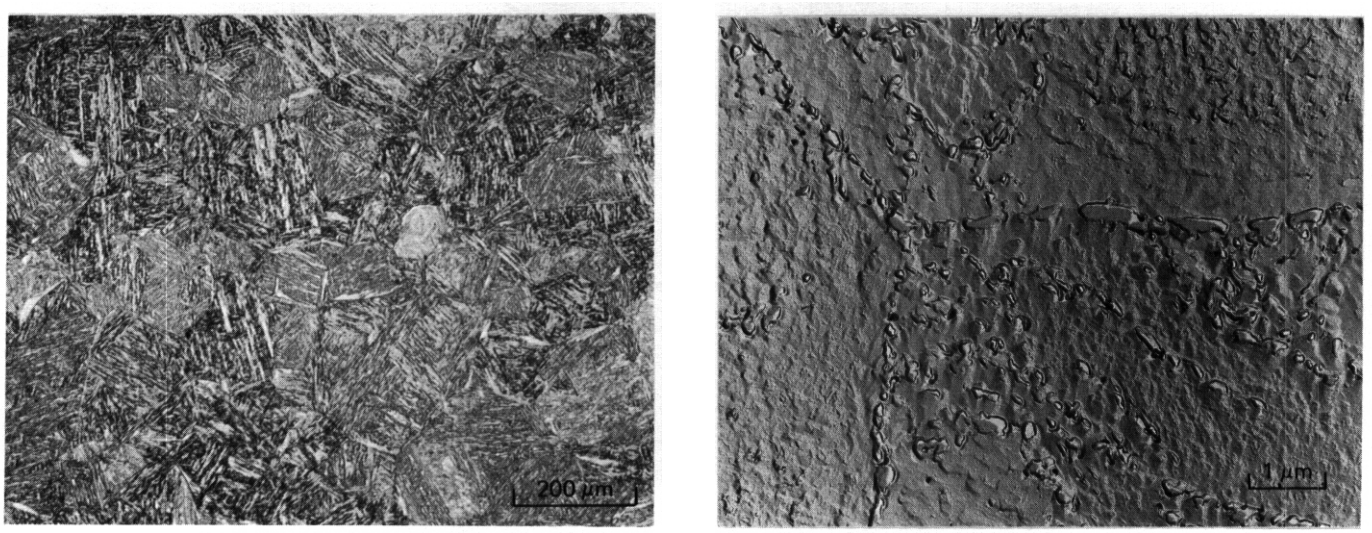

Figure 1. HT-9 quenched-and-tempered martensite microstructure; a) optical micrograph of prior austenite grain structure; and b) TEM replica micrograph of coarse carbide precipitation at prior austenite grain boundary.

Figure 2. Optical micrograph of swaged-and-retempered microstructure showing effacement of prior austenite grain structure.

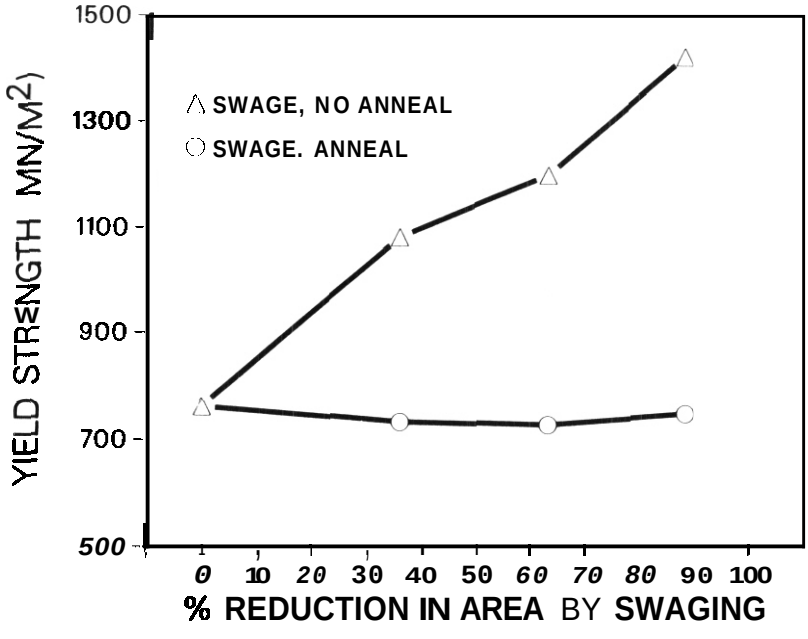

Figure 3. The effects of swaging and retempering on the yield strength (0.2% offset) of HT-9. The yield strength increases with the % reduction in area by swaging. Subsequent annealing at 730°C returns the strength of swaged material to that of the original quenched-and-tempered (0% swaged) condition.

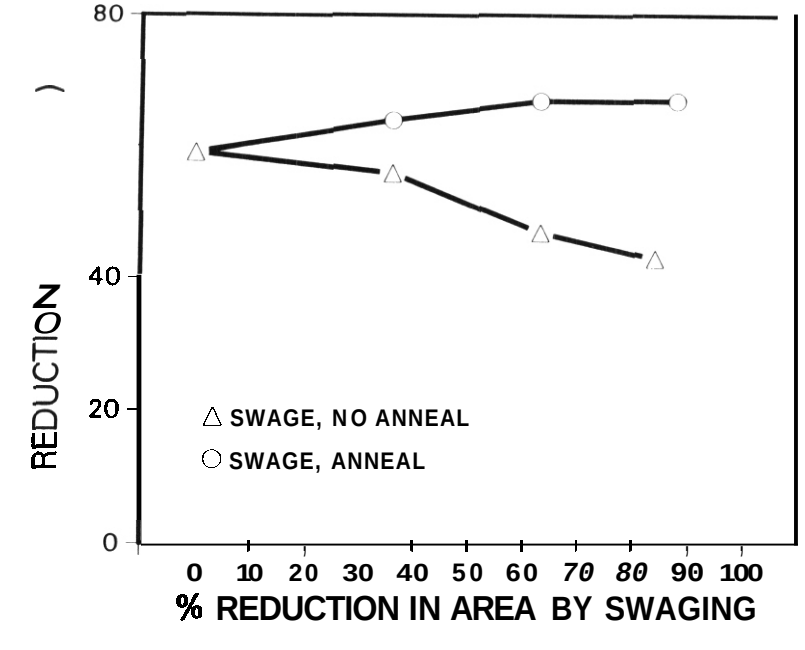

Figure 4. The effects of swaging and retempering on the tensile ductility of HT-9. The ductility decreases with the % reduction in area by swaging. After annealing at 730°C the ductility of the swaged material is superior to that of the quenched-and-tempered (0% swaged) conditions.

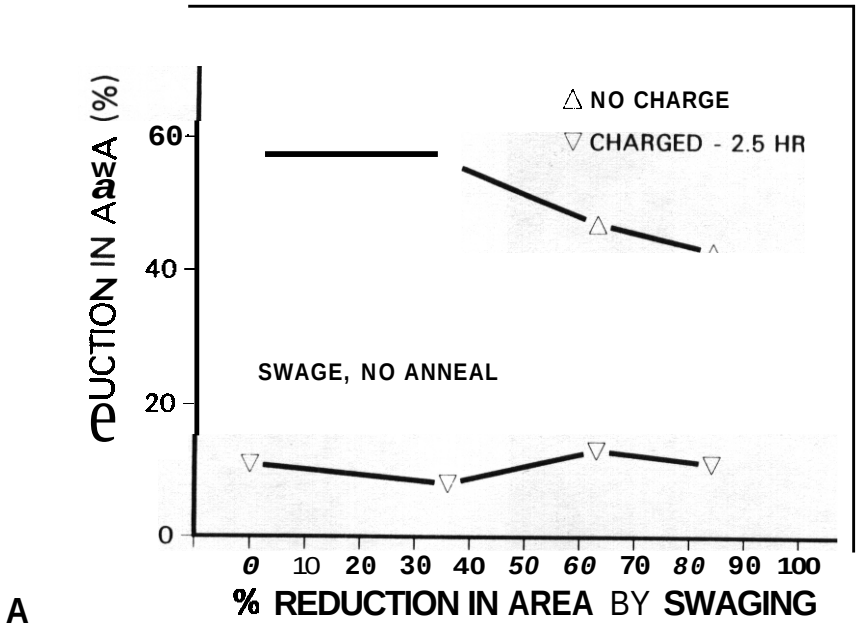

A

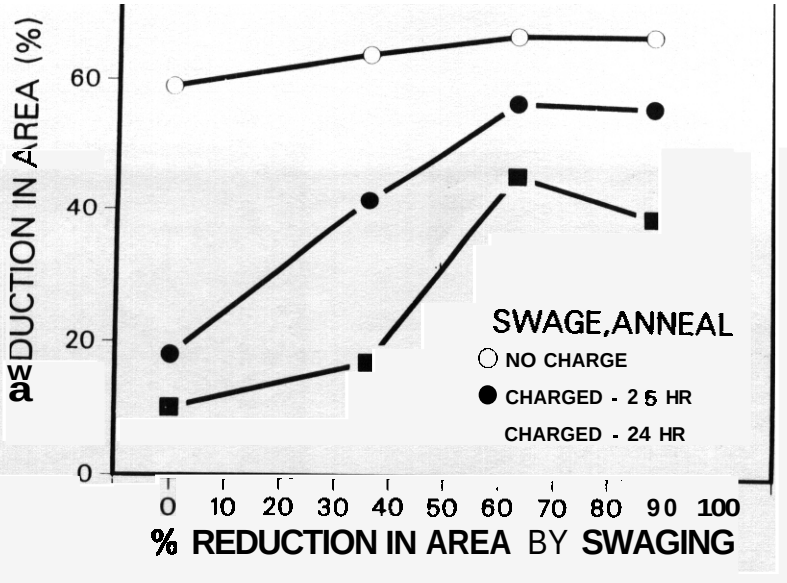

B

Figure 5. a) The effects of hydrogen charging for 2.5 hours on the tensile ductility of quenched-and-tempered (0% swaged) and swaged (not retempered) HT-9.
b) The effects of hydrogen charging for 2.5 hours and 24 hours on the tensile ductility of quenched-and-tempered and swaged-and-annealed (730°C) HT-9.

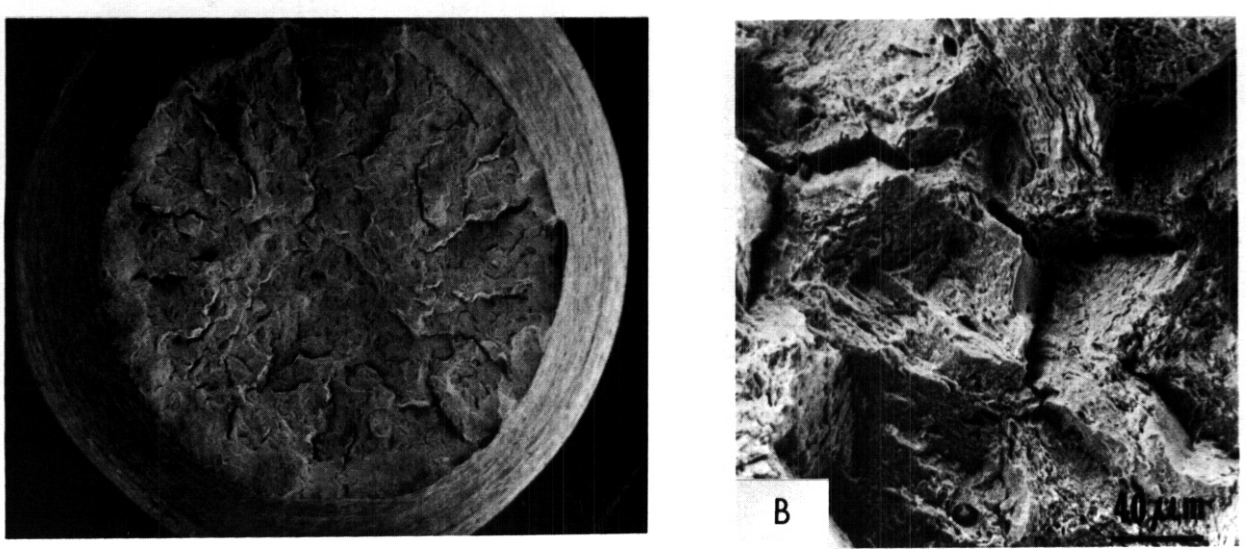

Figure 6. Uncharged quenched-and-tempered tensile fracture. SEM fractographs of a) cup-cone fracture and secondary cracking, and b) intergranular character of surface cracking.

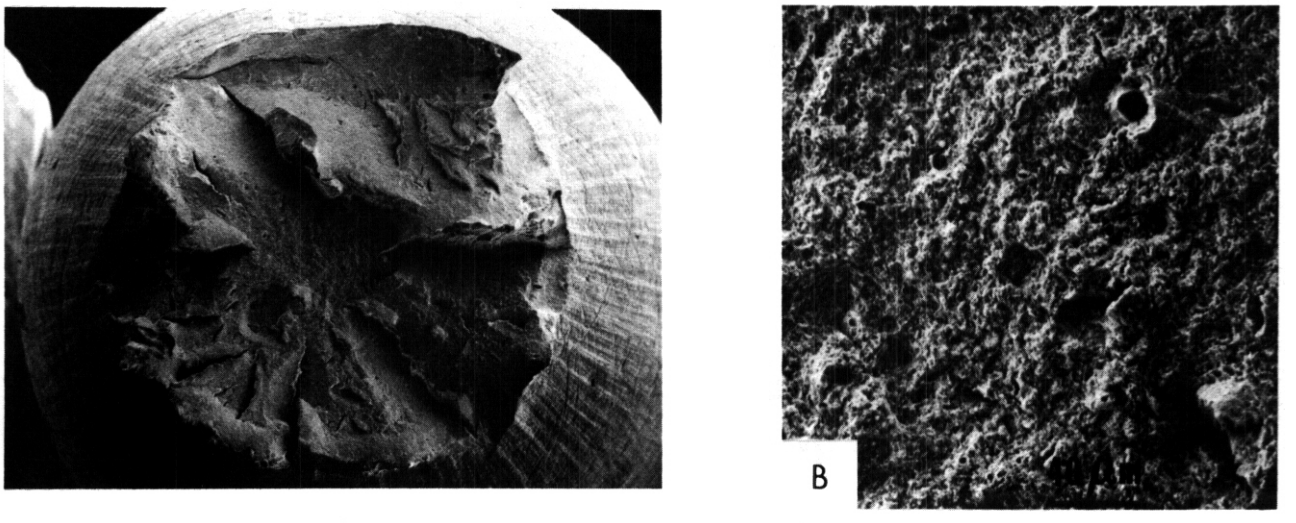

Figure 7. SEM fractographs of uncharged, swaged-and-retempered tensile fracture; a) cup-cone ductile fracture, and b) planar fracture path without grain boundary secondary cracking.

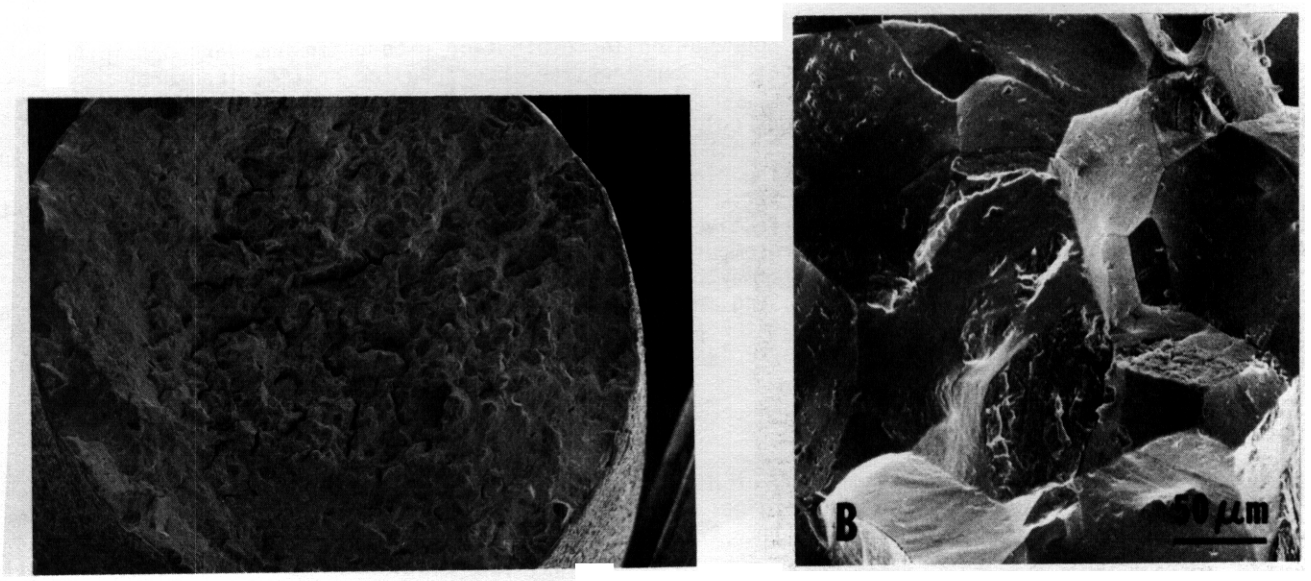

Figure 8. SEM fractographs of hydrogen charged (0.006 A/cm^2-150 min) quenched-and-tempered tensile fracture; a] brittle intergranular fracture surface, and b) smooth grain boundary facets.

Figure 9. SEM fractographs of hydrogen charged swaged-and-retempered tensile fracture; a) ductile fracture, and b) macroscopic dimples and mounds on the fracture surface.

associated with smaller carbides. Although hydrogen charging alters the fracture process of the swaged-and retempered specimens, they maintain much greater ductility after charging than the quenched-and-tempered material which fails by brittle intergranular fracture.

7.8.4.5 Uiscussion

Prior studies of this heat of HT-Y in the quenched-and-tempered condition have shown that the material is susceptible to grain boundary cracking both when uncharged and hydrogen charged [1,2]. This has been related to phosphorous segregation to prior austenite boundaries and a nearly continuous network of grain boundary carbides. In the uncharged condition, secondary cracking at prior austenite grain boundaries is by void nucleation and growth. As discussed by Cottrell [6], closely spaced grain boundary precipitates will favor ductile intergranular fracture. It has also been well documented that phosphorous segregation in combination with grain boundary precipitates C31 and internal hydrogen [4,5] enhances the tendency for intergranular brittle fracture.

These experiments have demonstrated that cold swaging and subsequent retempering can improve the tensile ductility of HT-9 both with and without internal hydrogen. Most notable is that swaging and retempering eliminated secondary cracking along prior austenite grain boundaries in the uncharged tensile fractures and intergranular brittle fracture after charging. Swaging alone or insufficient swaging reductions (36%) are not as effective in improving tensile ductility. The improved ductility resulting from swaging and retempering is related to the mechanical distortion of the prior austenite grain boundaries. This may be because swaging increases the surface area of the prior austenite grains, thereby decreasing the segregant concentrations and carbide area fraction at these surfaces. Swaging also elongates the prior austenite grains parallel to the tensile axis; thus prior austenite grain boundaries are less favorably oriented for stress induced intergranular fracture.

7.8.5 Conclusions

Cold swaging and subsequent retempering of HT-9 improved both the uncharged and hydrogen charged tensile ductilities compared to the original quenched-and-tempered properties. For the 84% swaying reauction, the unchargea tensile auctility increased by 13% and the hydrogen charged (2.5 hr) ductility more than tripled compared to the unswaged specimens. However, the improvement in tensile ductility was dependent on swaging reduction; the tensile properties of those specimens reduced 36% and retempered were not as good as those swayed 63% and 84% and retempered. The increase in tensile ductility for the swaged-and-retemperea specimen (63% and 84% reductions) was associated with a change in fracture mode compared to the quenched-and-tempered specimens. In the uncharged conditions, the swaged-and-retempered specimens did not exhibit secondary cracking along prior austenite grain boundaries as observed for the unswaged specimens, and when hydrogen charged they failed by transgranular dimpled rupture rather than intergranular brittle fracture.

7.8.6 References

1. J. M. Hyzak and W. M. Garrison, Jr., "Hydrogen Embrittlement of ESR Processed 12Cr-1Mo Steel", ADIP Semiannual Progress Report, DOE/ER-0045/8, March 1982, pp. 401-413.

2. J. M Hyzak and W. M. Garrison, Jr., Topical Conference on Ferritic Alloys for Use in Nuclear Energy Technologies, June 19-23, 1983, Metallurgical Society of AIME, in press.

3. C. L. Briant and S. K. Banerji, Metall. Trans. A., 1979, Vol. 10A, p. 1729.

4. I. Olefjord, Intl. Metals Rev., 1978, Vol. 4, p. 149.

5. Ph. Lemble, A. Pineau, J. L. Castagne, Ph. Dumoulin and M. Guttman, Metal Science, 1979, Vol. 13, p. 496.

b. A.H. Cottrell, The Mechanical Properties of Matter, Wiley, New York, 1964, p. 322.

7.9 THE EFFECT OF PREHEAT ON THE MICROSTRUCTURE, HARDNESS AND TOUGHNESS OF HT-9 WELDMENTS - T. A LECHTENBERG AND J. R. FOULDS (GA TECHNOLOGIES)

7.9.1 ADIP Task

The Department of Energy (DOE)/Office of Fuslon Energy (OFE) has cited the need to investigate ferritic/martensitic alloys under the ADIP program task, Ferritic Steels Development (Path E).

7.9.2 Objective

A perceived Issue of martensitic steels is the ability to be readily welded. Preheating of weld joints is recanmended by producers of the 12Cr-1Mo steel (HT-9) to minimize cracking, but the recommendations give a wide latitude (200-450C). It is the purpose of this work to contribute to understanding the effect of preheat on welding behavior and resultant mechanical properties such as strength and Impact toughness In order to define the preheat limitations more quantitatively.

7.9.3 Summary

Prior studies have shown that HT-9 plates up to 1" thick can be successfully welded with preheats as low as 100°C. The use of a 100°C preheat of the base metal prior to welding HT-9 results in an increased toughness over that for a 400C preheat by about 13.5 Joules and a ductile-brittle transition temperature of -12°C which is 14°C lower than for 400°C preheated condition.

SEM examinations showed that there were significant increases in the dendrite spacing and Increased segregation due to the slower cooling rates in the 400°C preheat weld. This Segregation is commensurate with depletion of the "ferritizers" Cr, Mo, and W In the the surrounding matrix accompanied by Increases In the Ni concentrations. These results indicate the lowest preheat compatible with good welding practice should be used. The Investigation is continuing using TEM and SEM In the weld metal and HAZ. These results will be reported in further ADIP semiannuals.

7.9.4 Progress and Status

7.9.4.1 Introduction

In the last three years in which martensitic steels have been studied in Path E, welding has been done on fully restrained plates of thicknesses ranging fran 0.125 to 1.0 inches (for example, see Ref. 1). Thus far. preheats as low as 100C have been successfully used on plates of thickness 1.0 $Inch^2$.

HT-9 has been used successfully In Europe for many years. mainly as boiler tubing and piping in heat exchangers and boilers. However, the alloy has not been employed In structures as large and complex as those expectd for fusion machines. Some designs for the first wall and breeding blankets require relatively thick-wall tubing, while others dictate thin-walled, large outer diameter tubes which would be welded to manifolds. The preheat required will be different for the various designs because of the varying tolerance for distortion and relief of residual stresses. In one example of an HT-9 structure, the tube banks have a wall thickness of 0.227 cm and an outer diameter of 10.14 cm. This is a complicated design where tubes are bent in order to shape around the plasma, and are connected to headers at the top and bottom. In such a structure, it may be important to minimize the distortion during welding thus requiring a minimum preheat. However, counterposing this are the stresses Induced during welding which would be maximized by a lower preheat. For this reason, It is Important to determine the exact latitude in preheat that is permissible.

7.9.4.2 Experimental

Plates of the fusion AOD/ESR heat of HT-9 used for welding were given the standard heat treatment of 1050C for half hour and 760C for 2.5 hours both followed by an air cool. The plates were monitored for temperature by thermocouples attached to the surface, and the time was begun for heat treatment five minutes after the surface of the 0.5 In. plates came to the desired temperature. Prior to welding, the plates were machined to provide a 75° single V-groove with a 0.25 In. root gap and 0.06 In. root face. The welds were performed by the gas-tungsten arc process using MTS-4 filler wire and heat inputs of 26 kJ/in/pass. Each weidment required 6 passes. The plates were fully restrained by being tack welded to a large, reinforced backing. Interpass temperature, cooling rates and the preheat were monitored by thermocouples. The plates were given the standard 760°C for 2.5 hours post-weld heat treatment. The preheat and interpass temperatures were RT, 100C. and 400C.

Transverse weldment sections were Charpy Impact tested In the T-S orientation, the notch located in the center of the weld bead propagated in the plate thickness direction fra final to Initial weld pass. The specimens were 0.05 in. undersize In thickness. Charpy impact testing was performed on a microprocessor controlled ETI300 drop-weight Impact tester.

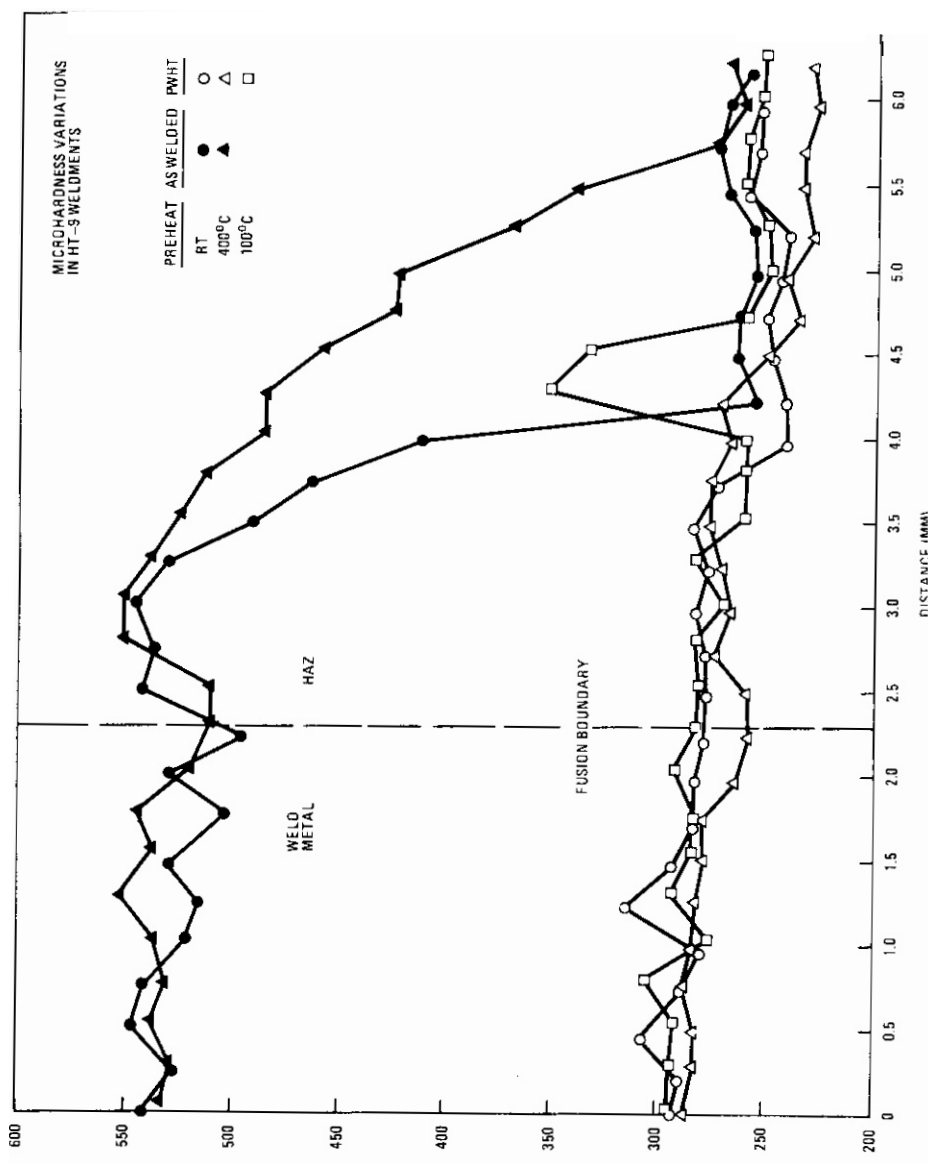

Fig. 7.9.1 **Microhardness variations in** HT-9 **weldments**

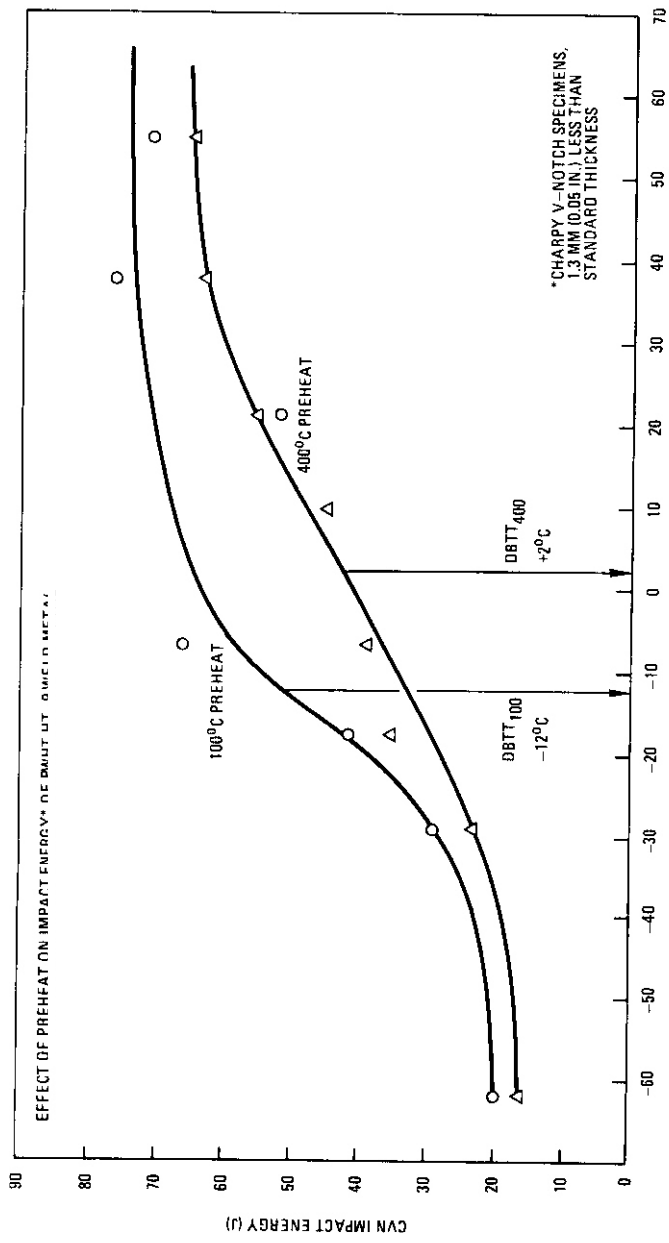

Fig. 7.9.2 Effect of Preheat on Impact energy* of PWHT HT-9 weld metal

7.9.4.3 The Effect of Weldment Preheating on the Mechanical Properties

Microhardness measurements were performed on the room temperature and 400C preheated as-welded condition and on the RT, 100C, and 400C preheat in the PWHT'ed conditions. These data are presented in Figure 7.9.1. As observed, the changes in the as-welded hardness profiles delineate the fusion zone/heat affected zone/base metal/ boundaries. The as-welded microhardness of the central weld metal region is about 535 DPH and shows little variation with preheat. At the fusion boundary, which was also discerned optically. there is a decrease in the hardness to 490DPH and then a recovery. This area is where ferrite is expected to form upon cooling. This hardness 'trough' is broader for the higher preheat condition although having the same depth. The HAZ is also wider for the 400°C preheat, being about 1.9 mm. After a 760C, 2.5 hr PWHT'ment the weld hardness decreased from about 530 DPH to 260DPH for all three preheat conditions. In all PWHT'ed conditions, the hardness in the heat-affected zones is lower than in the weld metal. The decrease is about 30-45 DPH. This **is** seen in Figure 7.9.1 for the RT, 100C and 400C preheat conditions. The PWHT'ed hardness is similar for all three conditions excepting for the 100C at approximately where the HAZ boundary is. At this point it increases about 100DPH then decreases within 0.75 mm to the base metal average of 260 DPH. This is being investigated.

Charpy V-notch specimens machined with the notch in the center of the weld metal were tested at temperatures from -62°C to 100°C. The data **is** presented in Figure 7.9.2. The transition curves for these weldments show that there are two differences seen, the upper shelf energy is 74.5J for the 100C preheat while it is 61.0J for the 400C preheated condition. Also, the DBTT is somewhat lower for the 100C preheat. It was measured as -12°C for the 100°C preheat and 2°C for the 400°C preheat. The enhanced effect of a higher cooling rate (lower preheat temperature, higher cooling rate) on the transition curves is in agreement with reported observations[3].

7.9.4.4 The Effect of Preheat on the Weld Microstructure

Optical macrographs of two weldments are shown in Figure 7.9.3. Figure 7.9.3a is of the as-welded condition with no preheat while the as-welded condition with 400°C preheat is shown in Figure 7.9.3b. There are two effects of higher preheat seen at this magnification. The first **is** that the weld beads and heat affected zones are larger, and the second **is** that the dendritic structure is coarser and more clearly defined. A closer inspection shoved that the 400C preheat had significantly less segregation as evidenced by coring. Coring, which is elemental segregation during solidification, often leads to precipitation in weld metal dendrite boundaries. Higher magnification optical micrographs of the weldments are shown in Figure 7.9.4. The weld with no preheat in Figure 7.9.4a has dendrite boundaries clearly outlined by a second phase. In Figure 7.9.4b, there is less evidence of coring but the phase that does exist in the boundaries (probably ferrite based on an **EDAX** analysis described below) is larger and better defined and spaced further apart due to larger dendrites. These effects are seen more clearly in Figure 7.9.5a, the RT preheat condition, showing the coring phase and a relatively finer dendritic structure as compared to the 400C preheat in (b) which clearly shows the coarser dendritic structure and a greater fraction of the dark appearing phase surrounding the barely visible ferrite core. Within the dendrites, typical martensitic structures are observed. The higher preheat temperature effected a slower weld metal cooling rate, increased the fraction of the dark ferrite surrounding phase and coarsened the dendrite structure, the latter being the controlling microstructural feature in fracture. It is possible, however. that this would change during thermal aging or service as segregants begin to play a more important role in the fracture pracess.

An EDAX analysis was performed on the phases seen in the weldments to determine the degree of segregation of major constituents. In general, for both preheat conditions, the phase within the dendrite boundaries contained elevated levels of ferriteforming elements Cr and Mo, while the surrounding area was depleted in them but contained elevated levels of NI. It was concluded from this that the phase in the dendrite boundaries was ferrite.

A closer inspection on the SEM of the phases in the dendrite boundaries revealed that there was a chranium rich phase surrounded by what may be another phase which appears dark on the SEM. These were surrounded by areas depleted in chranium and molybdenum. The light interdendritic phase seen in Figure 1.9.5 more evident at the lower preheat, appears to be ferrite, while the darkest area in which the ferrite seems to rest has an even higher chranium concentration. Recently. chranium rich ferrite in AISI 316 weld metal has been shown to exhibit a propensity for $M_{23}C_6$ precipitation at the ferrite– matrix interface with short term exposures at elevated temperatures (650°C)[3]. The relative proportion of the darkly etched phase surrounding ferrite appears to increase with an increased preheat temperature or Slower cooling rate. Longer times at carbide-forming temperatures with a slower cooling rate points to the possibility of the dark regions canprising carbides formed from interdendritic ferrite.

The EDAX results are given in Table 7.9.1 for the interdendritic ferrite and surrounding phases for both preheats. The higher preheat weld showed more segregation not visbie optically. The dendrites are not decorated as canpletely as one sees in the lower preheat (e.g., compare Figures 7.9.5a and 7.9.5b). SEM micrograhs show that there are two phases at the boundary, a light-appearing ferrite core in a dark-appearing matrix, the relative proportions of which depend on the preheat temperature or cooling rates.

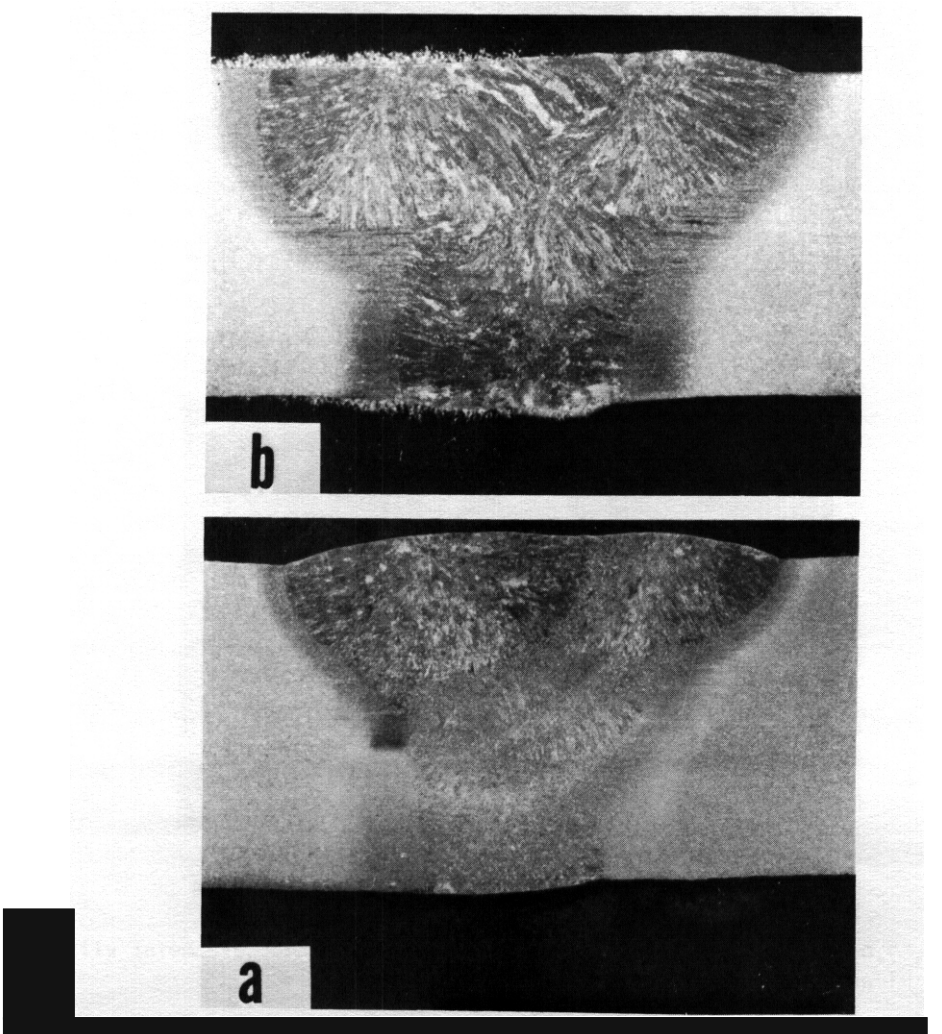

Fig. 7.9.3 Optical photomicrographs of the as-welded (a) RT and 400C preheat conditions. (5X)

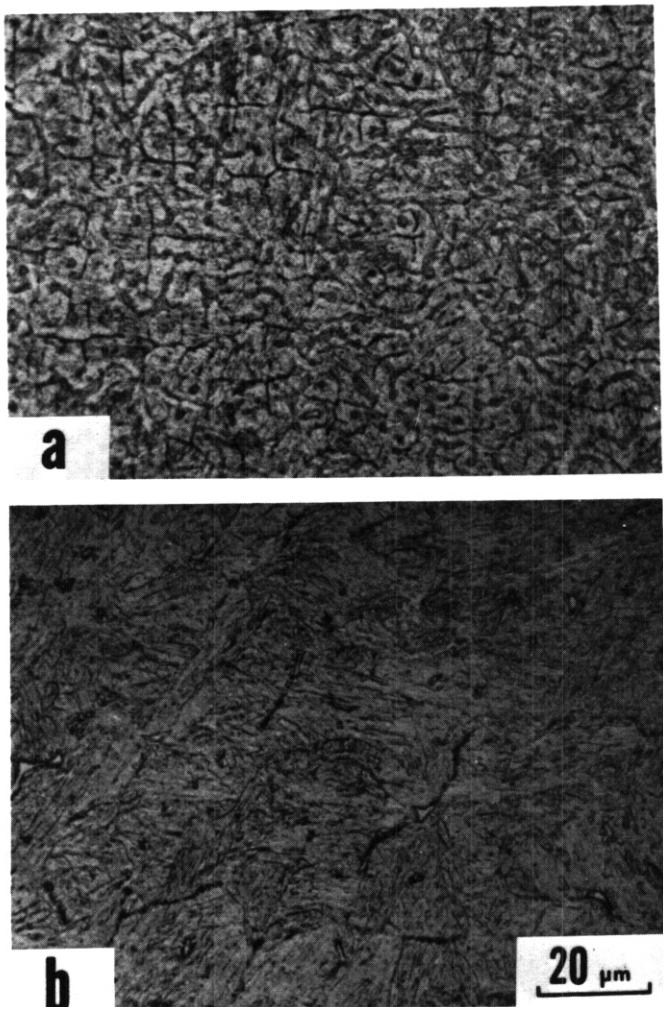

Fig. 7.9.4. Optical photomicrographs of the as-welded weld metal with (a) RT and (b) 400C preheat. (1000X)

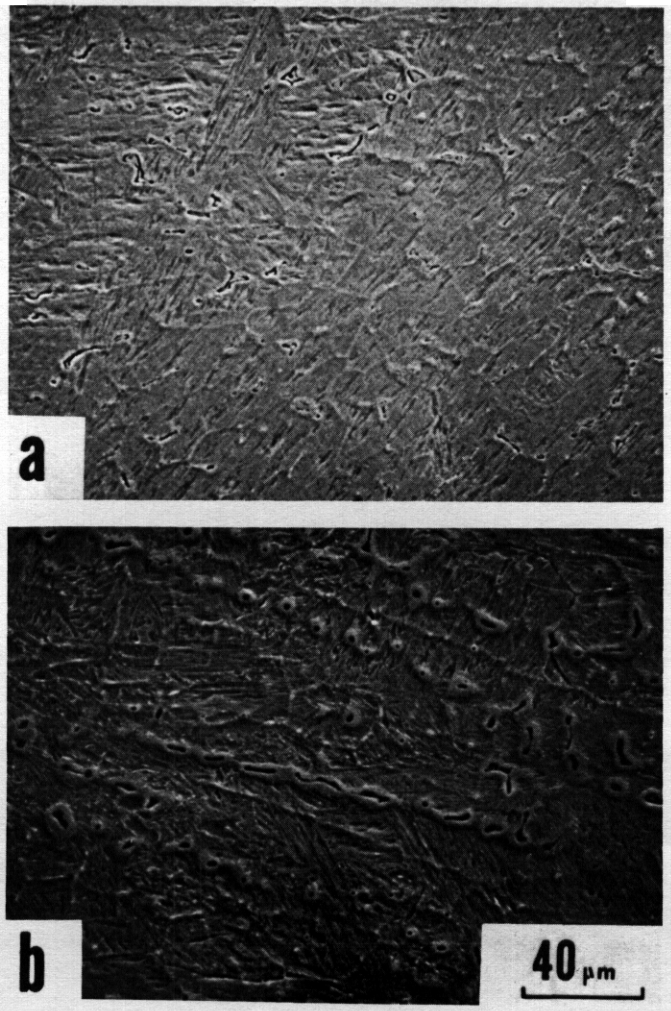

Fig. 7.9.5. Scanning electron micrographs of weldments in the (a) RT and (b) 400C preheat conditions, and both in the as-welded condition. (500X)

Table 7.9.1. Chemlcai composition* (wt%) of Interdendrltlc ferrite and surrounding areas In RT and 400°C preheat as-welded weld metal

Interdendrltic Ferrite Core			Dark Region Surrounding Ferrite		Depleted Zone Adjacent to Dendrite Boundary (grey)		Light Area (Weld Matrix)	
	RT	400	RT	400	RT	400	RT	400
Si	.60	.29	.50	.65	.32	.41	.49	.50
Mo	1.82	1.88	1.44	1.91	.60	.75	.59	.57
V	.30	.25	.22	.42	.16	.22	.10	.91
Cr	15.81	15.95	16.62	19.69	13.31	14.88	11.79	11.97
Mn	.70	.69	.76	.75	,69	.72	.54	.61
NI	-0-	-0-	.18	.10	.33	.17	.16	.10
W	.34	.16	.29	.45	.66	.37	-0-	.31

* From EDAX

7.9.5 Conclusions

Hlgher preheating results in coarser dendrltlc weld metal structures and Increased corlng brought on by segregatlon of ferrite-formlng elements. These coarse microstructural features appear to affect the weld toughness causing a decrease In the upper shelf from 74J to 61J when the preheat Increases from 100°C to 400°C. Furthermore, with this decrease In upper shelf toughness was also observed an increase in the DBTT fran -12°C to 2°C.

7.9.6 References

1. Llppold, J. and Lechtenberg, T., ADIP Semlannual Report DOE/ER-0045/7 for perlod ending 30 September 1981, p. 204.

2. Rosenwasser. S. et al, ADIP Quarterly Report DOE/ER-0045/1 for perlod ending 31 December 1979. p. *82.*

3. Garrison. W. and Hyzak, J. ADIP Semlannual Report DOE/ER- 0045/9 for perlod 31 December 1982.

4. Foulds, J. and Moteff, J., Met. Trans. 13A(1), 1982. pp. 173, 174.

7.10 AN ASSESSMENT OF FABRICATION METHODS FOR AN HT-9 FIRST WALL/BLANKET MODULE

T. A Lechtenberg and J. F. Hildebrand (GA Technologies., San Diego, CA)

7.10.1 ADIP Tasks

Alloy Development for Irradiation Performance. Ferritic Steel Development.

7.10.2 Objective

The object of this work was to assess the manufacturing and fabrication procedures for a first wall/blanket structure using HT-9 material. The TASKA blanket module was chosen as a representative reactor structure.

7.10.3 Summary

The first wall/blanket module structure for the TASKA tandem mirror reactor design is discussed relative to proposed materials and procedures for the fabrication. The TASKA design is a major reactor study for a near-term engineering test facility, the main objective of which was to develop a preconceptual design that could provide engineering design information for a Demonstration Fusion Power Reactor. This design was chosen for this study because HT-9 was used as the structural material and $Pb_{83}Li_{17}$ liquid metal as the breeder/coolant for the central cell modules, and presently is the only complete reactor study having done so. Frar the design, an assessment was made of materials, product forms and methods of assembly, heat treating, and joining to produce the unit. The results show that HT-9 can be used as a structural material for TASKA blankets. The tubes are 10.14 cm O.D. and 0.117 cm thick and cold bent to conform to the required shape of less than the manufacturers recommended maximum 2d bend radius. Welding recommendations include preheat of not less than 250°C and a post-weld heat treatment of 760°C for 2.5 hrs. The configuration of the pipe-to-manifold weidments and inspectability requirements suggest this module can be manufactured to present-day code requirements. Furthermore, the essential leak-tightness for a pressure boundary in the tubes appears practical. The results indicate a good feasibility that the proposed TASKA can be fabricated.

7.10.4.1 Description of TASKA Blanket

TASKA has a cylindrical shape formed by modules of the inner and outer walls or blankets. The tubes act as the first wall/blanket. Banks of thin-walled, HT-9 tubes bent to produce the cylindrical cavity for the plasma are attached to upper and lower manifolds as shown by Figure 7.10.1. The modules also interlock by a "step" with adjacent modules to reduce neutron streaming at the seams as shown by Figure 7.10.2.

Table 7.10.1. Pertinent dimensions for Taska tubes

Tube - HT-9	O. D.	10.14 cm (4 In.)
	Wall	0.227 cm (0.090 In.)
Transition Tube - HT-9	O.D.	5.0 cm (1 In.)
	Wall	0.175 cm (0.070 In.)
Manifold Plate - HT-9	Thickness	1.7 cm (0.670 In.)

A vertical cross section through the center of a module, Figure 7.10.1 shows eleven rows of HT-9 tubes on either side of the plasma zone. The end of each tube is attached to a smaller diameter tube by means of a conical transition section. The small diameter tube is then attached to the manifold. One side of the innermost large diameter tubes faces the plasma and becomes the effective first wall.

A horizontal cross section through two adjacent modules, Figure 7.10.2 shows the stepping of the tubes where the modules interface. it also shows the staggering of tubes needed to allow the two modules to slide out relative to each other at this interface. The modules shown have an axial length of 104 cm and have a blanket thickness of 100 cm. The radius to the front surface of the first tube row Is 46 cm. There are ten tubes in the front row and a total of 208 tubes In each module. A separation of 1 cm per meter is allowed between modules at room temperature. At operating temperature the gaps close to m0.4 cm.

The pertinent blanket/tube parameters are given in Table 7.10.1. The large diameter tubes are 10.14 cm O.D, and the wall thickness is 0.227 cm. The transition tubes are 5 cm O.D. and have a wall thickness of 0.175 cm. The axial centerline distance between tubes is 10.45 cm and the radial centerline distance is 9.05 cm. The 2-D bend radius toward the manifold is consistent with the minimum bend radius that can be produced without buckling the HT-9 tube wall in tubing of this size. The design of the blanket is such

TABLE 7.10.2.

Tube & pipe material standards that include 12Cr - 1Mo ferritic/martensitic steel alloys (a)

Standard No.	Standard Titles	Alloy Grade and/or Designation	Alloy Composition (wt %) Cr	Mo	C	Additions	Trade Names or Alloys	Known Producers of Alloy
BS 3604-78 (British)	Steel pipes and tubes for pressure purposes; ferritic alloy steel with specified elevated temperature proper-ies	CFS 762 HFS 762	12	1	0.2	0.3 V 0.5W-0.5Ni	(Equiv. to HT-9)	British Steel Corp.
None	This a l has been used in b form; ap-plicati have been in bar and rglogs	—	12	1 7	0 1	2.5Ni-0.3 V	Je hem M152	Bar: Samuel Fox & Co.,Ltd. British Steel Firth Brown, Ltd. Forgings: Steel, Peech & Tozer
DIN17175-79 (FRG)	Seamless steel tubes for elevated temp retur s	Werksoff No.	12	1	0.2	0 Ni-0.3V	HT-91	Mannesmann (Germany) Sandvik (Sweden)
Votuev Werkstoffbla + 110 (FRG)		Werkstoff No. 2.4935; X20CrMoVW121	12	1	0.2	0.5Ni-0.3V 0.5W-0.1Nb	HT-9	
None	Produc forms not kow	20KH12W F	12	0.6	0.2	0.7Ni-0.3V-0 .Ti 0.9W-0.1Nb-0 .Zu	Unknown	
		15KH12VNMF	12	0.6	0 15	0 Ni-0.2V 0 W		
		18KH12VMBFP	12	0.5	0 18	0.6Ni-0.2V 0.5W-0.3Nb-0 00Z		
-2006-73	Steel heat exchanger & communication tubes (closest applicable standard which only includes the lower Cr-Mo alloys)							

a) Manufacturing Process: Seamless tube and pipe, normalized and tempered

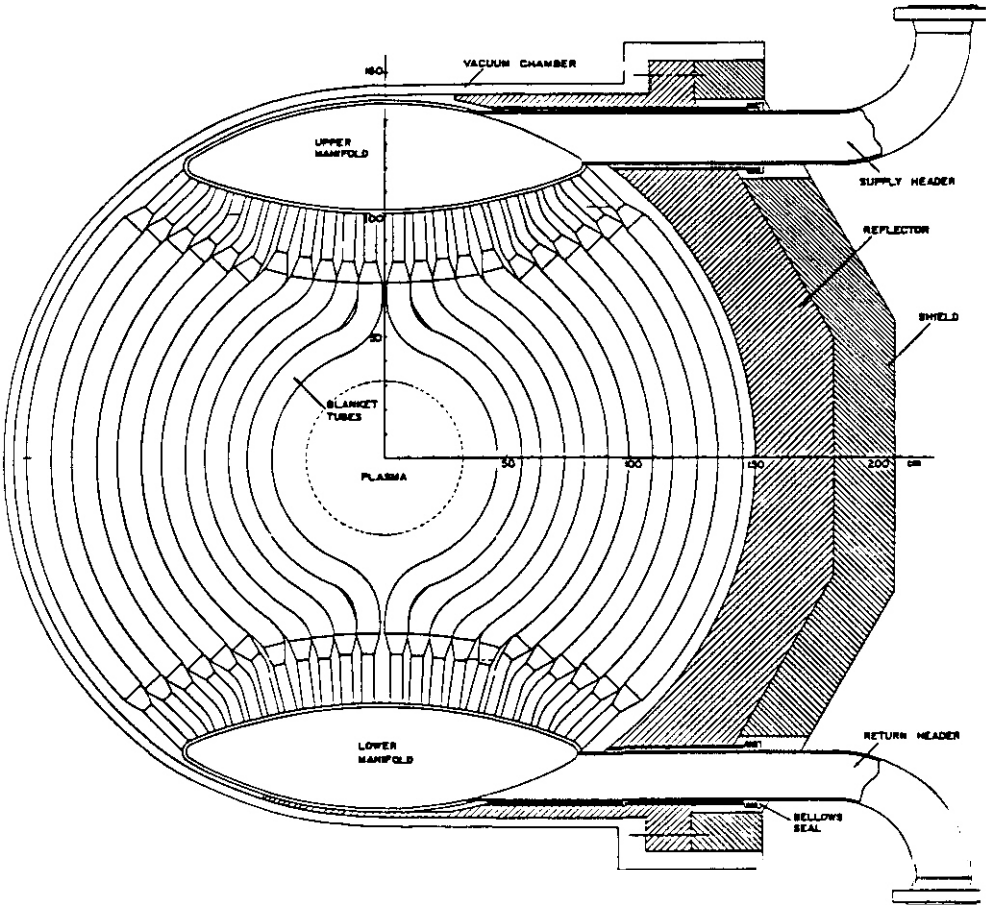

Fig. 7.10.1. Vertical Section of TASKA blanket

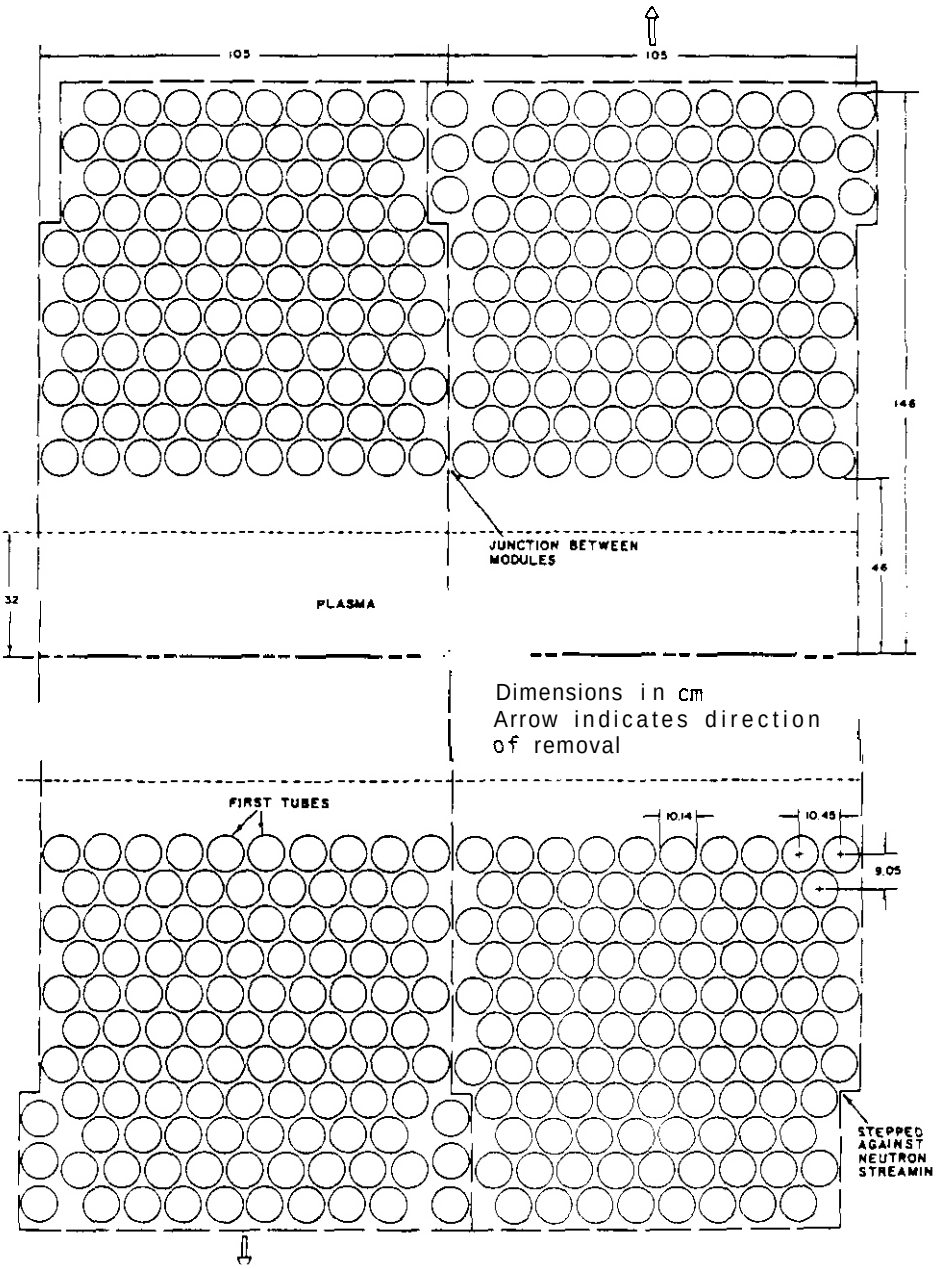

Fig. 7.10.2. Horizontal section through two blanket modules

that all welded joints are shielded by approximately 100 cm of $Pb_{83}Li_{17}$ (the coolant-breeder material) and the HT-9 tubes. This reduces radiation damage in the tube welds.

At this time, it is considered probable that the modules will be constructed in accordance with the intent of the ASME Boiler and Pressure Vessel Code, Section III, Division 1, Rules for Construction of Nuclear Power Plant Components. Section III invokes the pertinent requirements of Section II, Materials; Section V Non-destructive Examination; Section IX, Welding & Brazing Qualifications. It will be noted that HT-9 (like PCA and other candidate first wall materials) is not a currently approved ASME Code material. However. it is assumed that Code qualifications of HT-9 for use under Section III rules will be achieved at an appropriate future time.

7.10.4.2 Manufacturing and Processing HT-9 Tubes

Table 7.10.2 lists a number of ferritic tube and pipe material specifications for 12Cr-1Mo steels including the alloy grade and designation, and the names of known producers. This information is an indication of the degree of common use of HT-9 in the form of pipe and tubular products and their acceptance by industry and standards organizations outside the U.S. Table 7.10.3 lists some specific applications of HT-9, or the 12Cr-1Mo equivalent alloy, in CEGB boilers which successfully used welded tubes on the same order of size as those proposed for the TASKA plant blanket design. Those tubes were placed into service in the fully tempered condition. The manufacturers such as Sandvik recommend austenitization, air-cooling, tempering and finally air-cooling. This is done to produce a tempered martensite microstructure, relieve stresses and achieve recovery and recrystallization of any material work-hardened by the forming or tube-drawing process. Sandvik reports that cold bending is not a problem as long as the local deformation does not exceed the fracture strain. Tubes may be bent to a 2d radius. Although cold-bent tube was formerly stress-relieved, that practice was discontinued when it was demonstrated that cold work caused only a marginal reduction in rupture strength (Refs. 1 and 2).

7.10.4.3 Fabrication of HT-9 Tubes

Based on the design shown by Figure 7.10.1, there are several approaches to the fabrication of the modules. The design calls for 13 different shapes of tube. The lengths and bends are easily handled on an assembly line basis. The tube shapes may be made by free bending (2d min.) or the tubes may be filled with a soft material such as indium or Woods metal to minimize distortions during bending. The use of the filled tube method for bending will require some investigation to assure that the process does not cause metallurgical degradation of the tube or leave undesirable contaminants. In general tube shaping is not perceived as a fabrication problem.

The conical transition tube pieces may be formed by spinning a heavy wall tube to open a cone or a thin wall tube to close a cone. Alternatively, it may be cold-formed by rolling plate material and seam welding or cutting, shaping and welding tubular material, Figure 7.10.3.

7.10.4.4 Welding

In the U.S. the use of air hardening steels such as HT-9 in large, highly restrained, welded structures has been perceived as a feasibility issue. This is largely due to a lack of experience with the material. The Europeans on the other hand have used HT-9 extensively. particularly for steam piping as shown by Table 7.10.3. Those and other commercial experiences have demonstrated that this alloy is readily weldable when the proper procedures are employed. It must be recognized that an as-welded joint may contain considerable untempered martensite which is prone to brittle fracture. Hydrogen in the welds may create additional problems. For these reasons, weidlng of HT-9 requires additional care.

Weidlng HT-9 requires that the weld preparation (groove) be clean, free of dirt, hydrocarbons and grease, that it be properly preheated and that coated electrodes be baked to eliminate moisture. Preheating and maintaining temperature during welding is often necessary depending on the welding process and joint design In order to control the formation of martensite in the weld and HAZ. Weldments should be given a postweld heat treatment (PWHT) immediately after welding to relieve stresses, temper any martensite, and improve the toughness of the joint.

it appears to be appropriate to use 75° V-groove weld preparations for the tube and transition tube welds. All the welds will be full penetration In accordance with Code requirements.

A prerequisite of the tube to tube-sheet joint is that there be no crevices on the vacuum or tube side. The TASKA unit operates under a hard vacuum, hence designs creating tortuous mean free paths are to be avolded. With such a restriction, there are several approaches to the joint. For one type the plate could have punched holes with protruding lips on which to make the tube attachment welds (see Figure 7.10.4.a). For another. a short tube stub could be welded into punched or drilled holes. A fillet weld on the vacuum side and on the coolant side would seal the crevice (see Figure 7.10.4). These welds, however, would require Code inspection. These two joints would require an internal bore weld to attach the blanket-wall tubes to the tube stubs. A third design would require a counter bore on the tubesheet hole so that a full penetration weld could be made fran the coolant side of the tubesheet.

Table 7.10.3. Superheater and reheater applications of martensitic/ferritic steels in CEGB boilers

Material	Station	Oper. Temperature (°C)	Wall Dimensions Dia. (OD) (mm)	Thickness (mm)	Total Length (m)	Life (h)
12Cr-Mo-V	Aberthaw (2) "A" 1	430–460				16,900
	4	430–460				18,600
	Aberthaw (2) "B" 7	600–650 but can reach 800				3,700
	8					16,500
	9					11,000
	High Marnham (1) 5	540–650	54	4.5	18	35.000
	Staythorpe	550	58.5	4.5		4.000
	Northfleet (6)	540–850		121	24,000	20,000
	Bankside (6)	590			9	22.000
12Cr-1Mo	Kingsnorth (6)	Up to 622	49	6	10	8,400

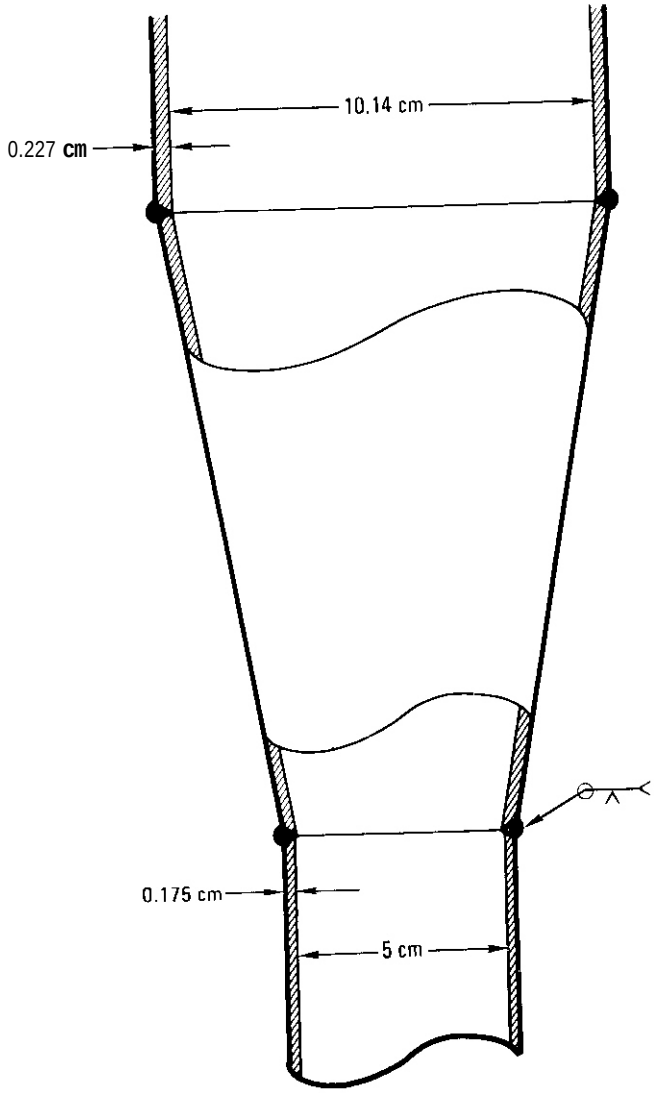

Fig. 7.10.3. Transition Tube Welds

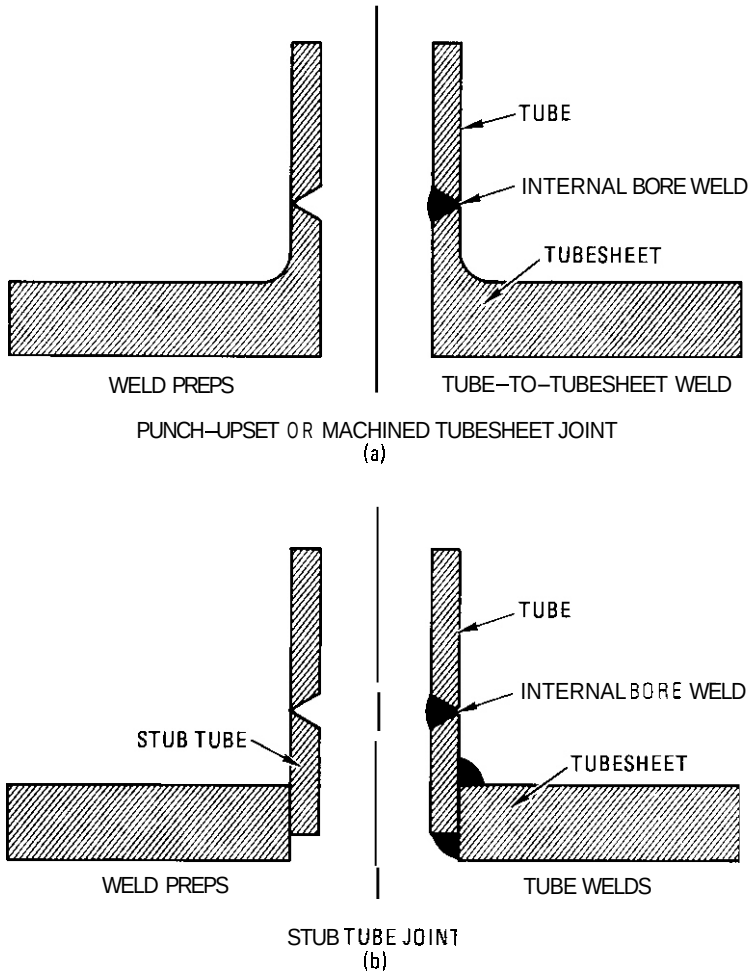

Fig. 7.10.4. Conceptual tube-to-tubesheet joints for manifold and tube weldments.

7.10.4.5 Heat Treatment

The recanmended heat treatment for HT-9 (Ref. 1 and 2) consists of an austenlzatlon at 1020-1070°C for 1/2 hour per Inch of materlal thickness and air cooling. A temper at 730-790°C for 1/2 to 2 hours and air cool lng completes the heat treatment. A stress relief heat treatment is accompi ished by heating the materlai at 700-750°C for 30 mlnutes and alr cooling. The HT-9 materials used for TASKA will need one or a combination of the heat treatments to develop the mechanical propertles and relieve fabrlcatlon stresses.

To produce a structure wlth minimum residual fabrlcatlon stress, It would be desirable to normallze and temper the entlre assembly. It is feaslble to build a furnace around the assembly and to support the structure to mlnlmlze dlstortlon and sagging. However. since TASKA consists of modules. the task of heat treating is made simpler in that It would requlre a smaller furnace and less bracing both of which would be reusable for multiple modules.

Another approach to stress relief would be to heat treat the subassembl les and stress relieve the welds. For example the bent tubes wlth connected transition pieces and small diameter extension tube would be normalized and tempered, likewise the tubesheet and tube stubs. The Internal bore welds connecting those two subassemblies and the final manlfold closure welds would be stress relieved locally.

The TASKA design and HT-9 materlal and processing permit flexlbillty of the fabrlcatlon methods whlch would need only mlnimai testlng for verification.

7.10.4.6 References

1. "Super 12%Cr Steels - An Update," Climax Molybdenum Co., Bulletin M571, 7/82.

2. "Sandvlk HT9," Sandvlk, May 1981.

7.11 IRRADIATION OF ESR ALLOY HT-9 AND ALLOY 9Cr-1Mo(MOD.) PLATES FOR FRACTURE TOUGHNESS ASSESSMENT - J. R. Hawthorne (Naval Research Laboratory)

7.11.1 ADIP Task

The Department of Energy (DOE)/Office of Fusion Energy (OFE) has stated the need to investigate ferritic alloys under the ADIP program task. Ferritic Steels Development (Path E)

7.11.2 Objectives

Alloy HT-9 and Alloy 9Cr-1Mo(Mod.) are being evaluated for a potential application as a first wall material in magnetic fusion reactors. objectives of the current research task were to irradiate an Alloy HT-9 plate from the Fusion Ferritic Program ESR reference heat at 300°C and an Alloy 9Cr-1Mo(Mod.) plate from another Program reference heat at 150°C, and to perform postirradiation notch ductility and fracture toughness tests showing the realtive magnitudes of radiation embrittlement produced in the two alloys.

7.11.3 Summary

During this period, irradiation exposures at 300°C and 150°C to $8x10^{19}n/cm^2$, E>0.1MeV, were undertaken for the Alloy HT-9 and Alloy 9Cr-1Mo(Mod.) plates, respectively. Specimen types include tension, Charpy-V(C_v), fatigue precracked Charpy-V(PCC_v) and half-size Charpy-V specimens and, in the case of the Alloy 9Cr-1Mo(Mod.), 2.54 mm thick compact tension specimens.

7.11.4 Progress and Status

7.11.4.1 Introduction

The ferritic stainless steel compositions, HT-9 and 9Cr-1Mo(Mod.), are being assessed for possible first wall applications in magnetic fusion reactors by the Magnetic Fusion Materials Program and for duct applications in liquid metal fast breeder reactors by the Cladding/Duct Alloy Development Program of the Department of Energy. For these proposed uses, fracture resistance properties before and after elevated temperature irradiation are being investigated. Specimen types include C_v specimens for notch ductility determinations, PCC_v specimens for dynamic fracture toughness (K_J) determinations and compact tension (CT) specimens for static fracture toughness determinations. Tensile property changes with irradiation are also being established for use in fracture resistance assessments.

Previous studies[1] evaluated an HT-9 plate representing AOD melt processing after irradiation at 93°C and 288°C. The current study on the HT-9 composition is aimed at evaluating ESR processing vs AOD processing and, through a joint program with ORNL (J. Vitek), the relative effects of a low vs. a high fluence level. For the latter. a set of half size C_v specimens from the NRL plate are being irradiated in HIFR at 300°C. The 150°C irradiation of the 9Cr-1Mo(Mod.) alloy on the other hand, is to establish its low temperature service capabilities and to test the postirradiation correlation of dynamic vs. static fracture toughness for this alloy.

7.11.4.2 Materials

The 15.2 mm (0.6-in) thick HT-9 plate, NRL Code ES9, was obtained from the electroslag remelted heat no. 9607R2. The chemical composition of the melt according to INCO is given in Table 1. Melt and ingot processing details are provided in reference 2. The plate was subsequently heat treated by the Armco Steel Company under contract. The reported heat treatment was 1050°C ± 14°C for 0.5 hours with air cooling plus 780°C for 4.0 hours and air cooling. Because of constraints of furnace chamber size, the plate was not heat treated as a single piece as requested but was cut into four sections approximately 8 x 15 inches in size. The two sections used for the reactor specimens (sections 6-6-1 and 6-6-2) were heat treated separately. The reserve section (6-6-3) was heat treated simulaneously with plate section 6-6-2 and will serve on a control material. Temperatures during heat treatment were monitored using mechanically-attached thermocouples. The extent of temperature gradients (small) across the plate sections was determined in advance, using an equivalent thickness test plate and multiple thermocouples.

The 9Cr-1Mo(Mod.) plate, NRL code VS, was received from ORNL in the fully heat treated condition. Its heat treatment was 1038°C for 1 hour with air cooling, followed by 760°C for 1 hour with air cooling. The plate was produced from the electroslag remelted heat no. 30176; the plate chemical composition according to Combustion Engineering Corporation (Chattanooga) is included in Table 1[3].

Specimens were taken from both plates to represent the longitudinal (strong) test orientation.

Table 7.11.1 Composition (wt-%) of HT-9 and 9Cr-1Mo(Mod.) plates

Plate	C	Si	Mn	P	S	Cr	Mo	Ni
HT-9	0.20	0.17	0.57	0.016	0.003	12.1	1.04	0.51
9Cr-1Mo(Mod.)	0.081	0.11	0.37	0.010	0.003	8.61	0.89	0.09
Plate	V	W	N	Al	Ti	Cu	Cb/Ta	B
HT-9	0.28	0.45	0.027	0.006	0.001	0.07	<0.001	<.001
9Cr-1Mo(Mod.)	0.209	<0.01	0.055	0.007	0.004	0.04	0.072	<.001

7.11.4.3 Material Irradiation

The specimens are being irradiated in two, individually temperature controlled assemblies. The assemblies are being irradiated in tandem in the C2 fuel lattice position of the water cooled reactor (UBR) at the State University of New York at Buffalo. Temperatures are being monitored continuously by means of thermocouples welded to the specimens (approximately 50 percent specimen coverage). Neutron fluences will be determined from iron neutron dosimeter wires placed within the specimen arrays and the neutron energy spectrum calculation developed by the Hanford Engineering Development Laboratory under contract. The target neutron fluence (E>0.1MeV) is $8x10^{19} n/cm^2$ to match the exposure condition of earlier NRL experimente in the UBR for the Magnetic Fusion Materials Program.

7.11.4.4 Preirradiation Material Properties

Tests are underway to define preirradiation notch ductility and fracture toughness properties; the experimental results and data comparisons should be available for the next report. Initial postirridiation data should also be available at that time.

7.11.4.5 Postirradiation Evaluation of Half Size (Miniature) C_v Specimens

Tests of the miniature C_v specimens from the current assemblies and from previous NRL irradiation experimente are not to be conducted at NRL; rather, the W E plans call for the specimen tests to be made at a site (to be selected) having the necessary equipment. HEDL and ORNL have the required (impact test) equipment installed or under construction. The irradiated specimens and a limited number of control specimens are available for immediate shipment.

7.11.4.6 Plans for the Next Reporting Period

Plans for the next reporting period are to complete the irradiation of the materials and to develop postirradiation data using the C_v, PCC_v and tensile test specimens. In addition, postirradiation CT tests will be initiated using the single specimen unloading compliance method for R curve determination.

7.11.4.7 References

1. J. R. Hawthorne. "Postirradiation Notch Ductility and Fracture Toughness Behavior of AOD Heat of Alloy HT-9" in Alloy Development for Irradiation Performance, Semi-Annual Progress Report for period ending March 31, 1982, DOE/ER-0045/8, Sept. 1982.

2. Communication to ADIP and DAFS Participants from T. Lechtenberg (General Atomic Co) March 18, 1982.

3. Private communication, V. K. Sikka (ORNL) to J. R. Hawthorne (NRL) dated April 2, 1981.

8.1 IRRADIATION EXPERIMENT STATUS AND SCHEDULE — M. L. Grossbeck (Oak Ridge National Laboratory)

A large number of planned, in-progress, and completed reactor irradiation experiments support the ADIP program. Table 8.1.1 summarizes the parameters that describe completed experiments. Experiments that have been removed from the reactor only recently. are currently undergoing irradiation. or are planned for future irradiation are included in the schedule bar charts of Table 8.1.2.

Experiments were under way during the reporting period in the Oak Ridge Research Reactor (ORR) and the High Flux Isotope Reactor (HFIR), which are mixed-spectrum reactors, and in the Experimental Breeder Reactor (EBR-II), which is a fast reactor.

During the reporting period experiments HFIR-CTR-39, -40, and -41 were removed from the HFIR. These are the first elevated-temperature HFIR experiments with tensile specimens of ferritic alloys. Experiment AD-2, containing ferritic alloys, also completed irradiation in EBR-II. Five elevated-temperature experiments containing tensile specimens of austenitic and ferritic alloys — HFIR-CTR-42 through -46 — were loaded into HFIR. Two of these were joint experiments with the European Community and Japan.

The ORR-MFE-4B spectral tailoring experiment developed a containment leak in October 1982. The capsule was removed from the reactor and disassembled in hot cells. Following diameter measurements on the pressurized tube specimens and removal of some transmission electron microscopy disk specimens, the specimens will be reencapsulated and the assembly returned to the reactor.

The initial scheduling of a new series of experiments for the HFIR, the HFIR-JP series, is shown on the final page of Table 8.1.2. The experiments are part of a joint program between the United States and Japan. They will contain specimens from both national programs, with the first eight experiments devoted to path A alloys. Irradiation will be in the outer target rod positions in the flux trap region of HFIR.

Table 8.1.1. Descriptive parameters for completed ADIP program fission reactor irradiation experiments

Experiment	Major objective	Alloy	Temperature (°C)	Displacement damage (dpa)	Helium (at. ppm)	Duration (months)	Date completed
			Experiments in ORR				
ORR-MFE-1	Scope the effects of composition and microstructure on tensile, fatigue, and irradiation creep	Paths A, B, C	250–600	2	≤10	4	5/78
ORR-MFE-2	Scope the effects of composition and microstructure on tensile, fatigue, and irradiation creep	Paths A, B, C	300–600	6	≤60	15	4/30
ORR-MFE-5	In-reactor fatigue crack growth	Path A	325–460	1	<10	2	2/51
			Experiments in EBR-II				
Subassembly X-264	Effect of preinjected helium on microstructure, tensile properties, and irradiation creep	316, PE-16, V–20% Ti, V–15% Cr–5% Ti, Nb–1% Zr	500–825	8	2–200	4	1/77
AA-X Subassembly X-287	Effect of preinjected helium on microstructure, tensile properties, and irrddidtion creep	316, PC-16, V–20% Ti, V–15% Cr–5% Ti. Nb–1% Zr	400–700	20	2–200	23	12/78
Subassembly X-2170	Stress relaxation	Titanium alloys	450	2		1	1/78
Pins B285, 8286, and B284	Swelling. fatigue crack growth, and tensile properties	Titanium alloys	370–550	25		14	9/79
			Experiments in HFIR				
HFIR-CTR-3	Swelling and tensile properties	PE-16, Inconel 600	300-700	4. 3–9	350–1800	3	2/75
HFIR-CTR-4	Swelling and tensile properties	PE-16	300–700	2.2–4.5	100–350	2	3/77

Table 8.1.1. (Continued)

Experiment	Major objective	Alloy	Temperature (°C)	Displacement damage (dpa)	Helium (at. ppm)	Duration (months)	Date completed
HFIR-CTR-5	Swelling and tensile properties	PE-16, Inconel 600	300-700	4.3–9	350–1800	3	4/75
HFIR-CTR-6	Swelling and tensile properties	PE-16, Inconel 600	300-700	4.3–9	350-1800	3	4/75
HFIR-CTR-7	Swelling and tensile properties	PE-16	300-700	9–18	1250-3000	7	8/77
HFIR-CTR-8	Swelling and tensile properties	PE-16	300–700	9–18	1250–3000	7	8/77
HFIR-CTR-9	Swelling and tensile properties	316, 316 t Ti	280–680	10–16	400-1000	6	5/77
HFIR-CTR-10	Sweliing and tensile properties	316, 316 + Ti	280–680	IC-16	400–1000	6	5/77
HFIR-CTR-11	Swelling and tensile properties	316, 316 + Ti	280–680	10–16	400–1000	6	5/77
HFIR-CTR-12	Swelling and tensile properties	316, 316 + Ti	280–680	7-10	200-500	4	2/77
HFIR-CTR-13	Swelling and tensile properties	316, 316 + Ti	280–680	7-10	200-500	4	2/77
HFIR-CTR-14	Fatigue	316	430	9–15	400–1000	7	12/77
HFIR-CTR-15	Fatigue	316	550	b-9	200–400	4	10/78
HFIR-CTR-16	Weld characterization, swelling, and tensile properties	316, PE-16, Inconel 600	55	b-9	150-2700	4	8/77
HFIR-CTR-17	Weld characterization	316	280–620	7-13	180–460	5.5	10/77
HFIR-CTR-18	Swelling and tensile properties	316, PE-16	280–700	17-27	1600-5600	12	6/78
HFIR-CTR-19	Weld characterization	316	280–620	7-10	200–500	4	12/77
HFIR-CTR-20	Fatigue	316	430	b-9	200–400	4	1/78
HFIR-CTR-21	Fatigue	316	550	9–15	400-1000	7	7/78
HFIR-CTR-22	Fatigue	316	430	b-9	200–400	4	3/75
HFIR-CTR-23	Fatigue	PE-16	430	b-9	370-1000	3.5	2/79
HFIR-CTR-24	Temperature calibration and tensile properties	316	300–620	2.2	30	1	12/78
HFIR-CTR-26	Swelling and tensile properties	316	284–620	30	1900	10	4/80
HFIR-CTR-27	Swelling and tensile properties	316	284–620	56	3500	18	1/81
HFIR-CTR-28	Swelling and tensile properties	316	370-560	30	1900	10	12/80
HFIR-CTR-29	Swelling and tensile properties	316	370–560	56	3500	18	8/81
HFIR-CTR-30	Swelling, microstructure, and ductility	Paths A, B, C, D, E	300–600	40	≤15,000	14	11/8/81
HFIR-CTR-31	Swelling, microstructure, and ductility	Paths A, B, C, D, E	300–600	20	≤7500	8	5/28/81
HFIR-CTR-32	Swelling, microstructure, and ductility	Paths A, 8, C, D, E	300–600	10	≤3000	4	12/81
HFIR-CTR-33	Swelling, tensile properties, weld characterization	Paths A and E	55	10	≤510	4	10/80
HFIR-MFE-T1	Swelling, tensile fatigue	Path E	55	30	≤300	12	8/10/82
HFIR-MFE-T2	Swelling, tensile fatigue	Path E	55	9	≤75	3	5/3/81
HFIR-MFE-T3	Impact properties	Path E	55	10	<85	4	12/24/81

Table 8.1.2. Objectives and schedule for current and planned ADIP program reactor irradiation experiments

Experiment designation	Major objective
A. Oak Ridge Research Reactor	
ORR-MFE-4	Effect of irradiation on tensile, fatigue, and irradiation creep of path A PCA (Prime Candidate Alloy) and path B base research alloys. Spectral tailoring to maintain correct He/dpa ratio. Irradiation on continuing basis. 330–600°C (1)
B. Experimental Breeder Reactor (EBR-II)	
Experiment plan depends on alloy availability. EBR-II space not yet identified.	Effect of irradiation on swelling, tensile, fatigue, and crack growth properties of V and Nb scoping alloys. 370, 450, 550, and 650°C. Position in reactor not finalized, therefore no fluence estimate. (4)
AD-2 (6 pins in separate subassemblies of row 4)	To supplement present EBR-II data on ferritic alloys with data on crack growth, fatigue, and fatigue toughness. Temperature 390, 450, 500, and 550°C. 19 and 38 dpa.

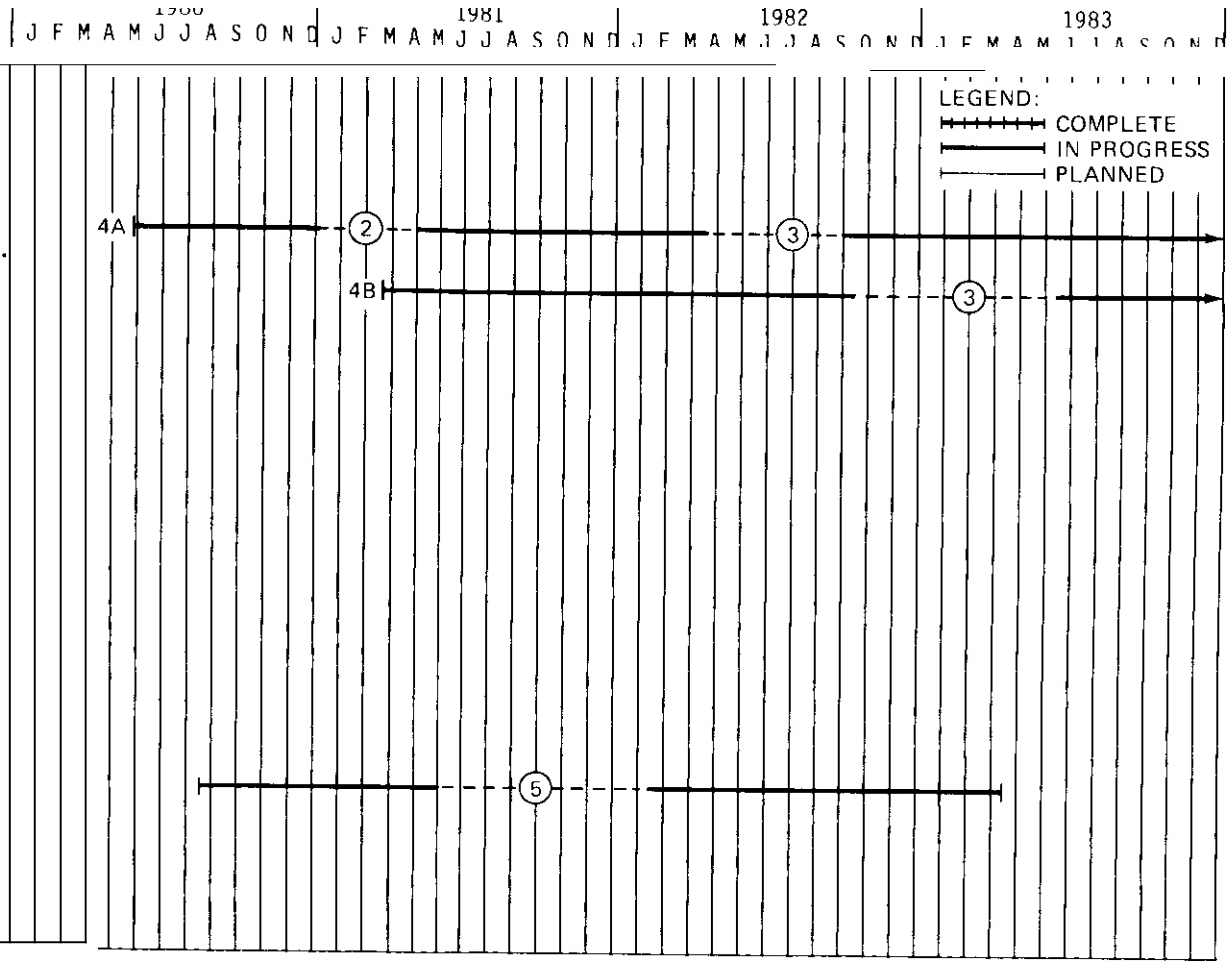

(1) MFE-4A operates at 330 and 400°C. MFE-4B will operate at 500 and 600 C

(2) Removed from reactor for thermocouple repairs.

(3) Removed from reactor for reencapsulation.

(4) Delayed for undetermined period.

(5) Interim examination. Experiment out of reactor Reencapsulated in subassembly X-344B.

Table 8.1.2. (Continued)

Experiment designation	Major objective	1981 J F M A M J J A S O N D	1982 J F M A M J J A S O N D	1983 J F M A M J J A S O N D	1984 J F M A M J J A S O N D
C. High Flux Isotope Reactor (HFIR)					
HFIR-MFE-RB1	Swelling, microstructure, crack growth, fracture toughness, impact, tensile, and fatigue properties of path E alloys. 10 dpa, 90 ppm He, 55°C.				
HFIR-MFE-RB2	Similar to HFIR-MFE-RB1, to 20 dpa, 200 ppm He.				
HFIR-MFE-RB3	Similar to HFIR-MFE-RB1, to 10 dpa, 90 ppm He.				
HFIR-CTR-34	Impact properties of path E alloys. 10 dpa, 0 to 75 ppm He, 300, 400°C.				
HFIR-CTR-35	Impact properties of path E alloys. 10 dpa, 0 to 75 ppm He, 300, 400°C.				
HFIR-CTR-36	Fatigue properties of path A alloys. 30 dpa, 2000 ppm He.				
HFIR-CTR-39	Swelling, tensile properties of path E alloys. 12 dpa, up to 90 ppm He, 300 to 500°C.				
HFIR-CTR 40	Swelling, tensile properties of path E alloys. 12 dpa, up to 90 ppm He, 300 to 500°C.				
HFIR-CTR 41	Swelling, tensile properties of path E alloys. 12 dpa, up to 90 ppm He, 300 to 500°C.				
HFIR CTR 42	Swelling, tensile properties of path A alloys. 20 dpa, 1100 ppm He, 300 to 600°C.				

Table 8.1.2. (Continued)

Experiment designation	Major objective	1982 J F M A M J J A S O N D	1983 J F M A M J J A S O N D	1984 J F M A M J J A S O N D	1985 J F M A M J J A S O N D
HFIR CTR 03	Swelling, tensile properties of path A alloys 20 dpa, 1100 ppm He, 300 to 600°C.				
HFIR-CTR-44	Swelling, tensile properties of path A alloys. 10 dpa, 500 ppm He, 250–400°C. Joint experiment of U.S., European Community, and Japan.				
HFIR-CTR-45	Similar to HFIR-CTR-44.				
HFIR-CTR-46	Impact properties of path E alloys. 10 dpa, 75 ppm He, 300 and 400°C.				
HFIR CTR 07	Impact properties of path E alloys. 40 dpa, 400 ppm He, 300 and 400°C.				
HFIR-CTR-48	Similar to HFIR CTR 47				
HFIR-CTR-49	Tensile properties of path E alloys 40 dpa, 400 ppm He, 300 to 600°C.				
HFIR-CTR-50	Similar to HFIR CTR 03				
HFIR-CTR-51	Swelling, tensile properties of low-activation alloys. 20 dpa, 300–600°C				
HFIR-MFE-100	Swelling, tensile properties of Paths A, C, E alloys. 100 dpa, 300–600°C				

Table 3.2 (Continued)

Experiment designation	Major objective	1983 J F M A M J J A S O N D	1984 J F M A M J J A S O N D	1985 J F M A M J J A S O N D	1986 J F M A M J J A S O N
HFIR-JP-1[1]	Swelling, tensile and fatigue properties, and microstructure of path A alloys. 300–600°C, 30 dpa, 2000 ppm He.				
HFIR-JP-2	Similar to HFIR-JP-1.				
HFIR-JP-3	Similar to HFIR-JP-1, but to 50 dpa 3500 ppm He.				
HFIR-JP-4	Similar to HFIR-JP-3.				
HFIR-JP-5	Similar to HFIR-JP-1.				
HFIR-JP-6	Similar to HFIR-JP-1.				
HFIR-JP-7	Swelling, tensile properties and microstructure of path A alloys. 55°C, 50 dpa, 2000 ppm He.				
HFIR-JP-8	Similar to HFIR JP-3				

[1] The HFIR JP experiment series is a joint program shared by the U.S. and Japan Fusion Reactor Materials activities

8.2 FUSION PROGRAM RESEARCH MATERIALS INVENTORY — F. W. Wiffen, T. K. Roche [Oak Ridge National Laboratory), J. W. Davis (McDonnell Douglas Company), and T. A. Lechtenberg (GA Technologies)

8.2.1 ADIP Tasks

ADIP Task I.D.I, Materials Stockpile for MFE Programs.

8.2.2 Objective

Oak Ridge National Laboratory maintains a central inventory of research materials to provide a common supply of materials for the Fusion Reactor Materials Program. This will minimize unintended material variations and provide for economy in procurement and for centralized record keeping. Initially this inventory is to focus on materials related to first-wall and structural applications and related research, but various special purpose materials may be added in the future.

The use of materials from this inventory for research that is coordinated with or otherwise related technically to the Fusion Reactor Materials Program of DOE is encouraged.

8.2.3 Materials Requests and Release

Materials reauests shall be directed to the Fusion Proaram Research Materials Inventorv at ORNL (Attention: F. W. Wiffen). Yaterials will be released directly if

(a) the material is to be used for programs funded by the Office of Fusion Energy, with goals consistent with the approved Materials Proaram Plans of the Materials and Radiation Effects Branch.

(b) the requested amount of material is available without compromising other intended uses.

Materials requests that do not satisfy both (a) and (b) will be discussed with the staff of the Materials and Radiation Effects Branch, Office of Fusion Energy, for agreement on action.

8.2.4 Records

Chemistry and materials preparation records are maintained for all inventory material. All materials supplied to program users will be accompanied by summary characterization information.

8.2.5 Summary of Current Inventory and Material Movement During Period October 1, 1982, to March 31, 1983

A condensed, qualitative description of the content of materials in the Fusion Program Research Materials Inventory is given in Table 8.2.1. This table indicates the nominal diameter of rod or thickness of sheet for product forms of each alloy and also indicates by weight the amount of each alloy in larger sizes available for fabrication to produce other product forms as needed by the program. Material received into the inventory during this reporting is identified in Table 8.2.2. Table 8.2.3 gives the materials distributed frorn the inventory.

Alloy compositions and more detail on the alloys and their procurement and/or fabrication are given in this and earlier ADIP progress reports.

Table 8.2.1 Summary status of materials available in the fusion program research materials inventory

Alloy	Product form			
	Ingot or bar[a] weight (kg)	Rod diameter (mm)	Sheet thickness (mm)	Thin-wall tubing wall thickness (mm)
	Path A alloys			
Type 316 SS	900	16 and 7.2	13 and 7.9	0.25
Path A PCA[b]	490	12	13	0.25
USSR Cr-Mn Steel[c]		10.5	2.6	
NONMAGNE *30d*		18.5	10	
	Path a alloys			
PE-16		16 and 7.1	13 and 1.6	
8-1				
8-2				
B-3	180			
8-4	180			
B-6	180			

Table 8.2.1 (continued)

Alloy	Product form			
	Ingot or billet weight (kg)	Rod diameter (mm)	Sheet thickness (mm)	Thin-wall tubing, wall thickness (mm)
Path C alloys				
Ti-64			2.5 and 0.76	
Ti-6242S		63	6.3, 3.2, and 0.76	
Ti-56215			2.5 and 0.76	
Ti-38644			0.76 and 0.25	
Nb–1% Zr		6.3	2.5, 1.5, and 0.76	
Nb–5% Mo–1% Zr		6.3	2.5, 1.5, and 0.76	
V–20% Ti		6.3	2.5, 1.5, and 0.76	
V–15% Cr–5% Ti		6.3	2.5, 1.5, and 0.76	
VANSTAR-7		6.3	2.5, 1.5, and 0.76	
Path D alloy				
LRO-37e			3.3, 1.6, and 0.8	
Path E alloys				
HT9 (AOD fusion heat)[f]	3400		28.5, 15.8, 9.5, and 3.1	
HT9 (AOD/ESR fusion heat)	7000	25, 50, and 75	28.5, 15.8, 9.5, and 3.1	
HT9			4.5 and 18	
HT9 + 1% Ni			4.5 and 18	
HT9 + 2% Ni			4.5 and 18	
HT9 + 2% Ni + Cr adjusted			4.5 and 18	
T-9 modified[g]			4.5 and 18	
T-9 modified + 2% Ni			4.5 and 18	
T-9 modified + 2% Ni + Cr adjusted			4.5 and 18	
2 1/4 Cr-1 Mo			[h]	

[a]Greater than 25 mm, minimum dimension.

[b]Prime candidate alloy.

[c]Rod and sheet of a USSR stainless steel supplied under the U.S.-USSR Fusion Reactor Materials Exchange Program.

[d]NONMAGNE 30 is an austenitic steel with base composition Fe–14% Mn–2% Ni–2% Cr. It was supplied to the inventory by the Japanese Atomic Energy Research Institute.

[e]LRO-37 is the ordered alloy $(Fe,Ni)_3(V,Ti)$ with composition Fe–39.4% Ni–22.4% V-0.434 Ti.

[f]Alloy 12 Cr-1 MoVW, with composition equivalent to Sandvik alloy HT9.

[g]T-9 modified is the alloy 9 Cr-1 MoVNb.

[h]Material is thick-wall pipe, rerolled as necessary to produce sheet or rod.

Table 8.2.2. Fusion program research materials inventory receipts 10-1-82 to 3-31-83

Alloy	Heat identification	Product form	Product sizes (mm)	Product sizes (in.)	Quantity (m^2)	Quantity ($in.^2$)	Source
		Path *D* alloys — innovative *material* concepts					
LRO-37-HP	EB11581-2-1630	Sheet	3.3	0.131	0.1	156	Cabot Corp.
		Sheet	1.6	0.065	0.18	279	Cabot Corp.
		Sheet	0.8	0.031	0.21	326	Cabot Corp.
LRO-37-CG	EB11681-2-0735	Sheet	3.3	0.131	0.29	450	Cabot Corp.
		Sheet	1.6	0.065	0.32	496	Cabot Corp.
		Sheet	0.8	0.031	0.90	1395	Cabot Corp.

Table 8.2.3. Fusion program research materials inventory, disbursements 10-1-82 to 3-31-83

Alloy	Heat	Product form	Dimensions[a] (mm)	Quantity (m)	Quantity (m^2)	Sent to
		Path A alloys — austenitic stainless steels				
316 SS-Ref. heat	X-15893	Sheet	0.76		0.046	Radiation Effects Group, M&C Division, ORNL
Path A PCA	K-280	Bar	101	0.53		HEDL
Path A PCA	K-280	Rod	4.17	9.59		Radiation Effects Group, M&C Division, ORNL
Path A PCA	K-280	Sheet	0.25		0.023	Argonne National Laboratory
		Path *C* alloys — reactive *and refractory* alloys				
V-20% Ti	CAM 833-10	Sheet	0.76		0.046	Westinghouse
V-15% Cr-5% Ti	CAM 835 A	Sheet	0.84		0.051	Westinghouse
Vanstar-7	CAM 836 Bot.-4	Sheet	0.76		0.072	Westinghouse
		Path *E* alloys — *ferritic* steels				
HT-9	AOD/ESR-9607R2	Plate	16.3		0.061	Culham Laboratory, United Kingdom
	AOD/ESR-9607R	Plate	28.5		0.23	Univ. of California, Santa Barbara
		Plate	15.8		0.09	Univ. of California, Santa Barbara
		Plate	15.8		0.69	Naval Research Laboratory
		Plate	15.8		0.29	Sandia National Laboratories, Livermore

[a]Characteristic dimension — thickness for plate and sheet, diameter for rod and tubing.

9. MATERIALS COMPATIBILITY AND HYDROGEN PERMEATION STUDIES

9.1 CORROSION OF PATH A PCA, TYPE 316 STAINLESS STEEL, AND 12 Cr-1 MoVW STEEL IN FLOWING LITHIUM — P. F. Tortorelli and J. H. DeVan (Oak Ridge National Laboratory)

9.1.1 ADIP Task

ADIP Task I.A.3, Perform Chemical and Metallurgical Compatibility Analyses.

9.1.2 Objective

The purpose of this task is to determine the corrosion resistance of candidate first-wall materials to slowly flowing lithium in the presence of a temperature gradient. Corrosion and deposition rates are measured as functions of time, temperature, additions to the lithium, and flow conditions. These measurements are combined with chemical and metallographic examinations of specimen surfaces to establish the mechanisms and rate-controlling processes for dissolution and deposition reactions.

9.1.3 Sumnary

In lithium thermal convection loop (TCL) experiments, weight losses and dissolution rates of annealed and cold-worked path A prime candidate alloy (PCA), were slightly higher than those of type 316 stainless steel. The depth of the ferrite layer on type 316 stainless steel was constant between 3700 and 9000 h at 600°C but not at 570°C. Nitrogen level between 9 and *130* wt ppm in lithium did not affect short-term weight losses of type 316 stainless steel. The 12 Cr-1 MoVW steel showed measurable but small weight losses in thermally convective lithium between 350 and 500°C.

9.1.4 Progress and Status

We have continued our mass transfer studies of candidate first-wall materials in flowing lithium by use of previously described1 TCLs with accessible specimens. These loops are designed so that lithium samples can be taken and corrosion coupons can be withdrawn and inserted without interrupting the lithium flow. One such lithium-type 316 stainless steel TCL is being used to observe the dissolution behavior of path A PCA specimens with different thermomechanical treatments. Our purpose is to study the effects of microstructure on corrosion of austenitic stainless steel by lithium as well as to determine the dissolution rate of PCA relative to that of standard type 316 stainless steel. In the initial experiment, coupons of path A PCA alloys A1 and A3 were placed at the 600 and 570°C positions in a type 316 stainless steel TCL that had previously circulated lithium for greater than 10,000 h. Because of prior operation with lithium, the hot-leg surfaces of the loop were known to have a considerably higher iron concentration than the as-received PCA alloys. However, the cold leg of the loop had been replaced before operation with the PCA specimens. Composition for path A PCA (alloys A1, annealed, and A3, cold worked) is as follows:

Element	Composition (wt %)	Element	Composition (wt %)	Element	Composition (wt %)
Ni	15.9	Mn	1.9	Al	0.05
Cr	13.0	Si	1.7	C	0.05
Mo	1.9	Ti	0.5	N	<0.01

Both alloys were annealed for 15 min at 1175°C in argon and cold rolled 23 to 25%. Alloy A1 was annealed for an additional 15 min at 1175°C in argon.

The preceding progress report gave initial weight loss results for the first 3000 h of exposure of the path A PCA alloys.' The specimens were exposed an additional 4000 h before being permanently removed from the loop and replaced with other PCA specimens. The cumulative weight loss data for alloys A1 and A3 at 600°C are shown in Fig. 9.1.1 (dashed lines) as a function of exposure time. Note that the time dependence of the weight change in Fig. 9.1.1 is generally similar to that previously found3 for type 316 stainless steel. The rate of weight loss decreases with time until a steady state or linear dependence on time is reached. Once a linear dissolution rate has been attained, the slope of the weight loss versus time curve yields dissolution rates of 20.8 and 15.7 mg/(m²·h) for A1 and A3, respectively. Similar data for specimens of these alloys in the 570°C loop position are shown in Fig. 9.1.2 (dashed lines) and yield steady-state dissolution rates of 12.3 mg/(m²·h) for A1 and 12.1 mg/(m²·h) for A3.

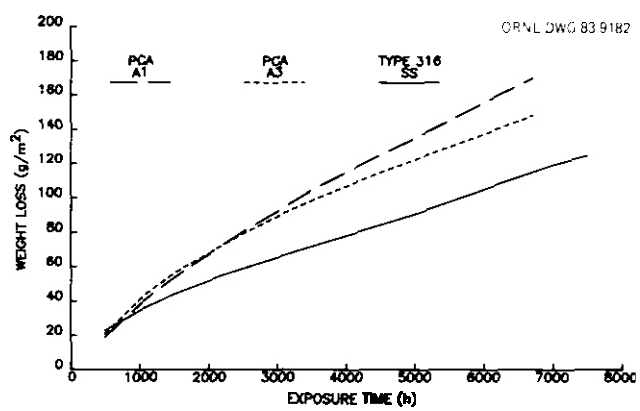

Fig. 9.1.1. Weight loss versus exposure time for Path A PCA alloys A1 (annealed) and A3 (cold-worked) and annealed type 316 stainless steel in thermally convective lithium at 600°C.

The differences in the overall weight losses and dissolution rates between A1 and A3 after 7000 h are relatively small, although the annealed specimen had a higher dissolution rate than the 25%-cold-worked alloy at 600°C. Note that, at both 600 and 570°C, the cold-worked specimens initially lost more weight than those that had been annealed. During this interval (<3000 h), the weight loss results are consistent with other (lower temperature) data on annealed versus cold-worked stainless steel in lithium.[4] Nevertheless, any difference between the dissolution rates of A1 and A3 is small relative to the difference between the PCA specimens and type 316 stainless steel. As shown in Fig. 9.1.1 which also compares weight losses at 600°C with similar data for type 316 stainless steel. The overall weight losses are measurably greater for the PCA specimens. This is presumably related to the greater concentration in PCA of nickel, which is preferentially corroded by the lithium.5 However, the difference in dissolution rates between type 316 stainless steel and the PCA alloys appears greater than effects merely of differences in the relative chemical activities of nickel in the alloys and may reflect an effect of nickel concentration on the morphology of the ferritic layer that develops at the lithium-exposed surface. (Surfaces of these specimens are being analyzed.) At 570°C the overall weight losses for PCA after 7000 h are comparable to those measured for type 316 stainless steel (see Fig. 9.1.2), although their steady-state dissolution rates (given above) again are greater than that of type 316 stainless steel [8.5 mg/(m²·h)].

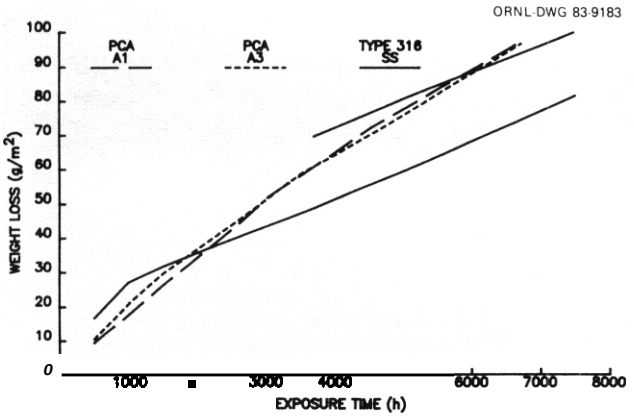

Fig. 9.1.2. Weight loss versus exposure time for Path A PCA alloys A1 (annealed) and A3 (cold-worked) and annealed type 316 stainless steel in thermally convective lithium at 570°C. The two solid lines represent data from two different experiments with type 316 stainless steel.

Lithium corrosion experiments with type 316 stainless steel are continuing and provide a baseline for comparison with results for other austenitic and ferritic steels. Such studies are also being used to gain a detailed understanding of the preferential leaching process, whereby a porous, nickel-depleted ferrite layer forms on surfaces exposed to high-temperature lithium. The kinetics of this process is important in interpreting the weight change data and in assessing the total effect of corrosion on the containment material. It was reported earlier that the ferrite layer thickness on type 316 stainless steel exposed to thermally convective lithium at 600°C was the same at 3000 and 10,000 h and that such an observation is consistent with a dissolution rate that is constant with time (that is, the "steady-state" rate described above).[1] An evaluation of additional data from more recent loop experiments has confirmed the earlier result: at 600°C. very little change in ferrite layer thickness is noted between 3700 and 9000 h of exposure. This is illustrated by the optical-micrographs in Fig. 9.1.3, which show cross sections of type 316 stainless steel specimens exposed at 600°C in different loop experiments. Comparisons from one loop experiment to another do show some variations in ferrite layer thickness, particularly if the loop sizes are different. However, the layer thickness at the maximum 600°C temperature in any one loop is effectively constant after about 3700 h. Linear weight loss kinetics is also observed after this time interval. At specimen positions away from the 600°C position, for example at 570°C, a constant ferrite layer thickness does not appear to be reached until at least 9000 h. Although this would appear to be inconsistent with the observation of linear weight loss kinetics for specimens at this loop position, the contribution of these specimens to the total loop weight loss is not large, and the change in ferrite layer thickness after the onset of linear kinetics is also small. These results do suggest that the onset of linear weight change kinetics at temperatures below 550°C may require a significant fraction of the total reactor operating time.

Previously we reported that stainless steel loops operating at a maximum temperature of 600°C showed no measurable effect of the initial nitrogen concentration of the lithium (below a maximum concentration of 130 wt ppm) on short-term weight losses.[6] More recent data have confirmed this finding. Table 9.1.1. which contains all the relevant data, shows-no consistent trend between the starting nitrogen concentration of the lithium and the 500- and 1000-h weight losses of type 316 stainless steel at 600°C. Of course, the concentrations reported in Table 9.1.1 are relatively low, and higher concentrations may produce a deleterious effect. In static lithium tests. virtuallv all the corrosion is nitrogen-related (for nitrogen levels-in lithium greater than 500–1000 wt ppm).[7] A possible difference in

Table 9.1.1. Effect of nitrogen concentration in lithium on type 316 stainless steel in thermally convective lithium at 600°C

Exposure time (h)	Nitrogen in lithium (wt ppm)		Weight loss (g/m²)
	Initial	Final	
500	9	1	11.4
	26	11	10.5
	30		23.1
	44	59	20.2
	124		10.2
	128		19.6
1000	30	38	34.8
	124	48	14.0

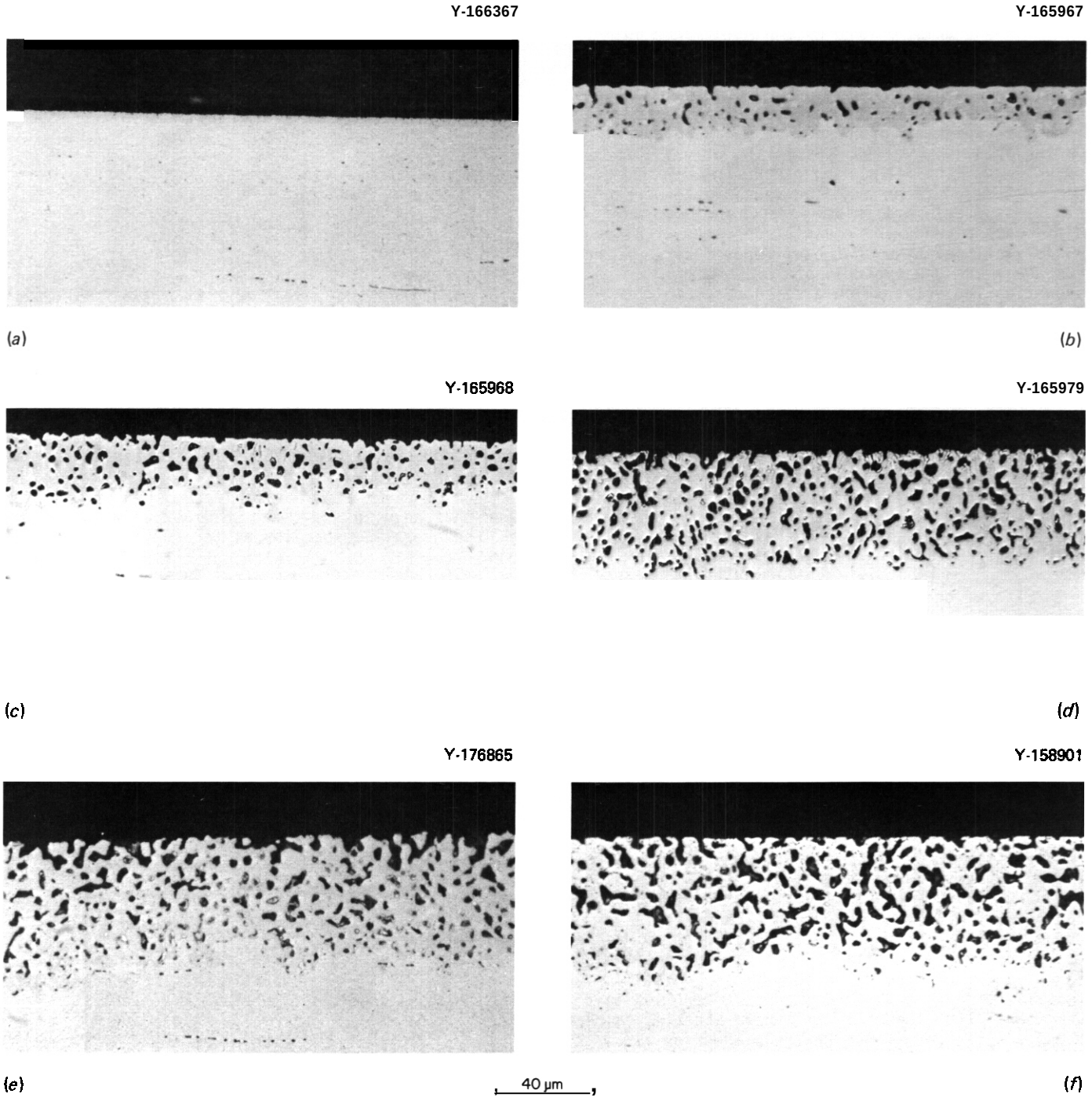

Fig. 9.1.3. Polished cross sections of type 316 stainless steel exposed to thermally convective lithium at 600°C in several different experiments. *(a)* 500 h. *(b)* 3000 h. (c) 3500 h. (*d*) 3700 h. (e) 7500 h. (*f*) 9000 h.

nitrogen effects in these two types of experiments (aside from any due to differing concentrations) may be the extent and rate of nickel and chromium depletion from the hotter stainless steel surfaces in the loop tests such that a smaller dependence on nitrogen in the 600°C convection loop system is associated with the relatively rapid ferrite layer formation and the concomitant high rate of nickel and chromium dissolution into the lithium.

In the preceding progress report, we presented corrosion results from a lithium–12 Cr-1 MoVW steel TCL operating at a maximum temperature of 500°C with a temperature difference of 150°C (ref. 2). The experiment was continued until a total coupon exposure time of 10,088 h was accumulated. The specimens were then removed and are being destructively examined. The longer term data have confirmed what was reported previously:* in contrast with the general behavior observed in nonisothermal liquid metal corrosion loops,

all loop specimens suffered small weight losses and, in general, the weight losses of the cooler specimens were as great as or greater than those of the hotter coupons. In fact, the largest cumulative weight loss was measured for the specimen at the lowest temperature (350°C). A close examination of the weight change data revealed that, although the weight losses were about the same around the loop (except at 350°C), greater than half of these total weight losses were recorded after just the first 522 h of exposure (see Table 9.1.2). Furthermore, with the exception of the 500 and 350°C specimens, the weight change behavior between 522 and 10,088 h showed no discernible trend with time (for example, see Fig. 9.1.4). In these cases, weight losses tended to be offset by weight gains during other intervals such that no trend of increasing weight loss with exposure time could be established. At 500°C, weight losses increased slightly with time (see Fig. 9.1.5), but at 350°C a definite general monotonic increase of weight loss occurred as a function of exposure time (see Fig. 9.1.6). Concentrations of nitrogen and oxygen in the loop lithium were low (<100 wt ppm).

Table 9.1.2. Weight losses of 12 Cr-1 MoVW exposed to thermally convective lithium

Coupon temperature (°C)	Coupon position	Weight loss (g/m^2)	
		In 522 h	In 10,088 h
500	Hot leg	5.7	10.8
500	Hot leg	4.0	6.8
480	Hot leg	6.6	7.4
460	Hot leg	6.8	9.4
440	Hot leg	5.4	5.1
420	Hot leg	5.7	7.7
400	Hot leg	4.6	7.1
425	Cold leg	6.3	8.0
415	Cold leg	5.7	6.0
400	Cold leg	4.3	5.4
380	Cold leg	5.4	6.8
365	Cold leg	4.6	6.8
350	Cold leg	a 3	22.8

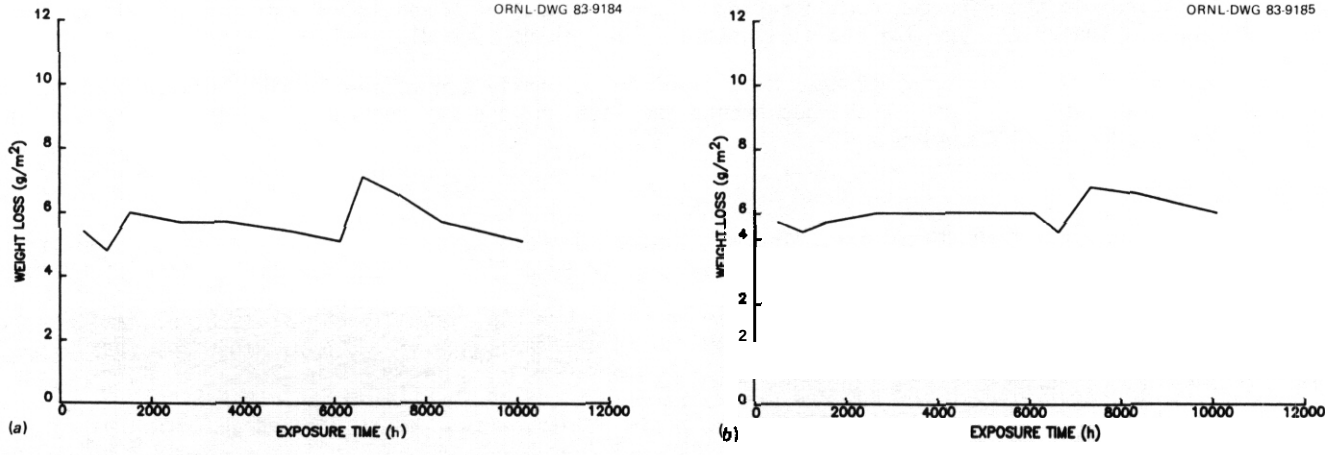

Fig. 9.1.4. Weight loss versus exposure time for 12 Cr-1 MoVW steel in thermally convective lithium. (*a*) 440°C. (*b*) 415°C.

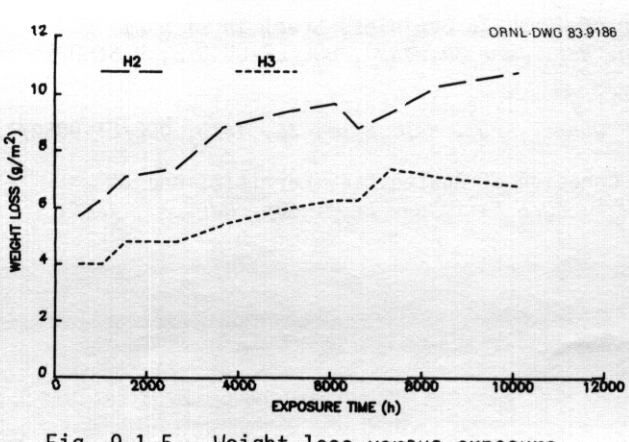

Fig. 9.1.5. Weight loss versus exposure time for 12 Cr-1 MoVW steel in thermally convective lithium at 500°C (maximum loop temperature). Specimen H2 was located in the surge tank just above the loop hot leg, and specimen H3 was located just at the top of the hot leg.

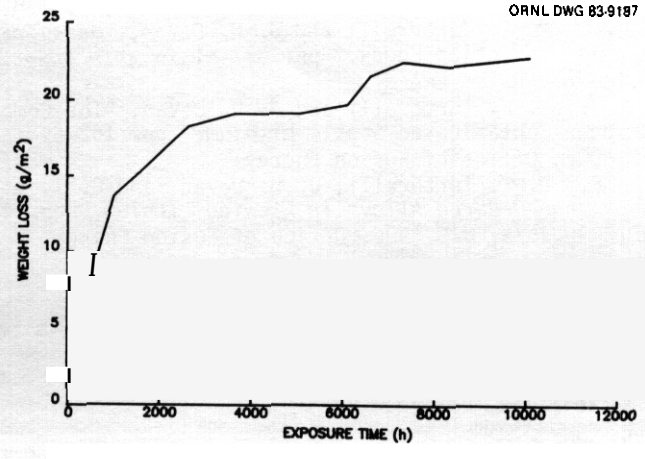

Fig. 9.1.6. Weight loss versus exposure time for 12 Cr-1 MoVW steel in thermally convective lithium at 350°C (minimum loop temperature).

Unlike the data for the other specimens, the weight losses shown in Figs. 9.1.5 and 9.1.6 can be reasonably approximated by straight lines determined by the method of least squares. Under the assumption of linear kinetic behavior, the slopes of these lines can then be used to yield approximate dissolution rates of these specimens (as was done above for the austenitic alloy). From the data for exposure times greater than 1000 h, an average rate of 0.4 mg/(m^2·h) was determined for the 500°C specimens (H2 and H3), while the rate for the 350°C coupon was 1.0 mg/(m^2·h). The 500°C rate is the same as that measured at 500°C for type 316 stainless steel exposed to lithium for a long period of time (partly at 600°C).[8] We had expected that the steady-state corrosion rates would indeed prove to be similar between type 316 stainless steel and the 12 Cr-1 MoVW steel, since the dissolution process controlling the weight loss of the former steel produces a ferrite surface layer similar in composition to the latter steel. However, the pattern of weight changes around the respective loops indicates that the corrosion mechanisms may *not* be the same for the two steels under the conditions tested, and the similarity in corrosion rates may just be coincidental.

Although the weight changes in the 12 Cr-1 MoVW steel loop are relatively small, it is nevertheless important to understand the corrosion mechanisms operating in the loop. In particular, we need to determine whether the higher corrosion rate measured at 350°C in this loop as compared with the rate at 500°C is symptomatic of a change in corrosion mechanism as system temperatures fall below 500°C. Toward this end, we plan to determine the corrosion behavior of the 12 Cr-1 MoVW steel loop in the 500 to 600°C temperature range.

9.1.5 Conclusions

1. Weight losses and dissolution rates of path A PCA in thermally convective lithium were greater than those of type 316 stainless steel and may be attributed to the higher nickel concentration of PCA. At long times and higher temperature (600°C), the annealed PCA suffered slightly more dissolution than did 25%-cold-worked PCA.
2. The depth of the ferrite layer on type 316 stainless steel exposed to thermally convective lithium at 600°C was approximately constant with exposure time between 3700 and 9000 h. At 570°C, the ferrite layer depth was not constant during this time interval.
3. Variations in the nitrogen concentration of lithium between 9 and 130 wt ppm did not affect the short-term weight losses of type 316 stainless steel in a lithium–type 316 stainless steel thermal convection loop.
4. The dissolution process of 12 Cr-1 MoVW steel in thennally convective lithium between 500 and 350°C was sluggish. The pattern of weight changes around the lithium loop may suggest a change in corrosion mechanism as temperatures decrease below 500°C.

9.1.6 References

1. J. H. DeVan and J. R. DiStefano, "Thermal-Convection Loop Tests of Type 316 Stainless Steel in Lithium," pp. 200-208 in *ADIP Quart. Prog. Rep. Mar. 31, 1978*, DOE/ET-0058/1, U.S. DOE, Office of Fusion Energy.
2. P. F. Tortorelli and J. H. DeVan. "Corrosion of Path A PCA. Type 316 Stainless Steel. and Fe–12 Cr-1 MoVW Steel in Flowing Lithium," pp. 290-303 in *ADIP Semiannu. Prog. Rep. Sept. 30, 1982,* DOE/ER-0045/9, U.S. DOE, Office of Fusion Energy.
3. P. F. Tortorelli, J. H. DeVan, and J. E Selle, "Corrosion in Lithium Stainless Steel Thermal-Convection Systems," pp. 13-44—54 in *Proc. 2d Int. Conf. Liquid Metal Technology in Energy production,* CONF-800401-P2, U.S. Department of Energy, 1980.
4. O. K. Choora and D. L. Smith., "Environmental Effects on Properties of Structural Allovs," pp. 304–13 in *ADIP Semiannu. Prog. Rep. Sept. 30, 1982*, DOE/ER-0045/9, U.S. DOE, Office of Fusion Energy..
5. P. F. Tortorelli and J. H. DeVan, "Effect of Nickel Concentration on the Mass Transfer of Fe-Ni-Cr Alloys in Lithium," *J. Nucl. Mater.* 103&104, 633–38 (1981).
6. P. F. Tortorelli and J. H. DeVan, "Mass Transfer of Type 316 Stainless Steel in Lithium Thermal-Convection LOOPS," pp. 337–41 in *ADIP Quart. Prog. Rep. June 30,* 1980, DOE/ER-0045/3, U.S. DOE, Office of Fusion Energy.
7. P. F. Tortorelli and J. H. DeVan, "The Compatibility of Type 316 Stainless Steel with Nitroaen-Contaminated Static Lithium." pp. 162–69 in *ADIP Quart. Prog. Rev. Sept.* 30. 1919. DOE/ET-0058/7, U.S. DOE, Office of Fusion Energy.
8. P. F. Tortorelli., J. H. DeVan. and C. T. Liu. "Corrosion of Austenitic, Ferritic, and Long-Range-Ordered Alloys in Flowing Lithium," pp. 482–90 in *ADIP Semiannu. prog. Rep. Mar. 31, 1982,* DOE/ER-0045/8, U.S. DOE, Office of Fusion Energy.

9.2 CORROSION OF TYPE 316 STAINLESS STEEL IN STATIC Pb–17 at. % Li — P. F. Tortorelli and J. H. DeVan (Oak Ridge National Laboratory)

9.2.1 ADIP Task

ADIP Task I.A.3, Perform Chemical and Metallurgical Compatibility Analyses.

9.2.2 Objective

The purpose of this program is to determine the chemical compatibility of fusion reactor candidate materials with possible coolants and tritium-breeding materials. Specimens are exposed to static lithium, lead-lithium, and lead melts to identify the kinetics and mechanisms that govern corrosion. Other program objectives are (1) to determine the effects of N, C, H, and O on apparent solubilities of metals in lithium and lead-lithium; (2) to determine the carbon and nitrogen partitioning coefficients between alloys and these melts; (3) to determine the effects of soluble (Ca, Al) and solid (Y, Zr, Ti) active metal additions on corrosion by lithium and lead-lithium; and (4) to determine the tendencies for mass transfer between dissimilar metals.

9.2.3 Summary

The surface morphology and composition of type 316 stainless steel specimens exposed to static Pb–17 at. % Li between 400 and 700°C were studied. Preliminary results indicated nickel depletion throughout this temperature range and relative chromium surface enrichment for those specimens suffering the highest weight losses.

9.2.4 Progress and Status

A molten lead-lithium alloy is a potential tritium-breeding medium for fusion reactors.[1] We are therefore studying the compatibility of candidate structural alloys with molten lead-lithium by exposing tensile specimens of type 316 stainless steel and 12 Cr-1 MoVW steel to the low-melting (235°C) eutectic composition of Pb–17 at. % Li. The specific experimental procedures have been described previously.[2] Weight change data from these experiments[2,3] indicated that the weight losses of type 316 stainless steel and 12 Cr-1 MoVW steel exposed to static molten Pb–17 at. % Li were greater than the losses in pure lithium under similar conditions. In addition, the maximum weight losses for type 316 stainless steel exposed to static Pb–17 at. % Li at 300, 400, 500, 600, and 700°C for 1000, 3000, and 5000 h occurred at 600°C, and among the 500, 600, and 700°C exposures, the 3000-h weight losses were greater than those measured for specimens exposed for 1000 and 5000 h (ref. 3). Such behavior could be explained by either the formation of a surface corrosion product at higher temperatures and longer times or residual lead accumulating in the specimens.[3] However, subsequent x-ray diffraction of the surfaces exposed at 300, 400, and 500°C revealed essentially no evidence of corrosion product compounds or elemental lead.

During the current reporting period, work related to Pb–17 at. % Li compatibility involved (1) the preparation and assembly of equipment for a type 316 stainless steel thermal-convection loop experiment with Pb–17 at. % Li, (2) the design and initial fabrication of a slow-strain-rate testing system for liquid metal embrittlement studies of austenitic and ferritic alloys, and (3) detailed analysis of previously tested specimens to study the relevant corrosion process(es) and to correlate surface morphology and composition with the weight change results. This work is continuing, but preliminary results for type 316 stainless steel exposed to Pb–17 at. % Li at 400, 500, 600, and 700°C will be summarized below.

Significant variations in both surface morphology and composition among different specimens were observed. These can be seen in Figs. 9.2.1 and 9.2.2, which show scanning electron micrographs of surfaces of specimens exposed for 3000 h at 500, 600, and 700°C and for 5000 h at 400, 500, and 600°C, respectively. Note in Fig. 9.2.1 that the surface of the 600°C specimen was smoother than those at 500 and 700°C, although the weight losses at 600°C were significantly greater than those at the other temperatures.[3] The nodules on the surfaces of the 500 and 700°C specimens (such as those denoted *A* and *B*) generally had lower relative nickel and chromium concentrations than the surfaces as a whole (Table 9.2.1) [based on energy-dispersive x-ray analysis (EDS)]. In general, analysis of the upper nodules on most of the specimens revealed the same trend of lower nickel and chromium concentrations. For example, in Fig. 9.2.2, the nodules denoted *C* and *D* had lower Cr/Fe and Ni/Fe ratios than the underlying matrix (see Table 9.2.1). The only exceptions were the particles observed on the 600°C surface exposed to Pb–17 at. % Li for 5000 h [Fig. 9.2.2(*c*)]. As illustrated by the data in Table 9.2.1 for nodule *E*, these particles were less depleted in nickel (on the basis of relative decrease) but did have lower Cr/Fe ratios relative to the surrounding matrix.

Our preceding progress report presented results from x-ray diffraction of the specimens exposed to Pb–17 at. % Li at 300, 400, and 500°C and from an initial EDS study of a specimen exposed at 500°C for 5000 h (ref. 4). That study showed that type 316 stainless steel was depleted in nickel on exposure to the static lead-lithium melt at those temperatures. Further EDS has confirmed this: the data in Table 9.2.2 show that the overall nickel concentration of the exposed surfaces was less than that of an unexposed type 316 stainless steel. Care was taken to note whether an EDS spectrum was taken over an area in the shoulder (unstressed) or gage section of a specimen (which had been tensile tested after exposure to the melt). This

M-16847

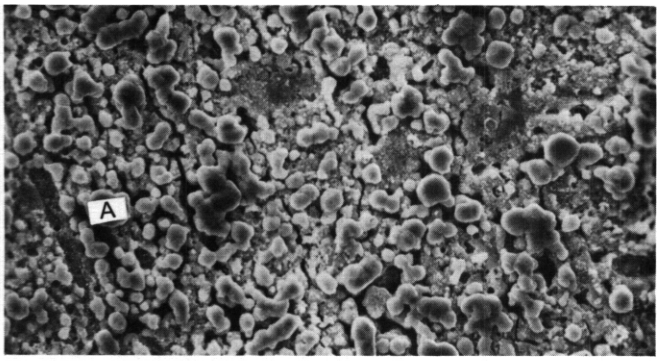

(a) 20 μm

M-16879

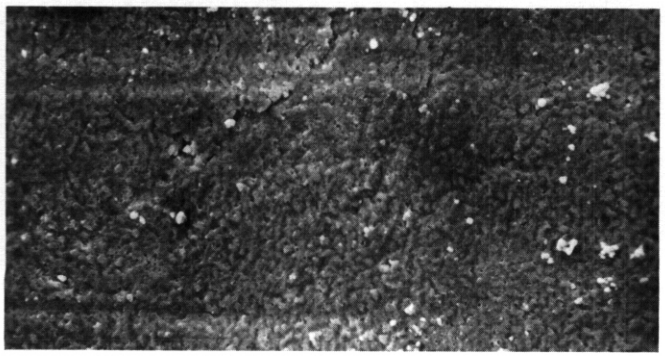

(b) 20 μm

M-16890

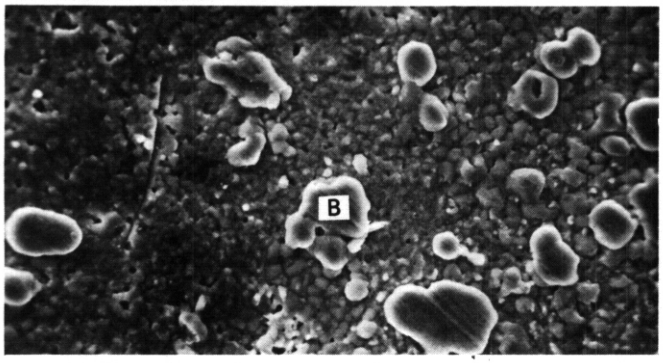

(c) 20 μm

Fig. 9.2.1. Type 316 stainless steel exposed to static Pb–17 at. % Li for 3000 h at *(a)* 500°C, *(b)* 600°C, and *(c)* 700°C. Letters denote features selected for x-ray analysis.

M-16907

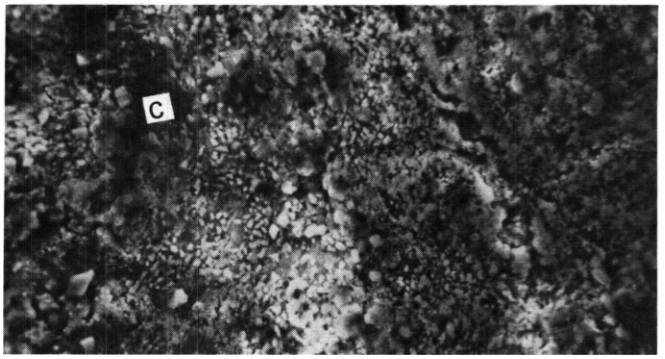

(a) 20 μm

M-16876

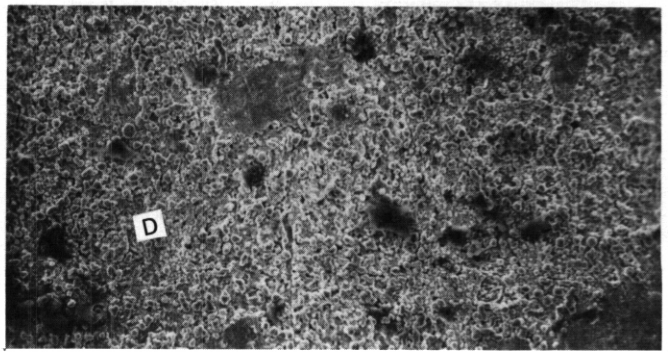

(b) 0.1 mm

M-16924

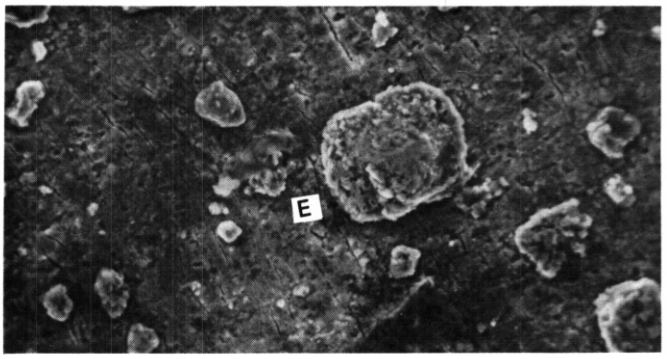

(c) 20 μm

Fig. 9.2.2. Type 316 stainless steel exposed to static Pb–17 at. % Li for 5000 h at *(a)* 400°C, *(b)* 500°C, and (c) 600°C. Letters denote features selected for x-ray analysis.

was necessary because spectra taken in the stressed area of the specimen sometimes contained information less characteristic of the surface region if surface cracking had exposed underlying material that had not been in contact with the liquid metal. The data in Table 9.2.2 are therefore the average $K\alpha$ ratios for the shoulder area of each specimen. The observed nickel depletion is similar to the result of the dissolution process in flowing lithium systems.[5] However, such nickel depletion does not occur in static lithium under conditions similar to the present capsule experiments with Pb–17 at. % Li.

Table 9.2.2 also contains data on the average Cr/Fe $K\alpha$ ratios. Interestingly, there is generally no overall chromium depletion from the surfaces (except at 400°C), and the surfaces with the highest Cr/Fe ratios (600°C, 3000 h) are those that suffered the largest weight losses. Although the measured oxygen concentration of the starting lead was low, such an observation possibly suggests that a principal corrosion process (in addition to nickel depletion) may be the formation of a chromium oxide (such as Cr_2O_3) during exposure to the Pb–17 at. % Li. This oxide would then be reduced during the specimen cleaning procedure (which uses low-temperature molten lithium to remove the residual lead[2]). Such an oxidation process could allow relative chromium surface enrichment due to concurrent dissolution of nickel and iron. If an oxide film were developed during the test, this might also account for the decrease in corrosion rate after 3000 h and the decrease in corrosion rate above 600°C. However, any final interpretation of these results must await completion of our surface analysis (EDS, x-ray diffraction) of exposed specimens.

The surface of the specimen with the highest weight loss, exposed at 600°C, was, in certain areas, unusually rough and characterized by an acicular structure standing in relief above a more rapidly corroded matrix (see *A* in Fig. 9.2.3). These areas showed a lower average $K\alpha$ ratio for Cr/Fe (0.76) and a higher average ratio for Ni/Fe (0.15) than the remaining smoother surface (see *B* in Fig. 9.2.3). (Because of this variation, the $K\alpha$ ratio data for this specimen are not included in Table 9.2.2.) Because the roughened areas appear to lie below the level of the smoother surrounding matrix, these spots may have undergone accelerated corrosion such that the acicular structure is in relief while the underlying matrix is more representative of the original composition (thereby yielding an Ni/Fe $K\alpha$ ratio near that of unexposed type 316 stainless steel and a lower Cr/Fe ratio). This would explain the higher weight loss of this specimen. Such a process may be related to the formation of a corrosion product compound (as discussed above) that is ultimately removed from the surface. The localized nature of the attack may be related to variations in surface composition or to the time to complete wetting.

Table 9.2.1. Ratios of $K\alpha$ peaks for selected areas on type 316 stainless steel surfaces exposed to Pb–17 at. % Li

Exposure temperature (°C)	Exposure time (h)	Feature[a]	$K\alpha$ peak ratios			
			Feature		Surrounding matrix	
			Cr/Fe	Ni/Fe	Cr/Fe	Ni/Fe
500	3000	*A*	0.21	0.01	0.47	0.03
700	3000	*B*	0.38	0.02	0.54	0.03
400	5000	*C*	0.10	0.01	0.17	0.05
500	5000	*D*	0.19	0.01	0.56	0.05
600	5000	*E*	0.29	0.07	0.84	0.09

[a]Features identified in Figs. 9.2.1 and 9.2.2.

Table 9.2.2. Average $K\alpha$ peak ratios for unstressed areas of type 316 stainless steel exposed to Pb–17 at. % Li

Exposure temperature (°C)	Exposure time (h)	$K\alpha$ peak ratios	
		Cr/Fe	Ni/Fe
	0	0.40	0.13
400	5000	0.30	0.08
500	3000	0.43	0.02
500	5000	0.51	0.03
500	5000	0.47	0.05
600	3000	2.12	0.08
600	5000	0.63	0.07
700	3000	0.56	0.03

M-16859

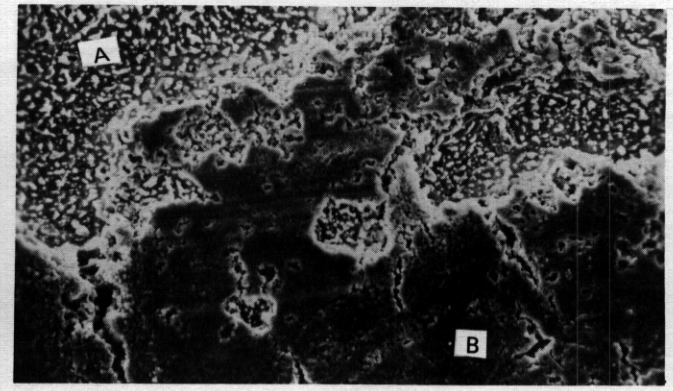

Fig. 9.2.3. Specimen of type 316 stainless steel showing rough spots after exposure to static Pb–17 at. % Li for 3000 h at 600°C. *A* indicates rough area, *B* smooth.

9.2.5 Conclusions

1. In general, nickel was depleted from type 316 stainless steel exposed to static Pb–17 at. % Li at 400 to 700°C.

2 Relative chromium enrichment was observed for those specimens suffering the highest weight losses. Such a result indicates possible corrosion product (oxide) formation during exposure.

9.2.6 References

1. D. K. Sze, R. Clemmer, and E. T. Cheng, *LiPb, A Novel Material for Fusion Applications*, UWFDM-378, University of Wisconsin, Madison, October 1980.
2. P. F. Tortorelli and J. H. DeVan, "Compatibility of Austenitic and Ferritic Steels with Pb–17 at. % Li," pp. 300–311 in *ADIP Semiannu. Frog. Rep. Sept. 30, 1981*, DOE/ER-0045/7, U.S. DOE, Office of Fusion Energy.
3. P. F. Tortorelli and J. H. DeVan, "Corrosion of Austenitic and Ferritic Steels in Static Pb–17 at. % Li," pp. 500–506 in *ADIP Semiannu. Frog. Rep. Mar. 31, 1982*, DOE/ER-0045/8, U.S. DOE, Office of Fusion Energy.
4. P. F. Tortorelli and J. H. DeVan, "Corrosion of Ferrous Alloys in Static Pb and Pb–17 at. % Li." pp. 314–22 in *ADIP Semiannu. Prog. Rep. Sept. 30, 1982*, DOE/ER-0045/9, U.S. DOE, Office of Fusion Energy.
5. P. F. Tortorelli and O. K. Chopra, "Corrosion and Compatibility Considerations of Liquid Metals for Fusion Reactor Applications," *J. Nucl. Mater.* 103&104, 621-32 (1981).

9.3 ENVIRONMENTAL EFFECTS ON PROPERTIES OF STRUCTURAL ALLOYS - O. K. Chopra and D. L. Smith (Argonne National Laboratory)

9.3.1 ADIP Task

ADIP tasks I.A.3, Perform Chemical and Metallurgical Compatibility Analyses.

9.3.2 Objective

The objective of this program is to investigate the influence of chemical environment on the corrosion and mechanical properties of structural alloys under conditions of interest for fusion reactors. Test environments to be investigated include lithium, lead-lithium, helium, and water. Emphasis will be placed on the combined effect of stress and chemical environment on corrosion and mechanical behavior of materials. Initial investigations are focused on the influence of flowing lithium and lead-lithium environments on corrosion and mechanical properties of structural materials.

9.3.3 Summary

Corrosion data are presented for several austenitic and ferritic steels exposed at temperatures between 700 and 755 K in flowing lithium and Pb-17 Li environments. The results indicate that dissolution rates for both steels are an order of magnitude greater in Pb-Li than in lithium. Tensile data for cold-worked Type 316 stainless steel show that a flowing environment has no effect on the tensile properties of Type 316 stainless steel at temperatures between 473 and 773 K.

9.3.4 Progress and Status

9.3.4.1 Lithium Environment

The effects of a flowing lithium environment on the corrosion behavior and low-cycle fatigue properties of ferritic and austenitic steels are being investigated. Tests are conducted in a forced-circulation lithium loop equipped with a cold-trap purification system to control the concentration of nonmetallic elements, e.g., N, C, and H. The cold-trap temperature is maintained at 498 K (225°C). By hot trapping with Ti or Zr foils (or use of dissolved getters), the nitrogen level in lithium is reduced to ~50 wppm, which is considerably below that attainable by cold trapping alone. During the tests, the concentration of carbon and hydrogen in lithium was ~8 and 120 wppm, respectively.

Data obtained from corrosion tests (with or without constant applied stress) and continuous-cycle fatigue tests indicate that the concentration of nitrogen in lithium is the single most important parameter in controlling the compatibility and mechanical properties of materials in lithium environments.[3] The fatigue life of HT-9 alloy at 755 K in lithium containing 1000-1500 wppm nitrogen is a factor of 2 to 10 lower than in lithium with <200 wppm nitrogen. Fatigue life of HT-9 alloy in low-nitrogen lithium is independent of strain rate in the range of 4×10^{-2} to $4 \times 10^{-4} s^{-1}$, whereas, in high-nitrogen lithium a decrease in strain rate decreases fatigue life. Furthermore, a 4.0-Ms (1100-h) preexposure of the alloy to low-nitrogen lithium has no effect on the fatigue properties. The reduction in fatigue life in high-nitrogen lithium is attributed to internal corrosion of the material. Specimens tested in high-nitrogen lithium show internal corrosion along grain and martensitic lathe boundaries and intergranular fracture. Fatigue data also indicate that the fatigue lives of HT-9 alloy and Types 304 and 316 stainless steel in low-nitrogen lithium at 755 K are greater than in air.

Corrosion data indicate that the dissolution rates of austenitic and ferritic steels exposed at 755 K in lithium containing ~200 wppm nitrogen are a factor of 2 to 4 greater than in low-nitrogen (i.e., 50 wppm) lithium. For identical lithium purity the dissolution rate of ferritic HT-9 alloy and Fe-9Cr-1Mo steel is an order of magnitude lower than for the Types 304 and 316 stainless steel. The dissolution rate for cold-worked Type 316 stainless steel is a factor of 2 to 3 greater than that for the annealed steel. For annealed Type 316 stainless steel, the corrosion rate in cold-trapped flowing lithium at 755 K is an order of magnitude greater than that observed in static lithium or thermal convection loops.[4,5] After exposure to lithium, the austenitic stainless steels develop a very porous ferrite layer due to depletion of nickel from the steel. The ferritic steels show little or no internal penetration.

During the current reporting period, corrosion tests were conducted at 755 and 700 K with several ferritic and austenitic steels to study the time and temperature dependence of corrosion in lithium. Tensile tests were performed with 20% cold-worked Type 316 stainless steel in flowing lithium and in vacuum to investigate the possible embrittlement of the material in lithium at temperatures between 473 and 773 K. Flat specimens, 5.59 x 1.27 mm in cross section and 22.23-mm gauge length were used for the tensile tests. All tests were performed at an initial strain rate of $4 \times 10^{-4} s^{-1}$. During the corrosion and tensile tests the nitrogen content in lithium was between 150 and 200 wppm.

The corrosion behavior was evaluated from measurements of weight loss and depth of internal penetration (i.e., thickness of the ferrite layer for austenitic stainless steels). The weight loss for solution-annealed Types 304L and 316 stainless steel, 20% cold-worked Type 316 stainless steel, and Path-A PCA alloy

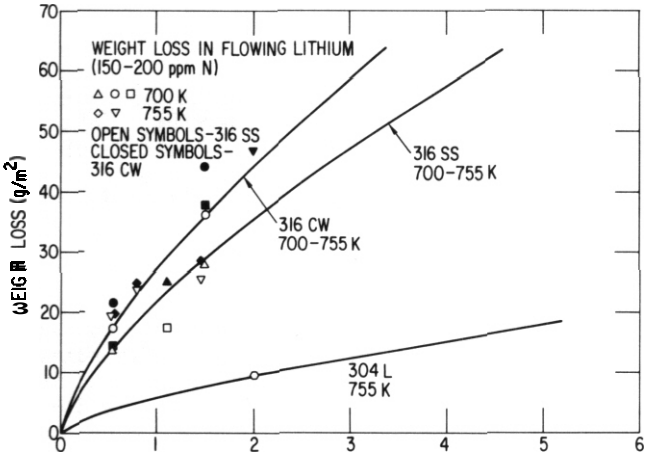

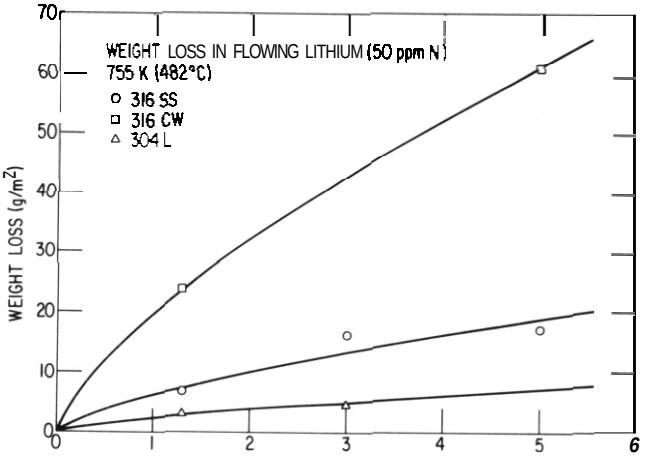

Table 9.3.1. Values of constant K for austenitic stainless steels exposed at 700 and 755 K to flowing lithium of different purities

Material	Conditions of Lithium Exposure		
	755 K (482°C)		700 K (427°C)
	High N	Low N	High N
304L	0.0460	0.0185	-
316 SS	0.1732	0.1577	0.1732
316 CW	0.2148	0.1577	0.2183
PCA	0.4974	-	0.3214

The weight losses of ferritic HT-9 alloy and Fe-9Cr-1Mo steel exposed at 700 and 755 K to flowing lithium of different purities are shown in Fig. 9.3.4. The results indicate that the weight losses of steels are an order of magnitude lower than those of the austenitic stainless steels. Furthermore, the weight losses of ferritic steels follow a linear law with time and yield a constant value for the dissolution rate.

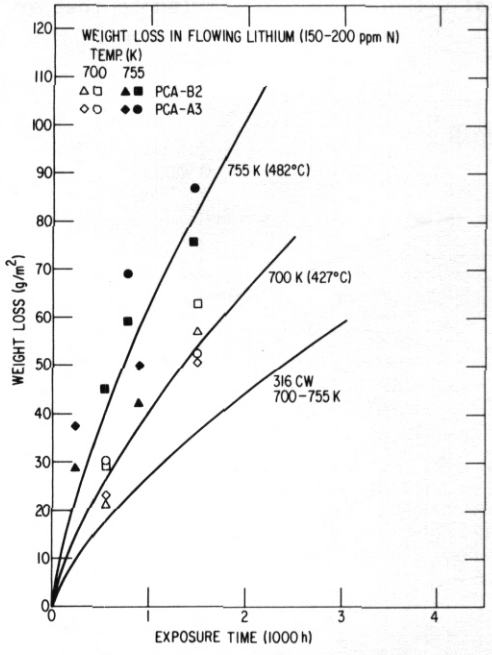

Fig. 9.3.3. Weight loss versus exposure time for Path-A PCA alloy exposed at 700 and 755 K to flowing lithium containing 150-200 wppm nitrogen. Each symbol type represents weight loss for a single specimen after various exposure times.

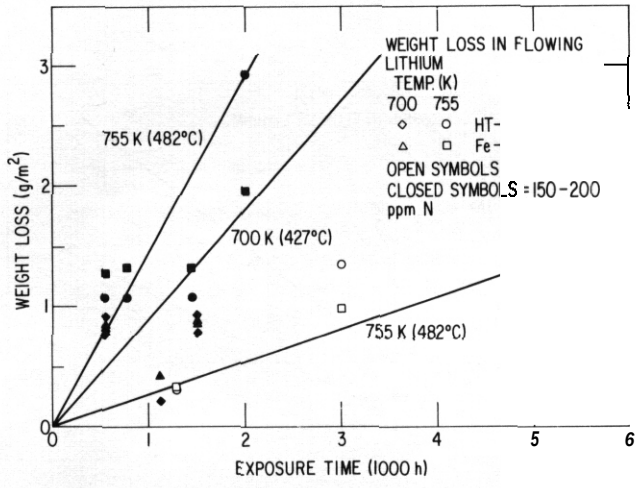

Fig. 9.3.4. Weight loss versus exposure time for HT-9 alloy and Fe-9Cr-1Mo steel exposed at 700 and 755 K to flowing lithium containing 50 or 150-200 wppm nitrogen.

Metallographic examination of the exposed specimens revealed that the austenitic stainless steels develop a porous ferrite layer whereas the ferritic steels show little or no internal penetration.[2,3] The depth of internal penetration, i.e., the thickness of the ferrite layer, in austenitic stainless steels increases with time. Fig. 9.3.5 shows the internal penetration for Type 316 stainless steel exposed to flowing lithium at 755 K for up to 18.0 Ms (5000 h). Data for low-nitrogen lithium follow a linear growth law and yield growth rates of 90 and 140 μm/y for annealed and cold-worked Type 316 stainless steels, respectively. Internal corrosion in specimens exposed to high-nitrogen lithium is slightly greater than in in specimens exposed to low-nitrogen lithium.

The influence of lithium environment on the tensile properties of 20% cold-worked Type 316 stainless steel was investigated by conducting tensile tests in flowing lithium and in vacuum at temperatures between 473 and 773 K (200 and 500°C). Fig. 9.3.6 shows the ultimate strength and total elongation of the material in lithium and vacuum. All tests were performed at an initial strain rate of ~4 x 10^{-4} s^{-1}. The results show that a lithium environment has no effect on the tensile properties of the steel. The values of tensile strength and total elongation in flowing lithium and vacuum are comparable.

9.3.4.2 Lead-Lithium Environment

A forced-circulation loop has been completed for conducting corrosion and mechanical tests of structural materials in a well-characterized liquid Pb-17Li environment. A detailed description and schematic of the loop were presented earlier.[3] The eutectic alloy was prepared in a mixing vessel and bottom poured into the loop. The loop has now operated for 14.7 Ms (4900 h); the initial 2.5 Ms (700 h) at a maximum temperature of 644 K (371°C) and subsequent operation at 727 K (454°C). The cold- leg temperature was maintained at 573 K (300°C). The eutectic alloy was analyzed to check the composition and determine the concentration of interstitial elements such as O, H, and C. Several analyses show that the alloy composition is Pb-16.3 Li and the concentrations of O, H, and N are 260, 22, and <10 wppm, respectively.

Corrosion tests were conducted with several austenitic and ferritic steels in flowing Pb-Li at 700 and 727 K (427 and 454°C). After exposure, the corrosion coupons were cleaned in static lithium at ~563 K (290°C). Subsequently, the specimens were washed in alcohol and water. This procedure was repeated several times till no further weight change was observed for the coupons. Control specimens were also exposed with the corrosion coupons in lithium to monitor any weight change during the cleaning operation. No measureable weight change was observed for the control specimens. The weight loss for annealed and cold-worked Type 316 stainless steel and the ferritic steels is shown in Figs. 9.3.7 and 9.3.8, respectively. The data for the capsule tests performed at ORNL[6] are also included in the figures. The results show that the dissolution

rates of both austenitic and ferritic steels in flowing Pb-Li are an order of magnitude greater than in flowing lithium. The overall corrosion behavior of the various alloys in Pb-Li is similar to that in

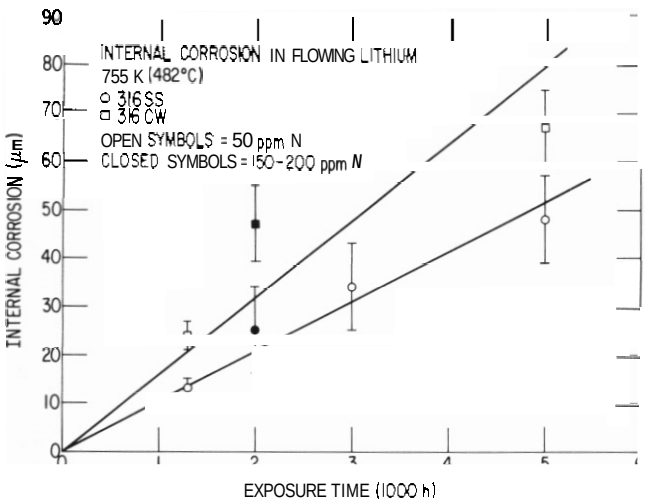

Fig. 9.3.5. Depth of internal corrosion for Type 316 stainless steel exposed to flowing lithium at 755 K.

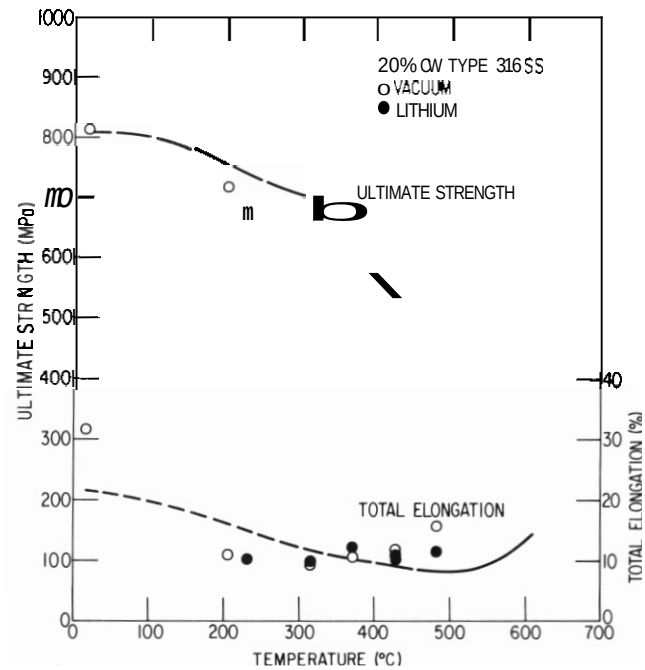

Fig. 9.3.6. Ultimate tensile strength and total elongation for 20% cold-worked Type 316 stainless steel tested in flowing lithium or vacuum. The curve represents the average values in air.

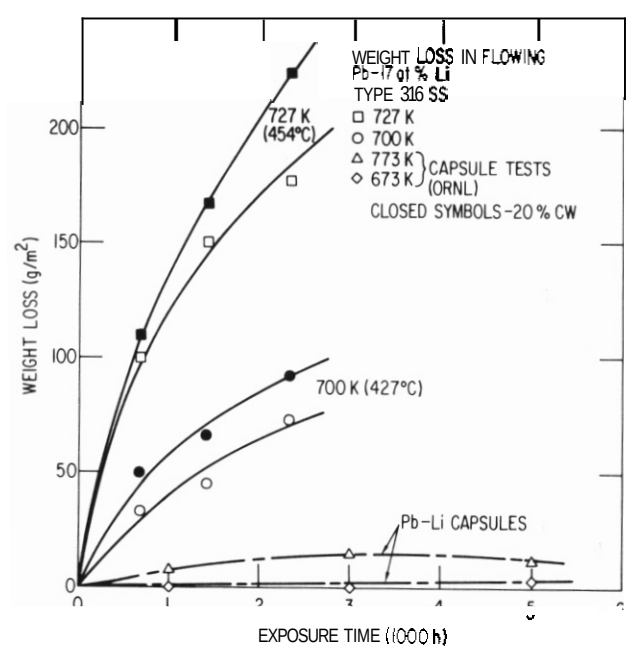

Fig. 9.3.7. Weight loss versus exposure time for annealed and 20% cold-worked Type 316 stainless steel exposed at 700 and 727 K to flowing Pb-Li. Each symbol type represents weight loss for a single specimen after various exposure times.

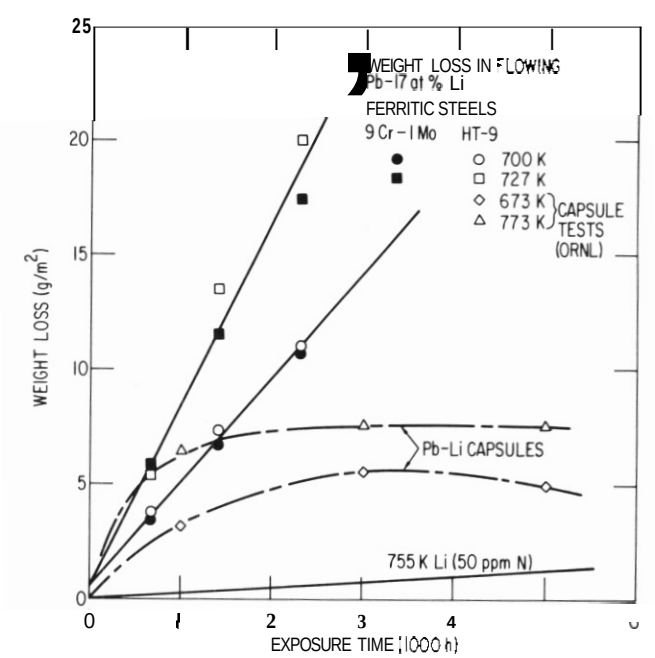

Fig. 9.3.8. Weight loss versus exposure time for ferritic HT-9 alloy and Fe-9Cr-1Mo steel exposed at 700 and 727 K to flowing Pb-Li. Each symbol type represents weight loss for a single specimen after various exposure times.

lithium. For example, the weight losses in the austenitic stainless steels are an order of magnitude greater than in the ferritic steels, and the weight loss for cold-worked Type 316 stainless steel is higher than in the annealed steel. The weight losses in the austenitic steels follow a power law with time, whereas weight loses of ferritic steels are linear.

Metallographic examination of the exposed specimens revealed that the austenitic stainless steels develop a weak and porous ferrite layer. This layer broke off easily during mounting or polishing of the specimens. Such internal corrosion was not observed for the ferritic steels.

Specimens of Path-A PCA alloy were also exposed for 3.26 Ms (905 h) to flowing lithium at 700 and 727 K. Weight loss in the specimens after the first cleaning in lithium was comparable to that of cold-worked Type 316 stainless steel. However, the PCA specimens continued to show weight loss upon subsequent cleaning. Consequently, an accurate value for weight loss could not be obtained for these specimens. After each cleaning, greyish flakes or powdery deposits were observed on the specimen surfaces. Metallographic examination of the deposits revealed that the grey flakes were sections of the ferrite layer that broke off from the specimen surface. Micrographs of the loose ferrite layer are shown in Fig. 9.3.9. The surface has a very porous and etched appearance. The twin boundaries can be seen clearly. Energy dispersive x-ray analysis showed that the surface layer consisted of >90% Fe and ~5% Cr. Additional corrosion tests are being conducted to evaluate the compatibility of PCA alloy in a flowing Pb-Li environment.

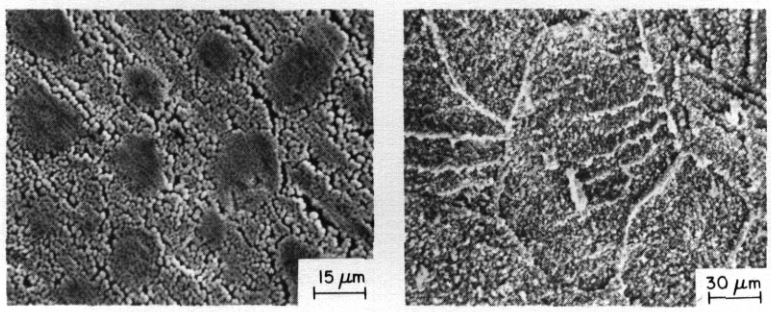

Fig. 9.3.9. Micrographs of the loose surface layer of ferrite on PCA alloy exposed at 727 K for 3.26 Ms in a flowing Pb-Li environment.

9.3.5 Conclusions

The corrosion data for austenitic and ferritic steels in flowing lithium at 700 nd 755 K indicate that weight losses for austenitic stainless steels follow a power law with time, whereas weight losses of ferritic steels follow a linear law. For identical exposure conditions, weight loss in the different austenitic stainless steels increases in the following order: annealed Type 304L, annealed Type 316, cold-worked Type 316, and PCA alloy. The dissolution rates of the ferritic steels are an order of magnitude lower. The austenitic steels develop a porous ferrite scale after exposure, and the ferritic steels show no internal corrosion. The thickness of the ferrite layer increases with time and may be expressed by a linear growth law.

Tensile data for cold-worked Type 316 stainles steel indicate that a flowing lithium environment has no effect on the tensile strength or total elongation of the steel. The tensile properties in flowing lithium and in vacuum are comparable.

Corrosion tests in a flowing Pb-17Li environment indicate that the dissolution rates for both austenitic and ferritic steels in Pb-Li are an order of magnitude greater than in flowing lithium. The influence of time, temperature, or alloy composition on the corrosion behavior in Pb-Li is similar to that in flowing lithium.

9.3.6 References

1. O. K. Chopra and D. L. Smith, "Effects of Lithium Environment on the Fatigue Properties of Ferritic and Austenitic Steels," J. Nucl. Mater, pp. 103-104, 651-656 (1981).

2. O. K. Chopra, D. L. Smith, and W. E. Ruther, "Environmental Effects on Properties of Structural Alloys," pp. 491-499 in Alloy Development for Irradiation Performance: Semiannual Progress Report for Period Ending March 31, 1982, Oak Ridge National Laboratory, DOE/ER-0045/8.

3. O. K. Chopra and D. L. Smith, "Environmental Effects on Properties of Structural Alloys," pp. 304-313 in Alloy Development for Irradiation Performance: Semiannual Progress Report for Period Ending September 30, 1981, Oak Ridge National Laboratory, DOE/ER-0045/9.

4. P. F. Tortorelli and J. H. Devan, "Corrosion of Path A PCA, Type 316 Stainless Steel and Fe-12Cr-1MoVW Steel in Flowing Lithium." ibid., pp.290-303.

5. P. F. Tortorelli, J. H. Devan, and R. M. Yonco, "Compatibility of Fe-Cr-Mo Alloys with Static Lithium." paper presented at Corrosion/81 T-2-1 Meeting, Toronto, Canada, 1981.

6. P. F. Tortorelli and J. H. Devan, "Corrosion of Ferrous Alloys in Static Pb and Pb-17 at % Li," pp. 314-322 in Alloy Development for Irradiation Performance: Semiannual Progress Report for Period Ending September 30, 1981, Oak Ridge National Laboratory, DOE/ER-0045/9.

9.4 COMPATIBILITY OF VANADIUM ALLOYS WITH HIGH-TEMPERATURE WATER — P. F. Tortorelli and J. H. DeVan (Oak Ridge National Laboratory)

9.4.1 ADIP Task

ADIP Task I.A.3, Perform Chemical and Metallurgical Compatibility Analyses.

9.4.2 Objective

The purpose of this task is to determine the compatibility of Path C vanadium alloys with high-temperature water for application to water-cooled fusion reactors. Candidate alloys are exposed to high-purity water in a stainless steel autoclave (with and without a hydrogen overpressure) to qualitatively determine (1) the extent of oxidation of the alloys and (2) the tendency for hydrogen uptake by these materials.

9.4.3 Summary

Weight gains of Path C vanadium alloys (V–20% Ti, V–15% Cr–5% Ti, Vanstar-7) exposed to 300°C water for 100 h were relatively small and not significantly affected by hydrogen overpressure.

9.4.4 Progress and Status

A recent investigation[1] showed that V–15% Cr and V–15% Cr–5% Ti undergo only limited oxidation in high-purity water and therefore may be considered for use with a water coolant in a fusion reactor. Consequently, we have conducted additional experiments to examine the effects of oxygen suppressants, particularly hydrogen, on the oxidation rate in water and on the potential for hydrogen uptake by these vanadium alloys. Several sets of tensile specimens of the three Path C alloys — V–20% Ti, V–15% Cr–5% Ti, and Yanstar-7 (V–9% Cr–3% Fe–1.2% Zr) — were exposed for 100 h to deaerated, deionized water in a stainless steel autoclave at 300°C to partially simulate pressurized water reactor conditions. The average steam pressure in the autoclave was about 9.0 MPa (1.3 ksi). After cooling from the exposure temperature, the specimens were removed from the autoclave, dried, and then imnediately weighed and tensile tested in air at room emperature. Portions of the specimens were used for microhardness determination (within 12 h of removal rom the autoclave) and hydrogen analysis (within 30 h). These analyses were performed as quickly as possible to avoid loss of hydrogen. Cross sections of the specimens were subsequently polished and etched for detai 1ed metal lographic examination.

The weight change, hardness, nd hydrogen concentration data are isted in Table 9.4.1, which also ontains data for control specimens. Consideration of the weight' change data shows that, although the growth rate of the oxide scale was signifi- ant over the 100-h test duration, he scale appears extremely protec- ive. Longer term experiments ill be needed to assess the oxida- ion kinetics. Although the weight ains per unit time are at least 0 times those reported previously1 For an exposure temperature of 250°C ather than the 300°C of our experiments), metallographic obser- vation of polished and etched cross sections revealed 1ittle apparent oxidation of the vanadium alloys (see Figs. 9.4.1–9.4.3). Also, as shown by the data in Table 9.4.1 and the micrographs in Figs. 9.4.1 through 9.4.3, the hydrogen overpressure had no effect: hardnesses, hydrogen concentrations, and tensile proper- ies were similar for the specimens xposed to water regardless of the presence of added hydrogen. This result is significant because ther- modynamic calculations of hydrogen artitioning predict a measurable ptake of hydrogen under equilibrium conditions with an 83-kPa (12-psi)

Table 9.4.1. Weight change, hardness, and hydrogen concentration for vanadium alloys exposed to deaerated water for 100 h at 300°C

Material condition	H_2 pressure (kPa)	H_2 pressure (psi)	Weight change (g/m^2)	Hardness (DPH)	Hydrogen content (wt ppm)
V–20% Ti					
Annealed, control				256	4
Annealed	0	0	+1.6	232	28
Annealed	83	12	+1.8	230	29
Cold worked	83	12	+0.2	320	22
Cold worked, control				313	15
V–15% Cr–5 Ti					
Annealed. control				276	4
Annealed'	0	0	+1.7	217	23
Annealed	83	12	+0.8	209	23
Cold worked	83	12	-0.5	336	16
Cold worked, control				332	17
*Vans*tar–7					
Annealed, control				231	4
Annealed	0	0	+1.4	202	17
Annealed	83	12	+0.9	198	17
Cold worked	83	12	–0.7	280	9
Cold worked, control				281	8

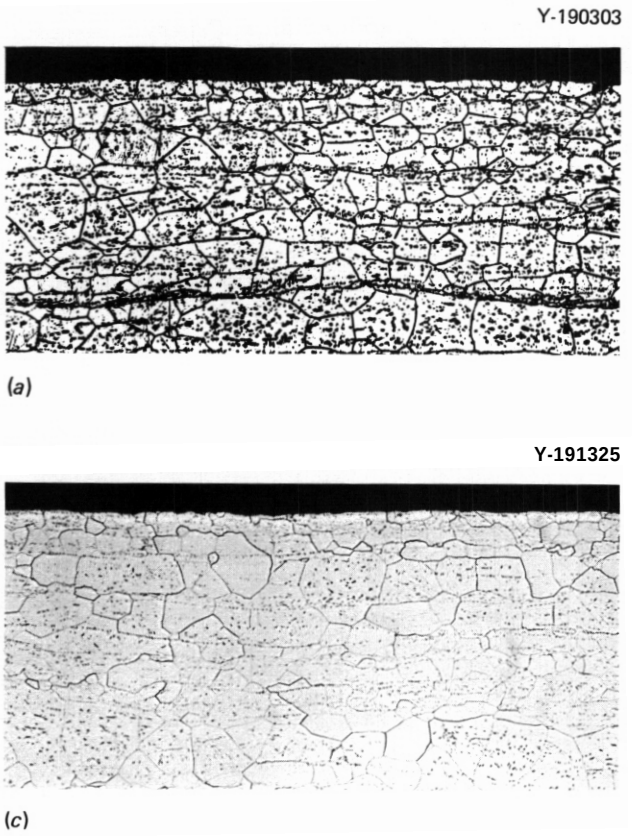

Fig. 9.4.1. Polished and etched cross sections of V–20% Ti exposed at 300°C for 100 h. (a) Control, held in vacuum. (b) Water, no hydrogen overpressure, (c) Water, 83 kPa hydrogen.

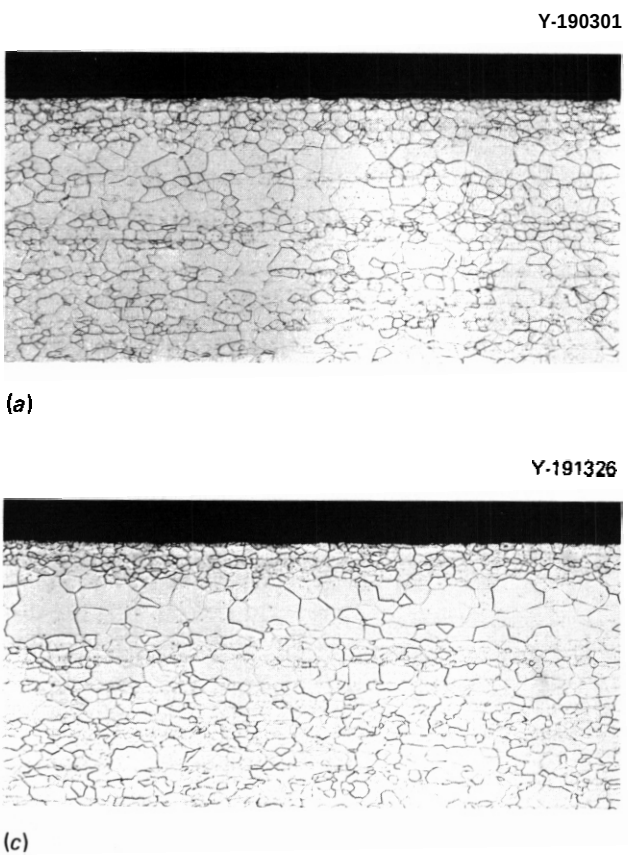

Fig. 9.4.2. Polished and etched cross sections of V–15% Cr–5% Ti exposed at 300°C for 100 h. (a) Control, held in vacuum. (b) Water, no hydrogen overpressure. (c) Water, 83 kPa hydrogen.

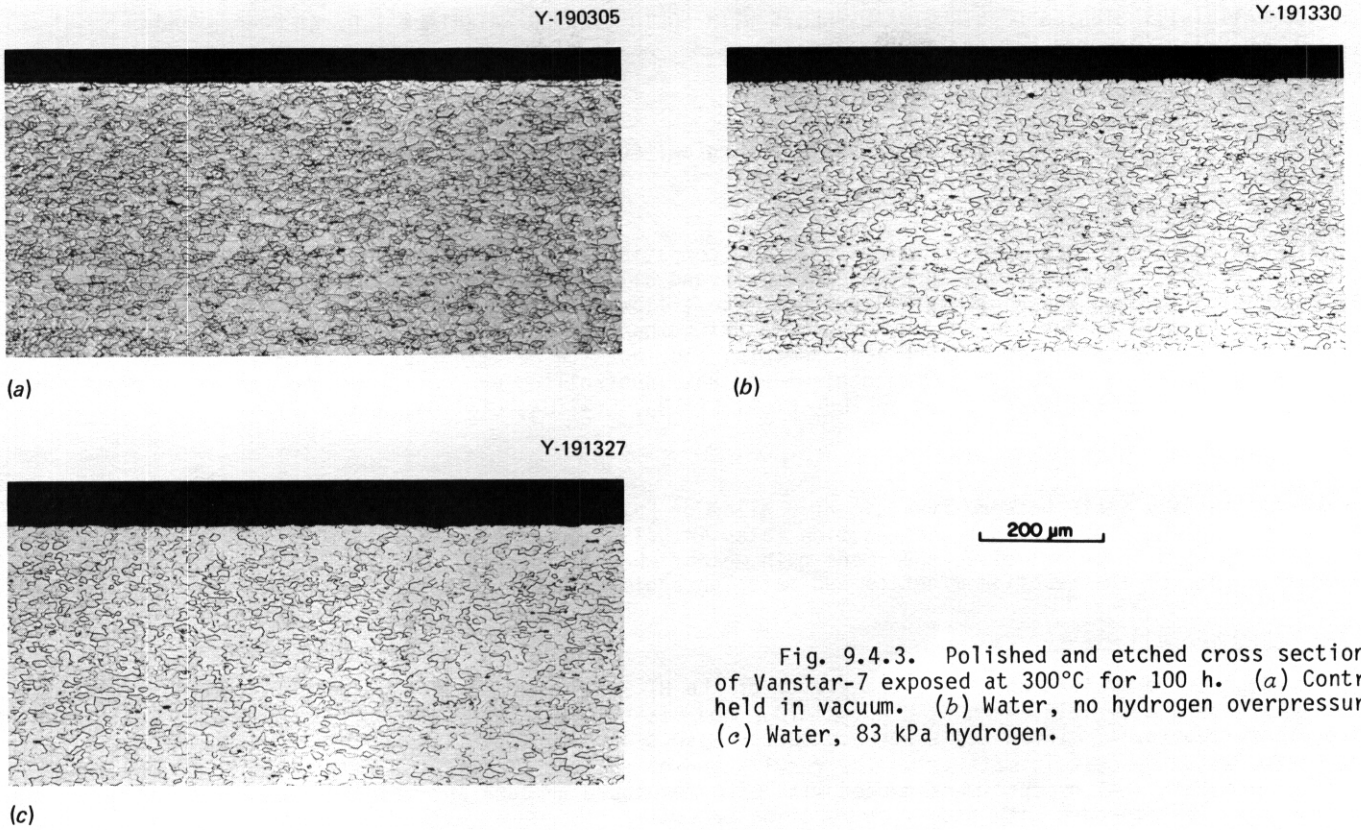

Fig. 9.4.3. Polished and etched cross sections of Vanstar-7 exposed at 300°C for 100 h. (*a*) Control, held in vacuum. (*b*) Water, no hydrogen overpressure. (*c*) Water, 83 kPa hydrogen.

hydrogen pressure.[2] These results suggest that the thin oxide film provides an effective hydrogen barrier on the vanadium alloys under our exposure conditions, in accord with a related study of hydrogen permeation through vanadium.[3] Further experiments with these alloys are planned to expand the above results and to gain a better understanding of the hydrogen uptake process.

9.4.5 Conclusions

1. According to initial results, the Path C vanadium alloys V–20% Ti, V–15% Cr–5% Ti, and Vanstar-7 appear to have acceptable oxidation rates in water at 300°C.
2. No effect of a hydrogen overpressure of 83 kPa (12 psi) on the compatibility of the vanadium alloys in 300°C water was observed.

9.4.6 References

1. O. K. Chopra, D. L. Smith, and W. E. Ruther, "Environmental Effects on Properties of Structural Alloys," pp. 491–99 in *ADIP Semiannu. Prog. Rep. Mar. 31, 1982*, DOE/ER-0045/8, U.S. DOE, Office of Fusion Energy.
2. E. Veleckis and R. K. Edwards, "Thermodynamic Properties in the Systems Vanadium-Hydrogen, Niobium-Hydrogen, and Tantalum-Hydrogen," *J. Phys. Chem.* 73, 683–92 (1969).
3. T. Namba et al., "Hydrogen Permeation Through Vanadium and the Effect of Surface Impurity Layer on It," *J. Nucl. Mater.* 105, 318–25 (1982).

9.5 COMPATIBILITY STUDIES OF STRUCTURAL ALLOYS WITH SOLID BREEDER MATERIALS - O. K. Chopra and D. L. Smith (Argonne National Laboratory)

9.5.1 ADIP Task

ADIP Task I.A.3, Perform Chemical and Metallurgical Compatibility Analyses.

9.5.2 Objective

The objective of this task is to evaluate the compatibility of solid breeder materials with structural alloys. The interactions between breeder materials and alloys are investigated as a function of temperature, time, and environmental parameters (i.e., flowing helium environments with different moisture contents). Reaction rates are determined by measuring the weight change, depth of internal penetration, and thickness of corrosion scales. These measurements, coupled with metallographic evaluation of the alloy surfaces, are used to establish the mechanisms and rate-controlling processes for the corrosion reactions. Breeder materials to be investigated include Li_2O, $LiAlO_2$, Li_2SiO_3, Li_2TiO_3, and Li_2ZrO_3.

9.5.3 Summary

Compatibility tests between ferritic HT-9 alloy or Fe-9Cr-1Mo steel and Li_2O pellets in a flowing helium environment indicate that the reaction rates in helium containing 93 ppm H_2O are greater than in helium with 1 ppm H_2O. All alloy specimens gain weight whereas the Li_2O pellets lose weight after exposure. Data on the reaction kinetics and metallographic evaluation of the alloy specimens are presented.

9.5.4 Progress and Status

A comparative evaluation of the reactivity of the HT-9 alloy and Type 316 stainless steel with solid tritium-breeding materials, such as Li_2O, $LiAlO_2$, and Li_2SiO_3 at 973 and 773 K (700 and 500°C) was presented in earlier reports.[1,2] Those tests were conducted with sealed capsules constructed from different alloys and packed with the ceramic material. The results indicated that Li_2O is the most reactive of the three breeder materials. Alloy specimens packed with Li_2O developed an adherent reaction scale consisting of the ceramic material embedded with iron-rich reaction products.

A significant result from the capsule compatibility tests was that the thickness of the reaction scale or depth of internal penetration was the same after 3.6 and 7.2 Ms (1000 and 2000 h). This behavior suggests that the interactions between alloy and ceramic stop after a short time. It is probable that in a closed system, such as in a sealed capsule, the chemical activity of the reactive species decreases with time. For a better understanding of the nature of the corrosive interactions, compatibility tests were conducted in a flowing-helium environment with controlled partial pressures of oxygen and hydrogen. Such experiments simulate the conditions projected for blanket structures during reactor operation.

A detailed description of the compatibility test facility was presented earlier.[3] Alloy specimens ~10 x 10 x 0.4 mm in size were sandwiched between two ~12-n-diameter by ~2.4-n-thick pellets of Li_2O (88% theoretical density) and mounted in a specimen holder such that the surface of the ceramic pellets was exposed to the flowing-gas environment. Figure 9.5.1 shows the specimen holder and the various alloy/ceramic reaction couples. A separate nickel foil (without Li_2O pellets) was placed downstream from the couples to study the deposition behavior. The gas environment was provided by premixed gas mixtures of He, H_2O, and H_2. Compatibility tests were conducted at 823 K for 1.8, 3.6, and 7.2 Ms (500, 1000, and 2000 h) in flowing helium with 93 ppm H_2O and 1 ppm H_2 and for 3.6, 9.0, and 14.4 Ms (1000, 2500, and 4000 h) in flowing helium with 1 ppm each of H_2O and H_2. During the test, the flow rate of the gas mixture through each specimen exposure tube was ~0.45 cm^3/s. This flow rate corresponds to a velocity of ~1.6 mm/s. Four reaction couples consisting of HT-9 alloy, Fe-9Cr-1Mo steel, 20% cold-worked Type 316 stainless steel, and either pure nickel or annealed Type 316 stainless steel were included in each compatibility test. Data on the reaction kinetics and a metallographic evaluation of the alloy specimens exposed in flowing helium containing 93 ppm H_2O and 1 ppm H_2 were presented in the last progress report.[3]

During the current reporting period, weight-change measurements and metallographic examination were performed on the alloy specimens exposed at 823 K in flowing helium containing 1 ppm each of H_2O and H_2. Figure 9.5.2 shows the alloy and Li_2O specimens fran the various reaction couples exposed for 14.4 Ms. After exposure, all alloys gained weight, whereas the Li_2O pellets lost weight. There was a net loss in weight for the total reaction couple. In some instances, the reaction scale on the ferritic HT-9 alloy and Fe-9Cr-1Mo steel spalled off when the specimens were removed from the holder; consequently, the weight gain of the alloys could not be determined for several reaction couples. The weight changes for the different alloys are given in Table 9.5.1.

Metallographic examination of the alloy specimens revealed that the reaction scale on the specimen surface consisted of a very uniform and dense layer of outer scale and a porous layer of subscale. The depth of internal penetration and the total scale thickness on ferritic alloys exposed with Li_2O in a

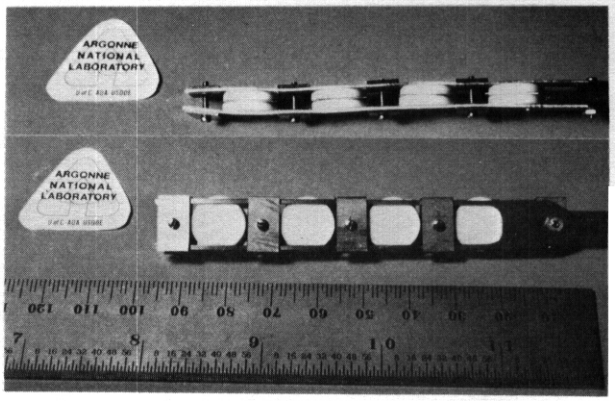

Fig. 9.5.1. Specimen holder and the various alloy/ceramic reaction couples.

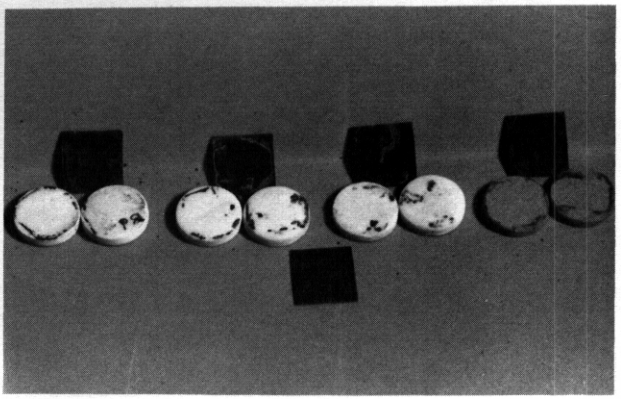

Fig. 9.5.2. Alloy and ceramic specimens from various reaction couples after a 14.4-Ms exposure at 823 K in helium containing 1 ppm each of H_2O and H_2.

Table 9.5.1. Weight change for alloys exposed with Li_2O at 823 K in a flowing helium environment containing 93 or 1 ppm H_2O and 1 ppm H_2

Exposure Time, Ms (h)	Weight Gain, mg					
	HT-9 Alloy	Fe-9Cr-1Mo	316 CW	316 SS	Pure Ni	Ni Foil[a]
		Helium with 93 ppm H_2O and 1 ppm H_2				
1.8 (500)	2.7	3.6	6.3	b	0.1	b
3.6 (1000)	2.3	3.5	6.2	4.6	b	0.6
7.2 (2000)	17.6	c	19.2	b	6.0	0.4
		Helium with 1 ppm H_2O and 1 ppm H_2				
3.6 (1000)	3.2	6.5	6.6	b	1.0	0.1
9.0 (2500)	7.3	2.5	7.2	c	b	0.6
14.4 (4000)	8.7	c	10.9	b	1.9	1.4

[a] Exposed without the Li_2O pellets and located downstream from the reaction couples.
[b] Not tested.
[c] Weight change could not be determined because the scale spalled off.

flowing-gas environment are plotted as a function of time in Fig. 9.5.3. The depth of internal penetration represents the actual metal loss and was obtained from the difference between the initial thickness and sound metal remaining, i.e., the unreacted metal. The results indicate that the corrosion behaviors of ferritic HT-9 alloy and Fe-9Cr-1Mo steel are similar. Internal penetration and total scale thickness under various test conditions are approximately the same for both steels.

Figure 9.5.3a indicates that the depth of internal penetration of the specimens exposed in helium containing 1 ppm H_2O reaches a constant value after an initial period of rapid interaction. The average value for the depth of internal penetration is ~15 μm after 3.6. 9.0, and 14.4 Ms exposure. The specimens exposed in helium containing 93 ppm H_2O may exhibit similar behavior. However, the longest duration of the tests with 93 ppm H_2O was 7.2 Ms and the penetration depth increased gradually with time. After the 7.2-Ms exposure, the average value of penetration in helium containing 93 ppm H_2O was greater than that in helium with 1 ppm H_2O.

The thickness of total reaction scale for the specimens exposed in helium with either 93 or 1 ppm H_2O increases with time. As seen earlier for the penetration depth, the total scale thickness of the specimens exposed in helium containing 93 ppm H_2O is greater than that for specimens exposed in helium with 1 ppm H_2O. For both moisture contents, the data follow a power law and the reaction rate decreases with time. It is probable that the total scale thickness also reaches a saturation value after longer exposure times. However, the scale thickness for the long-duration tests could not be determined because the scales had

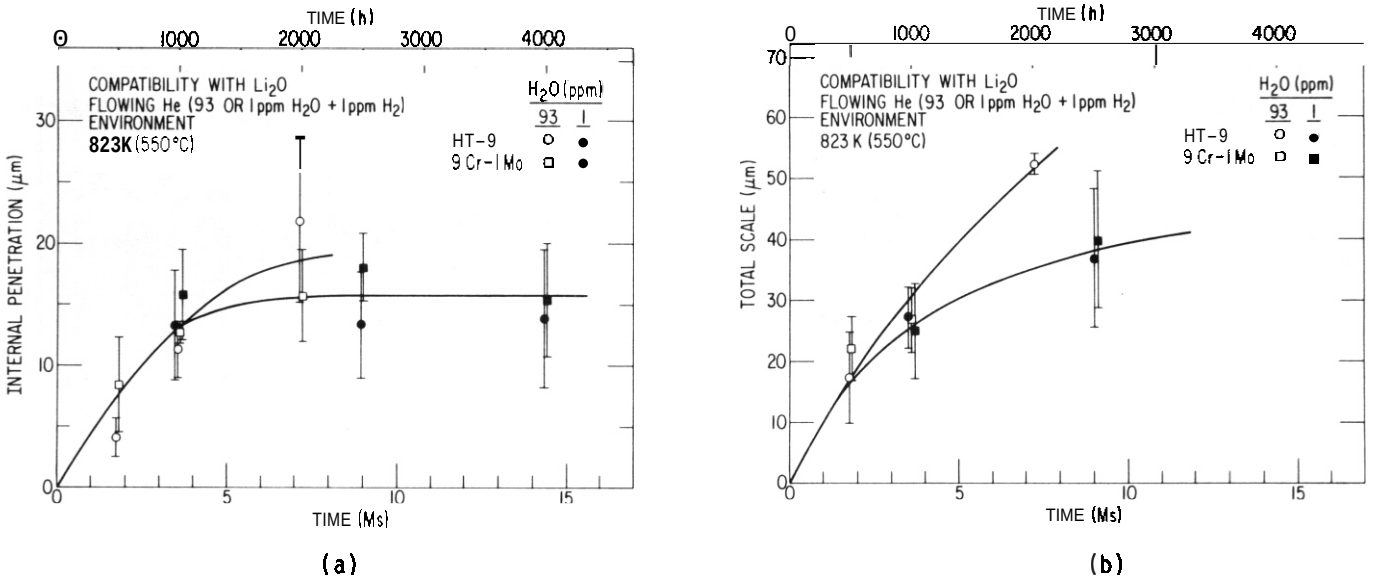

Fig. 9.5.3. (a) Internal penetration and (b) total scale thickness for HT-9 and Fe-9Cr-1Mo steel specimens exposed with Li_2O pellets at 823 K in flowing helium containing 93 or 1 ppm H_2O and 1 ppm H_2.

spalled off. Measurements of the depth of internal penetration and total scale thickness for the Type 316 stainless steel specimens are in progress.

Micrographs of the reaction scales on HT-9 alloy and Fe-9Cr-1Mo steel specimens exposed with Li_2O at 823 K in flowing helium containing 1 ppm H_2O and H_2 are shown in Figs. 9.5.4 and 9.5.5, respectively. All specimens show a very uniform and dense outer scale, a porous subscale. and corrosive penetration in the bulk material. Similar behavior was observed for specimens exposed in helium containing 93 ppm H_2O and 1 ppm H_2. The outer scale and subscale for HT-9 alloy and Fe-9Cr-1Mo steel show identical features. However, bulk penetration in the HT-9 alloy is uniform whereas the Fe-9Cr-1Mo steel exhibits penetration

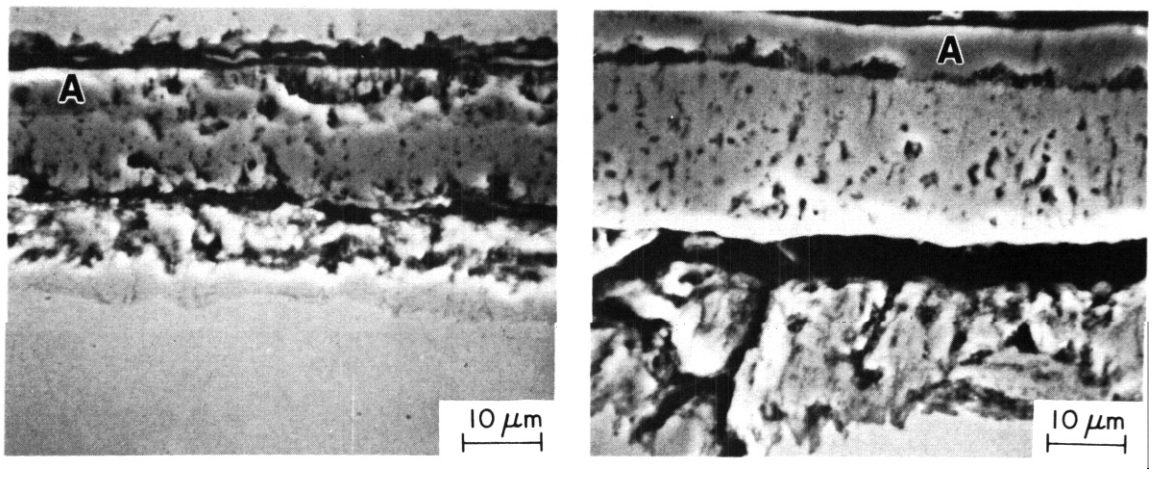

Fig. 9.5.4. Micrographs of the reaction scales on HT-9 alloy exposed with Li_2O pellets at 823 K for (a) 3.6 Ms and (b) 9.0 Ms in flowing helium containing 1 ppm each H_2O and H_2.

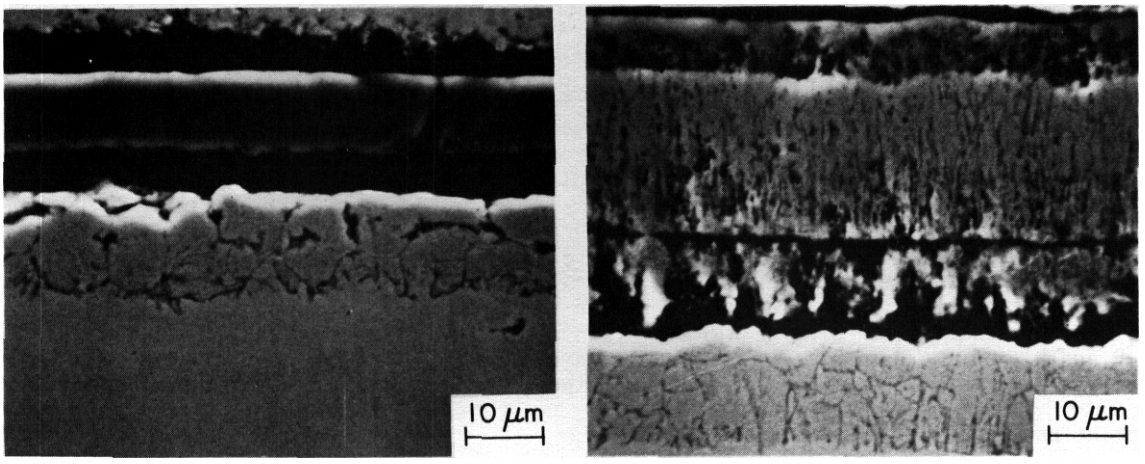

Fig. 9.5.5. Micrographs of the reaction scales on Fe-9Cr-1Mo Steel exposed with Li_2O pellets at 823 K for (a) 3.6 Ms and (b) 9.0 ms in flowing helium containing 1 ppm each H_2O and H_2.

along grain or martensitic lathe boundaries. The outer scale on both ferritic steels has a dark surface layer (region A in Fig. 9.5.4) which often disintegrated during mounting or polishing of the specimens. The entire outer scale spalled off in some specimens when the reaction couples were separated or removed from the specimen holder. Such specimens showed a net loss in weight as well as in thickness.

Energy dispersive x-ray analyses of the various regions of the reaction scale, on both of the ferritic steels exposed in helium containing 1 ppm H_2O, fndicate that the outer scale is primarily lithium-iron oxide. The chemical composition of the dark surface layer of the outer scale was 57% Fe and 0.3% Cr and the dense scale contained 69% Fe and 0.5% Cr. The porous subscale consisted of 48% Fe, 18%Cr, and 2% Mo. Enrichment of V (only for Fe-9Cr-1Mo steel) and Si was also observed in the subscale. Electron microprobe analyses of the reaction scale yielded oxygen concentrations between 25 and 30%. These results suggest ~4% Li (obtained by difference) in the reaction scale. The dark surface layer may contain ~12%Li.

The Li_2O pellets from the various reaction couples lost weight after exposure and their weight loss in helium containing 93 ppm H_2O was greater than in helium with 1 ppm H_2O. Figure 9.5.6 shows the weight loss, expressed as a percent of the initial weight, of the Li_2O pellets exposed with the ferritic steels. The results can be expressed by a linear law and yield weight losses of 12.2 and 3.8%/year of Li_2O exposed in

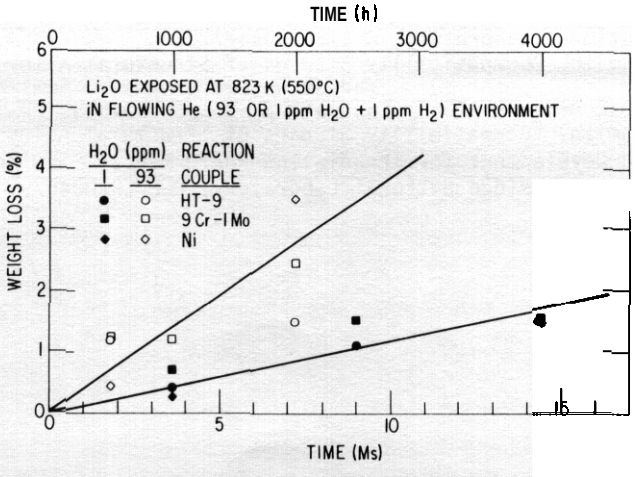

Fig. 9.5.6. Weight loss for Li_2O pellets exposed with different alloys at 823 K in flowing helium containing 93 or 1 ppm H_2O and 1 ppm H_2.

helium with 93 ppm and 1 ppm H_2O, respectively. These values are 2 to 3 orders of magnitude greater than those predicted fran equilibrium reaction kinetics. However, two separate interactions, viz., gas-pellet and alloy-pellet interactions, contribute to the measured weight loss. The moisture in the helium environment reacts with Li_2O to form LiOH gas whfch is carried away by the flowing gas stream. This reaction leads to a net weight loss for Li_2O as well as to the total reaction couple. The alloy-pellet interactions in the presence of moisture lead to the formation of ternary oxides of Li and Fe or Cr on the alloy surface. Such reactions result in a weight loss for Li_2O, a weight gain for the alloy specimen, and a net weight gain for the total reaction couple. Data on weight change show between 1- and 12-mg (i.e., 0.1 to 1.2%) loss in weight for the various reaction couples, indicating that the gas-pellet interactions dominate the weight loss for the Li_2O pellets.

The weight loss for Li_2O pellets exposed with pure nickel specimens is included in Fig. 9.5.6. The nickel specimens showed significant internal corrosive attack and weight gain, particularly after long exposure times. However, the dense outer reaction scale was not observed and the weight gain of the nickel specimens was a factor of 5 to 10 lower than that for the ferritic steels.

Metallographic examination of Type 316 stainless steel specimens exposed in helium containing 1 ppm each of H_2O and H_2 is in progress. X-ray diffraction and electron microprobe analyses of the reaction scales on both ferritic and austenitic steels are being conducted to positively identify the various phases.

9.5.5 Conclusions

Data from the compatibility tests in a flowing- helium environment indicate that the reaction rates in helium containing 93 ppm H_2O are greater than in helium with 1 p p H_2O. All alloy specimens gain weight after exposure. Both ferritic steels exposed in helium with either 93 or 1 ppm H_2O develop a dense iron-rich scale and a porous chromium-rich subscale. The dense outer scale tends to spall off easily. The pure nickel specimens also show corrosive penetration and weight gain. However, the weight gain for nickel is significantly lower than that for the ferritic steels.

Measurements of the reaction-scale thickness indicate that the depth of internal penetration, i.e., actual metal loss, for ferritic specimens exposed in helium containfng 1 ppm H O reaches a constant va ue after ~3.6 Ms. A similar behavior was observed earlier from compatibility tesb with sealed capsules.' The specimens exposed in helium containing 93 ppm H_2O show a gradual increase in penetration up to 7.2 Ms. The penetration depth may reach a constant value for longer exposure times. For both moisture contents, the thickness of the total reaction scale follows a power law and the reaction rate decreases with time. Additional data are required to establish the long-term reaction kinetics as a function of moisture content in helium.

The Li_2O pellets exposed with the various reaction couples show weight loss and there is a net loss in weight for the total reaction couple. The weight loss in helium containing 93 ppm H_2O is greater than in helium containing 1 ppm H_2O. The weight loss for Li_2O pellets follows a linear law and yields weight loss values of 12.2 and 3.8%/year in helium with 93 and 1 ppm H_2O, respectively. These values are significantly greater than those predicted from equilibrium reaction kinetics. However, the weight-loss for the Li_2O pellets results fran both gas- and alloy-pellet interactions.

9.5.6 References

1. O. K. Chopra and D. L. Smith, "Environmental Effects on Properties of Structural Alloys," pp. 321-327 in Alloy Development for Irradiation Performance: Semiannual Progress Report for Period Ending September 30, 1981, Oak Ridge National Laboratory, DOE/ER-0045/7.

2. O. K. Chopra and D. L. Smith, "Compatibility Studies of Structural Alloys with Solid Breeder Materials," pp. 507-513 in Alloy Development for Irradiation Performance: Semiannual Progress Report for Period Ending March 31, 1982, Oak Ridge National Laboratory, DOE/ER-0045/8.

3. O. K. Chopra and D. L. Smith, "Compatibility Studies of Structural Alloys with Solid Breeder Materials," pp. 323-338 in Alloy Development for Irradiation Performance: Semiannual Progress Report for Period Endin Se tembe [redacted] Oak Ridge National Laboratory, DOE/ER-0045/9.

DOE/ER-0045/10
Distribution
Category
UC-20, 20c

DISTRIBUTION

1–6. Argonne National Laboratory, 9700 South Cass Avenue, Argonne, IL 60439

L. Greenwood
V. Maroni
R. F. Mattas
R. E. Nygren
D. L. Smith
H. Wiedersich

7–8. Battelle-Pacific Northwest Laboratory, P.O. Box 999, Richland, WA 99352

J. L. Brimhall
D. Dingee

9. Brookhaven National Laboratory, Upton, NY 11973

C. L. Snead, Jr.

10–193. Department of Energy, Technical Information Center, Office of Information Services, P.O. Box 62, Oak Ridge, TN 37830

For distribution as shown in TID-4500 Distribution Category, UC-20 (Magnetic Fusion Energy), and UC-20c (Reactor Materials)

194–200. Department of Energy, Office of Fusion Energy, Washington, DC 20545

M. M. Cohen
G. M. Haas
T. C. Reuther, Jr. (5 copies)

201. Department of Energy, Oak Ridge Operations Office, P.O. Box E. Oak Ridge, TN 37830

Office of Assistant Manager for Energy Research and Development

202. Energy Technology Engineering Center, P.O. Box 1449, Canoga Park, CA 91304

ETEC Library

203–204. GA Technologies, Inc., P.O. Box 81608, San Diego, CA 92138

T. A Lechtenberg
D. I. Roberts

205207. Lawrence Livermore National Laboratory, P.O. Box 808, Livermore, CA 94550

E.N.C. Dalder
M. Guinan
C. M. Logan

208. Los Alamos National Laboratory, Mail Stop H809, Los Alamos, NM 87545

M. S. Wechsler

209. Massachusetts Institute of Technology, *138* Albany Street, Cambridge, MA 02139

O. K. Harling

210–211. Massachusetts Institute of Technology, 77 Massachusetts Ave., Cambridge, MA 02139

N. J. Grant
V. B. Vander Sande

212–213. McDonnell Douglas Astronautics Company, East, P.O. Box 516, St. Louis, MO 63166

J. W. Davis
D. L. Kummer

214. Mellon Institute, Schenley Park, Pittsburgh, PA 15213

J. C. Williams

215. National Materials Advisory Board, 2101 Constitution Ave., Washington, DC 20418

K. M. Zwilsky

216–217. Naval Research Laboratory, Washington, DC 20375

Superintendent, Materials Science and Technology Division
J. A Sprague

218–254. Oak Ridge National Laboratory, P.O. Box X, Oak Ridge, TN 37830

Central Research Library (2 copies)
Document Reference Section
Laboratory Records Department (2 copies)
Laboratory Records Department, RC
ORNL Patent Section
E. E. Bloom (10 copies)
D. N. Braski
F. R. Cox (3 copies)
J. H. DeVan
I. T. Dudley
M. L. Grossbeck
R. L. Klueh
R. A. Lillie
C. T. Liu
K. C. Liu
L. K. Mansur
P. J. Maziasz
C. J. McHargue
T. K. Roche
A. F. Rowcliffe
J. L. Scott
P. F. Tortorelli
3. M. Vitek
F. W. Wiffen

255–256. Rensselaer Polytechnic Institute, Troy, NY 12181

D. Steiner
N. Stoloff

257–258. Sandia National Laboratories, Livermore Division 8316, Livermore, CA 94550

W. Bauer
J. Swearengen

259. Science Applications, Inc., 1200 Prospect, La Jolla, CA 92037

H. Gurol

260–262. University of California, Department of Chemical, Nuclear, and Thermal Engineering, Los Angeles, CA 90024

M. A Abdou
R. W. Conn
N. M Ghoniem

263. University of California, Santa Barbara, CA 93106

G. R. Odette

264. University of Missouri, Department of Mechanical and Aerospace Engineering, Columbia, MO 65211

M. Jolles

265. University of Virginia, Department of Materials Science, Charlottesville. VA 22901

W. A. Jesser

266. University of Wisconsin, 1500 Johnson Drive, Madison, WI 53706

W. G. Wolfer

U S GOVERNMENT PRINTING OFFICE 1983 646 055/168

267–268. Westinghouse Electric Company, Advanced Energy Systems Division, P.O. Box 158, Pittsburgh, PA 15236

W. A. Boltax
R. E. Gold

269–276. Westinghouse Hanford Company, P.O. Box *1970,* Richland, WA *99352*

H. R. Brager
D. G. Doran
A. M. Ermi
F. A. Garner
D. S. Gelles
E. C. Opperman
R. W. Powell
J. L. Straalsund